

# High Efficiency Photochemical Water Splitting on III-Nitride Nanowires

Md Golam Kibria



Department of Electrical and Computer Engineering  
Faculty of Engineering, McGill University, Montréal  
April 2015

A thesis submitted to McGill University in partial fulfillment of the requirements of  
the degree of Doctor of Philosophy

---

© Md. Golam Kibria 2015

*To my Loved Ones*

# Table of Contents

Acknowledgement .....	7
Contribution of Authors .....	9
List of Figures .....	11
List of Acronyms .....	17
Abstract .....	19
Abrégé .....	21
<b>Chapter-1</b>	
<b>Introduction</b> .....	23
1.1 Overview .....	23
1.1.1 Renewable Energy Options .....	23
1.1.2 Solar Energy .....	23
1.1.3 Importance of Solar Energy Storage .....	24
1.1.4 Necessity for Solar Water Splitting .....	24
1.2 Basic Principles of Solar Water Splitting .....	25
1.3 Motivation for Using Group-III Nitride for Water Splitting .....	29
1.4 A Brief Review on the Metal/Non-metal Nitrides for Water Splitting .....	31
1.4.1 PEC Water Splitting Studies using Metal-/Non-metal Nitrides .....	31
1.4.2 Photochemical Water Splitting Studies using Metal-/Non-metal Nitrides .....	35
1.5 Motivation for Choosing “Nanowire” as a Water Splitting Photocatalyst .....	36
1.6 Organisation of the Thesis .....	37
1.7 Conclusions .....	39
<b>Chapter-2</b>	
<b>Growth and Characterization of III-Nitride Nanowires</b> .....	40
2.1 Introduction .....	40
2.2 III-Nitride Nanowire Growth Techniques .....	40
2.3 Characterization Techniques of the Nanowires .....	42
2.3.1 Scanning Electron Microscopy (SEM) .....	42
2.3.2 Transmission Electron Microscopy (TEM) .....	43

2.3.3 Photoluminescence (PL) Spectroscopy .....	45
2.3.4 Raman Scattering Spectroscopy .....	46
2.3.5 X-ray Photoelectron Spectroscopy (XPS).....	47
2.3.6 Experimental Set-up for Photochemical Water Splitting .....	49
2.3.7 Deposition Process of Co-catalysts .....	50
2.4 Conclusions.....	52

### **Chapter-3**

#### **High Efficiency Overall Water Splitting on GaN Nanowire Arrays under Ultraviolet Light.....**

3.1 Introduction.....	53
3.2 Photochemical Water Splitting on GaN Nanowire Arrays .....	54
3.2.1 Test Reaction for GaN Nanowire .....	54
3.2.2 Role of Co-catalyst on Photocatalytic Activities .....	56
3.2.3 Characterization of Photodeposited Rh/Cr <sub>2</sub> O <sub>3</sub> Core-shell Nanostructures.....	58
3.2.4 Overall Water Splitting on Rh/Cr <sub>2</sub> O <sub>3</sub> Nanoparticle Decorated GaN Nanowires.....	60
3.3 Highly Efficient Overall Water Splitting on <i>p</i> -type GaN Nanowires.....	62
3.3.1 <i>n</i> - and <i>p</i> -type GaN Nanowire .....	62
3.3.1 Structural Characterization of GaN:Mg Nanowires.....	64
3.3.2 Near-surface Band Structure of GaN:Mg Nanowires .....	66
3.3.3 <i>p</i> -type Doping in GaN Nanowires.....	67
3.3.4 H <sub>2</sub> and O <sub>2</sub> Half Reactions.....	68
3.3.5 Rh/Cr <sub>2</sub> O <sub>3</sub> Co-catalyst Deposition on GaN:Mg Nanowires .....	70
3.3.6 Overall Pure Water Splitting on GaN:Mg Nanowires .....	72
3.3.7 Discussions on Efficiency and Stability.....	74
3.4 Conclusions.....	76

### **Chapter-4**

#### **One-Step Overall Water Splitting under Visible Light Using Multi-Band InGaN/GaN Nanowire Heterostructure .....**

4.1 Introduction.....	77
-----------------------	----

4.2 Growth and Characterization of InGaN/GaN Multi-band Nanowire Heterostructure.....	78
4.3 The Test Reactions for InGaN/GaN Nanowires.....	82
4.4 Rh/Cr <sub>2</sub> O <sub>3</sub> Co-catalyst Photodeposition on InGaN/GaN Nanowires.....	83
4.5 On the Valence State of Rh/Cr <sub>2</sub> O <sub>3</sub> Co-catalyst Particles.....	84
4.6 Overall Water Splitting on InGaN/GaN Nanowires.....	86
4.7 On the Stability of Rh/Cr <sub>2</sub> O <sub>3</sub> Co-catalyst.....	91
4.8 Conclusions.....	92

## **Chapter-5**

<b>Visible Light Driven Efficient Overall Water Splitting using <i>p</i>-type Group III-nitride Nanowire Arrays.....</b>	<b>93</b>
5.1 Introduction.....	93
5.2 Impact of Surface Band Bending on the Surface Electron and Hole Distribution.....	94
5.3 Growth and Characterization of InGaN:Mg Nanowires.....	96
5.4 Estimation of Nanowire Surface Band Bending from ARXPS.....	98
5.5 Band Bending in Equilibrium with Water.....	100
5.6 Role of Rh/Cr <sub>2</sub> O <sub>3</sub> Core-shell Co-catalyst.....	100
5.7 Overall Neutral Water Splitting.....	103
5.8 <i>p</i> -Type behavior of GaN:Mg and In <sub>0.2</sub> Ga <sub>0.8</sub> N:Mg from Open Circuit Potential (OCP) Measurement.....	107
5.9 Overall Water Splitting on <i>p</i> -GaN/ <i>p</i> -In <sub>0.20</sub> Ga <sub>0.80</sub> N Nanowires.....	109
5.10 Conclusions.....	114

## **Chapter-6**

<b>Defect-Engineered GaN:Mg Nanowire Arrays for Overall Water Splitting under Violet Light.....</b>	<b>115</b>
6.1 Introduction.....	115
6.2 Growth, Structural and Optical Characterization.....	116
6.3 Overall Water Splitting under Violet Light.....	121
6.4 Conclusions.....	124

## **Chapter-7**

<b>Strategies for Achieving Photochemical Overall Water Splitting under Red Light Irradiation</b> .....	125
7.1 Introduction.....	125
7.2 Development of InGaN Disk-on-wire Nanowire Heterostructures .....	126
7.3 InGaN Nanostructures on SiO <sub>x</sub> /Si Nanowires .....	129
7.4 Conclusions.....	133

## **Chapter-8**

<b>Dye-Sensitized Nanowire Photocatalyst for Water Splitting under Visible Light</b> .....	134
8.1 Introduction.....	134
8.2 Basic Principle of Dye-Sensitized Photocatalysts .....	134
8.3 Development of Dye-sensitized InGaN Nanowire Photocatalyst.....	135
8.4 Conclusion .....	141

## **Chapter-9**

<b>Conclusion and Future Directions</b> .....	142
9.1 Summary of the Thesis Work .....	142
9.2 Future Directions .....	144
9.2.1 Plasmon Enhanced Solar-to-Hydrogen Conversion on Metal Nitride Nanowire Arrays.....	144
9.2.2 Development of Earth Abundant Co-catalyst for Efficient Water Splitting .....	146
9.2.3 III-Nitride Nanowires for CO <sub>2</sub> Reduction.....	148
9.3 Conclusions.....	149
<b>List of Publications</b> .....	150
<b>APPENDIX-1</b> .....	157
<b>APPENDIX-2</b> .....	159
References.....	163

# Acknowledgement

First and foremost, I would like to express my heartfelt gratitude to Almighty ALLAH, the Most Gracious, the Most Merciful, for His countless blessings and mercy upon me. Surely I belong to Him, and to Him shall I return. He has blessed me with knowledge, strength, enthusiasm, and perseverance to complete this dissertation work in time and with this much capacity.

I would like to express my sincere gratitude to my advisor Prof. Zetian Mi for giving me the opportunity to work with him in such a well-equipped research facility at McGill University. I am grateful to him for introducing me to the exciting arena of solar-fuel generation. Throughout this research work, I have got utmost and continuous support, perfect guidance, thoughtful suggestions, magnificent cooperation, tremendous inspiration and valuable time from him. I am truly indebted to him for his strongest support in every step of this thesis work, and for allowing me to use the state-of-the-art research facilities very frequently for my research. I was fortunate to have him as my advisor, who was literally available 24/7 to provide feedback, suggestions and to arrange numerous growths to accelerate my research work.

I am indebted to the nanowire growers, especially F.A. Chowdhury, Dr. H. P. T. Nguyen, Dr. S. Zhao, and Dr. Kai Cui for their time and patience in growing a large number of high quality samples using MBE during the course of this dissertation work. I truly acknowledge their tireless efforts to keep the giant MBE machine alive for 24/7.

Special thanks to my colleagues Dr. Qi Wang, A. Connie, Dr. S. Zhao, Dr. S. Arafin, Dr. K. H. Li, and Dr. S. Fathololoumi for helping me out with PL measurement.

My sincere thanks to my PhD evaluation committee members, Prof. Ishiang Shih, Prof. Rob Sladek, and Prof. K. H. Bevan for their invaluable suggestions, comments and guidance on my thesis work. I really appreciate my PhD defence committee members Prof. Milica Popovich, Prof. Patanjali Kambhampati, Prof. Thomas Szkopek, Prof. K. H. Bevan, Prof. Jean Barrette, and Prof. Dunwei Wang for their time and constructive comments and suggestions on my thesis.

I am indebted to my colleagues for their time, suggestions and discussion throughout my PhD studies at McGill University. Here I am sincerely enlisting their names: Dr. H. P. T. Nguyen, Dr. S. Zhao, F.A. Chowdhury, Dr. Qi Wang, Dr. M. Harati, S. Fan, Dr. K. Cui, A. Connie, Dr. S. Arafin, Dr. K. H. Li, and Dr. S. Fatholouloumi, S. Sadaf, Dr. L. Li, Dr. S. Zhang, B. AlOtaibi, B. Huy Le, N. H. Tran, J. Kang, R. Wang, Dr. O. Salehzadeh, X. Liu, Dr. Y. Wang, Shih, S. Mukherjee, M. H. T. Dastjerdi, M. Djavid.

I would like to convey my heartfelt thanks to Dr. M. L. Trudeau at Science des Matériaux, IREQ, Hydro-Québec and Dr. David Liu at FEMR, McGill University for carrying out a lot of TEM studies on my samples.

I am grateful to the staff members of McGill Nanotools microfab (MNM) including Dr. Matthieu Manini, Donald Berry, Jun Lee, and Dr. Lino Eugene, for their technical support, training and discussions on my research and for helping me out in different cleanroom activities.

My heartfelt appreciation goes to my lovely wife Dr. Rafia Islam for her inspiration, love, support, patience and presence in my life.

Last but by no means the least; I appreciate the continuous support and love of my Mom Tahera Khatun and my Dad Md Amanat Hossain, my Father-in-law Dr. Rafiqul Islam, my mother-in-law Zannatul Ferdousi Islam, and other loved ones. This work would not have been possible without them.

This work is supported by the Natural Sciences and Engineering Research Council of Canada (NSERC), the Fonds de recherche sur la nature et les technologies, Canada Foundation for Innovation, the Climate Change and Emissions Management Corporation (CCEMC) and the Hydro-Quebec Nano-Engineering Program at McGill University.

## Contribution of Authors

This dissertation work includes the contribution of the candidate and many other individuals. The candidate and his advisor Prof. Zetian Mi conceived the idea and worked together closely in designing the nanowire heterostructure, planning the experiments and in writing the manuscripts. The sample preparation for the MBE growth was carried out by the candidate together with Dr. H. P. T. Nguyen, Dr. S. Zhao, F.A. Chowdhury, S. Fan, and S. Sadaf. The MBE growth of III-nitride nanowire was performed by F.A. Chowdhury, Dr. H. P. T. Nguyen, Dr. S. Zhao, S. Fan, and Dr. K. Cui under direct supervision of Prof. Zetian Mi. The Photoluminescence experiment was performed by the candidate together with A. Connie, Dr. S. Zhao, Dr. Qi Wang, Dr. S. Arafin, Dr. K. H. Li, and Dr. S. Fatholouloumi. The SEM imaging was performed by the candidate together with F. A. Chowdhury. The XPS analysis was performed by the candidate at McGill Institute for Advanced Materials (MIAM). Mr. Christophe Chabanier at Institut national de la recherche scientifique (INRS), Varennes (Quebec), Canada contributed to some of the XPS analysis. Dr. J. Lefebvre at Université de Montréal and Prof. Royston Paynter at INRS assisted in XPS data analysis. The micro-Raman analysis was performed by the candidate together with Dr. Qi Wang, Dr. S. Zhao and Timothy Gonzalez at the Department of Chemistry, McGill University; and the equipment was provided by Prof. Mark Andrews at the Department of Chemistry, McGill University. The TEM analysis was mostly carried out by M. L. Trudeau at Science des Matériaux, IREQ, Hydro-Québec, Canada. Some of the TEM analysis were performed at Canadian centre for Electron Microscopy (CCEM) at McMaster University, Hamilton, Canada, and some were by the candidate and Dr. David Liu at Facility for Electron Microscopy Research (FEMR), McGill University. The water splitting experimental set-up was designed by the candidate helped by Dr. Defa Wang. The experiments were performed by the candidate together with F. A. Chowdhury. B. AlOtaibi helped in PEC studies and discussions. Prof. H. Guo and Dr. Dongping Liu at the Department of Physics, McGill University are contributed to the result analysis and discussions. Dr. Shaofei Zhang

contributed to the calculation of photo-excited carrier distribution of nanowire structures by simulation program APSYS.

# List of Figures

Figure 1-1: (a) Photoelectrochemical (PEC) water splitting on nanowire photoelectrode, (b) Photochemical water splitting on co-catalyst nanoparticle decorated nanowire photocatalyst. ....	26
Figure 1-2: Schematic illustration of the three main process steps in photochemical water splitting on nanowire photocatalyst. ....	27
Figure 1-3: Schematic illustration of band edge requirements for overall water splitting reaction. ....	29
Figure 1-4: Band edge positions of commonly used photocatalysts. The oxidation and reduction potentials of water are also shown with green dotted lines. The red dotted line represents the band edge positions of $\text{In}_x\text{Ga}_{1-x}\text{N}$ with x increasing from left to right (0-1). ....	30
Figure 2-1: Veeco Gen II - Plasma-assisted molecular beam epitaxy system at McGill. ....	42
Figure 2-2: Schematic of electron beam line path in a transmission electron microscopy machine [104]. ....	44
Figure 2-3: Schematic illustration of the operating principal of X-ray photoelectron spectroscopy in studying a semiconductor material. Here, $\phi_{\text{sample}}$ and $\phi_{\text{spec}}$ are the work function of the sample and spectrometer, respectively. $E_B$ is the binding energy of the electron. $E_K(\text{sample})$ and $E_K(\text{spec})$ are the kinetic energy of the photo-excited electron and spectrometer measured electron, respectively. ....	48
Figure 2-4: Schematic illustration of the experimental set-up for photochemical water splitting. ....	50
Figure 2-5: Schematic illustration of two-step photodeposition process of Rh (core) and $\text{Cr}_2\text{O}_3$ (shell) co-catalyst nanoparticles on the nanowires. ....	51
Figure 2-6: Schematic illustration of the photodeposition mechanism of Rh co-catalyst on a semiconductor photocatalyst under photoexcitation [112]. ....	52
Figure 3-1: $\text{H}_2$ or $\text{O}_2$ evolution reaction in the presence of sacrificial reagents. (a) test reaction for $\text{H}_2$ evolution, (b) test reaction for $\text{O}_2$ evolution. ....	55
Figure 3-2: (a) $\text{H}_2$ evolution reaction and (b) $\text{O}_2$ evolution reaction in the presence of respective sacrificial reagents over GaN nanowires under a 300W full arc xenon lamp irradiation. The insets show the reaction mechanism. ....	56
Figure 3-3: Upward band bending on nominally undoped or n-type GaN, which drives holes to the nanowire sidewall and electrons into the bulk. ....	57
Figure 3-4: Schematic of electron transfer from photocatalyst to co-catalyst (process 1), $\text{H}_2$ evolution (process 2) for overall water splitting [25]. ....	58
Figure 3-5: (a) Low magnification TEM image shows uniform distribution of the Rh/ $\text{Cr}_2\text{O}_3$ nanoparticles on GaN nanowire surfaces. (b) HRTEM image and (c) HR-HAADF image clearly show the Rh/ $\text{Cr}_2\text{O}_3$ core-shell nanostructures deposited on GaN nanowires, (d) illustration of $\text{H}_2$ evolution on Rh (core)/ $\text{Cr}_2\text{O}_3$ (shell) nanoparticles as a co-catalyst for overall photocatalytic water splitting [25, 125]. ....	59
Figure 3-6: (a) HR-HAADF image and (b) EELS mapping image, (c–g) corresponding individual element mapping images and (h) RGB image (Red: Cr, Green: Rh, Blue: Ga), clearly showing the Rh/ $\text{Cr}_2\text{O}_3$ core/shell nanostructure deposited on GaN nanowires. ....	61

Figure 3-7: (a) Schematic illustration of water splitting on Rh/Cr <sub>2</sub> O <sub>3</sub> core-shell nanostructure deposited GaN nanowires and (b) Experimental overall photocatalytic water splitting on Rh/Cr <sub>2</sub> O <sub>3</sub> core-shell nanostructure deposited GaN nanowires, under a 300 W full arc xenon lamp irradiation for a duration of 18 hours.....	61
Figure 3-8: Schematic illustration of the energy band diagram of n-type GaN nanowire surface (a) prior to, and (b) at equilibrium with water. The upward band bending becomes more severe at equilibrium, which suppresses water reduction reaction. Schematic illustration of the energy band diagram of p-type GaN nanowire surface (c) prior to, and (d) at equilibrium with water. The downward band bending gets enhanced at equilibrium, which suppresses water oxidation reaction. ....	63
Figure 3-9: 45° tilted SEM images of GaN:Mg nanowires, with Mg effusion cell temperatures of (a) 200 °C, (b) 230 °C, (c) 250 °C, and (d) 265 °C. ....	65
Figure 3-10: (a) STEM-BF lattice image illustrating lattice fringes from defect-free single crystalline GaN:Mg nanowire (Sample B). (b) Room-temperature PL spectrum of sample B ( $T_{Mg}=230$ °C). (c) A top view SEM image of sample D ( $T_{Mg}=265$ °C) showing the nanowire density. The estimated fill factor is ~39% from this image.....	65
Figure 3-11: (a) $E_F-E_V$ for different GaN:Mg samples determined from ARXPS valence spectrum. The insets illustrate $E_F-E_V$ on the TEM image of a single nanowire and on an ARXPS valence spectrum. The dotted line separates two regimes, Regime I (n-type surfaces) and Regime II (p-type surfaces). (b) Typical room-temperature micro-Raman spectra of GaN nanowires with $T_{Mg}$ ranging from 200 °C to 280 °C. Si modes are pointed out with “*” and the dashed lines are guides to the eye. ....	66
Figure 3-12: Mg concentration for GaN:Mg epilayer ( $T_{Mg} = 250$ °C) as measured by secondary ion mass spectroscopy (SIMS). ....	68
Figure 3-13: (a) Evolution of H <sub>2</sub> from n- (Si-doped) and p-GaN ( $T_{Mg}=230$ °C) nanowire arrays in the presence of CH <sub>3</sub> OH and Rh co-catalyst. (b) Evolution of O <sub>2</sub> from n- (Si-doped) and p-GaN ( $T_{Mg}=230$ °C) nanowire arrays in the presence of AgNO <sub>3</sub> sacrificial reagent. Enhanced evolution of O <sub>2</sub> is measured for n-type GaN nanowires, which can be well correlated to the presence of upward surface band bending. The solid lines are guide to the eye. ....	69
Figure 3-14: (a) Low magnification STEM-SE image. (b) STEM-HAADF image of Rh/Cr <sub>2</sub> O <sub>3</sub> nanoparticle-decorated GaN:Mg nanowire. Crystalline Rh core and amorphous Cr <sub>2</sub> O <sub>3</sub> shell is clearly observed. ....	70
Figure 3-15: High resolution XPS spectra of (a) Rh 3d core level electrons, and (b) Cr 2p core level electrons. These XPS spectra were taken from sample D ( $T_{Mg} = 265$ °C) after photodeposition.....	71
Figure 3-16: (a) H <sub>2</sub> evolution rates for different GaN:Mg samples with and without co-catalyst in overall water splitting. The solid lines are guide to the eyes. (b) Schematic of Rh/Cr <sub>2</sub> O <sub>3</sub> decorated GaN nanowire and the water splitting mechanism. ....	72
Figure 3-17: (a) H <sub>2</sub> evolution rate and internal quantum efficiency (IQE) for different GaN:Mg samples in overall neutral water splitting. Reactions were performed using ~0.387 mg GaN nanowire catalyst in neutral water under illumination of a Xenon lamp (300 W). The sample size is shown in the inset. (b) Repeated cycles of overall pure water splitting for GaN:Mg: 265 °C (sample D), showing the stability of the nanowires. ....	73

Figure 3-18: The turn over number in terms of the ratio of the rate of H <sub>2</sub> molecules produced to the rate of absorbed photons as a function of time. ....	75
Figure 3-19: (a) A bird's-eye view SEM image of the GaN nanowire arrays after ~22 hours of overall water splitting. (b) Low magnification STEM-SE image of a single nanowire after overall water splitting reaction for ~22 hrs. (c) High resolution bright field TEM image after reaction, showing the stability of core-shell Rh/Cr <sub>2</sub> O <sub>3</sub> nanoparticles and GaN nanowire. ....	75
Figure 4-1: (a) Schematic of the InGaN/GaN nanowire heterostructure. (b) Room temperature photoluminescence spectra of InGaN/GaN nanowires arrays. ....	79
Figure 4-2: (a) UV-Visible diffuse reflectance spectroscopy (DRS) of as-grown InGaN/GaN nanowires. (b) Schematic of InGaN/GaN triple-band nanowire heterostructure. ....	79
Figure 4-3: Conduction-band and valence-band edge positions of GaN, In <sub>0.11</sub> Ga <sub>0.89</sub> N and In <sub>0.32</sub> Ga <sub>0.68</sub> N, derived from Ref. [41], depicts sufficient overpotential for oxidation and reduction of water. The redox potentials of water are also illustrated. All values of potentials are in eV relative to the vacuum level. ....	80
Figure 4-4: Flat band-diagram of InGaN/GaN nanowire heterostructure along the growth axis. ....	80
Figure 4-5: (a) A 45° tilted SEM image of GaN/InGaN nanowire heterostructures grown on GaN nanowire templates on Si (111) substrate. (b) High angle annular dark field (HAADF) image in pseudocolor display of an as-grown InGaN/GaN nanowire heterostructure, showing the atomic number contrast between InGaN (red) and GaN (green) layers. The unit of intensity scale is 10 <sup>4</sup> counts. ....	81
Figure 4-6: H <sub>2</sub> and O <sub>2</sub> half reactions under visible light. A long-pass ( $\lambda > 385$ nm) optical filter was utilized to optically excite only the InGaN material. (a) Evolution of H <sub>2</sub> from half reaction in the presence of CH <sub>3</sub> OH and Pt. (b) Evolution of O <sub>2</sub> from half reaction in the presence of AgNO <sub>3</sub> . The insets illustrate the reaction mechanism. The solid line is a guide to the eye. ....	82
Figure 4-7: TEM characterization of Rh/Cr <sub>2</sub> O <sub>3</sub> decorated InGaN/GaN nanowires. (a) High resolution TEM of Rh/Cr <sub>2</sub> O <sub>3</sub> nanoparticles on the lateral surfaces of nanowire. (b) Electron energy loss spectroscopy (EELS) spectrum image of Rh/Cr <sub>2</sub> O <sub>3</sub> deposited InGaN/GaN nanowire. (c–h) Elemental maps of the nanoparticle deposited InGaN/GaN nanowire, derived from the selected area in EELS spectrum image (b) with MLLS fitting. (i) RGB elemental mixing (red, Rh; green, Cr; blue, O) image showing the core-shell Rh/Cr <sub>2</sub> O <sub>3</sub> . ....	84
Figure 4-8: X-ray photoelectron spectroscopy (XPS) analysis of Rh/Cr <sub>2</sub> O <sub>3</sub> co-catalyst before and after overall water splitting. (a) High resolution XPS spectra of Rh3d core level electrons before and after overall water splitting (OWS). (b) High resolution XPS spectra of Cr2p core level electrons before and after OWS. ....	85
Figure 4-9: (a) Schematic of the photocatalytic overall water splitting reaction mechanism. (b) Overall pure water splitting on Rh/Cr <sub>2</sub> O <sub>3</sub> decorated InGaN/GaN nanowire arrays under full arc (>300 nm) 300 W Xenon lamp irradiation. ....	87
Figure 4-10: H <sub>2</sub> evolution from pure water splitting under full arc Xe-lamp, with and without Rh/Cr <sub>2</sub> O <sub>3</sub> co-catalyst deposition. For comparison, H <sub>2</sub> evolution is shown using an AM1.5G filter. The solid line is a guide to the eye. ....	88
Figure 4-11: Apparent quantum efficiency (AQE) and H <sub>2</sub> evolution rate as a function of wavelength of the incident light. The horizontal error bars represent the full-width-half-maximum of the optical filters. The H <sub>2</sub> evolution rate was derived from ~2 hrs of overall water splitting	

under each optical filter. The solid red line is a guide to the eye. The inset shows a typical nanowire sample used for overall water splitting. ....89

Figure 4-12: (a) SEM image of the InGa<sub>N</sub>/Ga<sub>N</sub> nanowire ensemble after overall water splitting, showing the stability of the nanowire heterostructure. (b) Low magnification TEM image of a single InGa<sub>N</sub>/Ga<sub>N</sub> nanowire after overall water splitting, further confirming the stability of the nanowire heterostructure. ....91

Figure 5-1: Schematic of carrier generation and radiative and non-radiative recombination processes. The four electron-hole water splitting mechanism is illustrated on *n*- (*p*-) doped semiconductors with upward- (downward-) surface band bending in the two bottom panels. While the reduction reaction is suppressed in presence of upward band bending, the oxidation reaction is suppressed in presence of downward band bending. ....95

Figure 5-2: Electron and hole distribution on a 100 nm diameter undoped In<sub>0.25</sub>Ga<sub>0.75</sub>N nanowire in the presence of ~0.37 eV upward surface band bending (inset) under certain excitation condition. ....96

Figure 5-3: (a) Schematic of In<sub>0.26</sub>Ga<sub>0.74</sub>N nanowire structure showing three InGa<sub>N</sub> nanowire segments on a Ga<sub>N</sub> nanowire template. (b) a 45° tilted SEM image of as-grown In<sub>0.26</sub>Ga<sub>0.74</sub>N nanowires on Si (111) substrate. (c) Room temperature μ-PL spectrum from as-grown In<sub>0.26</sub>Ga<sub>0.74</sub>N nanowires. ....97

Figure 5-4: (a) STEM-SE image of a single In<sub>0.26</sub>Ga<sub>0.74</sub>N nanowire. (b) EDXS elemental (In) mapping of the In<sub>0.26</sub>Ga<sub>0.74</sub>N nanowire. (c) STEM-HAADF image of a single In<sub>0.26</sub>Ga<sub>0.74</sub>N nanowire (Fig. 5-4b) reveals the existence of three segments of InGa<sub>N</sub> in Ga<sub>N</sub> nanowire. (d) HRSTEM-BF lattice image illustrating lattice fringes from a defect-free single crystalline In<sub>0.26</sub>Ga<sub>0.74</sub>N nanowire. ....98

Figure 5-5:  $E_{FS}-E_{VS}$  for different Mg doped In<sub>0.26</sub>Ga<sub>0.74</sub>N nanowire samples derived from ARXPS valence spectrum as shown in the insets. The error bars represent the accuracy of the linear extrapolation method. The error bar is defined by the s.d. ....99

Figure 5-6: (a) Downward band bending at the surface of *p*-type (bulk) InGa<sub>N</sub>:Mg before equilibrium with water. The downward band bending repels the photogenerated holes toward the bulk and the electrons toward the surface. (b) At equilibrium with water the downward band bending gets reduced. ....101

Figure 5-7: EDXS elemental mapping images clearly demonstrating (a) Rh distribution, (b) Cr distribution, and (c) Rh/Cr<sub>2</sub>O<sub>3</sub> core-shell composite nanoparticles on the nanowire nonpolar surface. (d) Room temperature μ-PL spectra from bare In<sub>0.26</sub>Ga<sub>0.74</sub>N:Mg nanowire and from Rh nanoparticle deposited In<sub>0.26</sub>Ga<sub>0.74</sub>N:Mg nanowire arrays. (e) Overall water splitting reaction mechanism on the nanowire photocatalyst. ....102

Figure 5-8: (a) H<sub>2</sub> evolution rate in overall neutral (pH~7.0) water splitting for different Mg doped In<sub>0.26</sub>Ga<sub>0.74</sub>N nanowire arrays under visible light (>400 nm). (b) The evolution of H<sub>2</sub> and O<sub>2</sub> with irradiation time from neutral (pH~7.0) water for Mg:200 °C doped In<sub>0.26</sub>Ga<sub>0.74</sub>N nanowire arrays under dark and visible light (>400 nm) irradiation. Active Ga<sub>N</sub>/InGa<sub>N</sub> catalyst weight ~0.32 mg. ....103

Figure 5-9: Flat-band diagram of the Ga<sub>N</sub>/In<sub>0.20</sub>Ga<sub>0.80</sub>N nanowire heterostructure, showing the conduction-band and valence-band edge positions of Ga<sub>N</sub>, In<sub>0.20</sub>Ga<sub>0.80</sub>N, and the underlying Si substrate. The redox potentials of water are also shown by the dotted lines. It is seen that Ga<sub>N</sub> and In<sub>0.20</sub>Ga<sub>0.80</sub>N possess sufficient overpotential for oxidation and reduction of water. The

photogenerated holes in Si substrate, however, do not possess sufficient potential for water oxidation, and hence Si substrate does not take part in overall water splitting reaction. All values of potentials are in eV relative to the vacuum level. ....	105
Figure 5-10: H <sub>2</sub> evolution in overall water splitting as a function of irradiation time with different long-pass filters. The dashed lines are guides to the eye. ....	106
Figure 5-11: (a) Schematic of core-shell Rh/Cr <sub>2</sub> O <sub>3</sub> nanoparticle decorated double-band <i>p</i> -GaN/ <i>p</i> -In <sub>0.20</sub> Ga <sub>0.8</sub> N nanowire photocatalyst. Five segments of InGaN were incorporated along the growth axis of GaN nanowires. The concept of double-band photocatalyst is illustrated in the inset. (b) Room temperature $\mu$ -PL spectrum from as-grown <i>p</i> -GaN/ <i>p</i> -In <sub>0.20</sub> Ga <sub>0.8</sub> N nanowire heterostructure. ....	106
Figure 5-12: STEM- HAADF image of a single <i>p</i> -GaN/ <i>p</i> -In <sub>0.20</sub> Ga <sub>0.8</sub> N nanowire reveals the existence of In <sub>0.20</sub> Ga <sub>0.8</sub> N segments in GaN nanowire. EDXS elemental mapping on the selected region of the In <sub>0.20</sub> Ga <sub>0.8</sub> N nanowire, showing the distribution of In, Ga and N. ....	107
Figure 5-13: Open circuit potential (OCP) measurement on <i>p</i> -GaN/ <i>p</i> -In <sub>0.20</sub> Ga <sub>0.80</sub> N nanowire arrays. (a) Under dark and full arc (>200 nm) illumination. (b) Under dark and visible light (>400 nm) illumination. The potential difference between light and dark is positive, indicating <i>p</i> -type behavior of GaN and In <sub>0.20</sub> Ga <sub>0.80</sub> N nanowire arrays. ....	108
Figure 5-14: (a) H <sub>2</sub> and O <sub>2</sub> evolution rates in overall water splitting with AM1.5G filter, and with different long-pass filters. Visible light activity is clearly demonstrated. (b) A snapshot of H <sub>2</sub> and O <sub>2</sub> gas bubble formation from neutral water under full arc illumination on a <i>p</i> -GaN/ <i>p</i> -In <sub>0.20</sub> Ga <sub>0.8</sub> N sample. A $\sim 3$ cm <sup>2</sup> sample (active GaN/In <sub>0.2</sub> Ga <sub>0.8</sub> N catalyst weight $\sim 0.48$ mg) was glued on a microscopic glass and immersed in neutral pH water for overall water splitting. ....	110
Figure 5-15: The solar-to-hydrogen (STH) conversion efficiency i.e. the energy conversion efficiency (ECE) under full arc illumination with AM1.5G filter vs. incident power density. As shown, the performance of the device significantly improves at high power densities. This can be attributed to light induced band flattening effect. The estimated STH conversion efficiency can reach 1.8% under concentrated full arc illumination ( $\sim 26$ suns). The solid line is a guide to the eye. ....	111
Figure 5-16: Weight normalized evolved H <sub>2</sub> and O <sub>2</sub> from overall neutral (pH $\sim 7.0$ ) water splitting on Rh/Cr <sub>2</sub> O <sub>3</sub> core-shell nanoparticle decorated <i>p</i> -GaN/ <i>p</i> -In <sub>0.20</sub> Ga <sub>0.80</sub> N nanowire arrays under full arc 300 W Xenon lamp illumination with AM1.5G filter. The reaction chamber was evacuated after each cycle. No sacrificial reagents were added with water. ....	113
Figure 5-17: SEM image of the <i>p</i> -GaN/ <i>p</i> -In <sub>0.20</sub> Ga <sub>0.8</sub> N nanowire after $\sim 6$ h of water splitting, demonstrating the stability of nanowires and Rh/Cr <sub>2</sub> O <sub>3</sub> co-catalyst. ....	113
Figure 6-1: (a) A 45° tilted high resolution scanning electron microscopy image of as grown GaN:Mg:260 °C sample. (b) Low temperature (20 K) PL spectrum of GaN:Mg samples in comparison to undoped GaN sample. ....	116
Figure 6-2: (a) Micro-Raman spectra of GaN:Mg:260 °C and GaN:Mg:200 °C nanowires. The curves are vertically shifted for clarity. (b) E <sub>2</sub> Raman line from GaN:Mg:260 °C and undoped GaN nanowires. ....	117
Figure 6-3: Schematic energy band diagram of GaN:Mg:260 °C nanowires illustrating the formation of V <sub>N</sub> and Mg related intra-gap states along with the redox potential of water (vs vacuum level). ....	119

Figure 6-4: (a) Evolution of H <sub>2</sub> from GaN:Mg:260 °C nanowire in presence of C <sub>6</sub> H <sub>15</sub> NO <sub>3</sub> hole scavenger and Rh co-catalyst. (b) Evolution of O <sub>2</sub> from GaN:Mg:260 °C nanowire in presence of AgNO <sub>3</sub> as electron acceptor.....	120
Figure 6-5: (a) Evolution of H <sub>2</sub> from GaN:Mg nanowire samples in presence of C <sub>6</sub> H <sub>15</sub> NO <sub>3</sub> hole scavenger and Rh co-catalyst with different intra-gap excitation using 300 W Xenon lamp. (b) Evolution of H <sub>2</sub> from overall neutral water splitting from the GaN:Mg samples with different intra-gap excitation using 300 W Xenon lamp.....	121
Figure 6-6: Repeated cycles of overall neutral water splitting for GaN:Mg: 260 °C sample showing the stability of the intra-gap states. ....	122
Figure 7-1: (a) Schematic of the InGaN/GaN nanowire heterostructure, (b) SEM image of the as-grown InGaN/GaN disk-on-wire nanostructure, (c) room temperature PL from the as-grown InGaN/GaN disk-on-wire nanostructure, (d) TEM image of a single nanowire showing the formation of InGaN nanodisk on GaN nanowire, (e) HRTEM image of hexagonal shaped InGaN nanodisk, and (f) formation mechanism of InGaN nanodisk on a GaN nanowire. ....	127
Figure 7-2: Schematic illustration of InGaN nanostructure growth on SiO <sub>x</sub> /Si nanowires. (a) Si substrate, (b) Ni thin film deposition, (c) Ni droplet formation after RTA, (d) Si nanowire formation after RIE, (e) SiO <sub>x</sub> formation after thermal oxidation, (f) MBE growth of InGaN nanostructure on SiO <sub>x</sub> /Si nanowires. ....	130
Figure 7-3: SEM image of (a) Si nanotubes, (b) Si nanowires, (c) InGaN nanostructure grown on Si nanowire, (d) Room temperature PL spectrum from InGaN nanostructure grown on SiO <sub>x</sub> /Si substrate. ....	131
Figure 8-1: (a) Schematic of the nanowire heterostructure. (b) SEM and (c) STEM-HAADF images of as-grown In <sub>0.25</sub> Ga <sub>0.75</sub> N nanowires. The inset shows a HRTEM lattice image of In <sub>0.25</sub> Ga <sub>0.75</sub> N nanowire. (d) Room temperature photoluminescence from In <sub>0.25</sub> Ga <sub>0.75</sub> N nanowire. (e) Rh nanoparticle decorated In <sub>0.25</sub> Ga <sub>0.75</sub> N nanowire.....	137
Figure 8-2: (a) UV-Vis absorption spectrum of 100 mM AN and 1 mM MC-540 dye before and after 12 hrs of adsorption. (b) H <sub>2</sub> evolution from 10 mM EDTA and 100 mM AN mixture under 300 W Xenon lamp with different long-pass filter.....	138
Figure 8-3: Repeated cycles of H <sub>2</sub> evolution from EDTA and AN mixture under 300 W Xenon lamp with 525 nm long-pass filter. ....	139
Figure 8-4: Reaction mechanism of MC-540 dye-sensitized In <sub>0.25</sub> Ga <sub>0.75</sub> N/Rh nanowires. ....	141
Figure 9-1: (a) Schematic of surface plasmon induced charge transfer mechanism, (b) Schematic illustration of the scattering mechanism [229]. ....	145

# List of Acronyms

AQE	Apparent Quantum Efficiency
APCE	Absorbed Photon Conversion Efficiency
BEP	Beam Equivalent Pressure
BF	Bright Field
CBE	Chemical Beam Epitaxy
CB	Conduction Band
CBM	Conduction Band Minimum
CVD	Chemical Vapor Deposition
DOS	Density of States
DFT	Density Function Theory
DRS	Diffuse Reflectance Spectroscopy
ECE	Energy Conversion Efficiency
EDS	Energy Dispersive Spectrum
EDXS	Energy Dispersive X-Ray Spectroscopy
EELS	Electron Energy Loss Spectroscopy
FWHM	Full Width at Half Maximum
HAADF	High Angle Annular Dark Field
HF	Hydrofluoric Acid
HRTEM	High Resolution Transmission Electron Microscopy
IPCE	Incident Photon Conversion Efficiency
IQE	Internal Quantum Efficiency
IR	Infrared
LED	Light Emitting Diode
LVM	Local Vibrational Modes
LO	Longitudinal Optical
MBE	Molecular Beam Epitaxy
MOCVD	Metal Organic Chemical Vapor Deposition

MQW	Multi Quantum Well
NHE	Normal Hydrogen Electrode
OWS	Overall Water Splitting
OCP	Open Circuit Potential
PEC	Photoelectrochemical
PL	Photoluminescence
RF	Radio Frequency
RIE	Reactive-Ion Etching
RTA	Rapid Thermal Annealing
SAG	Selective Area Growth
SEM	Scanning Electron Microscopy
SIMS	Secondary Ion Mass Spectroscopy
STH	Solar-to-hydrogen
STEM	Scanning Transmission Electron Microscopy
STEM-SE	Scanning Transmission Electron Microscopy- Secondary Electron
TCD	Thermal Conductivity Detector
TON	Turnover Number
TEM	Transmission Electron Microscopy
UV	Ultraviolet
VB	Valence Band
VBM	Valence Band Maximum
VLS	Vapor-Liquid-Solid
VPE	Vapor Phase Epitaxy
ARXPS	Angle Resolved X-ray Photoelectron Spectroscopy

# Abstract

The conversion of solar energy into hydrogen via water splitting process is one of the key sustainable technologies for future clean, storable and renewable source of energy. Therefore, development of stable and efficient photocatalyst material has been of immense interest, but with limited success. Here, we show that overall neutral water splitting can be achieved under ultraviolet (UV) and visible light irradiation using group-III nitride nanowire arrays grown by plasma-assisted molecular beam epitaxy. The Rhodium/Chromium-oxide core/shell nanoparticle decorated GaN nanowires show stable photocatalytic activity under UV irradiation, with the turnover number well exceeding any previously reported GaN particulate samples. Additionally, by tuning the surface Fermi-level with controlled Mg doping in GaN nanowires, we demonstrate that the internal quantum efficiency can be enhanced by nearly two orders of magnitude under UV irradiation. Furthermore, in order to utilize the abundant visible solar spectrum, we have designed a multi-band InGaN/GaN nanowire heterostructure, that can lead to stable hydrogen production from neutral (pH~7.0) water splitting under UV, blue and green light irradiation (up to ~ 560 nm), the longest wavelength ever reported. At ~440-450 nm wavelengths, the internal quantum efficiency is estimated to be ~ 13%. Moreover, we have designed a dual-band *p*-type InGaN/GaN nanowire heterostructure, wherein Mg doping is optimized both in GaN and InGaN nanowires to achieve stable and efficient overall water splitting under UV and visible light. An internal quantum efficiency of ~69% has been achieved for neutral (pH~7.0) water splitting, the highest value ever reported under visible light illumination (400-475 nm). Subsequently, we have demonstrated that the optical absorption edge of GaN nanowires can be reduced from 3.4 eV to 2.95 eV by introducing Mg-related acceptor and nitrogen vacancy related donor energy states. This band-engineered GaN nanowires exhibit stable overall water splitting under violet light (up to 450 nm). The internal quantum efficiency of Mg doped GaN nanowire reached ~43% at 375-450 nm. Detailed analysis further confirms the stable photocatalytic activity of the III-nanowire heterostructures. Finally, we have presented the first example of dye-sensitized InGaN nanowires for hydrogen generation under

green, yellow and orange solar spectrum (up to 610 nm). This work establishes the use of metal-nitrides as viable photocatalyst for solar-powered artificial photosynthesis for future large-scale hydrogen and methanol based economy.

## Abrégé

La conversion de l'énergie solaire en hydrogène par le procédé de décomposition de l'eau est l'une des technologies clés durable pour une future source d'énergie propre stockable et renouvelable. Par conséquent, le développement de matériel photocatalyseur stable et efficace a été d'un immense intérêt, mais avec un succès limité. Ici, nous montrons que toute séparation globale de l'eau neutre peut être réalisée sous irradiation ultraviolet (UV) et par lumière visible en utilisant des matrices de nanofils de nitrite de groupe-III cultivés par épitaxie par faisceau moléculaire assistée par plasma. Les nanoparticules cœurs/coquille Rhodium/Chromium-oxide cultivé par des nanofils de GaN montrent une activité photocatalytique stable sous irradiation UV avec un rendement catalytique (turnover number) bien supérieur à ceux qui ont déjà été rapportés avec des échantillons de particules de GaN. De plus, en réglant le niveau de Fermi-surface avec contrôle de dopage Mg dans les nanofils de GaN, nous démontrons que l'efficacité quantique interne peut être améliorée par près de deux ordres de grandeur sous irradiation UV. En outre, afin d'utiliser le spectre solaire visible abondant, nous avons conçu un nanofil hétéro-structures multi-bande InGaN/GaN, qui peut conduire à la production d'hydrogène stable à partir de la décomposition de l'eau neutre (pH ~ 7.0) sous irradiation UV, de lumière bleue et verte (jusqu'à ~ 560 nm), la plus longue longueur d'onde jamais enregistré. À des longueurs d'onde ~ 440-450 nm, l'efficacité quantique interne est estimé à ~13%. Par ailleurs, nous avons conçu une hétéro-structures de nanofil bi-bande de type p InGaN/GaN dans lequel le dopage en Mg est optimisé à la fois dans le GaN et dans le InGaN pour permettre la décomposition globale efficace et stable de l'eau sous UV et à la lumière visible. Un rendement quantique interne de ~ 69% a été atteint pour la décomposition de l'eau neutre (pH ~ 7.0), la valeur la plus élevée jamais enregistrée sous éclairage en lumière visible (400-475 nm). Finalement, nous avons démontré que la largeur de bande interdite des nanofils en GaN peut être réduite de 3.4 eV à 2.95 eV en introduisant des accepteurs à base de Magnésium et des donneurs d'azote à états d'énergie vacants. Cette ingénierie de bande des nanofils en GaN montre une décomposition globale stable de l'eau sous la lumière ultraviolette (jusqu'à 450 nm).

L'efficacité quantique interne des nanofils de GaN dopé au Mg a atteint 43 % à 375-450 nm. L'analyse détaillée confirme par la suite l'activité photocatalytique stable des hétéro-structures III des nanofils. Enfin, nous avons présenté le premier exemple de colorant-sensibilisés InGaN nanofils pour d'hydrogène génération en vert, jaune et orange du spectre solaire (jusqu'à 610 nm). Ce travail prouve l'utilisation de nitrures métalliques comme photocatalyseur viable pour la photosynthèse artificielle à l'énergie solaire pour une future économie basée sur la production à grande échelle d'hydrogène et de méthanol.

# Chapter-1

## Introduction

### 1.1 Overview

#### 1.1.1 Renewable Energy Options

Our planet is heading towards an energy famine. According to U.S. Department of Energy, the worldwide primary energy consumption in 2008 was ~17 terrawatts (TW), which is expected to be double by 2050 and triple by 2100 [1, 2]. Therefore, it is vital to find alternative carbon-neutral, storable and renewable energy carriers that can mitigate the current and future global energy appetite. Although, there are different types of energy sources currently available; not all of them can follow our current and future energy demand curve. For example, biomass offers a limited energy supply because of the low efficiency of photosynthesis (about one order of magnitude lower than existing solar-photovoltaic and solar-thermal technologies) [1, 3, 4]. Alternatively, nuclear energy plant is assumed to be a solution to this energy crisis. However, the deployment of expensive nuclear plant is difficult to build fast enough to cope up with the energy demand [5]. Also nuclear power plant requires widespread public acceptance, since they can be a point of catastrophic disaster as seen by the world recently in Fukushima, Japan. Wind energy is a poor choice because of its low energy density and intermittency [6]. Although fossil fuel can satiate the global energy crisis to some extent, they are not environmentally friendly. Burning fossil fuel emits greenhouse gas (GHG) and therefore creates environmental crisis.

#### 1.1.2 Solar Energy

Solar energy is expected to be the ultimate solution to this energy and environmental crisis. About  $1.2 \times 10^5$  TW power from sunlight falls on the Earth's surface in 1 hr, which is higher than the global energy consumed by all human activities in 1 year [7].

Approximately 600 TW power from sunlight strikes the Earth's terrestrial surfaces that can be used as practical sites for solar energy harvesting [8]. Covering 0.16% of the land on Earth with 10% efficient solar conversion systems would provide 20 TW of solar power, which is nearly twice the world's fossil fuel consumption rate [7]. Clearly, solar energy is the largest renewable carbon-free resource amongst all other renewable energy options.

### **1.1.3 Importance of Solar Energy Storage**

The major challenges in implementing large scale solar energy system are the low efficiency and the high manufacturing cost of solar panels [3]. Additionally, because of the diurnal nature and intermittency arising from variable atmospheric conditions, new technologies need to be developed to store solar energy, which can be released in a form that one desires. The current methods of storing solar energy, including potential energy (pumped-hydroelectric, compressed-air, electric charge in super/ultra capacitors), kinetic energy (flywheels), thermal energy (concentrated solar thermal, geothermal), and chemical energy (in the form of batteries or fuels) experience high cost of deployment, short time storage, low energy density, and efficiency to be implemented for large scale applications [1]. On the other hand, because of its high energy density by mass (143 MJ Kg) and environmental friendliness, hydrogen has been identified as a potential candidate as future energy carrier [1, 3].

### **1.1.4 Necessity for Solar Water Splitting**

At present, hydrogen is mainly produced from fossil fuels and therefore emits CO<sub>2</sub> [9]. However, H<sub>2</sub> needs to be produced from abundant natural resources, such as water and sunlight. Splitting water into H<sub>2</sub> and O<sub>2</sub> using sunlight allows storing solar energy in the form of chemical energy and makes solar energy 24 hours a day, 7 days a week [7, 8, 10]. This process produces hydrogen: a clean, storable and renewable source of energy. The released H<sub>2</sub> from water splitting can be used in fuel cells to produce electricity or can be directly combusted in an engine, wherein the reaction by-product is nothing but water [1, 3]. This process will make solar energy highly distributed, from small to large-scale

applications. Therefore, research on solar water splitting is an urgent need. However, the current technologies for solar water splitting in a cost effective and efficient way are still at their infancy [9, 10].

Since the discovery of photoelectrochemical water splitting on *n*-TiO<sub>2</sub> electrode in 1972 [11], considerable research has been done to find a stable and efficient photocatalyst material [9, 10, 12-17]. Over the last four decades, researches have mainly focused on metal oxides involving ions with filled or empty d-shell bonding configurations (i.e., Ti<sup>4+</sup>, Zr<sup>4+</sup>, Nb<sup>5+</sup>, Ta<sup>5+</sup>, W<sup>6+</sup>, Ga<sup>3+</sup>, In<sup>3+</sup>, Ge<sup>4+</sup>, Sn<sup>4+</sup>, and Sb<sup>5+</sup>) because of their inherent chemical stability [9, 18, 19]. However, because of the large band gap (>3.0 eV), metal oxides are mostly active under UV irradiation (<400 nm). In the solar spectrum, a small fraction (~4%) of solar energy lies in the UV region, in contrast to far more abundant (~46%) visible region. Therefore, it is imperative to explore new visible light driven photocatalyst for overall water splitting (i.e., simultaneous production of H<sub>2</sub> and O<sub>2</sub>) that are stable and highly efficient for practical and large scale hydrogen production system [20]. Researches on visible light responsive photocatalyst are limited as there are very few visible light responsive materials that satisfy the thermodynamic and kinetic potentials for overall water splitting, and are simultaneously stable against photocorrosion [21-24].

## 1.2 Basic Principles of Solar Water Splitting

There are mainly two approaches for solar water splitting: photoelectrochemical (PEC) and photochemical (or photocatalytic) water splitting [10, 18, 21, 25, 26], as schematically shown in Fig. 1-1. In PEC water splitting, the photogenerated carriers (electron or holes) in the semiconductor photocatalyst are channeled through a metallic conductor to an electrode, which is modified by co-catalysts (Fig. 1-1 a). In this case, some external bias is usually required for efficient carrier separation and to overcome the resistance between the electrodes in the solution [27]. This scheme of solar water splitting requires a high conductive electrolyte and high conductive substrate for efficient current conduction [28]. Because of the requirement of external circuitry, PEC water splitting is complex and expensive for practical applications. On the other hand, photochemical dissociation of water offers the simplest and potentially the most efficient approach; as

this spontaneous, wireless approach requires virtually zero energy input except light [9, 10, 29-33]. It is a wireless version of PEC water splitting in which the counter electrode is mounted on the photocatalyst surface in the form of micro/nano-electrode i.e., co-catalyst, as illustrated in Fig. 1-1 b. This scheme of solar water splitting does not require conductive electrolyte and conductive substrate for its operation. Therefore, this is a simple and low-cost approach that can be used for large-scale practical applications. One inherent problem with this approach is the simultaneous production of H<sub>2</sub> and O<sub>2</sub> in the same reaction chamber that needs to be separated for practical applications, such as in a Fuel cell.

In water splitting process, the solar energy is converted into chemical energy with a positive change in Gibbs free energy (i.e., uphill reaction) [9].

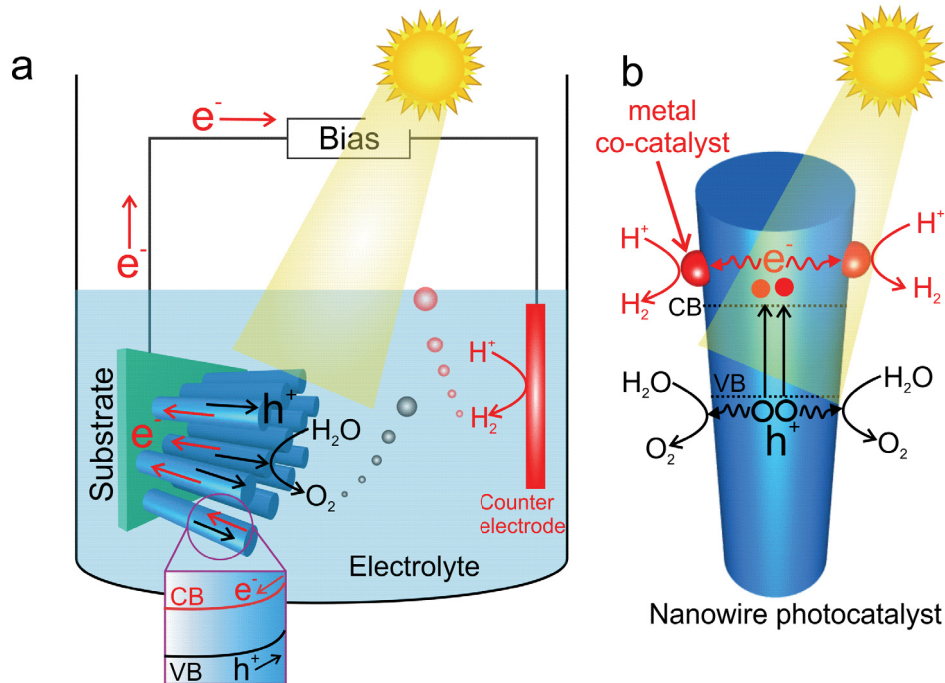


Figure 1-1: (a) Photoelectrochemical (PEC) water splitting on nanowire photoelectrode, (b) Photochemical water splitting on co-catalyst nanoparticle decorated nanowire photocatalyst.

Therefore, water splitting reaction can store 237.178 KJ/mol at 25 °C and 1 bar. This reaction resembles the photosynthesis by which green plants store solar energy and therefore regarded as artificial photosynthesis [30, 34-36].

The photocatalytic water splitting reaction generally involves three main processes [9, 13], as shown in Fig. 1-2. The first step is band gap absorption of photons and generation of electron-hole pairs. Thermodynamically, when the energy of incident light is larger than that of a band gap, electrons and holes are generated in the conduction and valence bands, respectively.

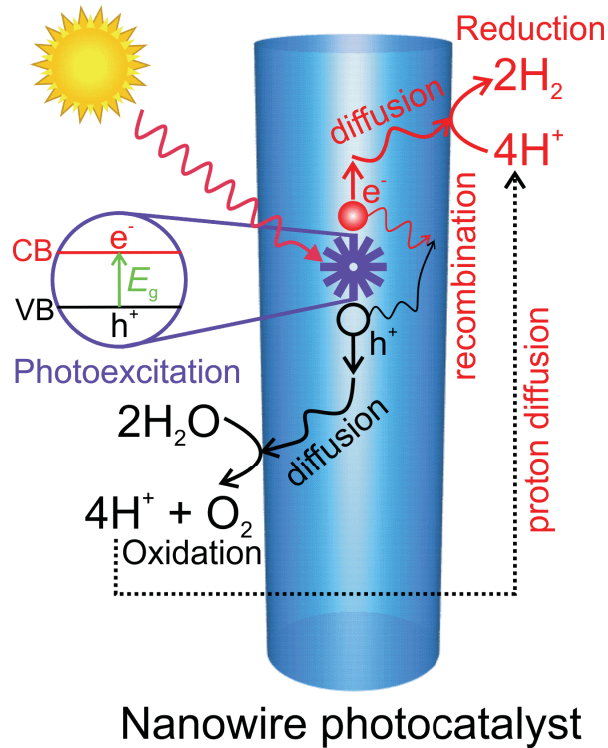
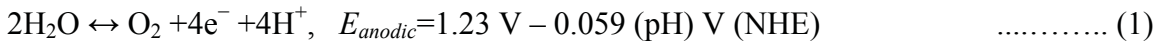


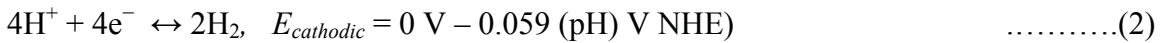
Figure 1-2: Schematic illustration of the three main process steps in photochemical water splitting on nanowire photocatalyst.

The second step consists of charge separation and migration of photogenerated carriers. The crystal structure, crystallinity and physical size of a photocatalyst strongly affect this step. If the crystalline quality of the photocatalyst is high, there will be fewer defects. The defects act as trapping and recombination centers between photogenerated electrons and holes, resulting in a decrease in the photocatalytic activity. Therefore, the higher the

crystallinity is, the higher the photocatalytic activity will be. The physical size of the photocatalyst also determines the activity of the photocatalyst. If the size is small, the photogenerated carriers will have to travel less distance to get to the surface and hence there will be less probability of carrier recombination. Therefore, development of high quality nanoscale material is of great interest. The final step involves the reduction and oxidation (redox) of water on the photocatalyst surface via the photogenerated electrons and holes, respectively. For water splitting, first, the O-H bonds of two water molecules has to be broken with the simultaneous formation of one O=O double bond as follows [1].



Since this reaction requires a high oxidizing potential, 1.23 V vs. NHE (pH=0), the top level of valence band has to be more positive than this potential, so that the photogenerated holes have enough energy to oxidize water. This reaction releases four protons (H<sup>+</sup>), which needs to be reduced by the photogenerated electrons to form two H<sub>2</sub> molecules [1].



Therefore, the conduction band minimum of the semiconductor has to be more negative than water reduction potential (0 V vs. NHE at pH=0). Thus, water molecules are oxidized by the holes to form O<sub>2</sub> and reduced by the electrons to form H<sub>2</sub> for overall water splitting. Therefore, the theoretical minimum band gap for water splitting is 1.23 eV that corresponds to light wavelength of about ~1000 nm. Besides having the band edge potential requirements, some overpotential is required for driving the oxidation and reduction reaction of water. Assuming 0.3 eV overpotential for each half of the redox reaction, and given that the energy difference between the oxidation and reduction potential of water is 1.23 eV, overall water splitting requires a minimum excitation energy of 1.83 eV (<677 nm) [30]. Figure 1-3 schematically illustrates the band edge requirement of a semiconductor material for overall water splitting.

From the reaction kinetic point of view, the surface characteristic of a photocatalyst (surface area and active sites) is of great importance for the redox reaction of water. Even if the photogenerated electrons and holes possess thermodynamic potentials for water splitting, they may recombine either radiatively or nonradiatively if there are no active sites on the photocatalyst surface. It has been demonstrated that the incorporation of metal co-catalyst such as Ni, Pt, Rh, RuO<sub>2</sub> introduces active sites for H<sub>2</sub> evolution and therefore significantly improves the photocatalytic activity [37]. Additionally, stability of the photocatalyst in aqueous solution is of great importance under photoirradiation.

### 1.3 Motivation for Using Group-III Nitride for Water Splitting

Group III-nitride compound semiconductors exhibit unique electrical and optical properties, including high carrier mobility, high peak drift velocity, relatively high absorption co-efficient, extreme chemical stability, and direct energy bandgap encompassing nearly the entire solar spectrum [38]. The inherent chemical stability of group-III nitrides makes them a suitable candidate for solar water splitting in harsh photocatalytic environment [38, 39].

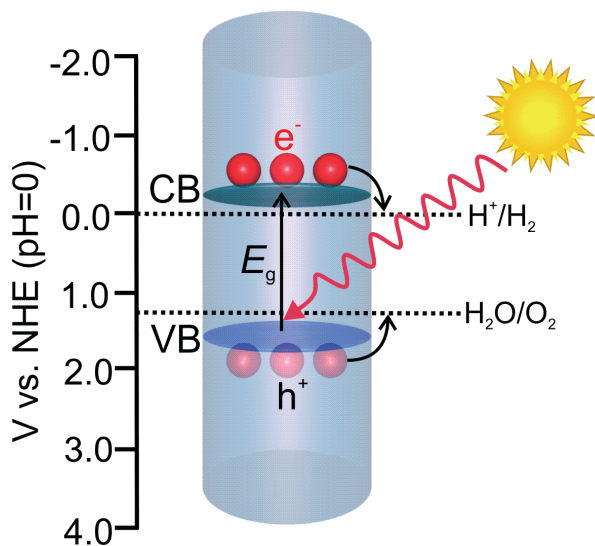


Figure 1-3: Schematic illustration of band edge requirements for overall water splitting reaction.

Due to the more negative potential of N 2p orbital than O 2p orbital, metal nitrides often possess a narrow bandgap which can absorb the visible portion of solar spectrum [25]. The typical electron mobility in III-nitrides is much higher; hence higher electron transfer efficiency is expected [38, 40]. Consequently, III-nitrides have emerged as the materials of choice for effectively harvesting solar energy for the generation of electricity and/or hydrogen. Among all group-III nitrides, GaN and InGaN satisfy the band edge requirements for water oxidation and reduction. Figure 1-4 shows the band alignments of GaN and InGaN along with the other commonly used photocatalyst materials. GaN is a wide band gap material with bandgap of 3.4 eV, which can absorb all photons with wavelengths less than  $\sim 365$  nm. Therefore, GaN is suitable to harness the UV part (4%) of solar spectrum. On the other hand, the bandgap of InGaN can be tuned from 3.4 to 0.65 eV by changing the In content [41], as shown in Fig. 1-4. Therefore, InGaN ternary alloy allows capturing the visible part (43%) of solar spectrum. Recently, a density function theory (DFT) calculation shows that the band edge potential of InGaN is suitable for water splitting for In compositions up to 50 % [41].

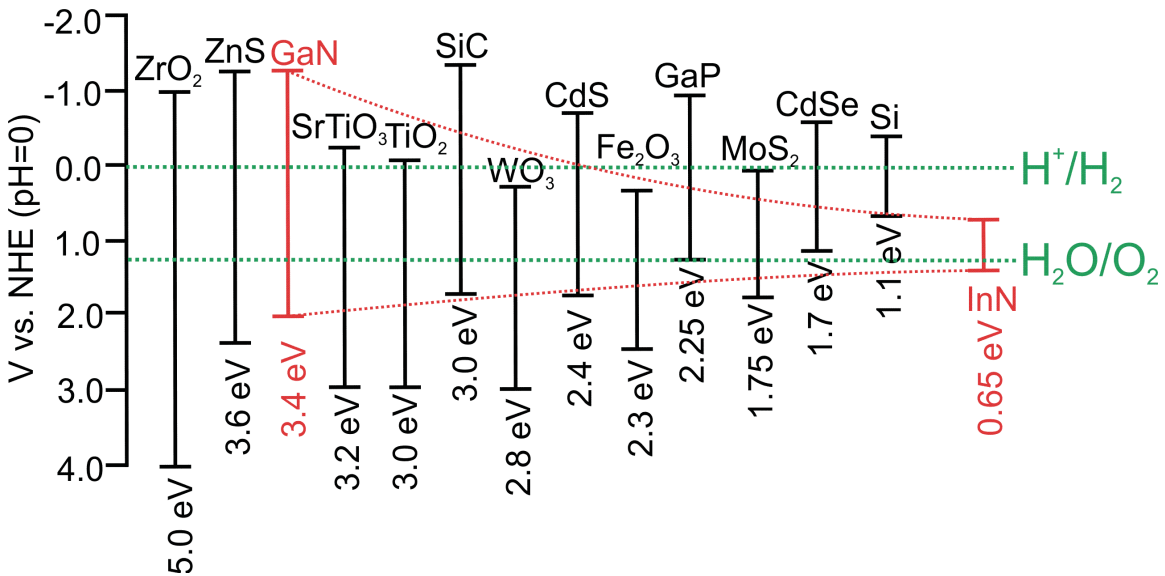


Figure 1-4: Band edge positions of commonly used photocatalysts. The oxidation and reduction potentials of water are also shown with green dotted lines. The red dotted line represents the band edge positions of  $\text{In}_x\text{Ga}_{1-x}\text{N}$  with  $x$  increasing from left to right (0-1).

Additionally, the band edge potentials of GaN was experimentally determined and found to straddle the redox potential of water [42, 43]. Therefore, the use of group-III nitride material has attracted great attention recently because of their excellent material properties, as discussed in the following section.

## **1.4 A Brief Review on the Metal/Non-metal Nitrides for Water**

### **Splitting**

Recently, the use of metal-/non-metal nitride material has attracted great attention as a new generation of photocatalyst because of their unique material properties i.e., band gap tunability, stability against photocorrosion, sufficient thermodynamic and kinetic potentials for water redox reaction. Although a number of PEC water splitting studies have been reported using metal-/non-metal nitrides, very limited number of studies are devoted to photochemical water splitting using metal-/non-metal nitride material. A brief summary of PEC and photochemical water splitting using metal-/non-metal nitrides is as follows.

#### **1.4.1 PEC Water Splitting Studies using Metal-/Non-metal Nitrides**

##### ***UV Light Responsive III-Nitrides***

By patterning a plain *n*-type GaN surface with metal stripes and *n*-GaN ridges I. Waki *et al.* achieved higher photocurrent density compared to plain *n*-GaN in 1M NaOH [44]. This higher photocurrent is attributed to eradication of current crowding effect and enhancement in effective surface area for photoelectrolysis. Current crowding effect has also been removed by placing immersed finger-type indium tin oxide (IF-ITO) ohmic contacts on *n*- and *p*-GaN photoelectrode to achieve enhanced photocurrent and H<sub>2</sub> generation rate [45, 46].

S. Kikawa *et al.* measured flat-band potentials of Ga-face and N-face *n*-GaN, and found that the conduction band edge of N-face is ~0.3 eV more negative than that of Ga-face GaN [47]. As a consequence, more hydrogen bubbles and cathodic current was observed on N-face than that of Ga-face GaN. In contrast, from Mott-Schottky analysis

Y.-G. Lin *et al.* concluded that the conduction band edge of Ga-polar GaN is  $\sim 0.4$  eV more negative than that of N-polar GaN [48]. While Ga-polar surface is found to have higher photoconversion efficiency at negative bias (vs Pt counter electrode), N-polar surface exhibit higher photoconversion efficiency at positive bias (vs Pt counter electrode).

A number of recent works have been devoted to the development of nanostructured electrodes for enhanced light absorption, suppressed carrier recombination, and efficient carrier extraction. Significant enhancement (up to 6 times) in photocurrent density is indeed demonstrated with GaN nanorod arrays compared to GaN planer photoelectrode [49]. The  $H_2$  evolution rate increased from 0.1 to 0.73 ml h<sup>-1</sup> cm<sup>-2</sup> and solar-to-hydrogen (STH) conversion efficiency increased from 0.04% to 0.26% using the nanorod arrays.

Incorporation of a suitable dopant in GaN photoelectrode is one of the strategies to enhance the device efficiency. M. Ono *et al.* reported carrier concentration dependent PEC properties of *n*-GaN photoanode [50]. Maximum photocurrent is measured with a carrier concentration of  $1.7 \times 10^{17}$  cm<sup>-3</sup>. K. Fujii *et al.* reported that the presence of alcohol in the electrolyte increases the  $H_2$  evolution rate nearly twice compared to that without alcohol [51]. The existence of alcohol further suppressed photocorrosion of GaN caused by self-oxidation. B. AlOtaibi *et al.* studied the PEC properties of undoped and Si-doped GaN nanowire arrays in HBr and KBr electrolyte [52]. Maximum IPCE values of  $\sim 15\%$  and  $\sim 18\%$  were measured for undoped and Si-doped GaN nanowires, respectively at 350 nm excitation. J. Wallys *et al.* further demonstrated that the electrochemical properties of MBE grown GaN nanowires can be tuned with controlled doping and external bias via the electrolyte [53]. Most recently, A. Nakamura *et al.* demonstrated a polarization-engineered GaN/AlN/GaN photocathode without *p*-type doping [54]. This novel photocathode showed stable and remarkably enhanced cathodic photocurrent compared to *p*-GaN in H<sub>2</sub>SO<sub>4</sub> electrolyte.

S.-Y. Liu *et al.* demonstrated visible light ( $400 \text{ nm} < \lambda < 600 \text{ nm}$ ) activity of Mn-doped GaN photoelectrode with an internal quantum efficiency of 61% at 450 nm [55]. This visible light response is attributed to the Mn-related intermediate band formed in the

bandgap of GaN. However, photocorrosion of the electrode was inevitable owing to the *n*-type character of Mn-doped GaN.

### ***Visible Light Responsive III-Nitrides***

J. Li *et al.* studied the PEC properties of *n*-InGaN epilayer grown by metal organic chemical vapor deposition (MOCVD) [56]. A drastic enhancement in photocurrent density and hydrogen evolution rate was demonstrated by increasing the In content from 20 to 40%. In another study, W. Luo *et al.* demonstrated good photostability and visible light response from MOCVD grown 60 nm thick In<sub>0.2</sub>Ga<sub>0.8</sub>N electrode in aqueous HBr solution [57]. The turn over number reached 847 after 4000 s irradiation, and incident photon conversion efficiency (IPCE) is nearly 9% at 400–430 nm. In a subsequent report, in order to enhance the IPCE, the authors have grown 250 nm thick In<sub>0.2</sub>Ga<sub>0.8</sub>N [58]. However, the In-rich InGaN phases on the surface reduced the photocurrent owing to the presence of surface recombination centers. By removing this In-rich InGaN phases using 1M HCl aqueous solution, the IPEC was found to increase from 15% to 42% at 400 nm with enhanced stability of the photocurrent. The authors further demonstrated an IPCE of 58% at 400-430 nm after surface treatment of In<sub>0.3</sub>Ga<sub>0.7</sub>N in H<sub>2</sub>SO<sub>4</sub> aqueous solution [59]. K. Aryal *et al.* reported excellent stability of *p*-In<sub>x</sub>Ga<sub>1-x</sub>N (0≤*x*≤0.22) epilayer in aqueous HBr solution [60].

A number of III-nitride nanostructures have recently been developed for efficient harvesting visible solar spectrum. N. H. Alvi *et al.* compared PEC properties of PAMBE grown In rich (40-50%) InGaN nanowall with that of planer InGaN [61]. Nearly 57% enhancement in H<sub>2</sub> evolution rate was revealed on nanowall structure. Y. J. Hwang *et al.* recently synthesized Si/InGaN core/shell hierarchical nanowire arrays to act as high surface area photoanode for water splitting [62]. The photocurrent density of hierarchical Si/InGaN nanowire increased by 5 times compared to that of InGaN nanowires on planer Si substrate. No obvious photochemical etching or oxidation of the nanowire was revealed from detailed HRTEM analysis. B. AlOtaibi *et al.* recently demonstrated stable PEC water splitting and H<sub>2</sub> generation under UV and visible light using *n*-type InGaN/GaN core/shell double-band nanowire heterostructure grown by PAMBE [63]. An

IPCE of 27.6% was reported at 350 nm at 1 V vs Ag/AgCl. L. Caccamo *et al.* synthesized single crystalline *n*-type GaN/In<sub>0.3</sub>Ga<sub>0.7</sub>N (core/shell) nanorods by selective area growth metal organic vapor phase epitaxy (MOVPE) [64]. The photocurrent density of GaN/In<sub>0.3</sub>Ga<sub>0.7</sub>N was found to be 10 fold higher than that of GaN nanorods at 1.35 V.

J. Kamimura *et al.* reported the PEC properties of *n*- and *p*-type InGaN nanowires grown by PAMBE for water splitting by *in situ* electrochemical mass spectroscopy (EMS) [65]. The anodic photocurrent exhibited by *n*-InGaN was attributed to the photocorrosion of the nanowires. In contrast, *p*-InGaN exhibited cathodic photocurrent caused by water reduction. An IPCE of 40% at a potential of -0.5 V/NHE was demonstrated across the entire visible spectrum (upto 750 nm), and both photocurrent and H<sub>2</sub> evolution were stable for 60 mins. J. Benton *et al.* studied the PEC properties of InGaN/GaN nanorod light emitting diode (LED) structure grown by MOCVD [66]. By incorporating NiO nanoparticles, the authors were able to significantly suppress the photochemical etching of the nanowires owing to self-oxidation by the photogenerated holes in aqueous NaOH solution. The NiO nanoparticles suppress carrier recombination and promote oxidation reaction on its surfaces rather than on the nanowire surface.

Most recently an *n*-InGaN working electrode has been developed which is biased by a GaAs solar cell [67]. By optimizing the electrolyte and incident light intensity, and introducing immersed ITO ohmic contacts on the *n*-InGaN working electrode, the operating point of the device was tuned to set to the maximum power point of the GaAs solar cell. A photoconversion efficiency of ~18-23% was demonstrated under optimized condition. In another study R. Dahal *et al.* realized a monolithic solar-PEC cell based on InGaN/GaN multiple-quantum well (MQW) solar cell [68]. A STH efficiency of 1.5% was reported without any external bias. Excellent chemical stability was further demonstrated for a prolonged period of time (7 days) in aqueous HBr solution.

### ***Other Nitrides***

V. Chakrapani *et al.* studied PEC properties of Tungsten nitride (W<sub>2</sub>N) nanowire array [69]. While W<sub>2</sub>N showed *n*-type behavior with good photoactivity at moderate bias,

prolonged photolysis resulted in photocorrosion of the nanowire. However, mixed phase  $W_2N-WO_3$  showed improved photo-stability.

X. Feng *et al.* synthesized highly oriented Tantalum nitride ( $Ta_3N_5$ ) nanotube array for visible light responsive photoelectrolysis [70]. In a two-electrode arrangement, an IPCE of 5.3% was achieved at 450 nm with 0.5 V bias in KOH solution. Y. Cong *et al.* studied the PEC water oxidation properties of  $Ta_3N_5$  nanotubes decorated with  $IrO_2$ ,  $Co_3O_4$ , Co-Pi, and Pt nanoparticles under visible light [71]. The  $Ta_3N_5$  nanotube showed three times higher photocurrent than regular  $Ta_3N_5$  film. The PEC water oxidation is reported to be improved by  $IrO_2$ ,  $Co_3O_4$ , and Co-Pi NPs; however Pt was ineffective.

#### 1.4.2 Photochemical Water Splitting Studies using Metal-/Non-metal Nitrides

##### *III-Nitrides*

J. Sato *et al.* reported the first example of non-oxide photocatalyst for overall water splitting.  $RuO_2$  nanoparticle dispersed  $\beta-Ge_3N_4$  photocatalyst successfully decomposed water into  $H_2$  and  $O_2$  under UV light [72].

Kocha *et al.* reported that the energetic position of the conduction band edge of GaN is dependent on the pH of the solution as follows:  $E_C = -0.49 - 0.055 \cdot pH$  (vs. NHE) [43]. Maeda *et al.* studied GaN powder and demonstrated the importance of crystallinity and need of a suitable co-catalyst [73]. Stable and stoichiometric decomposition of  $H_2O$  into  $H_2$  and  $O_2$  was demonstrated on well-crystallized GaN with  $Rh_{2-x}Cr_xO_3$  nanoparticles. T. Kida *et al.* further demonstrated that GaN powder is capable of producing  $H_2$  from water containing electron donor ( $Na_2S-Na_2SO_3$ ,  $CH_3OH$ ) without even loading a noble metal [74]. N. Arai *et al.* studied the effect of divalent metal ion ( $Mg^{2+}$ ,  $Zn^{2+}$ ,  $Be^{2+}$ ) doping on the photocatalytic activity of GaN powder for overall water splitting [75]. Divalent metal ion doped GaN powder showed significantly improved and stable activity in the presence of  $RuO_2$  co-catalyst. The role of metal ion dopant is to produce *p*-type GaN with enhanced concentration and mobility of holes for efficient water splitting. H. S. Jung *et al.* studied the photocatalytic activity of GaN nanowire grown by Ni catalyst-assisted metal-organic chemical vapor deposition [76]. By measuring the amount of

photodegraded dye solution, they demonstrated much better activity of GaN nanowires than that of GaN submicron dots or thin films. Additionally, stable and enhanced photocatalytic activity of GaN nanowire is observed in the pH range between 2 and 5, having much better activity than TiO<sub>2</sub> and ZnO nanowires.

Most recently, J. B. Park *et al.* reported the growth of high-area-density GaN nanowires on large-area graphene films using a Ni-catalyst assisted vapor-liquid-solid (VLS) method via chemical vapor deposition [77]. The as-grown GaN nanowires were transferred onto flexible polymer substrate to use as flexible photocatalyst. The photocatalytic activity of such GaN nanowires was tested by measuring the photodegradation of organic dye molecules under UV light. Long-term stability of GaN nanowire was further confirmed under acidic solution. By measuring photodegradation of methylene orange, W. Lai *et al.* recently reported visible light activity of InGaN nanodots grown on GaN/sapphire substrate [78].

### ***Other Nitrides***

L. Yuliaty *et al.* synthesized Ta<sub>3</sub>N<sub>5</sub> nanoparticles from mesoporous carbon nitride template, and showed that these nanoparticles had higher activity than bulk Ta<sub>3</sub>N<sub>5</sub> to generate H<sub>2</sub> in presence of methanol under visible light [79]. A metal-free earth-abundant photocatalyst is recently reported by X. Wang *et al.* wherein graphitic carbon nitrides (g-C<sub>3</sub>N<sub>4</sub>) was synthesized by thermal polycondensation of common organic monomers [80]. The g-C<sub>3</sub>N<sub>4</sub> photocatalyst showed stable photocatalytic activity to generate H<sub>2</sub> from water under visible light (upto 540 nm) in the presence of electron donors.

## **1.5 Motivation for Choosing “Nanowire” as a Water Splitting Photocatalyst**

The photocatalytic activity of the conventionally used powder samples is low because of inefficient light absorption, inefficient carrier separation, and low crystalline quality. On the other hand, one dimensional (1D) nanostructures, such as nanowires are

attractive owing to their unique electrical, optical and structural properties [81]. The 1D nanostructures provide extremely large surface-to-volume ratio, which significantly improves the reaction surface area [12, 82]. Because of the lateral strain relaxation, 1D nanowires are nearly free from dislocations or defects [82, 83]. As the size of the nanostructure decreases, the light absorption may be improved significantly via light trapping and scattering effects in nanowire arrays [14]. This trapped light would otherwise be lost by direct reflection from a flat surface. Therefore, less material is required to absorb the same amount of light. Additionally, the size of the nanostructures is usually smaller than the diffusion lengths of the photoexcited carriers. Thus, most of the carriers can easily migrate to the photocatalyst-water interface [14]. Hence, the charge trapping and recombination in the bulk can be avoided. Further, nanomaterials offer higher solubility due to their higher surface energy and higher surface area over bulk materials, leading to enhanced light absorption and improved quantum efficiency [13]. Furthermore, owing to the quantum confinement effect, the band structure of the nanomaterials can be engineered by tuning their size [14]. Therefore, a bulk material with inappropriate band alignment with respect to water redox potential can be tuned by changing their size to function as an appropriate catalyst for water reduction and/or oxidation [84]. Moreover, noble metal nanoparticles can be used to significantly enhance and extend the optical absorption of the nanomaterials through surface plasmon resonance [85]. Another important aspect of 1D nanowires is that they can be grown/synthesized on virtually any substrate, providing a distinct opportunity to integrate with low cost Si based solar cells [86]. Finally, one dimensional nanowires allow control over the photocatalyst crystal plane promoting either H<sub>2</sub> or O<sub>2</sub> evolution [87]. Consequently, significantly improved photocatalytic activity is expected from 1D nanoscale materials. It is therefore imperative to explore III-nitride nanowires as water splitting photocatalyst.

## 1.6 Organisation of the Thesis

This thesis work focuses on the design, growth, characterization, and performance evolution of III-nitride nanowire photocatalyst for efficient and stable photochemical

water splitting under UV and visible light.

Chapter-1 focuses on global energy crisis and the need for alternative energy sources that are renewable, storable and carbon-free. The concept of solar water splitting is introduced as a viable approach to provide sustainable, clean and storable energy. A brief review of the metal-/non-metal nitride photocatalysts and photoelectrodes is presented. Finally, the motivation for using III-nitrides in the form of 1D nanowires is discussed.

Chapter-2 presents the growth of catalyst-free vertically aligned III-nitride nanowires by plasma assisted molecular beam epitaxy. The optical and structural characterization techniques used in this study are briefly summarized. The experimental set-up for photochemical water splitting is described in detail.

Chapter-3 describes the first demonstration of wafer scale photochemical water splitting using GaN nanowire arrays. The achievement of high efficiency overall neutral water splitting under UV light is further described by using controlled Mg doping in GaN nanowire arrays.

Chapter-4 reports on the development of multi-band InGaN/GaN nanowire heterostructure for overall water splitting under visible light. Here we have demonstrated for the first time one-step overall neutral water splitting under UV, blue and green light (up to 560 nm).

Chapter-5 describes high efficiency and stable overall water splitting using *p*-type double band InGaN/GaN nanowire heterostructure under visible light (up to 475 nm). Here we have incorporated optimized Mg doping in GaN and InGaN nanowire arrays for efficient and stable overall water splitting under UV and visible light, for the first time.

Chapter-6 demonstrates a novel approach to transform UV light responsive GaN nanowire arrays into violet light (up to 450 nm) active photocatalyst for overall neutral water splitting. Here we have engineered the optical absorption of GaN by introducing Mg related donor and acceptor energy states to perform as a violet light active photocatalyst.

Chapter-7 describes the challenges to achieve overall water splitting under red light using high In content InGaN nanowire. To address those challenges two different strategies have been discussed and their current stage of development have been reported.

Chapter-8 reports the first example of dye-sensitized III-nitride nanowire photocatalyst for water splitting under green, yellow and orange solar spectrum.

Chapter-9 summarizes the present dissertation work along with the critical challenges that need to be addressed for large-scale application of III-nitride based photocatalyst for solar water splitting. Some future directions have been proposed to enable III-nitride based artificial photosynthesis system to achieve carbon-free energy and environment.

## **1.7 Conclusions**

Solar energy is the ultimate solution to mitigate the current and future energy crises. However, for widespread market penetration, solar energy has to be harnessed more efficiently and stored for small to large-scale, short to long-term applications. Solar water splitting allows producing H<sub>2</sub> gas, a clean, renewable and carbon-free energy carrier. Because of their unique material and structural properties, one-dimensional Group-III nitride nanowires possess immense potential for efficient harnessing of clean energy just from sunlight and water; therefore is the center focus of this thesis.

# Chapter-2

## Growth and Characterization of III-Nitride Nanowires

### 2.1 Introduction

As described in the previous chapter, the development of III-nitride photocatalyst in the form of one-dimensional nanowire is vital to achieve high efficiency solar water splitting. The III-nitride nanowires can be grown with or without the use of foreign metal catalyst (Au, Ni, Fe) on untreated or pre-patterned substrate. In this work, III-nitride nanowires are grown using catalyst-free self-assembled plasma-assisted molecular beam epitaxy (MBE). The catalyst-free growth can avoid the detrimental effects caused by the foreign metal catalyst. In this chapter, the growth of GaN and InGaN nanowires on Si (111) substrate is discussed. The optical properties of the nanowires are characterized by photoluminescence (PL), X-ray photoelectron spectroscopy (XPS), and micro-Raman spectroscopy. The structural properties are assessed by field emission scanning electron microscopy (FE-SEM), transmission electron microscopy (TEM), and energy dispersive X-ray spectroscopy (EDX). These wires are subsequently used for photocatalytic water splitting experiments. Furthermore, the experimental set-up for water-splitting, details of the experimental procedure and performance evolution is discussed.

### 2.2 III-Nitride Nanowire Growth Techniques

Since the first demonstration of Si nanowire whiskers in 1964 by Wagner and Ellis [88] in a vapor-liquid-solid (VLS) growth mode using Au catalyst, significant researches have been focused on the growth of nanowires. In the VLS mode, the foreign metal catalyst acts as nucleation center to initiate the nanowire growth. However, the metal catalyst atom creates deep level electronic states in the band gap and therefore, acts as a recombination site for the photogenerated carriers. On the other hand, the catalyst-free

MBE technique used in this study is attractive for technological aspects, as it does not require any foreign metal, and expensive advanced lithography. Additionally, self-induced catalyst-free MBE allows growing excellent crystalline quality nanowires, rendering them a potential photocatalyst for high efficiency solar water splitting.

The catalyst-free MBE growth of nitride nanowires was first coined independently by E. Calleja and K. Kishino [89-91]. It has been assumed that the catalyst-free spontaneous growth of nanowire follows VLS growth mode, wherein the Ga or In acts as a self-catalyst for the growth initiation [92-95]. However, recent experimental studies have ruled out this hypothesis [96, 97]. Independent studies have now confirmed that the catalyst-free growth can be well explained by a diffusion-induced mechanism [98]. In this model, the metal adatom migrate and form a nucleation site to form the nanowire due to surface inhomogeneities or local strain variation. Because of the higher sticking coefficient and lower chemical potential at the nanowire top compared to the side walls, the metal adatoms diffuse from the nanowire sidewalls to the top surface [99]. The axial growth is therefore enhanced. Additionally, due to higher diffusion length of metal adatoms than N, the axial growth is enhanced due to metal adatoms impinging on the top surface and on the side facets where they may reach the top due to surface diffusion [100, 101].

In this study, a Veeco Gen II MBE system with an integrated radio-frequency (RF) plasma source is used for the growth of nanowires, as shown in Fig. 2-1. A nitrogen rich growth condition is used that ceases nanowire radial growth and reduces nitrogen vacancy related defects in the nanowire [102]. The commonly observed growth orientation for wurtzite III-nitride nanowires is along the N-polar [000-1] direction (*c*-axis) [103].

Prior to loading into the MBE chamber, the Si (111) substrate is rinsed with acetone and methanol to remove organic contaminants and subsequently with 10% hydrofluoric acid (HF) to remove native oxide. *In situ* oxide desorption was performed at ~770 °C before the growth initiation until the formation of a clean Si (111) 7×7 reconstructed surface is confirmed by reflection high-energy electron diffraction (RHEED).

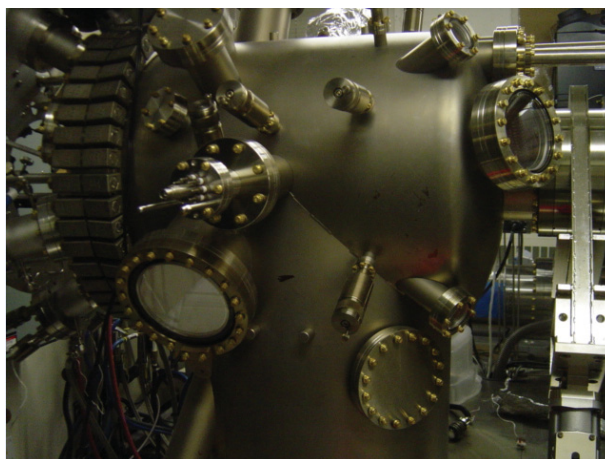


Figure 2-1: Veeco Gen II - Plasma-assisted molecular beam epitaxy system at McGill.

A thin (~one monolayer) Ga seeding layer was *in situ* deposited, which promotes the nucleation of nanowires. Thermal effusion cells were used for gallium (Ga), indium (In), and magnesium (Mg). Nitrogen radicals are supplied from a RF plasma source. The growth parameters include a growth temperature of  $\sim 750$  °C, nitrogen flow rate of 1.0 standard cubic centimeters per minute (sccm), a forward plasma power of  $\sim 350$  W, and a Ga beam equivalent pressure of  $\sim 6 \times 10^{-8}$  Torr. The In BEP is  $\sim 8 \times 10^{-8}$  Torr. The Mg effusion cell temperature is varied from 190 to 315 °C, which corresponds to Mg beam equivalent pressure (BEP) of  $\sim 1 \times 10^{-11}$  to  $\sim 3 \times 10^{-9}$  Torr. The growth temperature for GaN is  $\sim 750$  °C. The growth temperature for InGaN is in the range of 640 to 680 °C.

## 2.3 Characterization Techniques of the Nanowires

### 2.3.1 Scanning Electron Microscopy (SEM)

The dimension (height, diameter) and the areal density of the nanowires are assessed by field emission scanning electron microscopy (FEI Inspect F-50 FE-SEM) at an accelerating voltage of 5-10 KV and emission current of 5-10  $\mu$ A. No pretreatment of the sample is required due to the highly conductive silicon substrate, allowing a fast analysis of the nanowire morphology. The areal density of the nanowire is estimated from the top

view SEM image. The height of the nanowire is assessed from the 45° tilted edge view of the cleaved samples.

### **2.3.2 Transmission Electron Microscopy (TEM)**

In order to achieve atomic scale resolution, transmission electron microscopy (TEM) is performed.<sup>1</sup> With different operating modes of TEM, valuable information of the nanowire can be revealed; such as, the precise dimension (length, diameter) of individual nanowire, crystal structure, lattice parameter, defect density, elemental composition etc. The sample preparation for TEM analysis generally involves multiple steps such as mechanical grinding, polishing and ion milling to create a sufficiently thin sample for electron transmission. However, nanowire sample does not require these steps owing to their thin diameter (~30-100 nm). The nanowires can be easily scratched-off from the silicon substrate using a razor blade and subsequently transferred on a carbon coated copper grid for TEM analysis.

#### **TEM Operating Modes:**

A TEM can be used to obtain high resolution images as well as diffraction pattern [104]. Figure 2-2 illustrates the electron beam path in a TEM machine. Parallel electron beam is first scattered by the specimen and pass through an objective lens. All the electrons scattered from one point in the specimen is collected at one point on an image plane, creating an image of the specimen, as illustrated in Fig. 2-2. On the other hand, all electrons scattered in the same direction from different points on the specimen is collected at one point on the diffraction plane, generating a diffraction pattern of the specimen.

---

<sup>1</sup>The TEM analysis is performed at Hydro-Quebec, Facility for Electron Microscopy Research (FEMR), McGill University, and at École Polytechnique de Montréal.

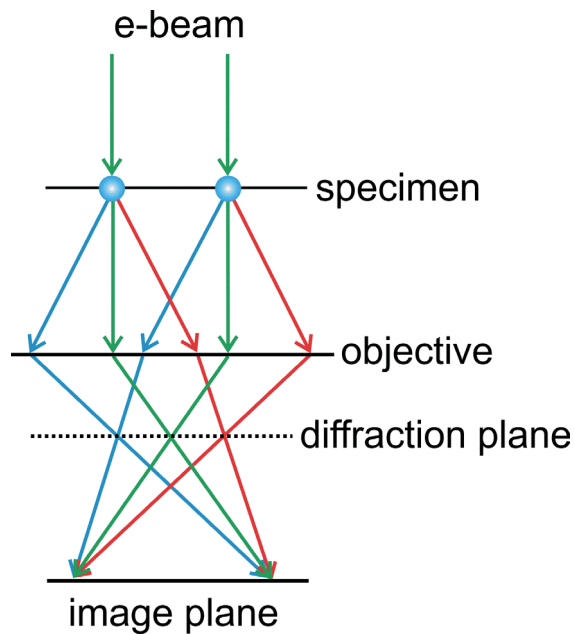


Figure 2-2: Schematic of electron beam line path in a transmission electron microscopy machine [104].

The most common mode of operation for a TEM is the bright field imaging mode. In this mode the image contrast is formed (classically) due to the occlusion and absorption of electrons in the specimen. The thicker region in the sample or regions with higher atomic number will appear dark, whilst thin regions or regions with no sample will appear bright. On the other hand, in case of high resolution TEM (HRTEM) imaging, a phase difference is utilized to generate contrast in the image. In the case of high angle annular dark field (HAADF) imaging, a ring shaped annular dark-field detector is used to collect only the electrons that are scattered at high angle [104]. The strength of interaction between the incident electrons and the atoms in the specimen is proportional to the square of the atomic number<sup>2</sup> ( $\propto Z^2$ ). Therefore, this imaging is highly sensitive to the atomic number ( $Z$ ) of the elements, i.e., easier for heavier elements than lighter elements. For this reason, metal atoms (In, Ga, Al) can only be seen in most of the TEM images of III-nitrides. This mode is also called  $Z$ -contrast mode.

---

<sup>2</sup> Atomic number (proton numbers) of the elements involved in this study: N (7), Ga (31), In (49).

In addition to the above mentioned TEM modes, energy dispersive detector can be utilized to detect the energy loss of the electrons due to the interaction with the atoms of the specimen. This technique is called electron energy loss spectroscopy (EELS), which allows determining the chemical elements by their specific absorption edges [105].

### **TEM Equipment:**

A CM200 microscope with an accelerating voltage of 200 kV was used to obtain bright-field TEM images. For scanning transmission electron microscopy-secondary electron (STEM-SE) and STEM-HAADF imaging, a Hitachi HD2700 Cs-corrected STEM with a cold field emission emitter operated at 200 kV and with an electron beam diameter of approximately 0.1 nm was used. STEM energy dispersive spectrum (EDS) analysis was performed using a 60 mm<sup>2</sup> silicon drift detector (SDD) from Bruker.

### **2.3.3 Photoluminescence (PL) Spectroscopy**

Photoluminescence (emission of light) is a non-contact, and non-destructive technique of probing the electronic structure of materials. PL spectroscopy is a very useful tool to assess the fundamental electrical and optical properties of materials, such as band gap, material quality, excitonic states, dopant incorporation, impurity states and recombination mechanism. In general, a light beam with photon energy higher than the band gap of the material is directed onto a sample where it excites electrons from the valence band to the conduction band, leaving behind a hole in the valence band. Hence, an electron-hole pair is generated in the material. The photo-excited electron and hole subsequently thermalize to the lowest energy states by phonon emission. This thermalization process is much faster than the radiative recombination process. The electron-hole pairs can recombine non-radiatively to generate phonons or radiatively by the emission of light with a certain wavelength corresponding to the band gap of the material.

The near-band-edge transition can be perturbed by a number of phenomenon [106]. The electron and hole can form a bound state, the exciton. The excitonic emission dominates the near-band-edge emission. The excitons can either be free ( $FX^A$ ,  $FX^B$ ,  $FX^C$ ,

depending on the contributing valence band) or bound to an impurity (donor or acceptor). The emission energy can be reduced by the emission of phonons (92 meV for GaN) or phonon replicas (red-shifted peak by  $n \cdot 92$  meV, where  $n=1, 2, 3, \dots$ ). Furthermore, the emission process can further be affected by Fermi-level pinning deep in the band gap. All of the above aspects play a role in the PL properties significantly.

A 325 nm He-Cd laser (Kimmon Koha) or a 405 nm laser was used as the excitation source for the PL measurement of the nanowire heterostructure. The PL was spectrally resolved by a high-resolution spectrometer, and detected by a photomultiplier tube. The laser beam was focused on the sample through a  $60 \times$  objective, with a circular beam size of around 5  $\mu\text{m}$ . The emitted light was collected by the same objective, and spectrally resolved by a high-resolution spectrometer (JY HR-550) and detected by a photon counting mode photomultiplier tube.

### **2.3.4 Raman Scattering Spectroscopy**

Raman spectroscopy is based on inelastic scattering of monochromatic light. Inelastic scattering refers to a process, wherein the frequency of the incident photons in the monochromatic light changes upon interaction with a sample. Photons are absorbed and reemitted by the sample. The frequency of the reemitted photon shifts upward or downward in comparison with the incident photon, and is called Raman effect. This shift is a very useful probe to provide important information about the strain state, crystal structure, phonon lifetime and phonon decay, rotational, vibrational and other low frequency transition in a material. The inelastic scattering of photon was first predicted by Adolf Smekal in 1923 [107], and was experimentally observed independently by C. V. Raman and K. S. Krishnan [108] in liquids, and by G. Landsberg and L. I. Mandelstam [109] in crystals in 1928. When photons are scattered by the atoms or molecules, about 99.999% photons undergo elastic scattering (Rayleigh scattering), and therefore do not provide any meaningful information about the sample. Since only 0.001% of the incident photon produce inelastic Raman signal, special measures should be taken to distinguish the very weak Raman signal from the predominant Rayleigh scattering [109]. The commonly used unit of Raman shift is  $\text{cm}^{-1}$ .

The Micro-Raman measurements were carried out at room-temperature with an external 488 nm Argon-ion laser through a 100× objective with a numerical aperture ~0.9. The focused laser spot size was ~1 μm and the estimated power on the sample was ~40 mW. The Raman signal was collected by a Synapse CCD air-cooled detector. The incident laser was parallel with the hexagonal *c*-axis of the nanowires, and the laser light was scattered without polarization analysis (*z*(*..*)*z* direction).

### 2.3.5 X-ray Photoelectron Spectroscopy (XPS)

X-ray photoelectron spectroscopy (XPS) or Electron Spectroscopy for Chemical Analysis (ESCA) is based on the *photoelectric effect*, which was first discovered by Albert Einstein in 1905 [110]. Physicist K. Siegbahn first used photoemission as an analytical tool in 1954 [111]. Unlike the above mentioned optical characterization techniques, XPS is a *surface-sensitive* technique. This non-destructive technique measures elemental composition, empirical formula, chemical and electronic state of the elements that exist within the top 0-10 nm in a given material. An XPS spectrum is generally obtained by irradiating a material with a beam of X-rays, and by simultaneously measuring the kinetic energy and the number of photo-excited electrons using an electron analyzer. Figure 2-3 schematically illustrates the photoemission process upon X-ray excitation from a semiconductor material and analysis by a spectrometer. The binding energy of the photoelectron relative to the Fermi-level can be measured from the kinetic energy of the photoelectrons. By analyzing the peak position and intensity of the binding energy, one can derive the chemical composition, chemical states/bonds and valence band structure [110]. In order to calibrate the peak position, Fermi energy level ( $E_F$ ) is generally used as a reference point for solid samples. Note that the sample holder and the spectrometer need to have the same grounding point to set the reference energy ( $E_F$ ) at 0 eV. If the sample is highly conductive, the standard reference metals (Cu-2*p*<sub>3/2</sub>, Ag-3*d*<sub>5/2</sub>, and Au-4*f*<sub>7/2</sub> peaks) mounted on the sample holder can be used to calibrate the binding energy. However, if the sample is non-conductive or poorly conductive, the charging

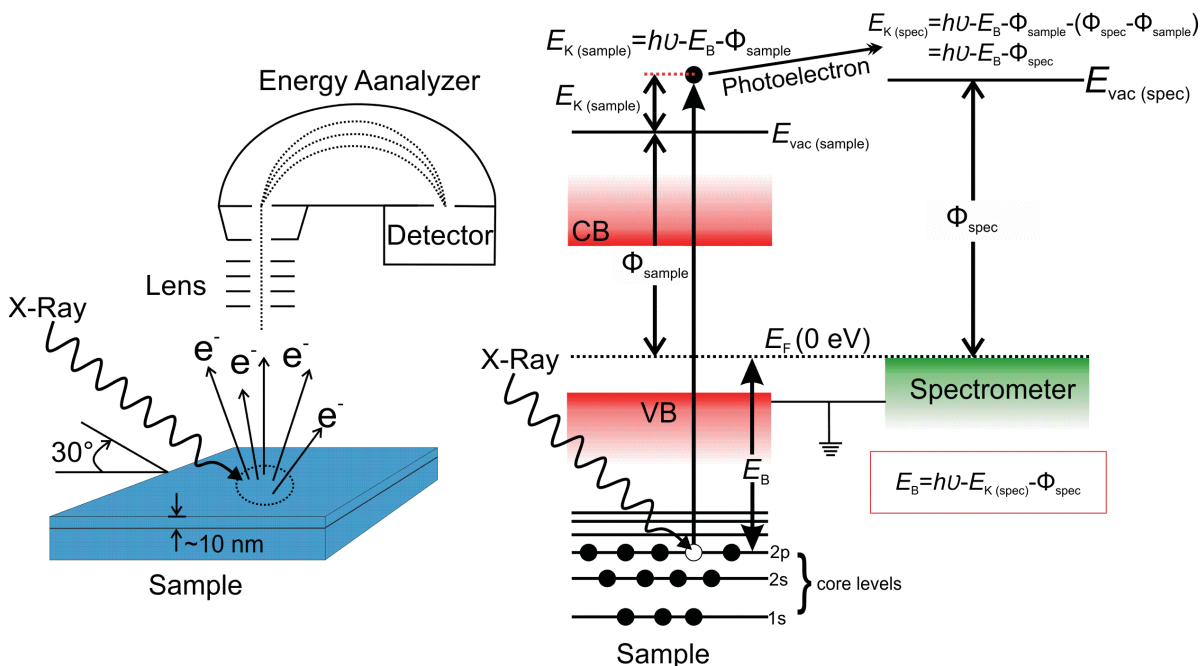


Figure 2-3: Schematic illustration of the operating principal of X-ray photoelectron spectroscopy in studying a semiconductor material. Here,  $\Phi_{\text{sample}}$  and  $\Phi_{\text{spec}}$  are the work function of the sample and spectrometer, respectively.  $E_B$  is the binding energy of the electron.  $E_{K(\text{sample})}$  and  $E_{K(\text{spec})}$  are the kinetic energy of the photo-excited electron and spectrometer measured electron, respectively.

effect<sup>3</sup> needs to be compensated by a low-energy electron flood gun. In this case, the binding energy needs to be carefully calibrated with adventitious carbon C-1s peak (285.0 eV), which arises from the adsorption of aliphatic hydrocarbons from the atmosphere.

### XPS Equipment:

The Thermo Fisher Scientific K-Alpha XPS system equipped with a monochromatic Al-K $\alpha$  X-ray source ( $h\nu=1486.6$  eV) and 180° double focusing hemispherical analyzer was used for the analysis. The analysis chamber pressure was  $10^{-8}$  Torr. The X-ray source is located at 60° with the surface normal to excite the nonpolar surfaces of nanowire arrays. The high resolution XPS spectra were obtained using an X-ray beam size of 400

<sup>3</sup> Accumulated positive charge on the sample due to escaping of photoelectron from the sample surface.

$\mu\text{m}$ , pass energy of 50 eV, and a step size of 0.1 eV. Individual peak fitting was performed using convolution of Lorentzian and Gaussian line shapes (L/G = 30%) with Avantage software (Thermo Scientific). The binding energies were calibrated with both Au  $4f$  (84.0 eV) and C  $1s$  (285.0 eV) peaks. The difference between the Fermi-level and the valance band maximum at the surface ( $E_{\text{FS}}-E_{\text{VS}}$ ) was estimated from XPS valence band spectrum, as explained in Chapter-3. The intersection between the linear extrapolation of the valence band leading edge and the baseline indicates the position of surface valence band ( $E_{\text{VS}}$ ) with respect to the surface Fermi level ( $E_{\text{FS}}$ , binding energy=0 eV).

### 2.3.6 Experimental Set-up for Photochemical Water Splitting

Figure 2-4 shows the experimental setup for photochemical water splitting. It is composed of a reaction system and an evaluation system. For the reaction system, an outer irradiation from a 300W Xenon lamp (Cemax, PE300BUV) with a quartz lid that secures adequate transmittance of both UV and visible light are adopted. A piece of the wafer sample together with a Teflon holder is placed at the bottom of the chamber and then appropriate solutions were added to the chamber. Distilled water (pH~7.0) was used for the neutral water splitting reaction. The water is purged with Ar for 30 mins before each experiment to remove residual gases dissolved in water. After evacuating the chamber using a vacuum pump, a Xenon lamp is turned on to start the reaction. A gas chromatograph (GC-8A, Shimadzu) equipped with a thermal conductivity detector (TCD) and high purity (99.9999 %) Ar carrier gas is employed for the evaluation of evolved gases ( $\text{H}_2$  and/or  $\text{O}_2$ ). A vacuum tight syringe is used for sampling the evolved gases. Sampling by a syringe is performed for a certain time depending on the activity of reaction. Dummy test was repeated to get the baseline, and calibration was carefully done to get the exact amount of evolved gases.

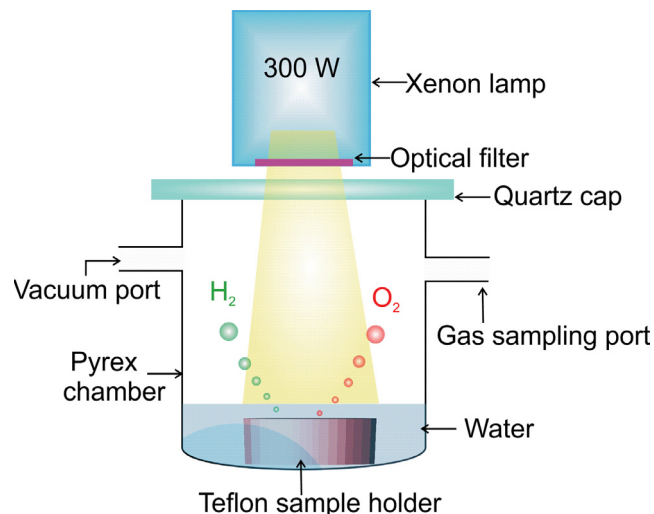


Figure 2-4: Schematic illustration of the experimental set-up for photochemical water splitting.

Long-pass and band-pass filters are also used for systematic investigation of wavelength dependence of photocatalytic activity and for measurement of quantum efficiency. The H<sub>2</sub> half reaction was performed in the presence of CH<sub>3</sub>OH (20 vol.%) as electron donor and Rh or Pt nanoparticles as co-catalyst. For O<sub>2</sub> half reaction, AgNO<sub>3</sub> (0.1 M) was used as electron acceptor. The experimental error in the evolution of H<sub>2</sub> and O<sub>2</sub> is estimated to be ~10%, which is ascribed to the manual sampling of the gases.

### 2.3.7 Deposition Process of Co-catalysts

As will be discussed in Chapter-3, co-catalyst nanoparticles are usually needed to enhance the carrier extraction efficiency and reduce the overpotential required for efficient water splitting [9]. The deposition of such co-catalysts on nanowire surfaces may be achieved through impregnation, adsorption, or photodeposition. Among these methods, photodeposition is easily applied to almost all noble metals. Most importantly, the co-catalyst nanoparticles can be selectively deposited on the active sites of the photocatalyst surface, since the metal cations in aqueous solution are reduced by photogenerated electrons into metal nanoparticles—which are always deposited on the surface of photocatalyst where electrons reside. In this regard, we have investigated the

photodeposition of Rh/Cr<sub>2</sub>O<sub>3</sub> core-shell nanoscale co-catalysts on our GaN nanowires. Details on the purpose of using core-shell structure are discussed in Chapter-3. The deposition of Rh/Cr<sub>2</sub>O<sub>3</sub> core/shell nanoparticles on the GaN and InGaN nanowires was performed following a two-step photodeposition process, as schematically illustrated in Fig. 2-5. First, 2-4 μL of 0.2 M Sodium hexachlororhodate (III) (Na<sub>3</sub>RhCl<sub>6</sub>, Sigma Aldrich), 12 ml of CH<sub>3</sub>OH, and 60 ml of distilled water (purged with pure Argon for 30 mins) were placed in a 460 ml Pyrex chamber (Kimble Chase) with quartz lid. The GaN (or InGaN) nanowire photocatalyst (on Si substrate) was placed in the Pyrex chamber using a homemade Polytetrafluoroethylene (PTFE) holder. The chamber was then pumped down for 10 mins, and subsequently irradiated for 30 mins using 300 W Xenon lamp (Cermax, PE300BUV) for photo-assisted deposition of Rh nanoparticles. The sample was dried in air for a few minutes. In the second step the Cr<sub>2</sub>O<sub>3</sub> was deposited following the above-mentioned procedure by 2-4 μL of 0.2 M potassium chromate (K<sub>2</sub>CrO<sub>4</sub>, Sigma Aldrich) as precursor. The Rh and Cr<sub>2</sub>O<sub>3</sub> thus forms a core and shell nanostructure, respectively on the nanowire surface, as will be discussed in detail in Chapter-3. Figure 2-6 illustrates the mechanism of photodeposition [112]. Upon irradiation of the semiconductor with light of appropriate wavelength, electrons and holes are generated in the conduction and valence band, respectively. These electrons can be used to reduce the metal ions (e.g., Rh<sup>3+</sup>) to metal (Rh) that will be simultaneously deposited on the surface of the semiconductor.

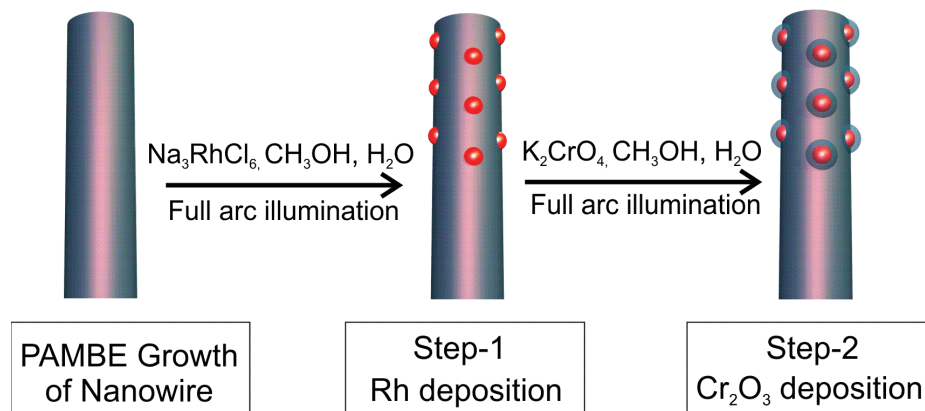


Figure 2-5: Schematic illustration of two-step photodeposition process of Rh (core) and Cr<sub>2</sub>O<sub>3</sub> (shell) co-catalyst nanoparticles on the nanowires.

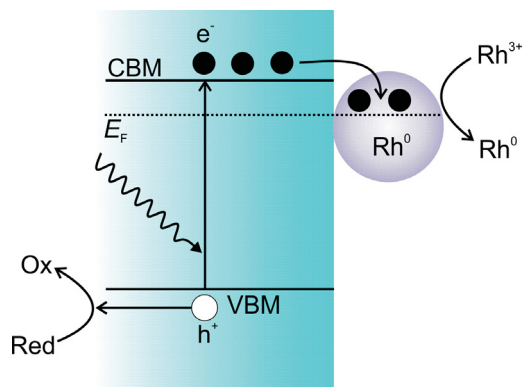


Figure 2-6: Schematic illustration of the photodeposition mechanism of Rh co-catalyst on a semiconductor photocatalyst under photoexcitation [112].

A hole scavenger such as an alcohol has to be present to avoid accumulation of positive charge during the photodeposition. The main reaction processes involved in the photoreduction of  $\text{Rh}^{3+}$  are as follows: (1) first the  $\text{Rh}^{3+}$  ions are adsorbed on the semiconductor surface, (2) the photoexcitation generates electron-hole pairs in the semiconductor, (3) the electrons reduce  $\text{Rh}^{3+}$  adsorbed preferentially on the surface of the semiconductor, (4) while the holes are irreversibly scavenged by the methanol. Continuous reduction of  $\text{Rh}^{3+}$  can create agglomeration of Rh nanoparticles onto the semiconductor. Therefore, optimization of photodeposition recipe (duration of photoexcitation, precursor concentration etc.) is vital to achieve efficient deposition of the nanoparticles.

## 2.4 Conclusions

In this thesis, plasma assisted molecular beam epitaxy is used to grow III-nitride nanowire photocatalyst on Si substrate. Different structural and optical characterization techniques have been used to investigate the structural and optical properties of the as-grown nanowires. Details of the experimental procedure of water splitting and the photodeposition technique adopted to incorporate co-catalyst nanoparticles onto the nanowire photocatalyst are discussed.

## Chapter-3

# High Efficiency Overall Water Splitting on GaN Nanowire Arrays under Ultraviolet Light

### 3.1 Introduction

Since the discovery of the Honda–Fujishima effect [11] in a TiO<sub>2</sub>/Pt photoelectrochemical cell in the early 1970s, the use of semiconductors for photocatalytic water splitting has attracted tremendous interest: for it enables the generation of clean and renewable hydrogen fuel directly from solar irradiation without the consumption of electric power. Over the past 4 decades, the development of photocatalysis has primarily focused upon large band gap metal oxides [9, 15, 113], and oxynitrides [22, 32, 114] such as (Ga<sub>1-x</sub>Zn<sub>x</sub>)(N<sub>1-y</sub>O<sub>y</sub>). Recently, the use of group III nitride semiconductors for water splitting has attracted considerable attention. Moreover, the inherent chemical stability of nitrides also favors their use in the harsh photocatalysis reaction environment [56, 57, 68]. Indeed, recent first-principles calculations suggest that a single H<sub>2</sub>O molecule can be efficiently cleaved in an *exothermic* reaction to form H<sub>2</sub> under photoexcitation on the nonpolar surfaces of GaN [115, 116]. Ab initio molecular dynamic simulations further show that the overall water oxidation reaction at GaN surfaces can be energetically driven by photogenerated holes [115].

The size, morphology, surface chemistry, and crystal structure of photocatalysts often play a crucial role in determining their photophysical and photocatalytic properties [12, 13]. Conventional photocatalysts are typically employed in the form of powders. However, as mentioned in Chapter-1, photocatalysts in the form of one-dimensional (1-D) nanostructures, such as nanowires, nanobelts, and nanotubes, are highly desired due to their extremely large surface-to-volume ratios and significantly enhanced light absorption. In this study, we have examined water splitting reaction on the nonpolar

surfaces (*m*-plane) of GaN nanowire photocatalyst, which can further serve as a new platform for spontaneous water splitting under visible and infrared light irradiation by incorporating indium [41, 117]. The capacity of GaN nanowires for water splitting is unambiguously confirmed by utilizing the hole-scavenger CH<sub>3</sub>OH and the electron-acceptor AgNO<sub>3</sub> to respectively fuel H<sub>2</sub> and O<sub>2</sub> half-reactions. To further enable efficient carrier extraction, we have incorporated co-catalytic Rh/Cr<sub>2</sub>O<sub>3</sub> core-shell nanostructures on the lateral GaN nanowire surfaces and have observed, for the first time, photocatalytic *overall* water splitting on metal nitride nanowires. Furthermore, we demonstrate that the near-surface band bending of catalyst-free GaN nanowires can be controlled with *p*-type Mg-dopant incorporation. With optimized surface charge properties, we show that the efficiency of spontaneous overall water splitting can be enhanced by more than two orders of magnitude.

## 3.2 Photochemical Water Splitting on GaN Nanowire Arrays

### 3.2.1 Test Reaction for GaN Nanowire

We begin our investigation of photocatalytic activity on GaN nanowire surfaces (i.e., the lateral nonpolar *m*-plane) by independently studying the H<sub>2</sub> and O<sub>2</sub> half-reactions in the presence of respective sacrificial reagents. When a photocatalytic reaction is carried out in an aqueous solution consisting of a reducing reagent (i.e., an electron donor or hole scavenger such as alcohol), photogenerated holes irreversibly oxidize the reducing reagent instead of water and thereby enhance H<sub>2</sub> evolution, as shown in Fig. 3-1a. On the other hand, when photogenerated electrons in the conduction band are consumed by oxidizing reagents (i.e., electron acceptors or electron scavengers such as Ag<sup>+</sup> and Fe<sup>3+</sup>), O<sub>2</sub> evolution reaction is enhanced, as illustrated in Fig. 3-1b. These reactions are usually called H<sub>2</sub> and O<sub>2</sub> half reactions, respectively. Normally, the overall water splitting will be carried out after performing these half reactions. For the GaN nanowires, we have used CH<sub>3</sub>OH as a hole scavenger to conduct the H<sub>2</sub> half-reaction and AgNO<sub>3</sub> as an electron acceptor to perform the O<sub>2</sub> half-reaction, respectively. The evolution of H<sub>2</sub> and O<sub>2</sub> over time is shown in Fig. 3-2a, b—the corresponding reaction processes are schematically

illustrated in the insets. More than 5  $\mu\text{mol}$  of  $\text{H}_2$  and 50  $\mu\text{mol}$  of  $\text{O}_2$  are produced after 4 h, which demonstrates that GaN nanowires satisfy the thermodynamic and kinetic potentials for  $\text{H}_2$  and  $\text{O}_2$  evolution.

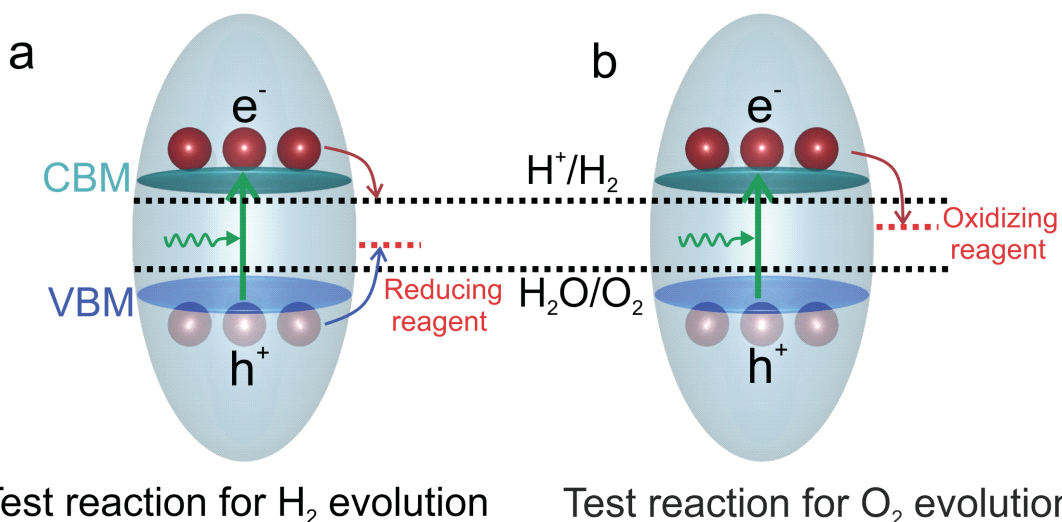


Figure 3-1:  $\text{H}_2$  or  $\text{O}_2$  evolution reaction in the presence of sacrificial reagents. (a) test reaction for  $\text{H}_2$  evolution, (b) test reaction for  $\text{O}_2$  evolution.

These observations are consistent with recent theoretical studies. The energy barriers for the first and second H-atom splitting on a pristine Ga-face are predicted to be  $\sim 0.10$  and  $\sim 1.42$  eV, respectively, which can be easily satisfied by the energy band potentials of GaN upon band gap excitation [118]. Additionally, ab initio molecular dynamic simulations further show that the overall water oxidation reaction at GaN nonpolar surfaces involves four proton-coupled electron transfer intermediate steps and can be energetically driven by photogenerated holes [115, 116, 119].

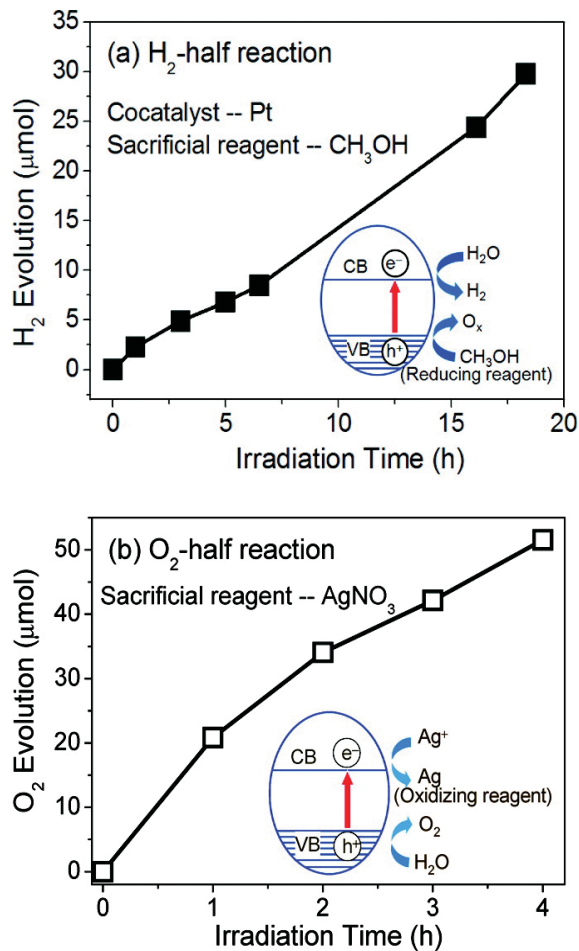


Figure 3-2: (a) H<sub>2</sub> evolution reaction and (b) O<sub>2</sub> evolution reaction in the presence of respective sacrificial reagents over GaN nanowires under a 300W full arc xenon lamp irradiation. The insets show the reaction mechanism.

### 3.2.2 Role of Co-catalyst on Photocatalytic Activities

Though H<sub>2</sub> generation on the nonpolar surfaces of GaN is expected to be exothermic and therefore very efficient under idealized theoretical conditions, in practice, semiconductor photocatalysis reaction rates are strongly influenced by surface charge properties. The presence of dangling bonds and/or surface defects may significantly degrade the photocatalytic activity through enhanced nonradiative recombination. Such defects also reduce the number of pristine sites available for H<sub>2</sub> evolution. Furthermore, due to the dominant *n*-type character of GaN, surface defects tend to pin GaN conduction

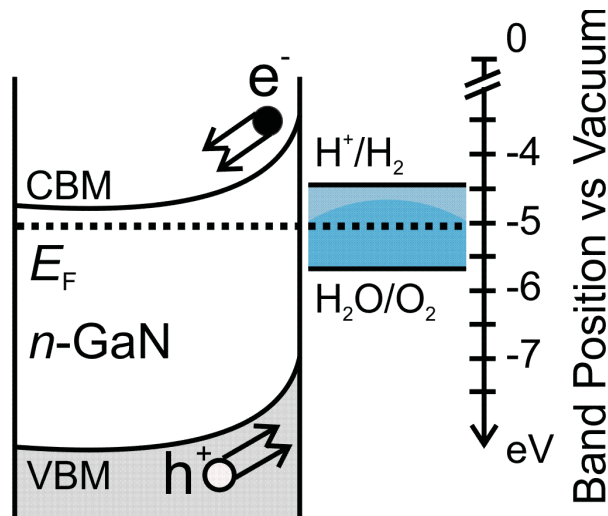


Figure 3-3: Upward band bending on nominally undoped or n-type GaN, which drives holes to the nanowire sidewall and electrons into the bulk.

and valence bands upward [120, 121], as shown in Fig. 3-3, resulting in a built-in electric field which drives excited electrons away from surface reaction sites, thereby exponentially reducing the rate of electron transfer to  $H^+$  ions [120, 122, 123]. For these reasons, as well as the experimental demonstration that  $O_2$  generation is a much more efficient process than  $H_2$  generation as shown in panels a and b of Fig. 3-2, it is essential to incorporate a suitable co-catalyst that can provide reaction sites and decrease the activation energy barrier for catalytic reactions. The co-catalyst enables efficient electron transfer to the surface by unpinning the bands at the co-catalyst/GaN interface and creates active sites for gas evolution [124]. The co-catalyst acts as a trap for the photogenerated carriers on the photocatalyst surface, as the Fermi level of the noble metal co-catalyst is always lower than the semiconductor photocatalyst. Therefore, enhanced photocatalytic activity is expected from co-catalyst incorporated photocatalyst. Figure 3-4 shows schematic of electron transfer from photocatalyst to co-catalyst (process 1), and  $H^+$  reduction to  $H_2$  (process 2). Co-catalyst deposition has been employed with most semiconductor photocatalysts developed to date in order to achieve efficient pure water splitting. Even a semiconductor photocatalyst possess band edges that are thermodynamically suitable for water splitting, co-catalysts such as Pt, NiO and  $RuO_2$  are usually loaded to introduce active sites.

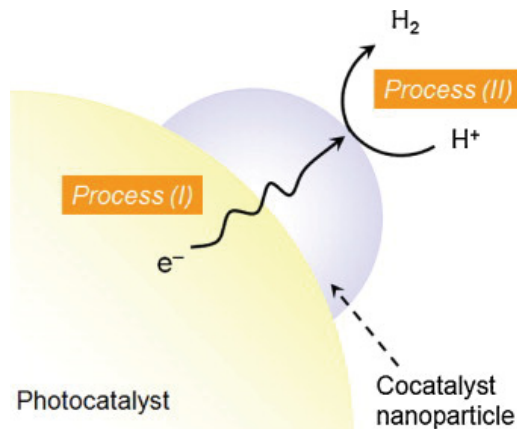


Figure 3-4: Schematic of electron transfer from photocatalyst to co-catalyst (process 1),  $H_2$  evolution (process 2) for overall water splitting [25].

Noble metals such as Pt and Rh are excellent promoters of  $H_2$  evolution but can also catalyze a backward reaction to form water ( $H_2O$ ) from  $H_2$  and  $O_2$ , thereby limiting their usefulness as co-catalysts for overall photocatalytic water splitting [125]. To avoid the  $H_2O$  forming back reaction, a transition-metal oxide that does not catalyze  $H_2O$  formation from  $H_2$  and  $O_2$  is usually employed as a diffusion barrier coating to prevent  $O_2$  interaction with the noble metal surface. Among the co-catalysts developed to date, core-shell-structured Rh/ $Cr_2O_3$  nanoparticles dispersed on a photocatalyst have been proven to enable  $H_2$  formation in oxynitride solid solutions [25]. While the Rh nanoparticles enhance water reduction reaction, the  $Cr_2O_3$  suppresses the backward reaction to form water from evolved  $H_2$  and  $O_2$  on Rh nanoparticles. Detailed electrochemical and *in situ* spectroscopic measurement reveals that the  $Cr_2O_3$  shell is permeable to protons and  $H_2$ , but not to  $O_2$ ; therefore  $Cr_2O_3$  does not interfere with proton reduction [124]. The deposition of such co-catalysts on nanowire surfaces is performed by photodeposition technique as discussed in Section 2.3.7 in Chapter-2.

### 3.2.3 Characterization of Photodeposited Rh/ $Cr_2O_3$ Core-shell Nanostructures

Scanning transmission electron microscopy (STEM, FEI Titan 80-300 Cubed equipped with an aberration corrector of the probe-forming lens and a high brightness electron source) was used to characterize the Rh/ $Cr_2O_3$  core-shell nanostructures

photodeposited on the GaN nanowires. Illustrated in Fig. 3-5a, a fairly uniform distribution of Rh/Cr<sub>2</sub>O<sub>3</sub> nanoparticles on the GaN nanowire lateral surfaces can be clearly seen. Figures 3-5b and 3-5c show a typical high-resolution transmission electron microscopy (HRTEM) image and a high-resolution high-angle annular dark field (HR-HAADF) image of the Rh/Cr<sub>2</sub>O<sub>3</sub> core-shell nanostructures photodeposited on the GaN nanowires, respectively.

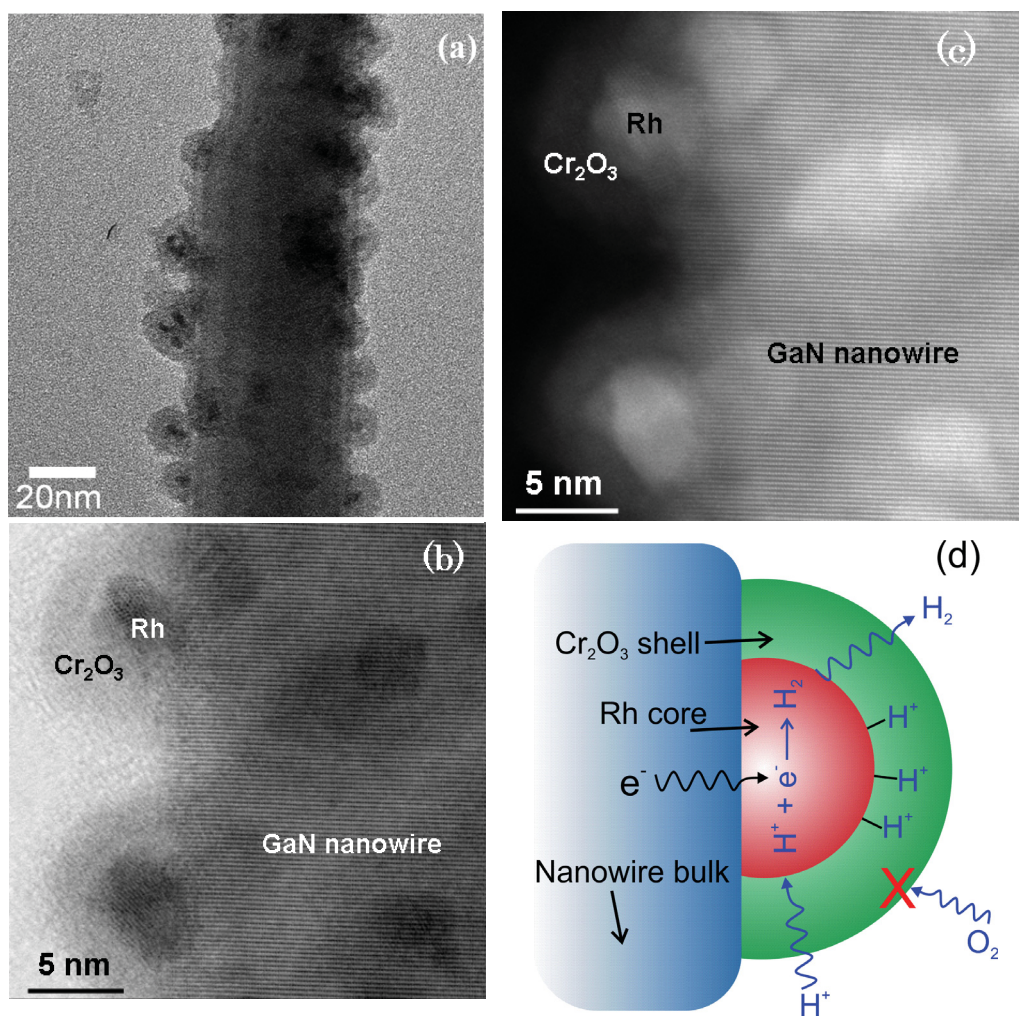


Figure 3-5: (a) Low magnification TEM image shows uniform distribution of the Rh/Cr<sub>2</sub>O<sub>3</sub> nanoparticles on GaN nanowire surfaces. (b) HRTEM image and (c) HR-HAADF image clearly show the Rh/Cr<sub>2</sub>O<sub>3</sub> core-shell nanostructures deposited on GaN nanowires, (d) illustration of H<sub>2</sub> evolution on Rh (core)/Cr<sub>2</sub>O<sub>3</sub>(shell) nanoparticles as a co-catalyst for overall photocatalytic water splitting [25, 125].

We can see that each GaN nanowire exhibits the nature of a single crystalline structure. For the Rh/Cr<sub>2</sub>O<sub>3</sub> core-shell structure, the metallic Rh core is well crystallized while the Cr<sub>2</sub>O<sub>3</sub> shell is likely amorphous. The reaction mechanism of H<sub>2</sub> evolution on Rh (core)/Cr<sub>2</sub>O<sub>3</sub> (shell) nanoparticles is illustrated in Fig. 3-5d. Moreover, electron energy loss spectrometry spectrum image (EELS-SI) was performed to study the elemental distribution in the Rh/Cr<sub>2</sub>O<sub>3</sub> core-shell nanostructure. In Fig. 3-6 the HR-HAADF and EELS images, corresponding individual element maps, and RGB images further show clearly the Rh/Cr<sub>2</sub>O<sub>3</sub> core-shell nanostructure are well deposited on GaN nanowires. By combining the HRTEM/HAADF images and the element mapping images, we have clearly confirmed that the Rh/Cr<sub>2</sub>O<sub>3</sub> core-shell nanostructures were successfully photodeposited on the lateral surfaces of the GaN nanowires.

#### **3.2.4 Overall Water Splitting on Rh/Cr<sub>2</sub>O<sub>3</sub> Nanoparticle Decorated GaN Nanowires**

Overall photocatalytic water splitting was carried out on the GaN nanowires photodeposited with Rh (core)/Cr<sub>2</sub>O<sub>3</sub> (shell) nanostructure, wherein the H<sub>2</sub> evolution was promoted by the noble metal (Rh) core while the backward reaction over the noble metal (water formation from H<sub>2</sub> and O<sub>2</sub>) was prevented by the Cr<sub>2</sub>O<sub>3</sub> shell [125]. Our own control experiment shows that without depositing a Cr<sub>2</sub>O<sub>3</sub> shell to cover the Rh nanoparticle core, pure water splitting was not observed. This is attributed to the fact that noble metals such as Rh and Pt, usually act to promote the H<sub>2</sub> + O<sub>2</sub> → H<sub>2</sub>O back reaction. A visual scheme of the pure water splitting process by GaN nanowires is illustrated in Fig. 3-7a. As expected, overall water splitting has been realized successfully on the GaN nanowires photodeposited with Rh (core)/Cr<sub>2</sub>O<sub>3</sub> (shell) nanostructures. Figure 3-7b shows the typical evolution of the photocatalytic water splitting reaction over time. In the two cycles displayed in Fig. 3-7b totalling ~ 20 hours, a steady and nearly stoichiometric evolution of H<sub>2</sub> and O<sub>2</sub> gases can be observed. No apparent degradation in the photocatalytic activity was observed after 20 hours. Repeated experiments yield similar results to those shown in Fig. 3-7b. It is also noted that the pH (~ 7.0) of the reactant solution was virtually invariant after the reaction.

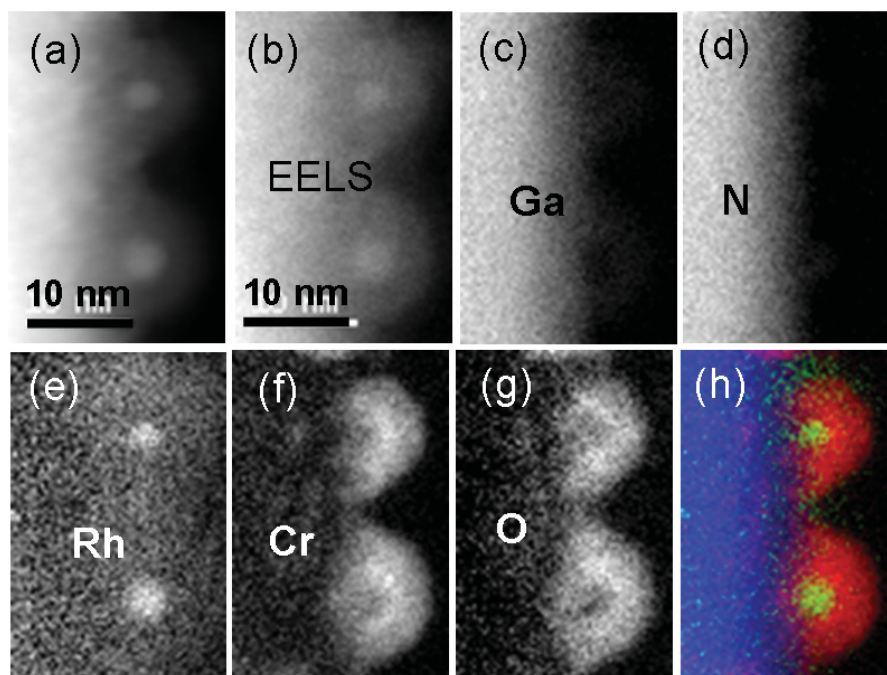


Figure 3-6: (a) HR-TEM image and (b) EELS mapping image, (c–g) corresponding individual element mapping images and (h) RGB image (Red: Cr, Green: Rh, Blue: Ga), clearly showing the Rh/Cr<sub>2</sub>O<sub>3</sub> core/shell nanostructure deposited on GaN nanowires.

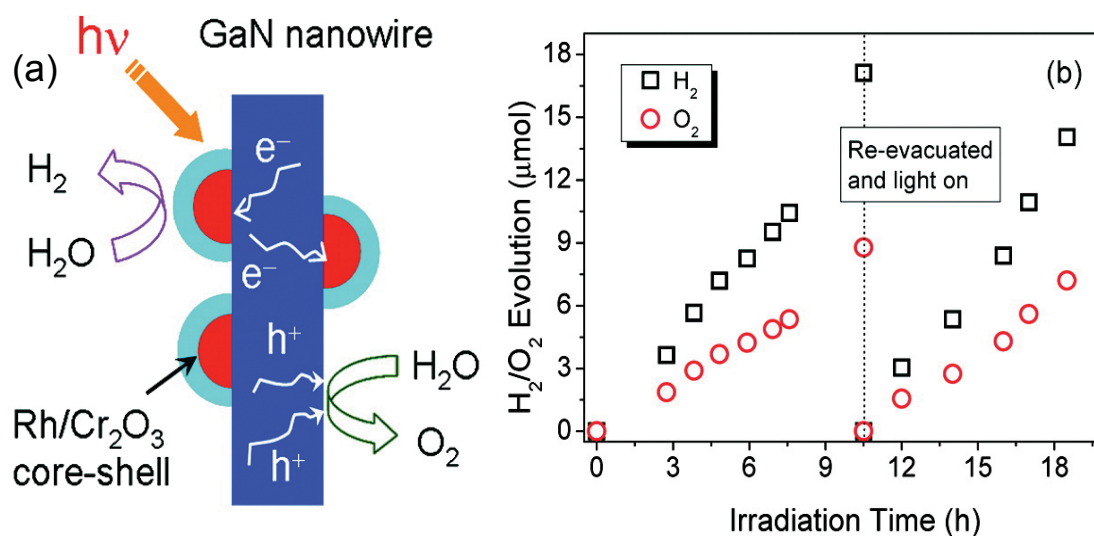


Figure 3-7: (a) Schematic illustration of water splitting on Rh/Cr<sub>2</sub>O<sub>3</sub> core-shell nanostructure deposited GaN nanowires and (b) Experimental overall photocatalytic water splitting on Rh/Cr<sub>2</sub>O<sub>3</sub> core-shell nanostructure deposited GaN nanowires, under a 300 W full arc xenon lamp irradiation for a duration of 18 hours.

Additionally, the turnover number (defined as the number of reacted electrons over the number of atoms in a photocatalyst) exceeded 6 after ~20 hours reaction time. These results further confirm that the evolution of H<sub>2</sub> and O<sub>2</sub> gases results from a photocatalytic reaction – i.e. our GaN nanowires are chemically stable in the whole reaction process. Preliminary measurements also show an apparent quantum yield of ~0.05%. However, the real quantum yield is expected to be significantly higher and can be further improved by optimizing the nanowire surface density, size, and doping concentration, as well as the H<sub>2</sub> evolution sites on the lateral surfaces of the nanowires. Moreover, through the use of tunable band gap epitaxial InGaN nanowires, high efficiency overall water splitting, and H<sub>2</sub> production under direct solar irradiation is achieved as discussed in Chapter-5.

### **3.3 Highly Efficient Overall Water Splitting on *p*-type GaN Nanowires**

#### **3.3.1 *n*- and *p*-type GaN Nanowire**

Recently, nanoscale photocatalysts have been intensively studied which can increase light absorption and charge carrier separation, and therefore enhance the quantum efficiency [15, 126, 127]. Fermi-level pinning, however, has been commonly measured on nanowire surfaces [128]. The resulting surface band bending creates an additional energy barrier for charge carrier transport to the photocatalyst-water interface [123], leading to significantly reduced reaction rate and extremely low efficiency [120, 129]. To date, the rational synthesis of nanostructured photocatalysts with controlled surface charge properties, *i.e.* tunable surface Fermi level and band bending, has remained a near-universal challenge [15]. Such uncontrolled surface charge properties can further contribute to the photo-corrosion and instability of various nanostructures under harsh photocatalysis conditions, severely limiting their practical applications.

Unique to the nonpolar GaN surfaces is that the occupied surface states are positioned outside of the fundamental energy bandgap and therefore do not create Fermi-level pinning [122],[130]. The nonpolar surfaces are also highly reactive for spontaneous dissociation of water molecules and possess low energy barrier for proton diffusion [115, 116]. Due to the surface contamination and/or the presence of any defects, however, an

upward (downward) band bending has been commonly measured on *n*- (*p*-) type GaN surfaces [121, 131]. When *n*-type GaN surfaces come into contact with water, the upward band bending becomes more severe, shown in Figs. 3-8a, b, which can suppress H<sub>2</sub>O reduction reaction. When *p*-type GaN surfaces are in equilibrium with water, the downward band bending can be enhanced, shown in Figs. 3-8c,d, which can limit the H<sub>2</sub>O oxidation reaction. In practice, weakly *n*-type or nearly intrinsic surfaces are often present on *p*-doped GaN nanowires, with the Fermi-level positioned slightly above the electrochemical potential of water. As a consequence, the downward band bending may actually be reduced when such *p*-doped GaN nanowires are in equilibrium with water. This provides a distinct opportunity to potentially realize balanced and therefore more efficient redox reactions through tuning the Fermi-level on nanowire surfaces. Since

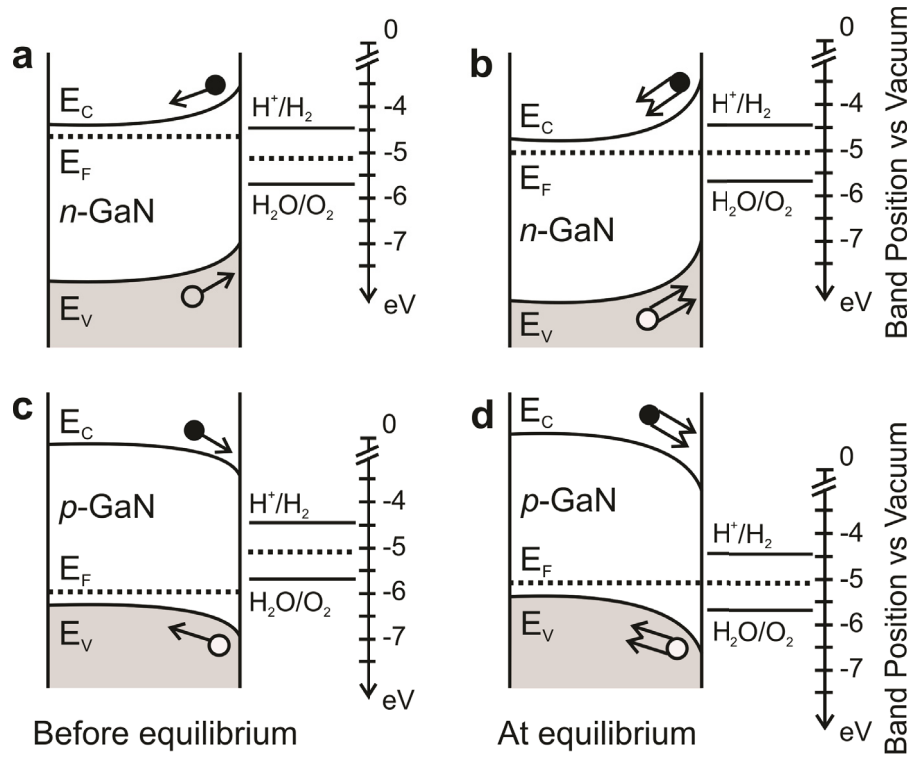


Figure 3-8: Schematic illustration of the energy band diagram of *n*-type GaN nanowire surface (a) prior to, and (b) at equilibrium with water. The upward band bending becomes more severe at equilibrium, which suppresses water reduction reaction. Schematic illustration of the energy band diagram of *p*-type GaN nanowire surface (c) prior to, and (d) at equilibrium with water. The downward band bending gets enhanced at equilibrium, which suppresses water oxidation reaction.

water oxidation is often the rate-limiting reaction [115, 132], *p*-doped nanowire photocatalyst can further enhance the overall water splitting efficiency by providing abundant free holes. To date, the achievement of *p*-doped GaN nanowires with tunable surface Fermi-level has remained challenging [133, 134]. The difficulty in achieving *p*-type surfaces for GaN nanowires is directly related to the presence of extensive *n*-type surface-states and defects, any unintentional impurity incorporation (particularly oxygen) [134], and the relatively large activation energy ( $\sim 170$  meV) of Mg acceptors in GaN [135]. Additionally, the direct incorporation of Mg dopant in the near-surface region of GaN nanowires suffers severely from the large surface desorption of Mg at high growth temperature ( $\sim 750$  °C) [136, 137]. Although *p*-type GaN nanowires have been demonstrated [133, 138], a precise control of their surface charge properties has not been studied previously.

### 3.3.1 Structural Characterization of GaN:Mg Nanowires

The GaN nanowires were grown on Si substrate by plasma-assisted MBE. The Mg-dopant concentration was varied by tuning the Mg effusion cell temperatures ( $T_{\text{Mg}}$ ) from 200 °C to 300 °C. Samples A, B, C, D, E and F correspond to  $T_{\text{Mg}}$  of 200 °C, 230 °C, 250 °C, 265 °C, 280 °C, and 300 °C, respectively. 45°-tilted SEM images of as-grown Mg doped GaN (denoted as GaN:Mg hereafter) nanowire samples are shown in Fig. 3-9. The nanowires are  $\sim 600$  nm in length,  $\sim 50$ -75 nm in diameter and vertically aligned to the substrate. Shown in Fig. 3-10a is a scanning transmission electron microscopy-bright field (STEM-BF) image, illustrating lattice fringes from defect-free single crystalline nanowire. The distance between the two adjacent fringes is about  $\sim 0.518$  nm which corresponds to the  $\langle 0001 \rangle$  direction, further confirming that the nanowires are grown along the *c*-axis, with their sidewalls being nonpolar *m*-planes [139]. Room-temperature photoluminescence (PL) measurement clearly shows (Fig. 3-10b) a single optical emission peak at  $\sim 365$  nm, corresponding to the bandgap of GaN (3.4 eV). For subsequent experiments  $\sim 2.8$  cm<sup>2</sup> wafer sample was used which corresponds to  $\sim 0.387$  mg ( $\sim 4.62$   $\mu\text{mol}$ ) GaN materials, considering the nanowire fill factors on Si substrate (estimated from Fig. 3-10c).

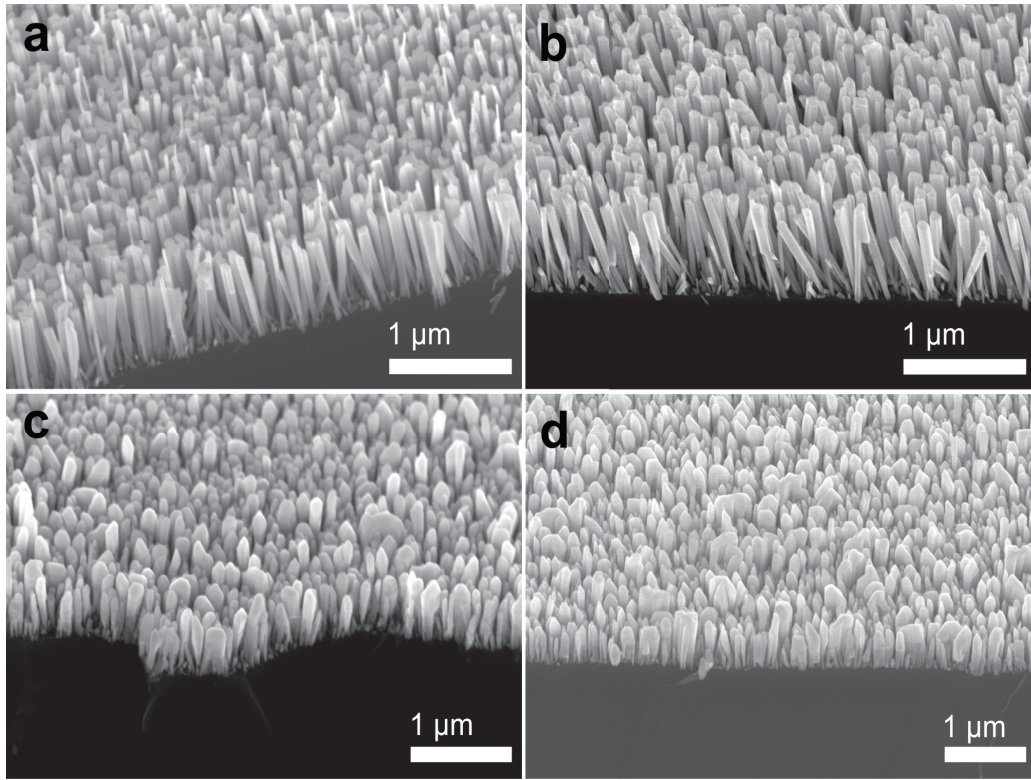


Figure 3-9: 45° tilted SEM images of GaN:Mg nanowires, with Mg effusion cell temperatures of (a) 200 °C, (b) 230 °C, (c) 250 °C, and (d) 265 °C.

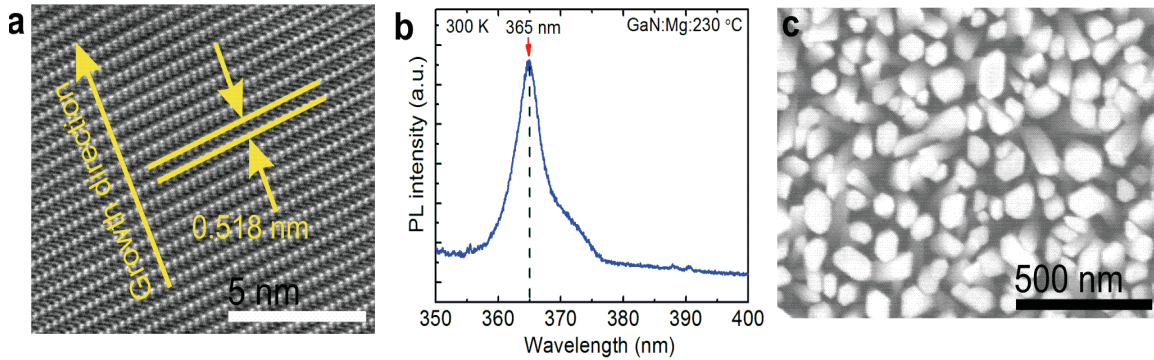


Figure 3-10: (a) STEM-BF lattice image illustrating lattice fringes from defect-free single crystalline GaN:Mg nanowire (Sample B). (b) Room-temperature PL spectrum of sample B ( $T_{\text{Mg}}=230$  °C). (c) A top view SEM image of sample D ( $T_{\text{Mg}}=265$  °C) showing the nanowire density. The estimated fill factor is  $\sim 39\%$  from this image.

### 3.3.2 Near-surface Band Structure of GaN:Mg Nanowires

The near-surface band structure of as-grown nanowires can be estimated by measuring the Fermi level ( $E_F$ ) relative to the valence band maximum (VBM,  $E_V$ ). The  $E_F-E_V$  in the near-surface region (Fig. 3-11a inset) was measured by recording angle-resolved X-ray photoelectron spectroscopy (ARXPS) valence spectrum (Fig. 3-11a inset) from the lateral nonpolar ( $m$ -plane) surfaces of the nanowire (as discussed in Chapter 2) [140]. Illustrated in Fig. 3-11a, the  $E_F-E_V$  is measured to be 2.63 eV for undoped GaN ( $T_{Mg}=0$  °C), which is similar to the  $E_F-E_V$  (2.6 eV) measured on  $n$ -type GaN surfaces by Wu *et al.* [141]. Two distinct regimes are clearly separated with dotted lines. Regime I ( $n$ -type surfaces), wherein the near-surface  $E_F-E_V$  stays nearly constant for  $T_{Mg}$  up to 230 °C, corresponds to the compensation of background  $n$ -type dopants by Mg acceptors [138]. Regime II ( $p$ -type surfaces), wherein the near-surface  $E_F-E_V$  decreases drastically with increase in  $T_{Mg}$ , is due to the enhancement in free hole concentration in GaN nanowires.

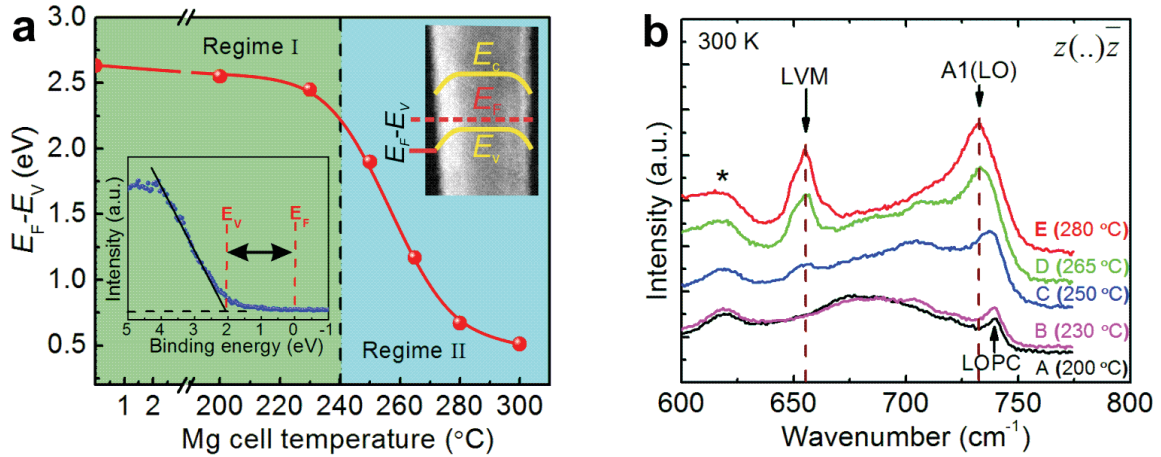


Figure 3-11: (a)  $E_F-E_V$  for different GaN:Mg samples determined from ARXPS valence spectrum. The insets illustrate  $E_F-E_V$  on the TEM image of a single nanowire and on an ARXPS valence spectrum. The dotted line separates two regimes, Regime I ( $n$ -type surfaces) and Regime II ( $p$ -type surfaces). (b) Typical room-temperature micro-Raman spectra of GaN nanowires with  $T_{Mg}$  ranging from 200 °C to 280 °C. Si modes are pointed out with “\*” and the dashed lines are guides to the eye.

In the relatively high bulk doping regime (samples C to F), variations of  $E_F-E_V$  in the bulk region with increasing Mg cell temperature is estimated to be in the range of tens of meV, which is much smaller than the variation measured in the near-surface region ( $\sim 2$  eV). Consequently, the reduction of  $E_F-E_V$  in the near-surface region, shown in Fig. 3-11a, can be directly correlated to the reduction in the downward surface band bending with increasing Mg dopant incorporation [142] [143]. Additionally, our detailed analysis reveals that variations in the surface band bending have a very small, or negligible dependence on the morphology of GaN nanowires.

### 3.3.3 *p*-type Doping in GaN Nanowires

Variations of the surface charge properties are further probed by micro-Raman measurements at room temperature. The evolution of the Raman mode in the range of 600-800  $\text{cm}^{-1}$  with Mg doping is illustrated in Fig. 3-11b. For nanowires with the lowest Mg doping levels (sample A,  $T_{\text{Mg}}=200$  °C and B,  $T_{\text{Mg}}=230$  °C), a narrow peak at  $\sim 741$   $\text{cm}^{-1}$  is present, which is attributed to the coupling between the longitudinal optical phonon-plasmon coupled (LOPC) mode [133, 144]. The appearance of the LOPC mode is associated with the weakly *n*-type surfaces for GaN nanowires at relatively low Mg doping (samples A and B), marked as Regime I in Fig. 3-11a, which can be gradually compensated with further increase in Mg doping/free hole concentration within nanowires. Accordingly, with the increment of Mg doping level for sample C ( $T_{\text{Mg}}=250$  °C), the LOPC mode gradually shifts to a lower frequency, and also its intensity becomes stronger due to the reduced coupling effect between the LO phonon and electron plasmon. With further increment of the Mg doping level in sample D ( $T_{\text{Mg}}=265$  °C), the frequency of the LOPC mode shifts to  $\sim 733$   $\text{cm}^{-1}$  (the original frequency of the pure uncoupled  $A_1$  (LO) mode). It indicates that the coupling between the LO phonon and electron plasma is completely suppressed in more heavily doped GaN nanowires, which is consistent with the measured surface-type (weakly *p*-type, Regime II shown in Fig. 3-11a). The presence of *p*-type surfaces, evidenced by both the ARXPS and the pure uncoupled  $A_1$  (LO) mode, is also well correlated with the appearance of an extra mode at

655  $\text{cm}^{-1}$  in sample C ( $T_{\text{Mg}} = 250\text{ }^\circ\text{C}$ ). Such a foreign Raman mode is attributed to the local vibrational modes (LVM) related to Mg impurity (Mg-N bond) [145]. Its intensity is directly proportional to the free hole concentration [141] and becomes stronger with further increment of Mg doping level in samples D ( $T_{\text{Mg}} = 265\text{ }^\circ\text{C}$ ) and E ( $T_{\text{Mg}} = 280\text{ }^\circ\text{C}$ ). Mg concentration for GaN:Mg epilayer ( $T_{\text{Mg}} = 250\text{ }^\circ\text{C}$ ) is measured by secondary ion mass spectroscopy (SIMS) as shown in Fig. 3-12. The growth rate of GaN:Mg epilayer is similar to that for GaN:Mg nanowires used in this work. SIMS analysis showed Mg concentration  $\sim 1.3 \times 10^{20}\text{ cm}^{-3}$  in the bulk GaN. Considering the commonly reported  $\sim 1\%$  doping efficiency of Mg acceptors due to the large ionization energy ( $\sim 170\text{ meV}$ ), the free hole concentration is estimated to be in the range of  $\sim 1 \times 10^{18}\text{ cm}^{-3}$  in the bulk GaN. This is in qualitative agreement with micro-Raman analysis of sample D (Fig. 3-11b).

### 3.3.4 $\text{H}_2$ and $\text{O}_2$ Half Reactions

The tunable surface Fermi-level and the engineered surface charge properties are essential to achieve controlled redox reactions. To demonstrate this hypothesis,  $\text{H}_2$  and  $\text{O}_2$  half reactions in the presence of respective sacrificial reagents were first performed using both *n*- (Si-doped) and *p*-type GaN nanowire arrays.

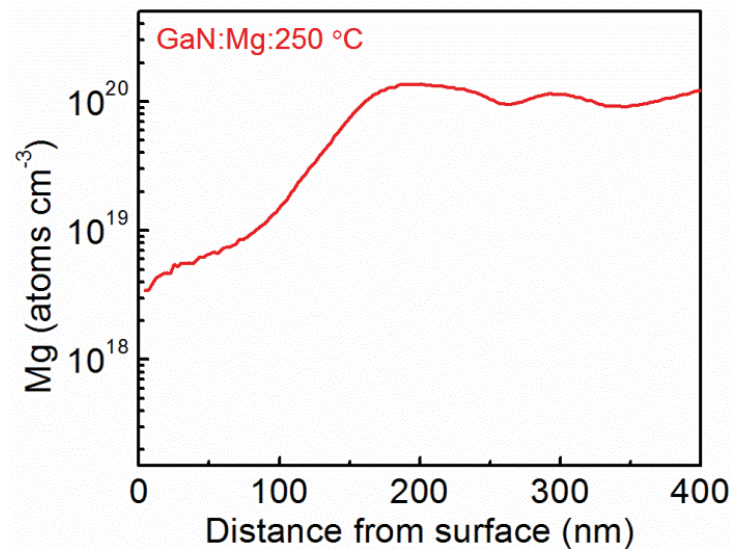


Figure 3-12: Mg concentration for GaN:Mg epilayer ( $T_{\text{Mg}} = 250\text{ }^\circ\text{C}$ ) as measured by secondary ion mass spectroscopy (SIMS).

Figure 3-13a shows the evolution of H<sub>2</sub> from *n*- and *p*-type (sample B,  $T_{Mg}=230$  °C) GaN nanowire arrays in the presence of CH<sub>3</sub>OH and Rh co-catalyst. The H<sub>2</sub> generation rate of *p*-type GaN nanowire is significantly higher than conventional *n*-type GaN nanowires, due to the downward band bending at the surface of *p*-type GaN (Fig. 3-8c, and Fig. 3-11a - Regime II). In contrast, as shown in Fig. 3-13b, the activity for O<sub>2</sub> generation is significantly enhanced on *n*-type GaN nanowires with an upward surface band bending (Fig. 3-8a, and Fig. 3-11a - Regime I). For overall water splitting and stoichiometric evolution of H<sub>2</sub> and O<sub>2</sub>, however, both oxidation and reduction reaction need to proceed simultaneously [9].

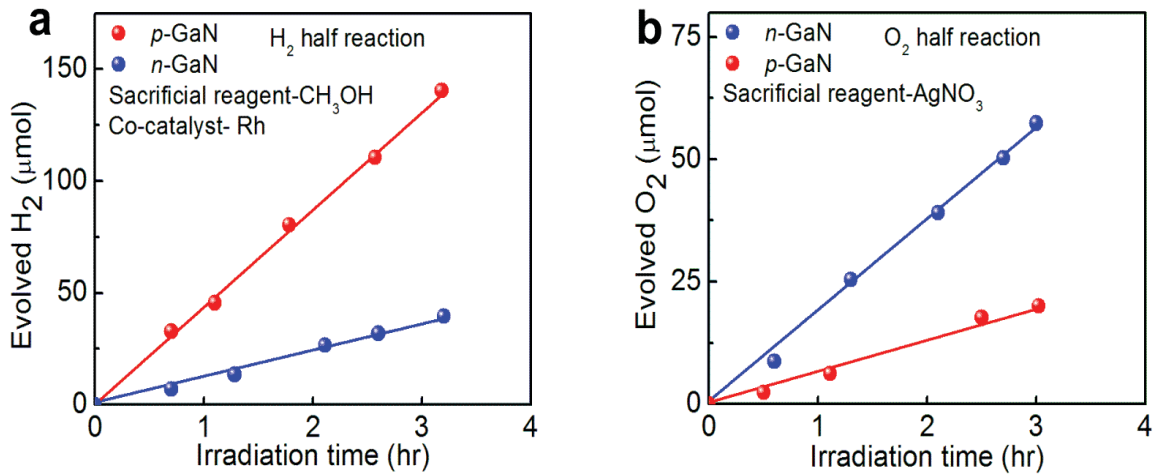


Figure 3-13: (a) Evolution of H<sub>2</sub> from *n*- (Si-doped) and *p*-GaN ( $T_{Mg}=230$  °C) nanowire arrays in the presence of CH<sub>3</sub>OH and Rh co-catalyst. (b) Evolution of O<sub>2</sub> from *n*- (Si-doped) and *p*-GaN ( $T_{Mg}=230$  °C) nanowire arrays in the presence of AgNO<sub>3</sub> sacrificial reagent. Enhanced evolution of O<sub>2</sub> is measured for *n*-type GaN nanowires, which can be well correlated to the presence of upward surface band bending. The solid lines are guide to the eye.

The presence of any upward or downward band bending will create additional uphill barriers for one of these two reactions and therefore severely limit overall water splitting efficiency. Since the downward band bending reduces with Mg concentration in the *p*-type surface regime (Fig. 3-11a, Regime II), efficient carrier transport and therefore high photocatalytic activity is expected for optimized *p*-doping levels.

### 3.3.5 Rh/Cr<sub>2</sub>O<sub>3</sub> Co-catalyst Deposition on GaN:Mg Nanowires

To further enhance the charge carrier extraction and provide more active sites for gas generation, Rh/Cr<sub>2</sub>O<sub>3</sub> co-catalyst nanoparticles are deposited on all the samples (A-F) using photodeposition process from liquid precursors [129]. Figure 3-14 shows (a) a low resolution STEM-secondary electron (SE) image, and (b) a STEM-high angle annular dark field (HAADF) image of Rh/Cr<sub>2</sub>O<sub>3</sub> nanoparticle decorated GaN:Mg nanowire. These images reveal that the Rh/Cr<sub>2</sub>O<sub>3</sub> nanoparticles are successfully deposited in the form of core-shell nanostructures on GaN nanowire surfaces. Additionally, the Rh core and GaN nanowire show single crystalline structure.

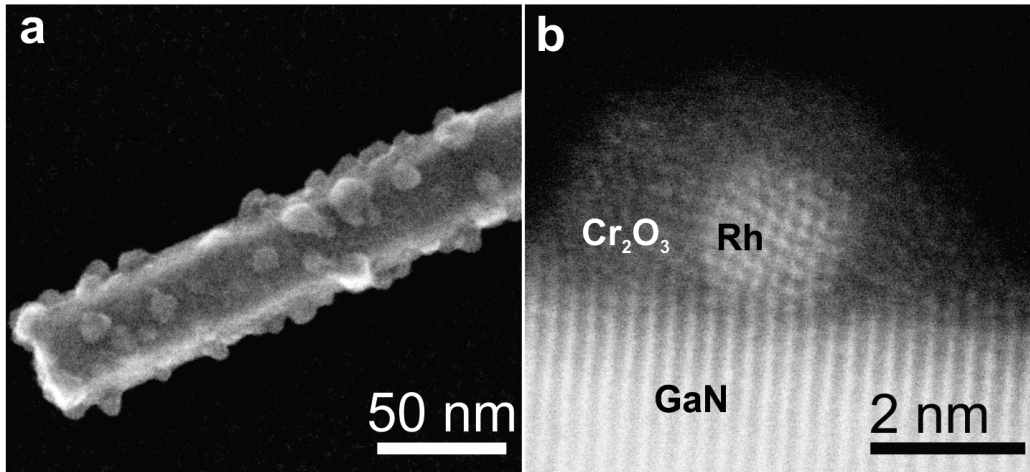


Figure 3-14: (a) Low magnification STEM-SE image. (b) STEM-HAADF image of Rh/Cr<sub>2</sub>O<sub>3</sub> nanoparticle-decorated GaN:Mg nanowire. Crystalline Rh core and amorphous Cr<sub>2</sub>O<sub>3</sub> shell is clearly observed.

The presence and valence state of the photodeposited Rh/Cr<sub>2</sub>O<sub>3</sub> co-catalyst nanoparticles on the GaN nanowire surface was confirmed by XPS analysis. Figure 3-15 shows a high-resolution XPS spectrum of (a) Rh 3d, and (b) Cr 2p core level electrons after photodeposition. Two spin-doublets were clearly resolved from Rh 3d peak after deconvolution using Lorentzian-Gaussian mixing functions (L/G=30%). The Rh 3d<sub>5/2</sub> peaks observed at 307.0 eV (blue line) and 309.68 eV (black) are attributed to metallic rhodium Rh<sup>0</sup> and mixed Rh-Cr oxide, respectively [146, 147]. The areas of the two deconvoluted XPS peaks (Fig. 3-15a) correspond to 41.23% and 58.77% of the photodeposited Rh particles are in metallic (Rh<sup>0</sup>) and mixed Rh-Cr oxide form, respectively.

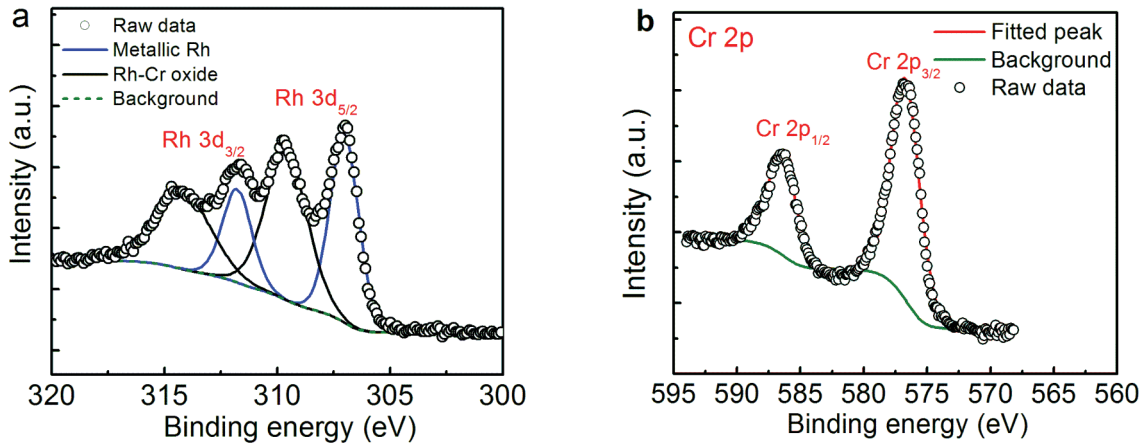


Figure 3-15: High resolution XPS spectra of (a) Rh 3d core level electrons, and (b) Cr 2p core level electrons. These XPS spectra were taken from sample D ( $T_{Mg} = 265\text{ }^{\circ}\text{C}$ ) after photodeposition.

The deconvolution of Cr 2p peak reveals one spin-doublet as shown in Fig. 3-15b. The Cr 2p<sub>3/2</sub> peak appeared at 576.83 eV is ascribed to the presence of Cr<sub>2</sub>O<sub>3</sub>, indicating the fact that the valence state of Cr in the co-catalyst is trivalent after photodeposition [147]. The surface compositions of Rh and Cr<sub>2</sub>O<sub>3</sub> were estimated to be 2.45 and 4.34 At.%, respectively, from the areas of the corresponding XPS peaks after Shirley background subtraction. Control experiments were performed to reveal the role of co-catalyst nanoparticles in enhancing the photocatalytic activity. We have performed overall water splitting reaction with and without the use of co-catalyst. Shown in Fig. 3-16a, the photocatalytic activity of GaN:Mg nanowires without co-catalyst follows the same trend as that with co-catalyst. The activity of GaN:Mg nanowires without co-catalyst is ~4-5 times lower than that of the respective samples with co-catalyst at different doping levels, indicating the significant influence of Rh/Cr<sub>2</sub>O<sub>3</sub> co-catalyst nanoparticles in charge carrier extraction and in enhancing the redox reactions. Note that the co-catalyst enhanced the activity at all doping levels. This reveals the fact that the change in band bending at the surfaces of GaN nanowires does not influence the catalytic activity of the supported metal particles (Rh). This is in contrast with the previously reported strong influence of support-material (oxides) on the photocatalytic activity of nanoparticles [148].

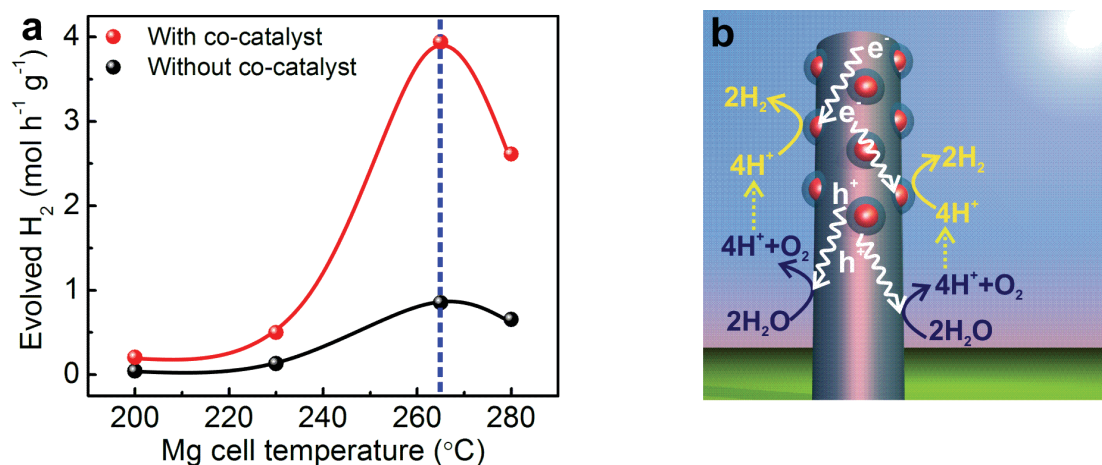


Figure 3-16: (a) H<sub>2</sub> evolution rates for different GaN:Mg samples with and without co-catalyst in overall water splitting. The solid lines are guide to the eyes. (b) Schematic of Rh/Cr<sub>2</sub>O<sub>3</sub> decorated GaN nanowire and the water splitting mechanism.

Figure 3-16b shows a schematic of the core/shell Rh/Cr<sub>2</sub>O<sub>3</sub> nanoparticle deposited GaN nanowire for overall water splitting, illustrating the reaction mechanism on the nonpolar surfaces of GaN nanowires.

### 3.3.6 Overall Pure Water Splitting on GaN:Mg Nanowires

The Rh/Cr<sub>2</sub>O<sub>3</sub> nanoparticle decorated GaN nanowires with different Mg doping levels are subsequently used for overall neutral (pH~7.0) water splitting under 300 W full arc Xenon lamp irradiation. Figure 3-17a shows the H<sub>2</sub> evolution rates for different GaN:Mg nanowire samples, which were derived from 6-hrs overall water splitting reaction on each sample. It is seen that the H<sub>2</sub> evolution rate first shows a dramatic increase with Mg cell temperature. Under relatively low doping levels (samples A and B), the photocatalytic activity is low, which is directly correlated to the very large downward surface band bending (Fig. 3-8d), due to the weakly *n*-type surface-nature as revealed from ARXPS and micro-Raman analysis (Fig. 3-11a - Regime I, and Fig. 3-11b). Dramatically enhanced overall water splitting performance was measured for sample D ( $T_{Mg}=265$  °C), and the H<sub>2</sub> evolution rate was nearly 4 mol h<sup>-1</sup>g<sup>-1</sup>, which is more than two orders of magnitude higher, compared to the nominally undoped GaN nanowires [129]. This drastic improvement can be well explained by the *p*-type surfaces with significantly

reduced downward band bending (Fig. 3-11a -Regime II, and Fig. 3-11b), which may become relatively flat in aqueous solution, thereby enabling balanced and much more efficient redox reactions. For samples E ( $T_{\text{Mg}}=280\text{ }^{\circ}\text{C}$ ) and F ( $T_{\text{Mg}}=300\text{ }^{\circ}\text{C}$ ), however, the activity shows a decreasing trend with increase in Mg cell temperature, which is likely to be related to the degradation of GaN nanowire crystalline quality at very high Mg-doping level [96, 133, 149]. At very high doping level ( $T_{\text{Mg}}=280\text{ }^{\circ}\text{C}$  and  $T_{\text{Mg}}=300\text{ }^{\circ}\text{C}$ ), the free hole concentration becomes saturated in GaN and therefore further increase in the hole concentration may not be achieved. This is evident from Fig. 3-11b, where no further increment of the LVM intensity is observed for sample E ( $T_{\text{Mg}}=280\text{ }^{\circ}\text{C}$ ), compared to sample D ( $T_{\text{Mg}}=265\text{ }^{\circ}\text{C}$ ). Ronamo *et al.* [150] reported similar doping behavior of Mg acceptors in GaN (0001) thin films.

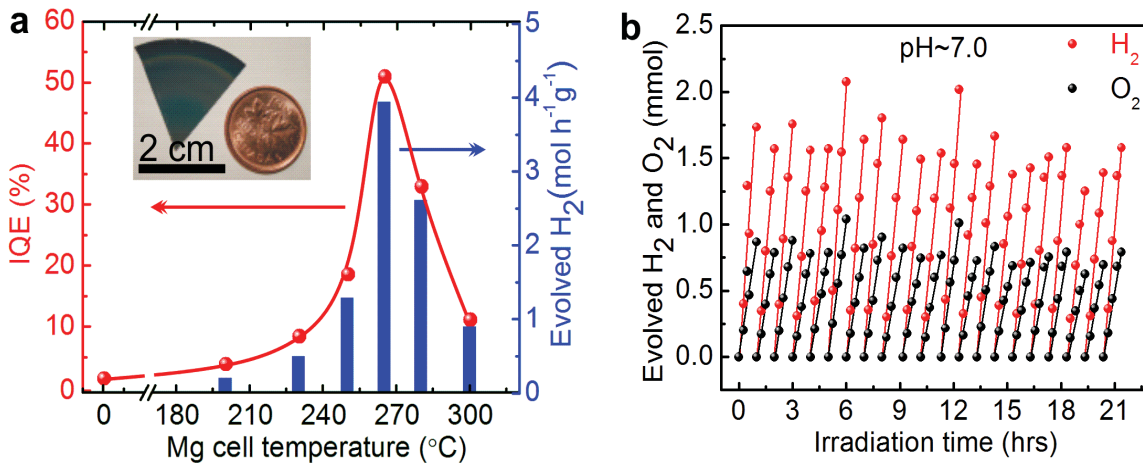


Figure 3-17: (a)  $\text{H}_2$  evolution rate and internal quantum efficiency (IQE) for different GaN:Mg samples in overall neutral water splitting. Reactions were performed using  $\sim 0.387\text{ mg}$  GaN nanowire catalyst in neutral water under illumination of a Xenon lamp (300 W). The sample size is shown in the inset. (b) Repeated cycles of overall pure water splitting for GaN:Mg:  $265\text{ }^{\circ}\text{C}$  (sample D), showing the stability of the nanowires.

Although the band bending reduces further for sample E ( $T_{\text{Mg}}=280\text{ }^{\circ}\text{C}$ ), the GaN material quality degrades. The degradation in the crystal quality of the nanowires is confirmed from the increment of full-width-at-half-maximum (FWHM) of the  $E_2$  peak in Raman spectra (not shown here) [151]. Additionally, at high Mg concentration, nitrogen vacancy ( $\text{V}_\text{N}$ ) related defects increase and compensate Mg doping. At high Mg concentration, Mg

can also act as donor-like compensation centers [152]. These defects work as *n*-type dopants and hence *p*-type dopants get compensated. In addition, the H<sub>2</sub> evolution rate depends on the surface band structure when the nanowire surface is in equilibrium with water, which may become less optimum for sample E with further reduced band bending. These factors contribute to the reduction in photocatalytic activity for samples E and F as shown in Fig. 3-17a. For optimum Mg-doping concentration (sample D), the apparent quantum efficiency (AQE) can reach ~18% (Appendix-I). The internal quantum efficiency (IQE), shown in Fig. 3-17a, is also derived for different Mg doped samples under ~200-365 nm wavelength (Appendix-I). It can reach ~ 51% for GaN nanowires with optimum surface band bending (sample D), which is the highest value reported for spontaneous overall water splitting under any broadband UV light irradiation to our knowledge [9, 19, 25].

### 3.3.7 Discussions on Efficiency and Stability

In order to reveal the stability of the GaN:Mg photocatalyst, repeated experiments were performed using the same sample. Figure 3-17b shows the evolution of H<sub>2</sub> and O<sub>2</sub> as a function of irradiation time for the optimized GaN:Mg (sample D) in neutral water. No sacrificial reagents were added in the reaction. The rates of H<sub>2</sub> and O<sub>2</sub> evolution were ~1,525 μmol h<sup>-1</sup> and ~763 μmol h<sup>-1</sup>, respectively. The H<sub>2</sub>/O<sub>2</sub> ratio is nearly 2:1, indicating a balanced redox reaction of water on the nanowire photocatalyst. Visible bubbles were clearly observed from the sample surface upon irradiation. The turnover number, defined as the ratio of the total amount of gas evolved (50,428 μmol) to GaN catalyst (4.62 μmol), exceeded ~10,915 during the course of ~22 hours of reaction. Repeated experiments on the same sample did not show any degradation of the photocatalytic activity, demonstrating excellent stability of the Mg-doped GaN nanowires. The turn over number in terms of the ratio of the rate of H<sub>2</sub> molecules formed to the rate of absorbed photons is also plotted as a function of time (Fig. 3-18), further confirming excellent stability of the nanowire photocatalyst. The slight variations in H<sub>2</sub> and O<sub>2</sub> evolution observed for different cycles are attributed to the variations in alignment between the light source and the sample surface.

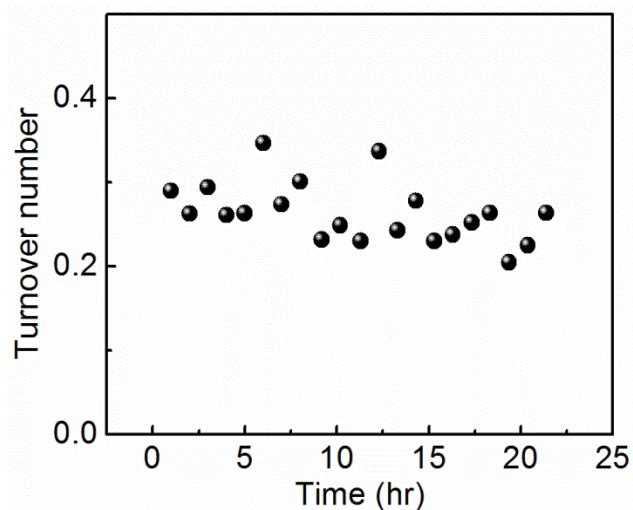


Figure 3-18: The turn over number in terms of the ratio of the rate of H<sub>2</sub> molecules produced to the rate of absorbed photons as a function of time.

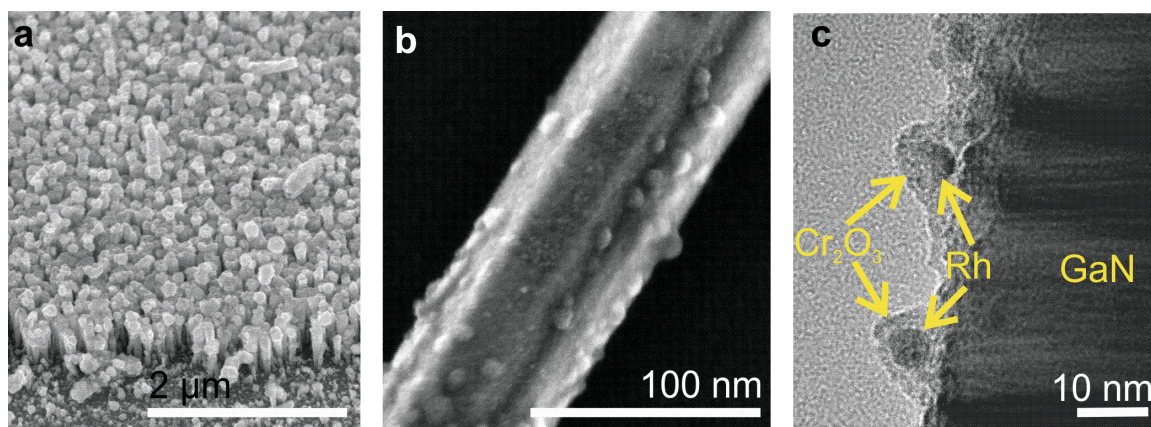


Figure 3-19: (a) A bird's-eye view SEM image of the GaN nanowire arrays after ~22 hours of overall water splitting. (b) Low magnification STEM-SE image of a single nanowire after overall water splitting reaction for ~22 hrs. (c) High resolution bright field TEM image after reaction, showing the stability of core-shell Rh/Cr<sub>2</sub>O<sub>3</sub> nanoparticles and GaN nanowire.

Figure 3-19a shows a SEM image of the nanowire arrays (sample D) after overall water splitting for ~22 hours. The nanowires remain stable during the course of the reaction. A higher magnification STEM-SE image of a single nanowire, shown in Fig. 3-19b, further confirms that the co-catalyst nanoparticle-decorated GaN nanowire were not etched during the course of reaction, which can be partially attributed to the strong ionic bonds

in III-nitrides [60]. The core-shell Rh/Cr<sub>2</sub>O<sub>3</sub> nanoparticles are also stable in photocatalytic environment, shown in the bright-field TEM image in Fig. 3-19c.

### 3.4 Conclusions

In summary, we have demonstrated that nonpolar surfaces of GaN nanowires possess the capacity for both H<sub>2</sub> and O<sub>2</sub> evolutions. With the incorporation of photodeposited Rh/Cr<sub>2</sub>O<sub>3</sub> core-shell structures as cocatalysts, photocatalytic neutral water splitting is achieved, for the first time, on wafer scale III-nitride nanowires grown by MBE. Furthermore, we have demonstrated that one of the major obstacles for achieving efficient and stable overall water splitting over the emerging nanostructured photocatalyst is directly related to the uncontrolled surface charge properties. By tuning the Fermi-level on the nonpolar surfaces of GaN nanowire arrays, we demonstrate that the quantum efficiency can be enhanced by more than two orders of magnitude. The internal quantum efficiency and activity on *p*-type GaN nanowires can reach ~51% and ~4.0 mol H<sub>2</sub> h<sup>-1</sup>g<sup>-1</sup>, respectively. The nanowires remain virtually unchanged after over 50,000 μmol gas (H<sub>2</sub> and O<sub>2</sub>) is produced; which is more than 10,000 times the amount of photocatalyst itself (~4.6 μmol). The essential role of Fermi-level tuning in balancing redox reactions and in enhancing the efficiency and stability is also elucidated.

## Chapter-4

# One-Step Overall Water Splitting under Visible Light Using Multi-Band InGaN/GaN Nanowire Heterostructure

### 4.1 Introduction

Over the last 40 years, researches have been largely focused upon metal-oxide based photocatalyst materials [9, 19] that are responsive mostly to ultraviolet (UV) light ( $\sim 4\%$  in solar spectrum). Success in finding abundant visible-light ( $\sim 43\%$  in solar spectrum) active material, however, has been very limited [22, 25, 26]. This is attributed to the lack of known single photocatalyst material (one-step system) which has (i) sufficiently narrow bandgap ( $< 3$  eV) to harness visible photons, (ii) suitable band-edge potentials for overall water splitting (*i.e.*, simultaneous production of  $H_2$  and  $O_2$ ), and (iii) a high level of stability against photocorrosion. In this regard, various energy-band engineering methods have been explored to transform UV-active materials into visible-light active photocatalyst but with limited success [15]. To date, most of these approaches cannot drive stable overall pure water splitting beyond the blue wavelength range [32, 153].

Here we have developed a fundamentally different approach, with the use of multi-band metal-nitride nanowire arrays, for achieving high-efficiency one-step hydrogen production from overall pure water splitting under visible-light irradiation. Compared to conventional oxide-based catalyst, the direct energy band gap ( $E_g$ ) of metal-nitrides, *e.g.*, InGaN can be tuned to encompass nearly the entire solar spectrum [38]. The large surface-to-volume ratios of nearly defect-free one-dimensional nanowires can further enhance the charge carrier separation, surface reaction rate and therefore the overall photocatalytic activity [10, 62]. In addition, a multi-bandgap nanowire heterostructure facilitates efficient matching and utilization of incident solar irradiation [154, 155]. In a

single-bandgap system, the photo-excited high-energy electrons (except the hot carriers) will rapidly (<10 ps) relax to an energy close to the bandgap with the dissipation of extra energy into heat. Therefore, to suppress the energy loss due to thermal relaxation, a better approach is to stack two or more absorbing materials with decreasing bandgap from front (towards light) to back, which provides effectively larger over-potential for water splitting reactions. According to Bolton's calculation [155], the ideal maximum energy conversion efficiencies for single-bandgap and dual-bandgap devices are 30.7% and 46%, respectively. Our experimental results have unambiguously demonstrated this concept.

## **4.2 Growth and Characterization of InGaN/GaN Multi-band Nanowire Heterostructure**

The catalyst-free InGaN/GaN multi-band nanowire heterostructures were grown by plasma-assisted MBE. Vertically aligned GaN nanowire templates were first formed on Si (111) substrate under nitrogen-rich conditions. As schematically shown in Fig. 4-1a, ten self-organized InGaN/GaN quantum dots were subsequently incorporated along the axial dimension of the GaN nanowires. The dot heights are ~3 nm, and indium compositions of the dots are varied in the range of ~15-50% to effectively cover a broad absorption wavelength range. Such unique InGaN/GaN dot-in-a-wire nanoscale heterostructures enable the harness of sunlight in the green spectral range, without the formation of extended defects and dislocations resulting from the large lattice mismatch (~11%) between InN and GaN [156]. To further enhance optical absorption in the blue wavelength range, an InGaN nanowire segment of ~30 nm height and average indium composition of ~11% was incorporated in the GaN nanowire, shown in Figure 4-1a, which is separated from the InGaN quantum dots by ~15 nm GaN layer. The top GaN nanowire segment is *p*-doped using Mg, which may lead to enhanced photocatalytic activity for GaN under UV irradiation. The photoluminescence (PL) spectrum of InGaN/GaN nanowire heterostructures, shown in Figure 4-1b, was measured at room temperature.

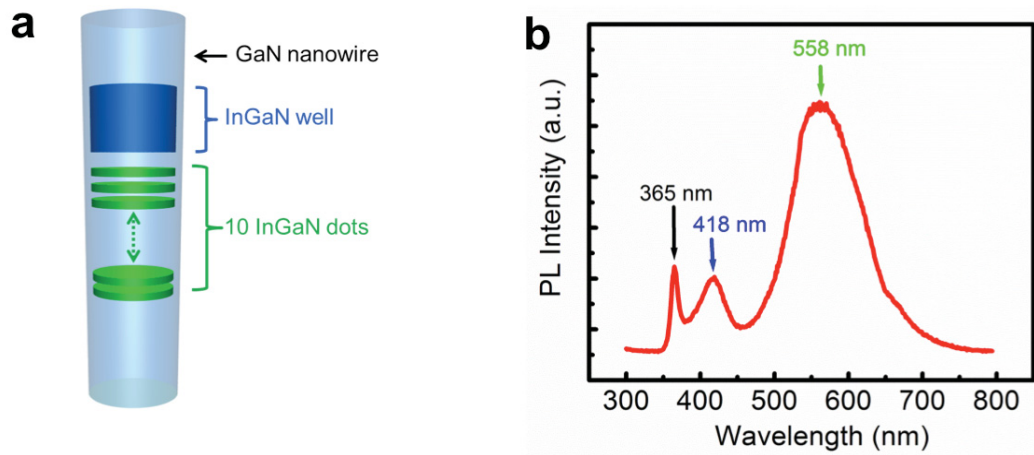


Figure 4-1: (a) Schematic of the InGaN/GaN nanowire heterostructure. (b) Room temperature photoluminescence spectra of InGaN/GaN nanowires arrays.

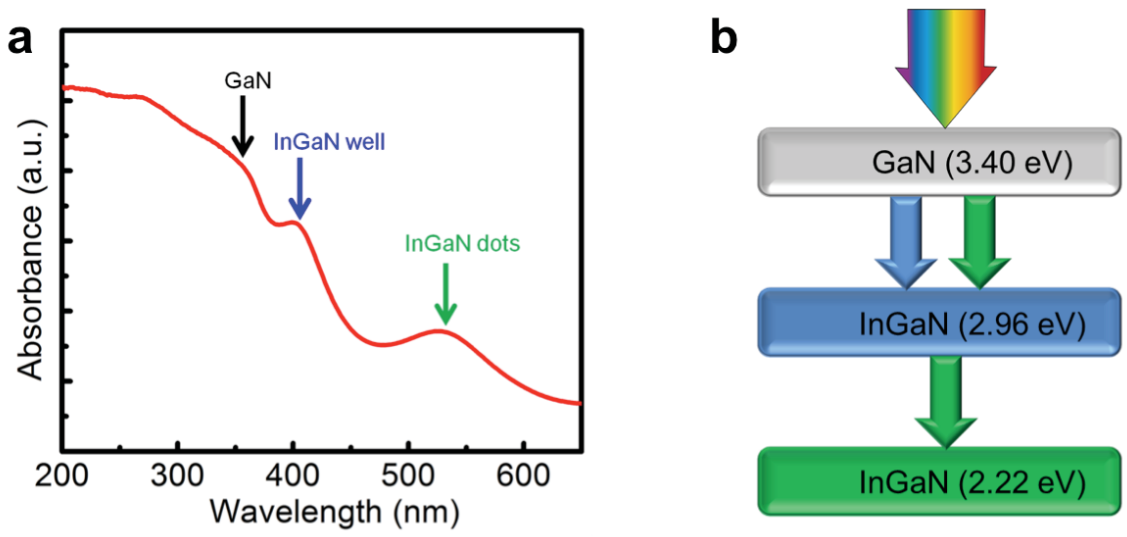


Figure 4-2: (a) UV-Visible diffuse reflectance spectroscopy (DRS) of as-grown InGaN/GaN nanowires. (b) Schematic of InGaN/GaN triple-band nanowire heterostructure.

It clearly shows the optical emission from GaN nanowire, InGaN ternary wire, and InGaN/GaN dot-in-a-wire structures, with the corresponding peak wavelengths at ~ 365 nm, ~418 nm, and ~558 nm, respectively. UV-Visible diffuse reflectance spectroscopy (DRS) studies further demonstrate optical absorption by the GaN, InGaN well and InGaN

dots (see Figure 4-2a). The average indium compositions for the InGaN ternary wire and InGaN dots were estimated to be ~11% and ~32%, respectively [157]. As illustrated in Figure 4-2b, the resulting InGaN/GaN nanowire heterostructure can function effectively as a triple-band structure for harvesting sunlight in the UV, blue, and green spectral range.

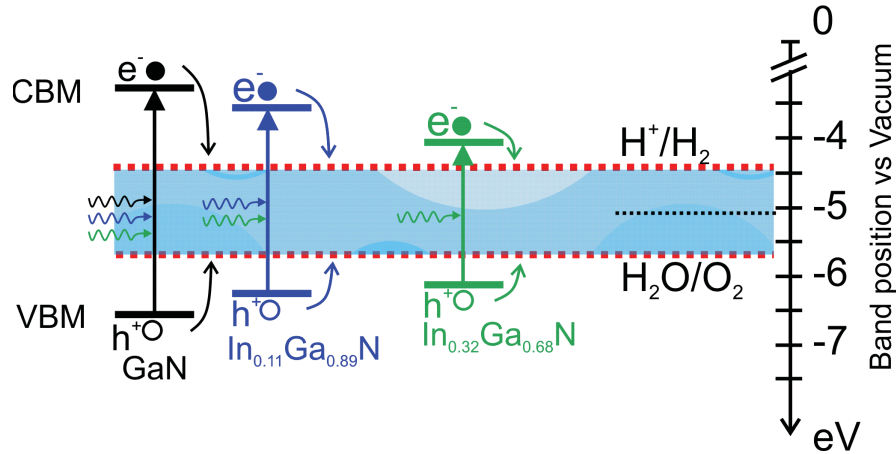


Figure 4-3: Conduction-band and valence-band edge positions of GaN, In<sub>0.11</sub>Ga<sub>0.89</sub>N and In<sub>0.32</sub>Ga<sub>0.68</sub>N, derived from Ref. [41], depicts sufficient overpotential for oxidation and reduction of water. The redox potentials of water are also illustrated. All values of potentials are in eV relative to the vacuum level.

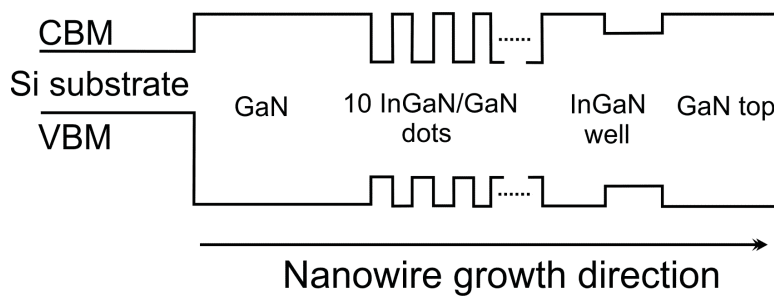


Figure 4-4: Flat band-diagram of InGaN/GaN nanowire heterostructure along the growth axis.

The band-edge positions [41] of GaN, In<sub>0.11</sub>Ga<sub>0.89</sub>N and In<sub>0.32</sub>Ga<sub>0.68</sub>N, with respect to water redox potential, is illustrated in Figure 4-3. As shown, both GaN and InGaN segments have sufficient overpotential for oxidation and reduction of water. Figure 4-4 is

the band-diagram of InGaN/GaN nanowire heterostructure. Due to the presence of conduction and valence band offsets at the Si/GaN interface, and insufficient oxidation potential of Si, the photo-excited carriers in Si substrate cannot migrate to GaN nanowire and hence do not take part in the water splitting reaction [158].

Shown in Fig. 4-5a is a 45° tilted scanning electron microscopy image of the as-grown InGaN/GaN nanowire ensemble on Si (111) substrate. The nanowires are vertically aligned to the substrate with nearly uniform height of ~ 500 nm and lateral sizes of ~ 30-70 nm, and the areal density is in the range of ~  $1.5 \times 10^{10} \text{ cm}^{-2}$ . Structural properties of InGaN/GaN nanowire heterostructures were further studied using scanning transmission electron microscopy (STEM) and spectrum imaging.

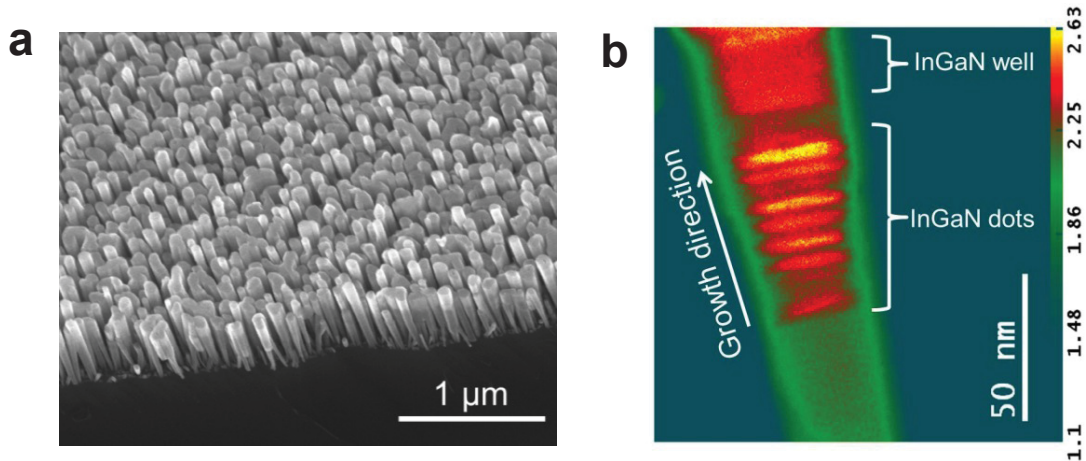


Figure 4-5: (a) A 45° tilted SEM image of GaN/InGaN nanowire heterostructures grown on GaN nanowire templates on Si (111) substrate. (b) High angle annular dark field (HAADF) image in pseudocolor display of an as-grown InGaN/GaN nanowire heterostructure, showing the atomic number contrast between InGaN (red) and GaN (green) layers. The unit of intensity scale is  $10^4$  counts.

A high-angle annular dark field (HAADF) image of an InGaN/GaN nanowire in a pseudocolor display is shown in Fig. 4-5b, illustrating the atomic number contrast between InGaN (red) and GaN (green). It is seen that ten InGaN/GaN quantum dots are vertically aligned along the growth direction of the wire. The InGaN nanowire segment can also be identified.

### 4.3 The Test Reactions for InGaN/GaN Nanowires

Recent studies [73, 75, 115, 116, 118, 119, 159] confirmed that the GaN surface possesses adequate thermodynamic and kinetic potential for overall water splitting. To further verify that InGaN possesses the required potential for overall water splitting, as predicted by DFT calculations [41], half reactions for individual evolution of H<sub>2</sub> and O<sub>2</sub> were first performed under visible-light illumination. A long-pass ( $\lambda > 385$  nm) filter was utilized to optically excite only the InGaN material. CH<sub>3</sub>OH (10 vol.%) and AgNO<sub>3</sub> (0.1 M) were used as sacrificial reagents for H<sub>2</sub> and O<sub>2</sub> half reactions, respectively.

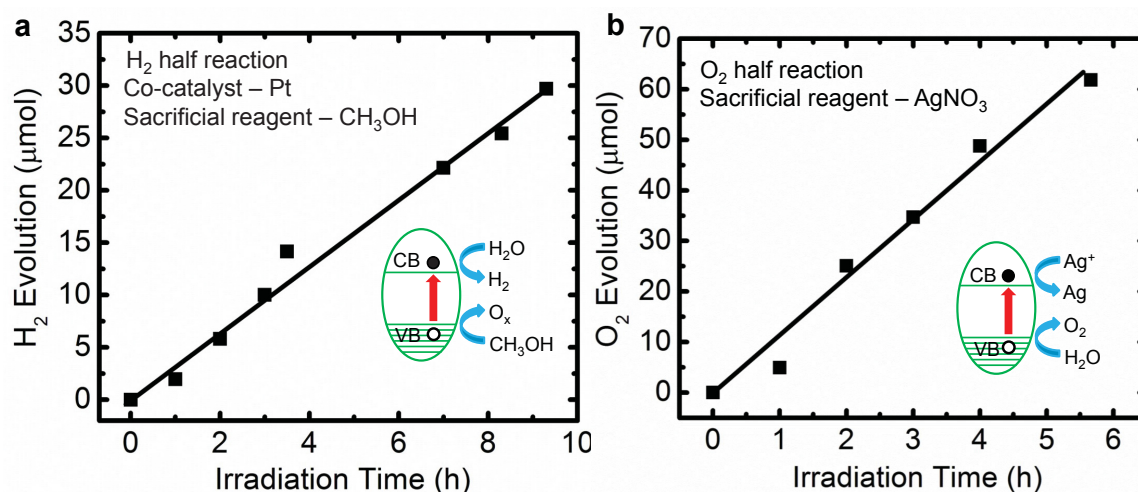


Figure 4-6: H<sub>2</sub> and O<sub>2</sub> half reactions under visible light. A long-pass ( $\lambda > 385$  nm) optical filter was utilized to optically excite only the InGaN material. (a) Evolution of H<sub>2</sub> from half reaction in the presence of CH<sub>3</sub>OH and Pt. (b) Evolution of O<sub>2</sub> from half reaction in the presence of AgNO<sub>3</sub>. The insets illustrate the reaction mechanism. The solid line is a guide to the eye.

Additionally, Pt (1 wt%) nanoparticles were *in situ* photodeposited from an aqueous H<sub>2</sub>PtCl<sub>6</sub> solution to accelerate H<sub>2</sub>O reduction reaction by introducing active reaction sites for gas evolution. The evolution of H<sub>2</sub> and O<sub>2</sub> exhibits a nearly linear increase over time, shown in Figures 4-6a and 4-6b, respectively. Over  $\sim 3$  μmol/hr of H<sub>2</sub> and  $\sim 10$  μmol/hr of O<sub>2</sub> were produced during the course of the experiment, which confirmed that the conduction and valence band edge potentials of the present In<sub>x</sub>Ga<sub>1-x</sub>N nanowires meet the thermodynamic and kinetic requirements for H<sub>2</sub> and O<sub>2</sub> evolution. Controlled

experiments further confirm that Pt nanoparticles can enhance the photocatalytic activity of our nanowire photocatalyst by nearly 20 times in the presence of sacrificial reagents.

#### 4.4 Rh/Cr<sub>2</sub>O<sub>3</sub> Co-catalyst Photodeposition on InGaN/GaN Nanowires

In addition to the thermodynamic and kinetic potential requirement, the efficiency of photocatalytic water splitting is strongly influenced by surface electronic structure and charge properties, as discussed in Chapter-3. Due to the presence of an upward band-bending on the surfaces of nominally undoped or *n*-type Ga(In)N [121, 131, 160], a potential barrier is formed which can result in significant reduction of electron transfer to the surface reaction sites, and hence limit the H<sub>2</sub> production efficiency. As discussed in Chapter-2 and Chapter-3, the Rhodium (Rh)/Chromium-oxide (Cr<sub>2</sub>O<sub>3</sub>) core-shell nanoparticles can act as excellent H<sub>2</sub>O reduction co-catalyst for H<sub>2</sub> evolution. In this regard, we have investigated the photodeposition of Rh/Cr<sub>2</sub>O<sub>3</sub> nanoparticles on the InGaN/GaN nanowire heterostructure [161]. Figure 4-7a shows a high resolution TEM (HRTEM) image of InGaN/GaN nanowires after photodeposition of Rh/Cr<sub>2</sub>O<sub>3</sub> nanoparticles. The structural characterization demonstrates that nanoparticles were deposited on the lateral surfaces of the crystalline nanowires. Additionally, an electron energy loss spectrometry (EELS) spectrum image (Fig. 4-7b) confirms that the Rh/Cr<sub>2</sub>O<sub>3</sub> nanoparticles formed a core/shell nanostructure on the nanowire surface. Due to the edge-overlap, the elemental distribution of In, Ga, N, O, Rh and Cr (Fig. 4-7c-h) in the nanowire photocatalyst was derived from the EELS spectrum image (Fig. 4-7b) with multiple linear least square (MLLS) fitting [162]. Our study reveals that the crystalline Rh nanoparticles are of ~5 nm, which are covered by ~2-3 nm thick amorphous Cr<sub>2</sub>O<sub>3</sub> shell. The Rh/Cr<sub>2</sub>O<sub>3</sub> core-shell nanostructures are also clearly illustrated in the RGB image with Rh, Cr and O signal overlaid, shown in Fig. 4-7i.

## 4.5 On the Valence State of Rh/Cr<sub>2</sub>O<sub>3</sub> Co-catalyst Particles

To confirm the presence and the valence state of the Rh/Cr<sub>2</sub>O<sub>3</sub> co-catalyst nanoparticles on the InGaN/GaN nanowires, XPS analysis was performed after photodeposition (before overall water splitting). Figure 4-8 shows a high resolution XPS

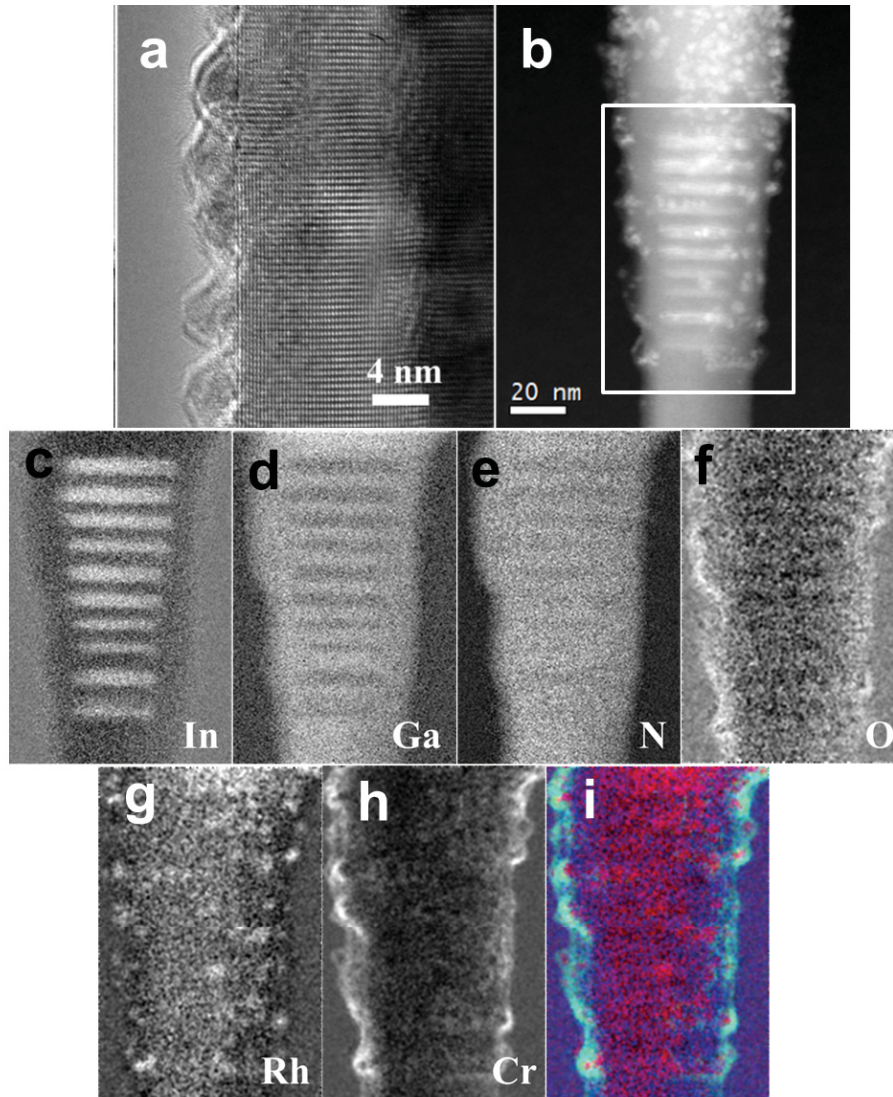


Figure 4-7: TEM characterization of Rh/Cr<sub>2</sub>O<sub>3</sub> decorated InGaN/GaN nanowires. (a) High resolution TEM of Rh/Cr<sub>2</sub>O<sub>3</sub> nanoparticles on the lateral surfaces of nanowire. (b) Electron energy loss spectroscopy (EELS) spectrum image of Rh/Cr<sub>2</sub>O<sub>3</sub> deposited InGaN/GaN nanowire. (c–h) Elemental maps of the nanoparticle deposited InGaN/GaN nanowire, derived from the selected area in EELS spectrum image (b) with MLLS fitting. (i) RGB elemental mixing (red, Rh; green, Cr; blue, O) image showing the core-shell Rh/Cr<sub>2</sub>O<sub>3</sub>.

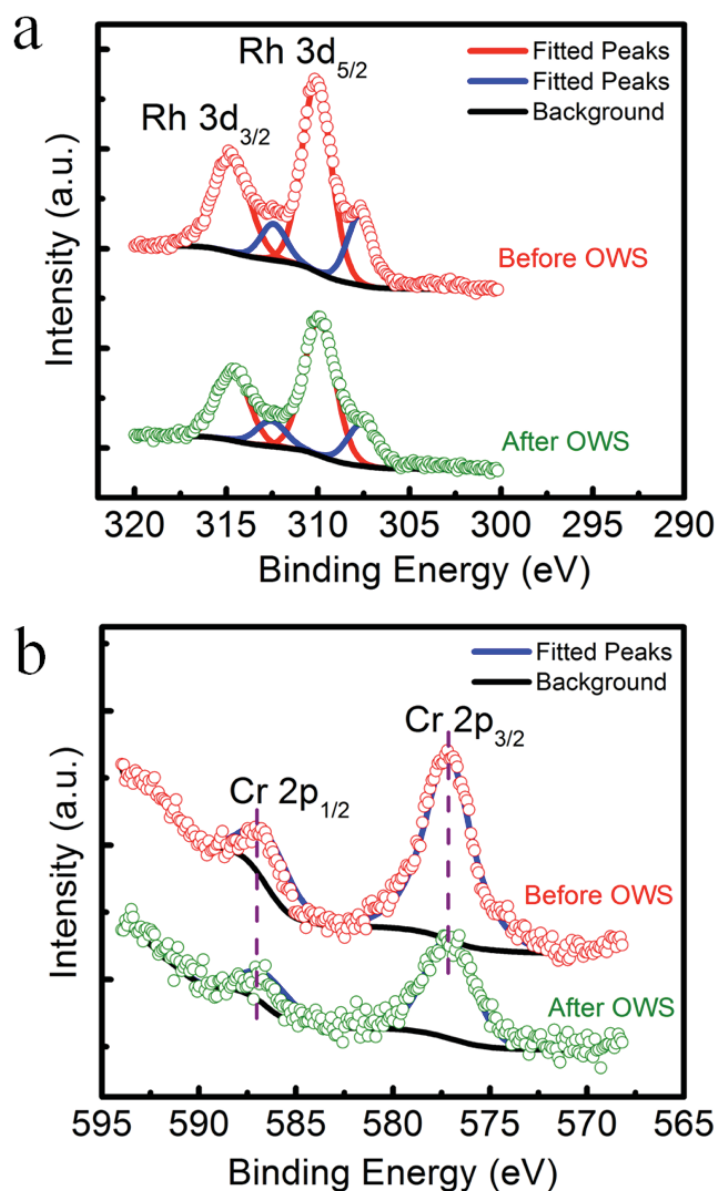


Figure 4-8: X-ray photoelectron spectroscopy (XPS) analysis of Rh/Cr<sub>2</sub>O<sub>3</sub> co-catalyst before and after overall water splitting. (a) High resolution XPS spectra of Rh3d core level electrons before and after overall water splitting (OWS). (b) High resolution XPS spectra of Cr2p core level electrons before and after OWS.

spectrum of (a) Rh3d, and (b) Cr2p core level electrons before overall water splitting. After deconvolution using Lorentzian-Gaussian mixing functions (L/G=30%), two spin-doublets were clearly resolved from Rh3d peak. The Rh3d<sub>5/2</sub> peak observed at 307.5 eV (blue line) is attributed to metallic rhodium Rh(0) [110]. This value is slightly higher than

the reported values for bulk metallic Rh (307.2 eV), and is commonly observed in nano-sized metal particles due to initial and final-state effects [163]. The Rh3d<sub>5/2</sub> peak at 309.69 eV (red line) is attributed to a mixed Rh-Cr oxide, indicating the interaction between Rh and Cr nanoparticles [146]. The areas of the two deconvoluted XPS peaks (Fig. 4-8a) correspond to 16.15% Rh in metallic (Rh<sup>0</sup>) form and 83.85% in mixed Rh-Cr oxide form. The deconvolution of Cr2p peak reveals one spin-doublet as shown in Fig. 4-8b. The Cr2p<sub>3/2</sub> peak, appeared at 576.9 eV is in good agreement with the reported values for Cr<sub>2</sub>O<sub>3</sub> [146]. Therefore, the valence state of Cr in the co-catalyst is trivalent after photodeposition. Note that no peak was observed near 579.0 eV which is assigned to Cr<sup>6+</sup>; indicating that all the Cr<sup>6+</sup> species in the precursor (K<sub>2</sub>CrO<sub>4</sub>) is photoreduced to form Cr<sub>2</sub>O<sub>3</sub> after photodeposition. The surface compositions of Rh and Cr<sub>2</sub>O<sub>3</sub> were 2.62 and 3.36 At.%, respectively, as estimated from the areas of the corresponding XPS peaks after Shirley background subtraction. A controlled experiment further confirmed that the deposited nanoparticles were indeed caused by photodeposition, and not via other processes, such as, physical deposition without the influence of light irradiation.

#### 4.6 Overall Water Splitting on InGaN/GaN Nanowires

In the subsequent photocatalytic overall pure water splitting experiments, ~3.3 cm<sup>2</sup> substrate was used under a 300 W full arc (> 300 nm) Xenon lamp. Considering the heights of ~440 nm and ~60 nm for GaN nanowire and InGaN nanowire segments, the corresponding material volumes are ~4.0 and ~0.38 μmol for GaN and InGaN, respectively. Figure 4-9a shows a schematic of the reaction mechanism on the Rh/Cr<sub>2</sub>O<sub>3</sub> core-shell nanoparticle-decorated InGaN/GaN nanowire heterostructure. As illustrated, redox reaction of water occurs on both GaN nanowire and InGaN nanowire segments. For the production of molecular H<sub>2</sub> and O<sub>2</sub>, four photons are simultaneously consumed to generate four holes (h<sup>+</sup>) and electrons (e<sup>-</sup>), which can catalyze water oxidation (2H<sub>2</sub>O+4h<sup>+</sup>→4H<sup>+</sup> + O<sub>2</sub>) and proton reduction (4e<sup>-</sup>+4H<sup>+</sup>→2H<sub>2</sub>) in overall water splitting, respectively.

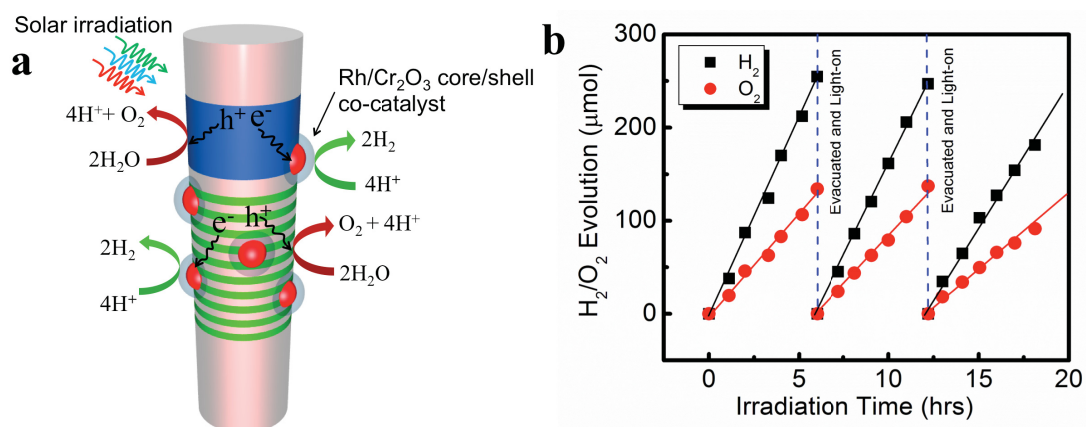


Figure 4-9: (a) Schematic of the photocatalytic overall water splitting reaction mechanism. (b) Overall pure water splitting on Rh/Cr<sub>2</sub>O<sub>3</sub> decorated InGaN/GaN nanowire arrays under full arc (>300 nm) 300 W Xenon lamp irradiation.

Figure 4-9b shows the overall neutral water (pH~7.0) splitting on Rh/Cr<sub>2</sub>O<sub>3</sub> photodeposited InGaN/GaN nanowire heterostructures under full arc (>300 nm) irradiation. Stoichiometric evolution of H<sub>2</sub> and O<sub>2</sub> was evident in the absence of any sacrificial reagents. More than 1056 μmol gases evolved (~683 μmol of H<sub>2</sub> and ~373 μmol of O<sub>2</sub>) during the course of ~18 hours of experiment, which is substantially greater than the total amount of GaN and InGaN catalyst (~4.38 μmol) used in this experiment; suggesting that the reaction proceeded catalytically. The water splitting activity of the InGaN/GaN nanowire photocatalyst is further confirmed by adopting an AM1.5G filter, as illustrated in Fig. 4-10. The photocatalytic activity with AM1.5G filter is 1.8 times lower than that under full arc illumination. The pH of water was invariant after the experiment, further indicating a balanced oxidation and reduction reaction of H<sub>2</sub>O. The turnover number (defined as the ratio of total amount of H<sub>2</sub> evolved to the amount of catalyst) exceeded 155 after ~18 hours of experiment under full arc (>300 nm) irradiation. The H<sub>2</sub> production rate is further calculated to be ~92 mmol hour<sup>-1</sup> g<sup>-1</sup> of photocatalysts, which is nearly an order of magnitude higher than any previously reported photocatalyst for overall water splitting under full-arc irradiation [164]. The measured overall reaction represents a collective effect from the redox reactions driven by the charge carriers in the GaN wire, InGaN ternary wire and InGaN quantum dots upon the

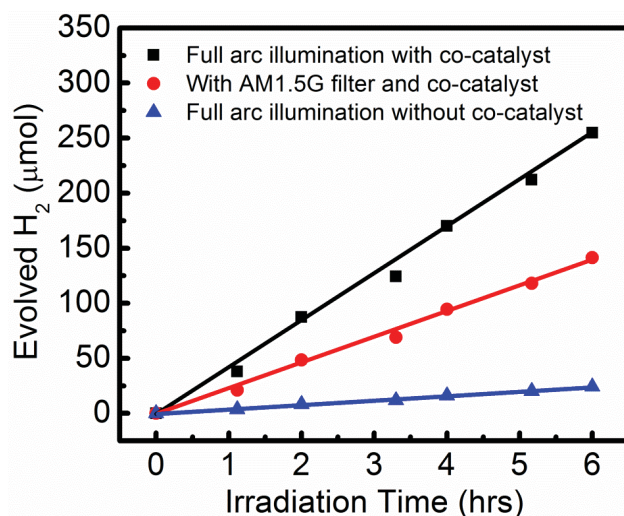


Figure 4-10: H<sub>2</sub> evolution from pure water splitting under full arc Xe-lamp, with and without Rh/Cr<sub>2</sub>O<sub>3</sub> co-catalyst deposition. For comparison, H<sub>2</sub> evolution is shown using an AM1.5G filter. The solid line is a guide to the eye.

absorption of photons in the UV and visible spectral range. In order to clarify the importance of Rh/Cr<sub>2</sub>O<sub>3</sub> co-catalyst, photocatalytic performance of InGaN/GaN nanowires was compared with and without co-catalyst, as shown in Figure 4-10. As can be seen, the use of Rh/Cr<sub>2</sub>O<sub>3</sub> nanoparticle co-catalysts can enhance the photocatalytic activity of InGaN/GaN nanowire heterostructures by nearly an order of magnitude. This improved activity is attributed to the introduction of active reaction sites, suppression of charge carrier recombination, and enhancement in charge separation along the lateral dimension.

To further evaluate the photocatalytic activity under visible light and to derive the apparent quantum efficiency (AQE) of the InGaN nanowire photocatalyst, the hydrogen and oxygen evolution rates were measured as a function of wavelength by adopting several band-pass filters. As shown in Fig. 4-11, steady evolution of H<sub>2</sub> and O<sub>2</sub> was clearly observed under blue and green light irradiation (400-560 nm), providing unambiguous evidence that In<sub>x</sub>Ga<sub>1-x</sub>N, for indium compositions of ~ 32% or lower, possesses suitable band-alignment and bandgap for overall pure water splitting.

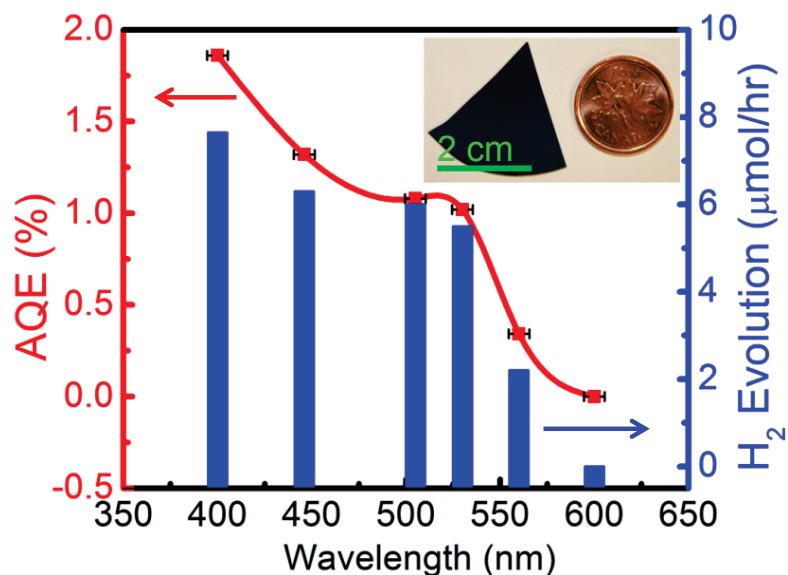


Figure 4-11: Apparent quantum efficiency (AQE) and H<sub>2</sub> evolution rate as a function of wavelength of the incident light. The horizontal error bars represent the full-width-half-maximum of the optical filters. The H<sub>2</sub> evolution rate was derived from ~2 hrs of overall water splitting under each optical filter. The solid red line is a guide to the eye. The inset shows a typical nanowire sample used for overall water splitting.

For comparison, no hydrogen can be observed under visible-light irradiation using structures without the incorporation of InGaN. As illustrated in Fig. 4-11, both the hydrogen-evolution rate and AQE decrease with increasing wavelength. The highest AQE (~1.86%) is achieved at ~395-405 nm, which consists of the contribution from InGaN ternary wire (PL peak ~418 nm) and ten vertically aligned InGaN quantum dots (PL peak ~558 nm). The longest wavelength (~560 nm) under which overall water splitting is achieved is in agreement with the PL peak (~558 nm) of the InGaN/GaN dot-in-a-wire structures, further confirming the photocatalytic activity of such quantum-confined nanoscale heterostructures. A typical wafer sample used in this study is also shown in the inset of Fig. 4-11. The internal quantum efficiency was estimated to be ~13% at ~440-450 nm, for an absorption coefficient of  $4 \times 10^4 \text{ cm}^{-1}$  for InGaN with an average indium composition of ~32 % [165] and a total dot layer thickness of ~30 nm. To our knowledge, this is the highest quantum efficiency reported in the visible wavelength range for overall neutral water splitting [33]. The turnover number under visible light (defined as the ratio of total amount of H<sub>2</sub> evolved under 400-600 nm irradiation as

shown in Figure 4-11 to the amount of InGaN catalyst) exceeded 73 after ~12 hours of experiment.

These studies correlate well with the dynamics of water dissociation at the (10 $\bar{1}$ 0) terminated GaN surfaces. First principles molecular dynamic simulations in recent past have suggested that the GaN (10 $\bar{1}$ 0) surfaces are very reactive for spontaneous dissociation of majority (~83%) of the water molecules,  $\text{H}_2\text{O} \rightarrow \text{H}^+ + \text{OH}^-$ , which is in direct contrast with the most studied photocatalyst,  $\text{TiO}_2$  [116]. In addition, the low effective free-energy barrier for proton diffusion on GaN (10 $\bar{1}$ 0) surface facilitates enhanced migration of protons from the  $\text{O}_2$  evolution reaction sites to  $\text{H}_2$  evolution sites, which can eventually lead to an increased  $\text{H}_2$  evolution in the present heterogeneous Rh/Cr $_2$ O $_3$  decorated InGaN/GaN nanowire photocatalyst. The achievement of overall neutral water splitting under blue and green light irradiation is also partly attributed to the inherent polarization-induced electric field in metal-nitrides[166] and the resulting quantum confined stark effect [167], that can effectively suppress the recombination of photogenerated electrons and holes, and promote the transfer of charge carriers to the semiconductor/water interface. In addition, the extremely low surface-recombination velocity of III-nitrides, compared to that of other semiconductors, can further reduce nonradiative surface recombination. It is also worthwhile mentioning that the diffusion of photoexcited charge carriers to the surface may be reduced by the presence of a thin (~2-3 nm) GaN layer at the nanowire surface (see Figure 4-5b), formed due to indium evaporation from the surface during the growth process, which may limit the overall water splitting reaction rate in the present InGaN/GaN nanowire heterostructure. Significantly improved photocatalytic activity is therefore expected by optimizing the growth of nearly homogeneous InGaN nanowires with controlled surface charge properties.

The stability of the nanowire photocatalyst was further confirmed by detailed structural and surface analysis after the overall water splitting reaction. The SEM and TEM images of the InGaN/GaN nanowire heterostructure, taken after 18 hours of water splitting reaction, are shown in Figures 4-12a and 4-12b, respectively. No evidence of nanowire corrosion was found. These results further support the excellent chemical

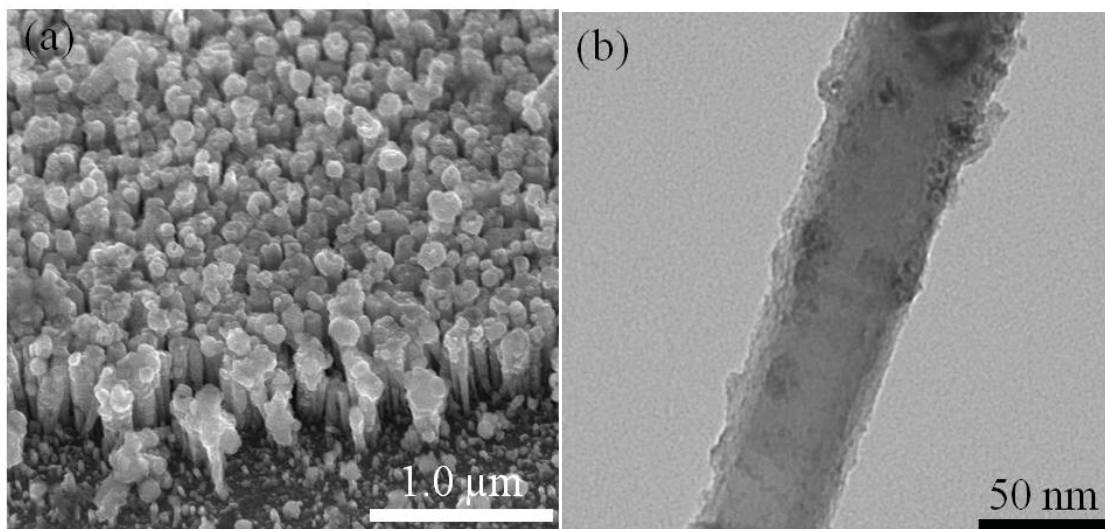


Figure 4-12: (a) SEM image of the InGaN/GaN nanowire ensemble after overall water splitting, showing the stability of the nanowire heterostructure. (b) Low magnification TEM image of a single InGaN/GaN nanowire after overall water splitting, further confirming the stability of the nanowire heterostructure.

stability of III-nitride semiconductors in harsh photocatalytic reactions [56], which is inherently related to the large difference in electronegativity between group III and group V elements.

#### 4.7 On the Stability of Rh/Cr<sub>2</sub>O<sub>3</sub> Co-catalyst

The Rh3d XPS peaks after overall water splitting reactions are shown in Fig. 4-8. Whilst the XPS peak position remained unchanged during the course of reaction, the XPS peak area (Figure 4-8a) for metallic Rh (307.5 eV) decreased from 16.15% (before the reaction) to 7.4% (after the reaction); suggesting that the metallic Rh particles are oxidized during the course of reaction. This is presumably due to the fact that some of the Rh particles may not be fully covered by the Cr<sub>2</sub>O<sub>3</sub> and therefore is vulnerable to oxygen. Also, even though the At.% of Rh3d remained nearly the same after overall water splitting, the Cr2p reduced from 3.36% (before the reaction) to 2.95% (after the reaction) (Figure 4-8b). The reason can probably be attributed to corrosion and hydrolysis of the Cr<sub>2</sub>O<sub>3</sub> co-catalyst. This could explain a slightly reduced activity over time (Figure 4-8b).

Also, the Cr2p peak position did not change upon ~18 hours of reaction (Figure 4-8b). This result also reveals that the trivalent state of the Cr did not change after the reaction.

## 4.8 Conclusions

In summary, we have demonstrated, for the first time, that InGaN, a widely used semiconductor for blue lasers, light emitting diodes, and power electronic devices, can function as a new material platform for one-step, stable production of solar-fuels *via* photochemical water splitting under direct UV and visible light irradiation. Our work also shows that the use of nanowire structures allows for the design of multi-band photocatalyst for efficient conversion of solar energy into clean fuels that was not previously possible by conventional photocatalysts, such as metal oxide powders. Multi-band InGaN/GaN nanowire heterostructures, decorated with Rhodium (Rh)/Chromium-oxide ( $\text{Cr}_2\text{O}_3$ ) core-shell nanoparticles can lead to stable hydrogen production from neutral (pH~7.0) water splitting under UV, blue and green-light irradiation (up to ~ 560 nm), the longest wavelength ever reported. At ~440-450 nm wavelengths, the internal quantum efficiency is estimated to be ~ 13%, the highest value reported in the visible spectrum. The turnover number under visible light well exceeds 73 in 12 hours. Detailed analysis further confirms the stable photocatalytic activity of the nanowire heterostructures. This wafer-level approach of water splitting offers recyclable and environmentally benign photocatalyst for large-scale practical applications.

# Chapter-5

## Visible Light Driven Efficient Overall Water Splitting using *p*-type Group III-nitride Nanowire Arrays

### 5.1 Introduction

In Chapter-3, we have shown that the photocatalytic activity of GaN nanowires under UV light can be significantly improved by introducing controlled amount of Mg dopant incorporation. To date, however, the efficiency of overall water splitting on InGaN and other visible light responsive photocatalyst has remained extremely low [9, 117, 168]. While much of the research has focused on enhancing visible light absorption through bandgap engineering [15], the detrimental effect of unbalanced charge carrier extraction/collection on the efficiency of the four electron-hole water splitting reaction has remained largely unexplored [169, 170]. For both GaN and InGaN, an upward band bending has been commonly measured on the *non*-doped or *n*-type doped materials [21-23]. In both materials, Mg can be used as a *p*-type dopant [25]. However, it has remained unknown if the concept of Fermi-level tuning can be extended into In-containing visible light active nitrides due to increased strain, defects, and In phase separation along with reduced over potential to straddle the redox potential. The incorporation of Mg in InGaN nanowires has been extremely challenging, due to the large background electron concentration and the presence of nitrogen vacancies with increasing Mg concentration [27]. While GaN and InGaN materials show great similarities, the growth of high quality Mg doped InGaN that can efficiently harness visible photons has been extremely challenging [26]. There are several fundamental limiting factors, including the formation of dislocations related to the large lattice mismatch (~ 11%) between InN and GaN, spinodal decomposition, In phase separation, and In surface segregation. These factors lead to a large number of non-radiative recombination centers, which limit the device

performance. In addition, the optimum growth temperatures for GaN and InN are drastically different ( $\sim 800$  °C for GaN vs.  $500$  °C for InN) due to the high vapor pressure of In over Ga, leading to very low In incorporation in InGaN.

In this work, we have performed extensive studies on the growth and characterization of Mg doped InGaN nanowires, including careful optimizations of the III/V flux ratio, doping concentration, growth temperature, and growth duration, which has led to drastically improved photocatalytic activities in the visible spectral range. Here, we have first demonstrated that the concept of Mg doping can be extended in InGaN nanowires and enable efficient overall water splitting under visible light irradiation (up to  $475$  nm). An apparent quantum efficiency of  $\sim 12.3\%$  has been achieved for overall neutral (pH $\sim 7.0$ ) water splitting under visible light illumination ( $400$ - $475$  nm). Moreover, using a double-band *p*-type gallium nitride/indium gallium nitride nanowire heterostructure, we show a solar-to-hydrogen conversion efficiency of  $\sim 1.8\%$  under concentrated sunlight.

## **5.2 Impact of Surface Band Bending on the Surface Electron and Hole Distribution**

Schematically illustrated in Fig. 5-1, after rapid nonadiabatic relaxation, photo-excited carriers may recombine radiatively or nonradiatively before diffusing to the near-surface region to drive redox reactions. In the emerging crystalline nanowire photocatalysts, wherein the carrier extraction efficiency is no longer diffusion-limited, the transport of spatially separated electron-hole pairs to the photocatalyst surfaces is often determined by the surface band structure [169]. Shown in the insets of Fig. 5-1, the presence of an upward- (downward-) surface band bending has been commonly measured for *n*- (*p*-) type semiconductor photocatalyst [121]. The energy barrier caused by the upward band bending repels the photo-excited electrons toward the bulk region, creating an electron depletion (hole accumulation) layer at the surface [129]. The estimation of electron and hole concentration in the  $\text{In}_{0.25}\text{Ga}_{0.75}\text{N}$  nanowire was performed by the simulation program APSYS. Specific carrier generation is introduced uniformly in the

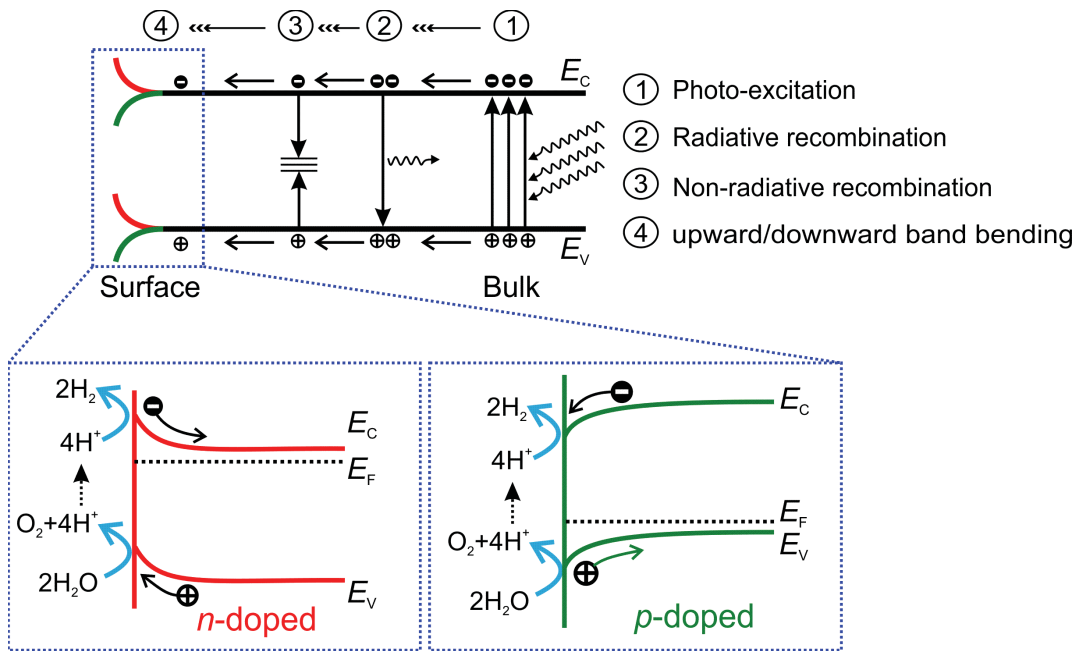


Figure 5-1: Schematic of carrier generation and radiative and non-radiative recombination processes. The four electron-hole water splitting mechanism is illustrated on *n*- (*p*-) doped semiconductors with upward- (downward-) surface band bending in the two bottom panels. While the reduction reaction is suppressed in presence of upward band bending, the oxidation reaction is suppressed in presence of downward band bending.

nanowire by defining a 405 nm light input to the structure, with a constant carrier generation rate of  $2.5 \times 10^{27} \text{ cm}^3 \cdot \text{s}^{-1}$ . Shockley-Read-Hall (SRH) lifetime of 100 ns [171] and Auger recombination coefficient of  $(1 \times 10^{-33} \text{ cm}^6 \cdot \text{s}^{-1})$  [172] are assumed in the calculation. The nanowire diameter and surface recombination velocity are considered to be 100 nm and  $5 \times 10^4 \text{ cm} \cdot \text{s}^{-1}$ , respectively. The surface trap density is  $\sim 1 \times 10^{14} \text{ cm}^{-2}$  [173]. A nominally undoped nanowire structure, with acceptor-like surface traps, is first simulated [174]. The presence of  $\sim 0.37 \text{ eV}$  upward band bending in the near surface region is assumed, which reduced to  $\sim 0.07 \text{ eV}$  under photo-excitation, owing to the screening effect by photogenerated carriers [175]. The calculated electron and hole distributions across the nanowire lateral dimension are shown in Fig. 5-2. It is seen that hole concentration is  $\sim 20$  times higher than that of electron in the near-surface region. The carrier distribution in *p*-type  $\text{In}_{0.25}\text{Ga}_{0.75}\text{N}$  with the presence of a downward surface

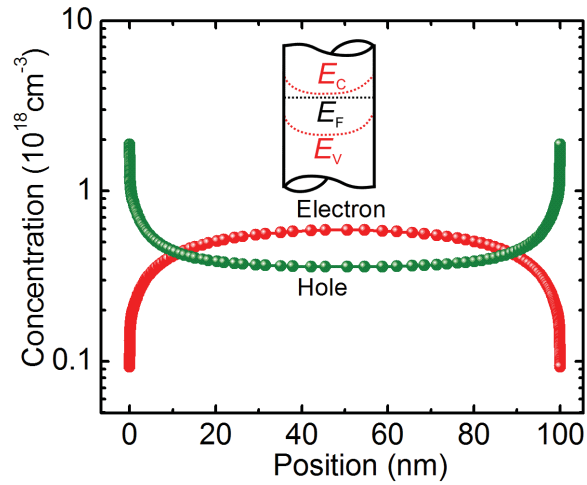


Figure 5-2: Electron and hole distribution on a 100 nm diameter undoped  $\text{In}_{0.25}\text{Ga}_{0.75}\text{N}$  nanowire in the presence of  $\sim 0.37$  eV upward surface band bending (inset) under certain excitation condition.

band bending has also been calculated. Electron accumulation and hole depletion in the near-surface region was clearly observed [176]. This upward band bending was one of the major obstacles causing the very low ( $\sim 1.86\%$  at 400 nm) apparent quantum efficiency (AQE) of overall water splitting on the InGaN/GaN multiband nanowire heterostructures, as discussed in Chapter-4. On the other hand, the downward surface band bending of *p*-doped metal-nitrides creates an energy barrier for the photogenerated holes, resulting in a hole depletion (electron accumulation) at the near-surface region. This hole depletion suppresses the first-half (water oxidation) of redox reaction, which governs the rate of overall water splitting [17]. Although the presence of surface band bending is advantageous for photoelectrochemical water splitting wherein oxidation and reduction reaction take place at different electrodes, it should be minimized for photochemical water splitting in order to achieve balanced, efficient, and stable redox reactions.

### 5.3 Growth and Characterization of InGaN:Mg Nanowires

The Mg doped InGaN (denoted as InGaN:Mg) nanowire arrays were grown on Si (111) substrate by MBE under nitrogen rich conditions [102]. Instead of direct formation of InGaN nanowires on Si substrate, a GaN nanowire template was used, which led to

controlled formation of InGaN nanowires with superior structural and optical properties [156]. In order to minimize nonradiative recombination resulting from misfit dislocations [177], three segments of InGaN ternary wires were incorporated along the growth direction of GaN nanowire, shown schematically in Fig. 5-3a. The InGaN/GaN nanowire segments were doped with divalent ( $\text{Mg}^{2+}$ ) ions as  $p$ -type dopant by controlling the effusion cell temperature of Mg ( $T_{\text{Mg}}$ ) from 190 to 240 °C. The GaN nanowire template was left undoped.

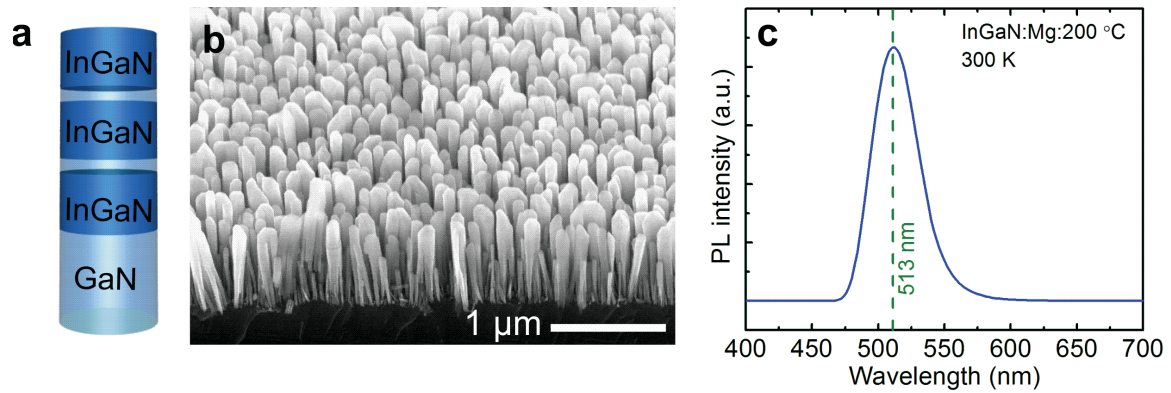


Figure 5-3: (a) Schematic of  $\text{In}_{0.26}\text{Ga}_{0.74}\text{N}$  nanowire structure showing three InGaN nanowire segments on a GaN nanowire template. (b) a 45° tilted SEM image of as-grown  $\text{In}_{0.26}\text{Ga}_{0.74}\text{N}$  nanowires on Si (111) substrate. (c) Room temperature  $\mu$ -PL spectrum from as-grown  $\text{In}_{0.26}\text{Ga}_{0.74}\text{N}$  nanowires.

A 45° tilted SEM image (Fig. 5-3b) of as-grown InGaN nanowire arrays ( $T_{\text{Mg}}=200$  °C) revealed vertically aligned nanowires, with the growth direction along the  $c$ -axis. The average height is  $\sim 400$ - $600$  nm, lateral sizes are  $\sim 40$ - $100$  nm, and the areal density is in the range of  $\sim 1.5 \times 10^{10} \text{ cm}^{-2}$ . The room temperature micro-photoluminescence ( $\mu$ -PL) spectrum (Fig. 5-3c) of InGaN nanowires clearly shows a single band-to-band optical emission peak at  $\sim 513$  nm, which corresponds to a bandgap of 2.42 eV and average In composition of  $\sim 26\%$  [41]. The broad emission peak reveals intra- and inter-nanowire In fluctuations, consistent with previous studies [178]. Detailed structural and elemental characterization was performed using scanning transmission electron microscopy (STEM) and energy dispersive X-ray scanning (EDXS) analysis.

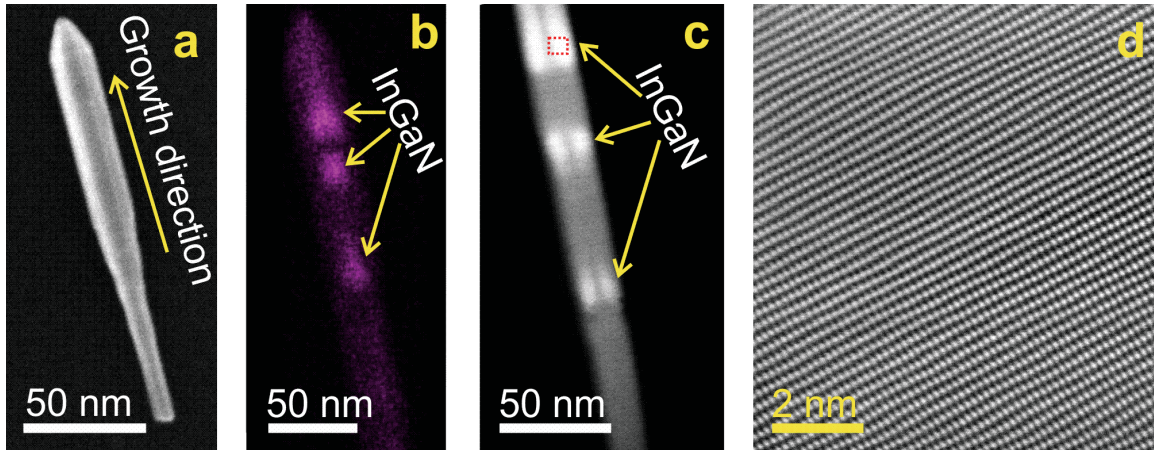


Figure 5-4: (a) STEM-SE image of a single  $\text{In}_{0.26}\text{Ga}_{0.74}\text{N}$  nanowire. (b) EDXS elemental (In) mapping of the  $\text{In}_{0.26}\text{Ga}_{0.74}\text{N}$  nanowire. (c) STEM-HAADF image of a single  $\text{In}_{0.26}\text{Ga}_{0.74}\text{N}$  nanowire (Fig. 5-4b) reveals the existence of three segments of InGaN in GaN nanowire. (d) HRSTEM-BF lattice image illustrating lattice fringes from a defect-free single crystalline  $\text{In}_{0.26}\text{Ga}_{0.74}\text{N}$  nanowire.

Figure 5-4a shows a STEM secondary electron (SE) image of a single  $\text{In}_{0.26}\text{Ga}_{0.74}\text{N}$  nanowire on a carbon film. EDXS elemental mapping (Fig. 5-4b) reveals the existence of three segments of  $\text{In}_{0.26}\text{Ga}_{0.74}\text{N}$  with total thickness of  $\sim 80$  nm within GaN nanowire. A STEM-high angle annular dark field (HAADF) image (Fig. 5-4c) further shows the atomic number contrast between  $\text{In}_{0.26}\text{Ga}_{0.74}\text{N}$  (brighter) and GaN (darker). No phase segregation or dislocations are observed in  $\text{In}_{0.26}\text{Ga}_{0.74}\text{N}$  or GaN layers, demonstrating excellent crystalline quality of the nanowires. Shown in Fig. 5-4d, the high crystalline quality of the  $\text{In}_{0.26}\text{Ga}_{0.74}\text{N}$  nanowires is further confirmed by clear lattice fringes in the high-resolution TEM image (of the selected region in Fig. 5-4c).

#### 5.4 Estimation of Nanowire Surface Band Bending from ARXPS

The near-surface band-structure of the  $\text{In}_{0.26}\text{Ga}_{0.74}\text{N}$  nanowires was revealed by recording angle resolved X-ray photoelectron spectroscopy (ARXPS) valence spectrum from the lateral nonpolar (*m*-plane) surfaces of the nanowires. Figure 5-5 shows the estimated  $E_{\text{FS}}-E_{\text{VS}}$  for different Mg doped  $\text{In}_{0.26}\text{Ga}_{0.74}\text{N}$  samples. For  $T_{\text{Mg}}=190$  °C, the estimated  $E_{\text{FS}}-E_{\text{VS}}$  is  $\sim 2.1$  eV, which is nearly close to the  $E_{\text{FS}}-E_{\text{VS}}$  ( $\sim 2.20$  eV) of intrinsic

In<sub>0.26</sub>Ga<sub>0.74</sub>N [179], indicating that the surface of In<sub>0.26</sub>Ga<sub>0.74</sub>N is barely doped at  $T_{\text{Mg}}=190$  °C. Under relatively low Mg effusion cell temperature (low Mg flux), the dopant incorporation in the near-surface region is limited by Mg desorption [180]. The surface of such InGaN:Mg nanowires remains *n*-type, which explains the commonly measured large downward band bending on *p*-type InGaN surfaces [38]. The dopant incorporation can be significantly enhanced in the near-surface region with an increase in  $T_{\text{Mg}}$  [180]. It is seen that  $E_{\text{FS}}-E_{\text{VS}}$  varies from 2.2 eV to 0.5 eV with increasing Mg dopant incorporation. Consequently, the lateral surfaces of InGaN nanowires can be transformed from *n*-type to weakly *p*-type.

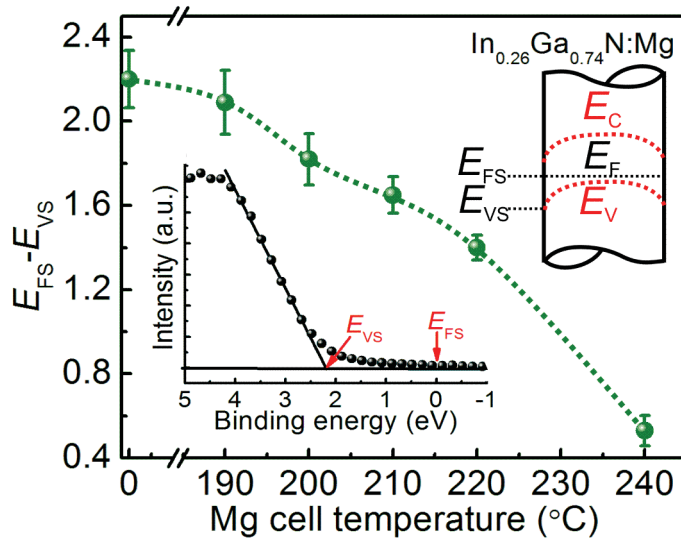


Figure 5-5:  $E_{\text{FS}}-E_{\text{VS}}$  for different Mg doped In<sub>0.26</sub>Ga<sub>0.74</sub>N nanowire samples derived from ARXPS valence spectrum as shown in the insets. The error bars represent the accuracy of the linear extrapolation method. The error bar is defined by the s.d.

The drastic reduction in  $E_{\text{FS}}-E_{\text{VS}}$  is further attributed to the reduction in downward band bending at the nanowire surface. Although the downward band bending caused by *p*-type doping accelerates proton reduction at the nanowire surface, it hinders the hole transport toward the nanowire-liquid interface. Therefore, by reducing the downward band bending with optimized dopant incorporation, the photocatalytic activity of the In<sub>0.26</sub>Ga<sub>0.74</sub>N:Mg nanowire can be significantly improved. The extremely large tuning range ( $\sim 1.7$  eV) of

the surface Fermi-level provides the distinct opportunity for achieving nearly flat band conditions for InGaN nanowire photocatalyst in equilibrium with water, thereby leading to very rapid diffusion of both photo-generated electrons and holes to the surfaces for high efficiency and balanced redox reactions that was not previously possible. Note that, the photoelectrons generated in the GaN region of the nanowires has negligible contribution to the drastic reduction in  $E_{FS}-E_{VS}$  (Fig. 5-5), as the near surface Fermi level of GaN:Mg barely changes in this doping regime ( $T_{Mg}=190-230$  °C), as shown in Fig. 3-11a.

## 5.5 Band Bending in Equilibrium with Water

Figure 5-6a shows downward band bending on the surface of *p*-type (bulk)  $In_{0.26}Ga_{0.74}N$  ( $T_{Mg}=200$  °C) prior-to equilibrium with water. This downward band bending gets reduced when it comes in equilibrium with water due to interfacial charge transfer, as illustrated in Fig. 5-6b. Upon photo-excitation, the remaining band bending may flatten out owing to the screening effect by the photogenerated carriers, which lead to enhanced carrier extraction.

## 5.6 Role of Rh/Cr<sub>2</sub>O<sub>3</sub> Core-shell Co-catalyst

Recent studies have shown that water molecules are dissociatively adsorbed on nonpolar III-nitride surfaces, leading to the formation of hydroxyl species for the subsequent oxygen evolution reaction [116]. Computational and experimental analysis suggest that the photogenerated holes on the nonpolar surfaces of GaN possess sufficient standard free energies to catalyze water oxidation [73, 115, 129]. A number of experimental studies have revealed that efficient water oxidation can proceed on the surface of nitrides and oxynitrides without oxidation co-catalyst [72, 73, 75]. To further promote H<sub>2</sub> evolution, Rh/Cr<sub>2</sub>O<sub>3</sub> core-shell co-catalyst [32] was photo-deposited on  $In_{0.26}Ga_{0.74}N:Mg$  nanowire surfaces, wherein the Rh nanoparticles can provide more active sites for H<sup>+</sup> reduction while the Cr<sub>2</sub>O<sub>3</sub> shell layer effectively prevents any backward reaction to form water.

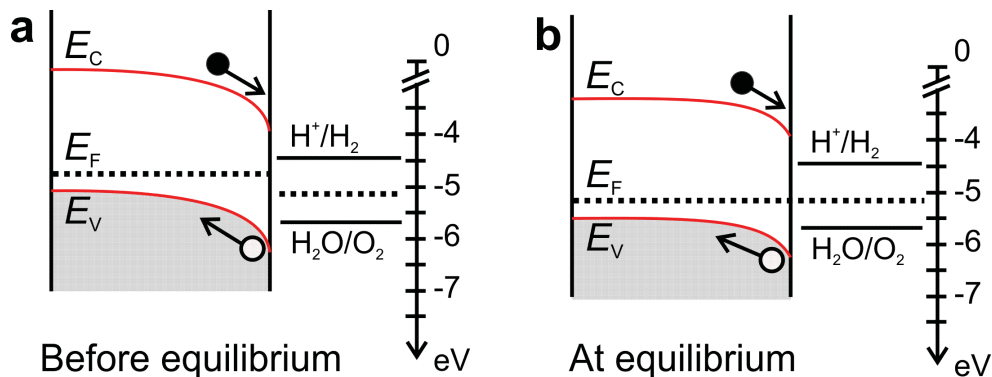


Figure 5-6: (a) Downward band bending at the surface of *p*-type (bulk) InGaN:Mg before equilibrium with water. The downward band bending repels the photogenerated holes toward the bulk and the electrons toward the surface. (b) At equilibrium with water the downward band bending gets reduced.

Additionally, Rh nanoparticles suppress radiative and/or non-radiative recombination inside the photocatalyst [181]. EDXS elemental (Rh, Cr) mapping (Fig. 5-7a, b, c) clearly demonstrates successful deposition of Rh/Cr<sub>2</sub>O<sub>3</sub> core-shell co-catalyst on In<sub>0.26</sub>Ga<sub>0.74</sub>N:Mg nanowire surfaces. Since the work function of Rh (4.9 eV) is larger than the electron affinity of In<sub>0.26</sub>Ga<sub>0.74</sub>N:Mg (3.95 eV), the photogenerated electrons in the conduction band can easily migrate from nanowire to Rh nanoparticles. Under the same excitation condition, the measured  $\mu$ -PL emission intensity of Rh/In<sub>0.26</sub>Ga<sub>0.74</sub>N:Mg composite is lower than In<sub>0.26</sub>Ga<sub>0.74</sub>N:Mg, confirming the fact that the photoexcited electrons are scavenged by the Rh particles, and therefore the carrier recombination is significantly suppressed (Fig. 5-7d) [182]. Since Rh nanoparticles can be active sites for backward reaction to form water, a Cr<sub>2</sub>O<sub>3</sub> shell layer is further photodeposited on the Rh nanoparticles. Our control experiment suggests that the activity of the nanowire photocatalyst without co-catalyst is  $\sim$ 4-5 times lower than that of the catalyst with co-catalyst. Figure 5-7e further shows the overall water splitting reaction mechanism on the nonpolar In<sub>0.26</sub>Ga<sub>0.74</sub>N:Mg nanowire surfaces.

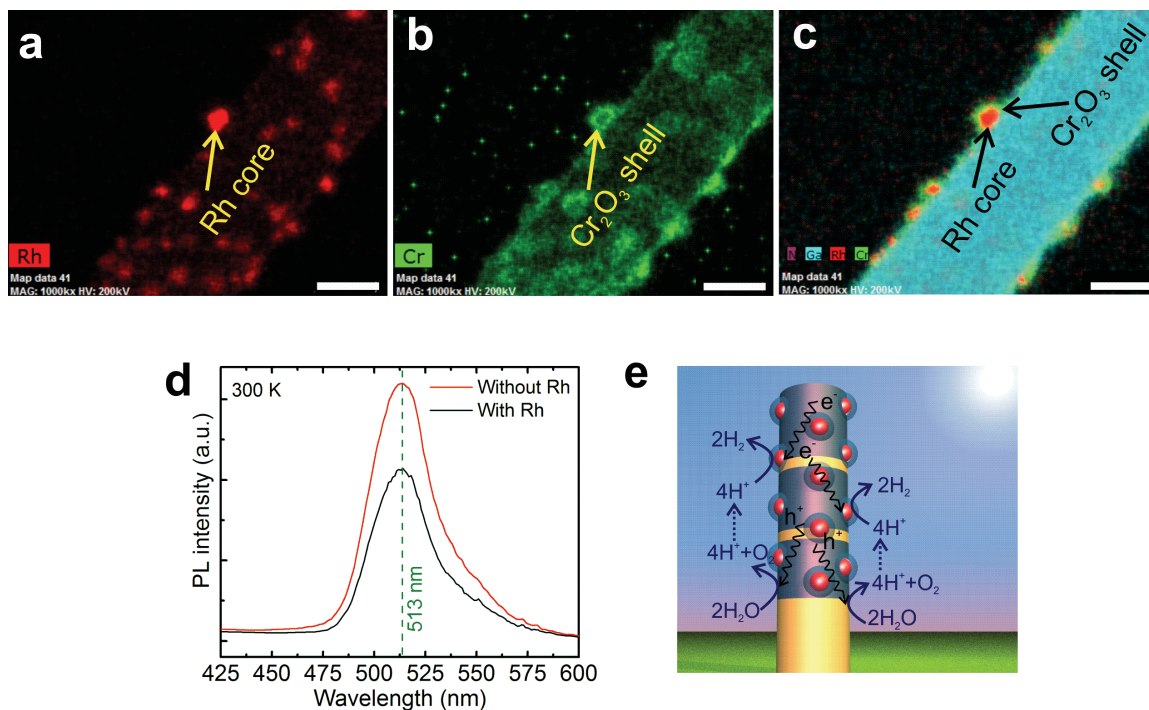


Figure 5-7: EDXS elemental mapping images clearly demonstrating (a) Rh distribution, (b) Cr distribution, and (c) Rh/Cr<sub>2</sub>O<sub>3</sub> core-shell composite nanoparticles on the nanowire nonpolar surface. (d) Room temperature  $\mu$ -PL spectra from bare In<sub>0.26</sub>Ga<sub>0.74</sub>N:Mg nanowire and from Rh nanoparticle deposited In<sub>0.26</sub>Ga<sub>0.74</sub>N:Mg nanowire arrays. (e) Overall water splitting reaction mechanism on the nanowire photocatalyst.

Note that, the presence of a thin ( $\sim$ 2-5 nm) GaN layer at the nanowire surface (caused by In evaporation during nanowire growth) creates additional potential barrier which prevents the electrons and holes from reaching the nanowire-water interface, resulting in low activity. However, owing to the high excitation condition ( $488 \text{ mW cm}^{-2}$ ) in our experiments, most of the photogenerated carriers can readily overcome this barrier and reach the semiconductor-liquid interface. The concentrated illumination is of particular interest for economically viable industrial production of hydrogen from photolysis as predicted by Y. Tachibana *et al* [30]. John Turner [31] estimated a realistic limit of the concentrated light that can be used for water splitting is in the range of 10-20 suns.

## 5.7 Overall Neutral Water Splitting

The co-catalyst decorated  $\text{In}_{0.26}\text{Ga}_{0.74}\text{N}:\text{Mg}$  nanowire photocatalyst ( $\sim 3 \text{ cm}^2$  wafer sample) was subsequently used for overall neutral water (pH $\sim 7.0$ ) splitting under visible light ( $> 400 \text{ nm}$ ) without the presence of any sacrificial reagents. The  $\text{H}_2$  evolution rates in overall water splitting for different Mg doped  $\text{In}_{0.26}\text{Ga}_{0.74}\text{N}$  nanowire arrays are shown in Fig. 5-8a. The evolution rates were derived from  $\sim 6 \text{ h}$  of water splitting for each sample. It is seen that the  $\text{H}_2$  evolution rate first increases drastically with  $T_{\text{Mg}}$ . The rate of  $\text{H}_2$  evolution can reach  $\sim 0.78 \text{ mol h}^{-1} \text{ g}^{-1}$  for the optimum Mg doped ( $T_{\text{Mg}}=200 \text{ }^\circ\text{C}$ )  $\text{In}_{0.26}\text{Ga}_{0.74}\text{N}$  nanowire arrays, which is more than  $\sim 30$  times higher than that of the nominally undoped sample. The observed optimized  $T_{\text{Mg}}$  in InGaN is relatively lower than that of GaN nanowires (as discussed in Chapter-3), which is attributed to the strong dependence of Mg ionization energy on In composition, and the low growth temperature of InGaN. The significantly enhanced activity can be well explained by the tuning of the surface Fermi-level and reduction in the downward surface band bending, shown in Fig. 5-5, which can lead to more balanced oxidation and reduction reactions in solution (Fig. 5-6).

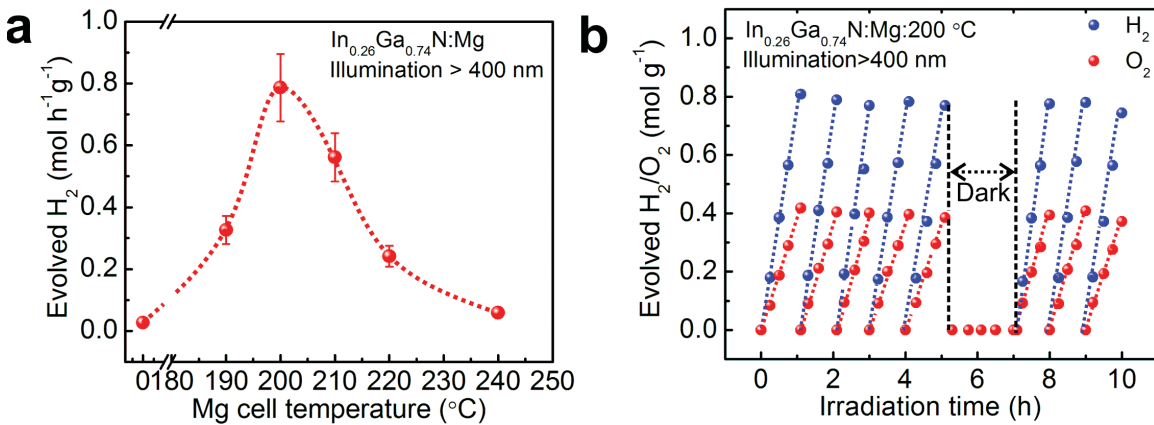


Figure 5-8: (a)  $\text{H}_2$  evolution rate in overall neutral (pH $\sim 7.0$ ) water splitting for different Mg doped  $\text{In}_{0.26}\text{Ga}_{0.74}\text{N}$  nanowire arrays under visible light ( $>400 \text{ nm}$ ). (b) The evolution of  $\text{H}_2$  and  $\text{O}_2$  with irradiation time from neutral (pH $\sim 7.0$ ) water for Mg:200  $^\circ\text{C}$  doped  $\text{In}_{0.26}\text{Ga}_{0.74}\text{N}$  nanowire arrays under dark and visible light ( $>400 \text{ nm}$ ) irradiation. Active GaN/InGaN catalyst weight  $\sim 0.32 \text{ mg}$ .

With further reduction in the surface band bending, however, the surface charge properties may become non-optimal for the efficient transfer of electrons and holes to the nanowire surfaces in solution, evidenced by the decrease of the overall water splitting efficiency with further increase in  $T_{\text{Mg}}$ . Additionally, the reduction in photocatalytic activity at relatively high  $T_{\text{Mg}}$  may be related to the deterioration of the crystal quality of the nanowires [183]. At high Mg concentration, Mg acts as donor like self-compensation center [183]. With increase in Mg concentration, nitrogen vacancy ( $V_{\text{N}}$ ) related defects increase (more discussions on this is in Chapter-6) due to reduced growth temperature  $\sim 600$  °C, leading to degradation of the structural quality [183]. These defects work as self-compensation centers in  $\text{In}_{0.26}\text{Ga}_{0.74}\text{N}$  at higher-doping levels. This could explain the reduction in photocatalytic activity for  $T_{\text{Mg}} > 200$  °C, as shown in Fig. 5-8a.

Figure 5-8b shows the evolution of  $\text{H}_2$  and  $\text{O}_2$  with irradiation time from neutral water from the optimum ( $T_{\text{Mg}}$ : 200 °C) Mg doped  $\text{In}_{0.26}\text{Ga}_{0.74}\text{N}$  nanowire arrays under visible light ( $>400$  nm) irradiation. The  $\text{H}_2/\text{O}_2$  ratio was nearly 2:1, indicating a balanced oxidation and reduction reaction of water. The pH of water before and after reaction remained nearly the same, further confirming stoichiometric evolution of  $\text{H}_2$  and  $\text{O}_2$ . Repeated cycles of water splitting demonstrate the stability of  $\text{In}_{0.26}\text{Ga}_{0.74}\text{N}:\text{Mg}$  nanowires. While proton reduction proceeds on Rh/ $\text{Cr}_2\text{O}_3$  co-catalyst surface, the oxidation of water proceeds on the nonpolar sidewalls of the nanowires. Note that the surface area of nonpolar  $\text{In}_{0.26}\text{Ga}_{0.74}\text{N}$  ( $\sim 3.0 \text{ m}^2 \text{ g}^{-1}$ ) nanowire side walls is nearly 10 times higher than the effective surface area of GaN particulate samples ( $0.3 \text{ m}^2 \text{ g}^{-1}$ ) [73]. Therefore, it is likely that the observed efficient water oxidation in the absence of oxidation co-catalyst is partly due to a high number of surface reaction sites. However, the exact mechanism of such efficient multi-step water oxidation reaction on metal-nitride surface remains unclear to date, and requires further detailed studies [17].

Our control experiment also confirms that photo-excited charge carriers in Si substrate do not take part in the photochemical reaction, which can be directly correlated to the presence of large band-offset at the Si/GaN interface and insufficient water oxidation potential of Si, as illustrated in Fig. 5-9 [158]. The wavelength dependent

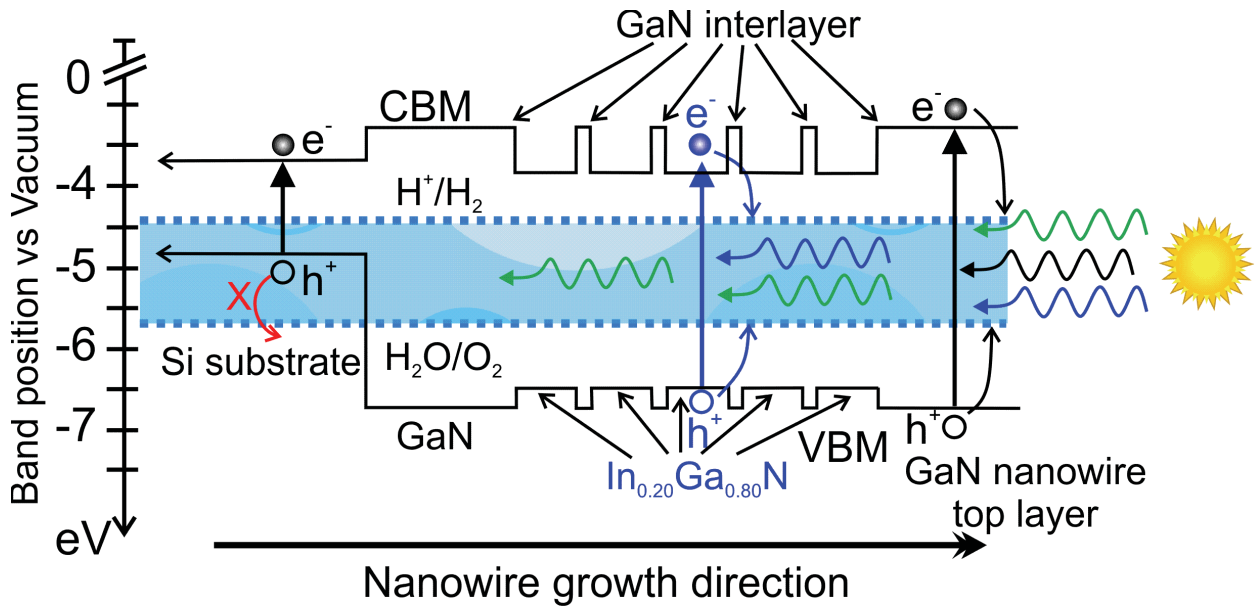


Figure 5-9: Flat-band diagram of the GaN/In<sub>0.20</sub>Ga<sub>0.80</sub>N nanowire heterostructure, showing the conduction-band and valence-band edge positions of GaN, In<sub>0.20</sub>Ga<sub>0.80</sub>N, and the underlying Si substrate. The redox potentials of water are also shown by the dotted lines. It is seen that GaN and In<sub>0.20</sub>Ga<sub>0.80</sub>N possess sufficient overpotential for oxidation and reduction of water. The photogenerated holes in Si substrate, however, do not possess sufficient potential for water oxidation, and hence Si substrate does not take part in overall water splitting reaction. All values of potentials are in eV relative to the vacuum level.

activity of In<sub>0.26</sub>Ga<sub>0.74</sub>N:Mg nanowires is revealed by performing overall water splitting with different long-pass filters, shown in Fig. 5-10. Significant activity was observed for excitation up to 520 nm, which is consistent with the band edge of In<sub>0.26</sub>Ga<sub>0.74</sub>N:Mg nanowires (PL peak ~ 513 nm, Fig. 5-3c).

We have subsequently developed multi-stacked broadband GaN:Mg/InGaN:Mg nanowire photocatalyst, schematically shown in Fig. 5-11a, wherein the surface charge properties and thicknesses of the GaN and InGaN segments are separately optimized to achieve maximum efficiency in the UV and visible wavelength range, respectively. In this case, five segments of InGaN ternary wires were incorporated along the growth direction of GaN nanowires to enhance light absorption, as shown in Fig. 5-11a. Shown in Fig. 5-11a inset, the GaN:Mg/InGaN:Mg nanowire photocatalyst can effectively function as a double-band heterostructure to efficiently harness UV and visible solar

photons. The room temperature  $\mu$ -PL measurement (Fig. 5-11b) reveals two band-to-band emission peaks at  $\sim 364$  nm and  $\sim 475$  nm, corresponding to bandgaps of GaN (3.4 eV) and InGaN (2.61 eV), respectively.

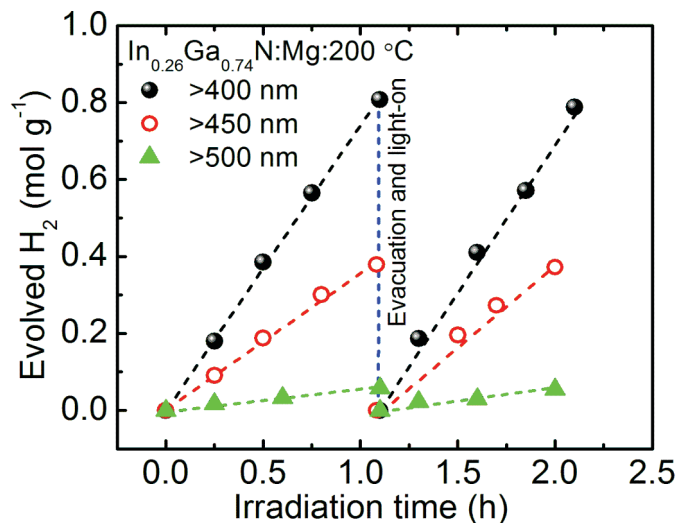


Figure 5-10: H<sub>2</sub> evolution in overall water splitting as a function of irradiation time with different long-pass filters. The dashed lines are guides to the eye.

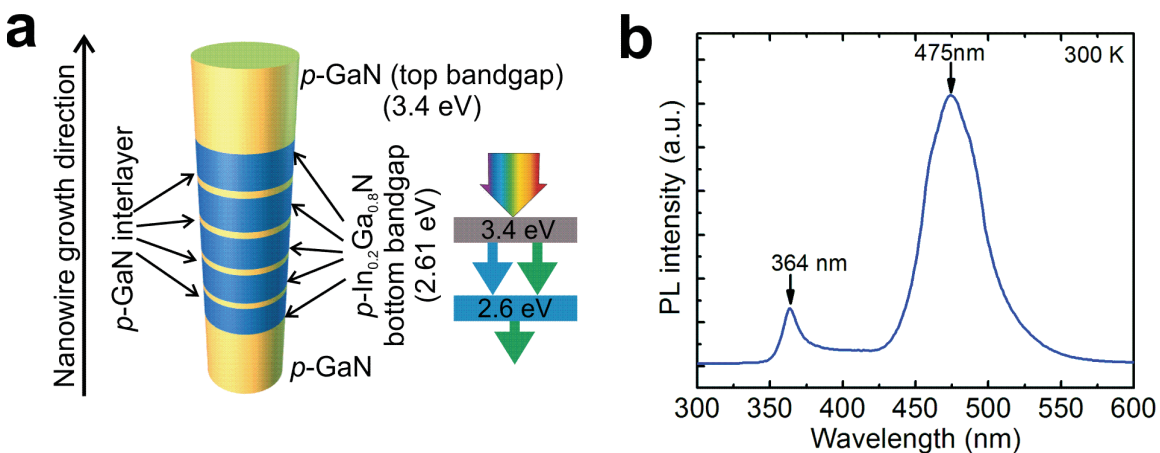


Figure 5-11: (a) Schematic of core-shell Rh/Cr<sub>2</sub>O<sub>3</sub> nanoparticle decorated double-band *p*-GaN/*p*-In<sub>0.20</sub>Ga<sub>0.8</sub>N nanowire photocatalyst. Five segments of InGaN were incorporated along the growth axis of GaN nanowires. The concept of double-band photocatalyst is illustrated in the inset. (b) Room temperature  $\mu$ -PL spectrum from as-grown *p*-GaN/*p*-In<sub>0.20</sub>Ga<sub>0.8</sub>N nanowire heterostructure.

The dual-bandgap system is adopted for better matching and utilization of solar spectrum, and to minimize the energy loss due to the rapid thermal relaxation of high-energy charge

carriers [155]. The average In composition in InGaN segments is ~20% [41]. The STEM-HAADF image, as shown in Fig.5-12, clearly shows the atomic number contrast between  $\text{In}_{0.2}\text{Ga}_{0.8}\text{N}$  segments (brighter contrast) and GaN nanowire. The  $\text{In}_{0.2}\text{Ga}_{0.8}\text{N}$  total thickness is ~185 nm. The EDX elemental (In, Ga, N) mapping image of the nanowire heterostructure is illustrated in the inset of Fig. 5-12. The *p*-type behavior of the GaN:Mg and  $\text{In}_{0.20}\text{Ga}_{0.80}\text{N}:\text{Mg}$  are confirmed by open-circuit potential (OCP) measurements, as discussed in the following section [120].

### 5.8 *p*-Type behavior of GaN:Mg and $\text{In}_{0.2}\text{Ga}_{0.8}\text{N}:\text{Mg}$ from Open Circuit Potential (OCP) Measurement

The *p*-GaN/*p*- $\text{In}_{0.20}\text{Ga}_{0.80}\text{N}$  nanowires were characterized by OCP measurement. Using three-electrode electrochemical cell configuration, the open circuit potential was performed in 1 mol/L HBr. The *p*-GaN/*p*- $\text{In}_{0.20}\text{Ga}_{0.80}\text{N}$  nanowire arrays (on Si substrate), a Pt wire, and a double-junction Ag/AgCl were used as the photoactive working electrode, counter electrode, and reference electrode, respectively.

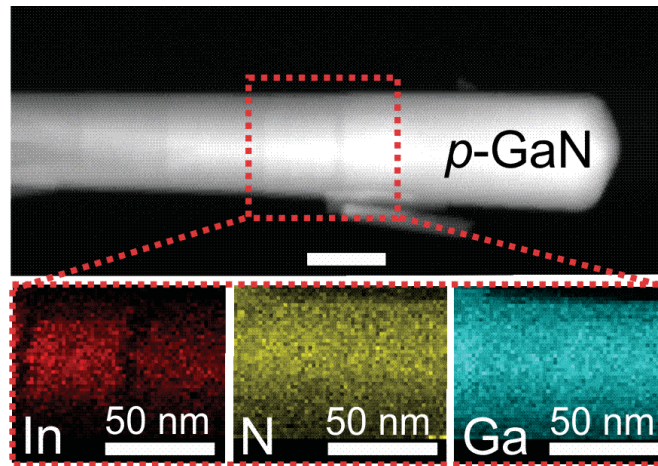


Figure 5-12: STEM- HAADF image of a single *p*-GaN/*p*- $\text{In}_{0.20}\text{Ga}_{0.80}\text{N}$  nanowire reveals the existence of  $\text{In}_{0.20}\text{Ga}_{0.80}\text{N}$  segments in GaN nanowire. EDXS elemental mapping on the selected region of the  $\text{In}_{0.20}\text{Ga}_{0.80}\text{N}$  nanowire, showing the distribution of In, Ga and N.

In-Ga eutectic alloy metal was deposited on the backside of the Si substrate to serve as an Ohmic contact. OCP measurements were performed by using a 300 W Xenon lamp (Cermax, PE300BUV) as an irradiation source. The reactor chamber was made of quartz for ample transmittance to both UV and visible light. The direction of the OCP shift,

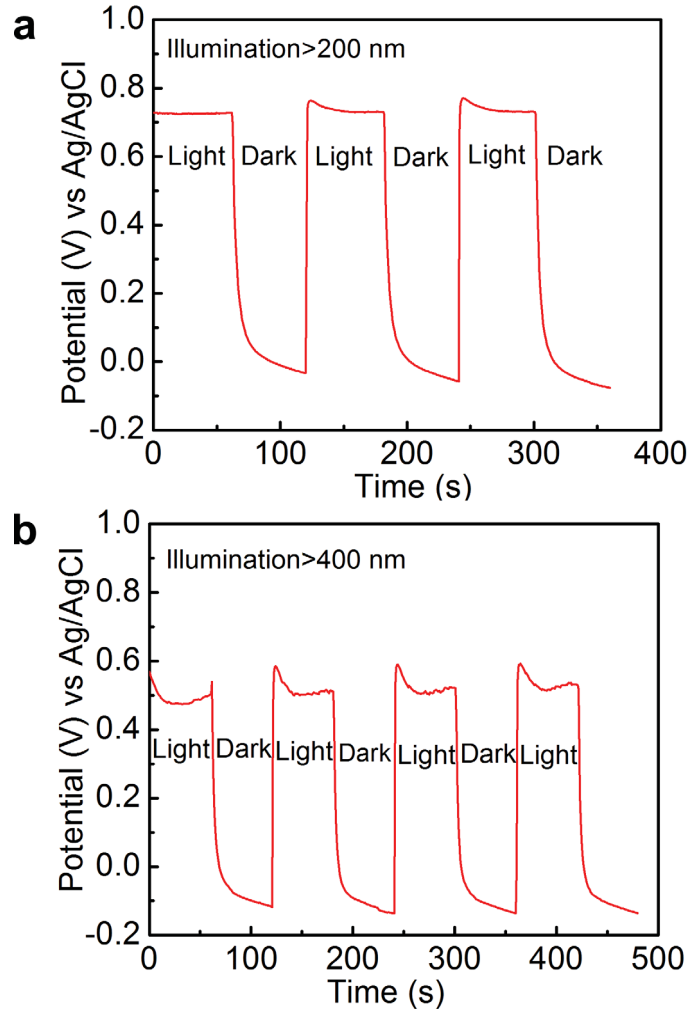


Figure 5-13: Open circuit potential (OCP) measurement on  $p$ -GaN/ $p$ -In<sub>0.20</sub>Ga<sub>0.80</sub>N nanowire arrays. (a) Under dark and full arc (>200 nm) illumination. (b) Under dark and visible light (>400 nm) illumination. The potential difference between light and dark is positive, indicating  $p$ -type behavior of GaN and In<sub>0.20</sub>Ga<sub>0.80</sub>N nanowire arrays.

upon illumination, can determine the conductivity type of the material [184]. For  $p$ -type material, the shift of the OCP upon illumination will be toward more positive potential

with respect to Ag/AgCl [120]. As shown in Fig. 5-13a, under full arc illumination the potential difference (with respect to Ag/AgCl) between light and dark is positive, indicating *p*-type behavior of GaN:Mg/In<sub>0.20</sub>Ga<sub>0.80</sub>N:Mg nanowires. In order to explore the conductivity type of In<sub>0.2</sub>Ga<sub>0.8</sub>N material, an optical long-pass filter (> 400 nm) was used to excite only the In<sub>0.2</sub>Ga<sub>0.8</sub>N segments. As shown in Fig. 5-13b, the open circuit potential upon illumination shifts to more positive potential, indicating *p*-type conductivity of the In<sub>0.2</sub>Ga<sub>0.8</sub>N:Mg material. The OCP for *p*-GaN/*p*-In<sub>0.20</sub>Ga<sub>0.80</sub>N were ~0.77 and ~ 0.62 V vs. Ag/AgCl under full arc (>200 nm) and visible light (>400 nm), respectively. Control experiments further suggest *n*-type behavior (negative difference between potentials under light and dark) of the conductivity in undoped and nominally Mg doped GaN and In<sub>0.20</sub>Ga<sub>0.80</sub>N segments (GaN:Mg:230 °C and In<sub>0.2</sub>Ga<sub>0.8</sub>N:Mg:190 °C). This is in agreement with our ARXPS analysis (Fig. 5-5), wherein the  $E_{FS}-E_{VS}$  is comparable to that of intrinsic GaN and InGaN. Because of the large background *n*-type dopants, the intrinsic GaN and InGaN shows *n*-type behavior [121], which is consistent with the observed behavior from OCP measurement. With further increase in Mg concentration in GaN and InGaN (GaN:Mg:250 °C and In<sub>0.2</sub>Ga<sub>0.8</sub>N:Mg:195 °C), weakly *p*-type characteristics is clearly observed. This further supports our ARXPS analysis that at this doping level a weakly *p*-type nanowire surface is formed (Fig. 5-5).

## 5.9 Overall Water Splitting on *p*-GaN/*p*-In<sub>0.20</sub>Ga<sub>0.80</sub>N Nanowires

With the incorporation of Rh/Cr<sub>2</sub>O<sub>3</sub> core-shell nanoparticles on the *p*-GaN/*p*-In<sub>0.20</sub>Ga<sub>0.80</sub>N nanowires, overall water splitting was performed with different long-pass filters in the absence of any sacrificial reagents under 300 W Xenon lamp irradiation. The rates of H<sub>2</sub> and O<sub>2</sub> evolution are shown in Fig. 5-14a, which are determined from ~6 h of water splitting. The H<sub>2</sub> and O<sub>2</sub> evolution rates were ~3.46 mol h<sup>-1</sup>g<sup>-1</sup> and ~1.69 mol h<sup>-1</sup>g<sup>-1</sup>, respectively, with the use of an AM1.5G filter. Visible bubbles of H<sub>2</sub> and O<sub>2</sub> were clearly observed (Fig. 5-14b) upon irradiation. The pH of water remained the same over the course of reaction, showing unambiguous evidence of balanced reaction. The photocatalytic activity decreased with increase in wavelength, limited by the optical absorption of the nanowire catalyst.

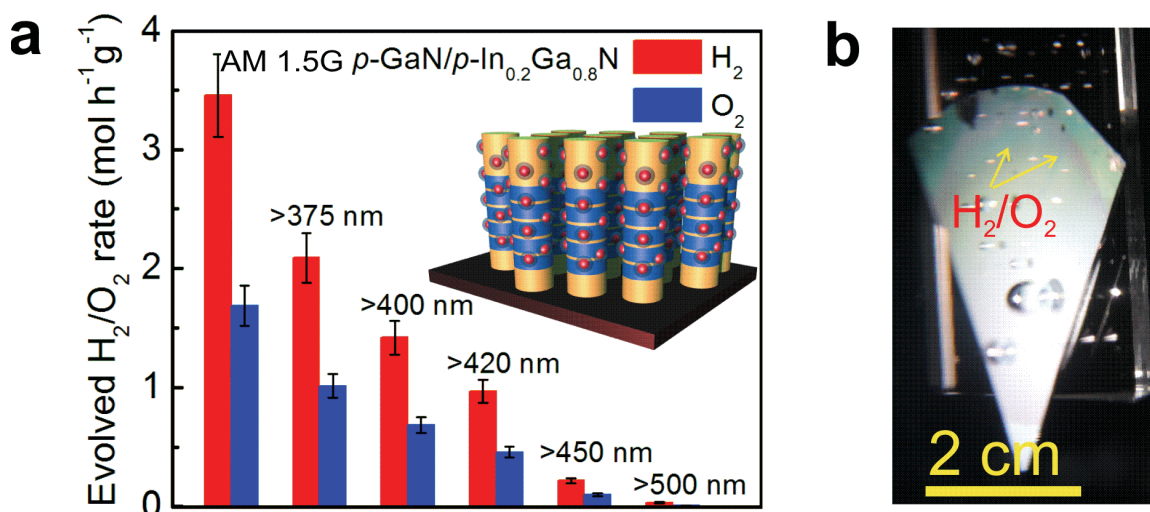


Figure 5-14: (a)  $H_2$  and  $O_2$  evolution rates in overall water splitting with AM1.5G filter, and with different long-pass filters. Visible light activity is clearly demonstrated. (b) A snapshot of  $H_2$  and  $O_2$  gas bubble formation from neutral water under full arc illumination on a  $p\text{-GaN}/p\text{-In}_{0.2}\text{Ga}_{0.8}\text{N}$  sample. A  $\sim 3 \text{ cm}^2$  sample (active  $\text{GaN}/\text{In}_{0.2}\text{Ga}_{0.8}\text{N}$  catalyst weight  $\sim 0.48 \text{ mg}$ ) was glued on a microscopic glass and immersed in neutral pH water for overall water splitting.

The APCE and AQE of the  $p\text{-GaN}/p\text{-In}_{0.2}\text{Ga}_{0.8}\text{N}$  double band nanowire photocatalyst are derived to be  $\sim 74.5\%$  and  $\sim 20\%$ , respectively (Appendix 2) in the wavelength range 200-475 nm. In the range of 400-475 nm, the APCE and AQE are estimated to be  $\sim 69\%$  and  $12.3\%$ , respectively (Appendix 2). Note that, taking into account light reflection and scattering, the APCE may be reduced by 10-15%. The achieved AQE of  $12.3\%$  at 400-475 nm of our photocatalyst is more than two times higher than the most efficient (AQE $\sim 5.9\%$  at 420-440 nm) and stable visible light active photocatalyst in overall water splitting reported to date [22]. Additionally, the energy conversion efficiency is estimated to be  $\sim 7.5\%$  under UV and visible light (incident power intensity  $\sim 488 \text{ mW cm}^{-2}$  for the wavelength range 200-475 nm) (Appendix 2), which is much higher than the recently reported values [126, 185, 186] for one-step overall water splitting and is comparable to that of wireless or wired water splitting cell comprised of integrated photovoltaic cells [31, 33]. Moreover, the solar-to-hydrogen (STH) conversion efficiency i.e. the ECE under full arc illumination with AM1.5G filter

(~26 suns) is estimated (Appendix II) to be ~1.8%, as illustrated in Fig. 5-15, which is an order of magnitude higher than that of recently reported one-step overall water splitting photocatalyst [126,185]. Although the STH conversion efficiency of *p*-GaN/*p*-In<sub>0.2</sub>Ga<sub>0.8</sub>N nanowire catalyst is lower than the recently reported ~5% STH efficiency of CoO nanoparticles [186] for overall water splitting, the stability (for over 10 hrs) of *p*-GaN/*p*-In<sub>0.2</sub>Ga<sub>0.8</sub>N nanowires is far better than that of CoO nanoparticles (deactivated after 1 hr). The turnover number (TON), in terms of the ratio of the total amount of gas (H<sub>2</sub> and O<sub>2</sub>) evolved per hour (~2.47 mmol) to the amount of *p*-GaN/*p*-In<sub>0.2</sub>Ga<sub>0.8</sub>N catalyst (~0.48 mg), exceeded ~5.15 mol h<sup>-1</sup>g<sup>-1</sup> under full arc illumination with AM1.5G filter. Under visible light (>400 nm) the TON is estimated to be ~2.0 mol h<sup>-1</sup>g<sup>-1</sup>.

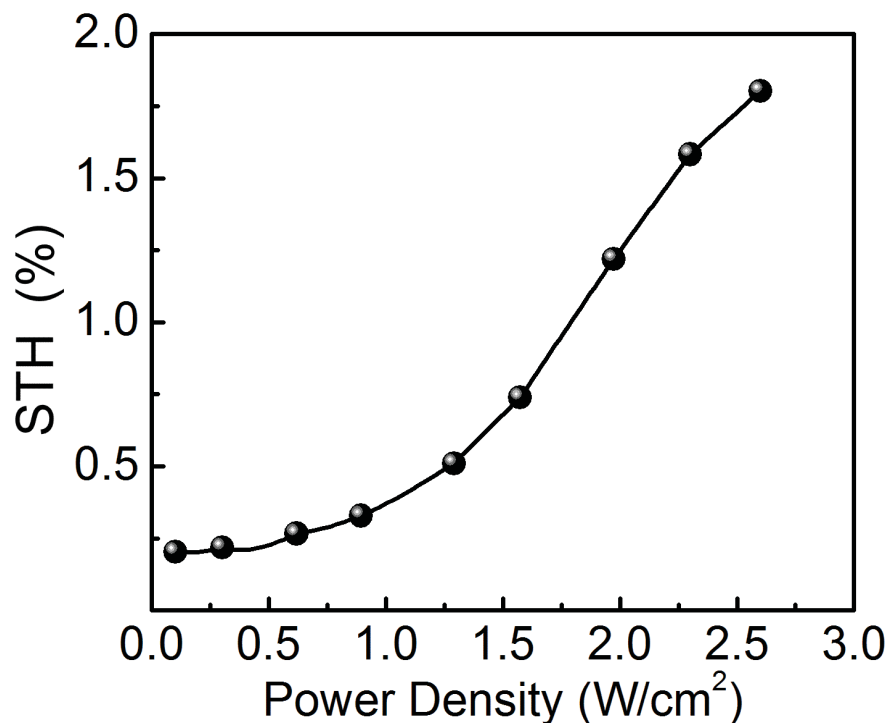


Figure 5-15: The solar-to-hydrogen (STH) conversion efficiency i.e. the energy conversion efficiency (ECE) under full arc illumination with AM1.5G filter vs. incident power density. As shown, the performance of the device significantly improves at high power densities. This can be attributed to light induced band flattening effect. The estimated STH conversion efficiency can reach 1.8% under concentrated full arc illumination (~26 suns). The solid line is a guide to the eye.

The extremely high TON can essentially overcome the barrier for large-scale practical applications of the III-nitride photocatalyst.

It is also worthwhile discussing the charge carrier separation mechanism of the present nanowire catalyst. Under nearly flat band conditions, the charge carrier separation and extraction is largely dominated by diffusion. In this study, the lateral dimensions of InGaN/GaN nanowires are in the range of 40-100 nm, which is much smaller than the diffusion lengths ( $\sim 200$ -300 nm) of photo-excited charge carriers. Our previous analysis of charge carrier transport in InGaN/GaN nanowire structures showed that  $\sim 90\%$  of the charge carriers can readily diffuse to the nanowire surface under flat band conditions [176]. Moreover, the incorporation of Rh-cocatalyst can further enhance the charge carrier separation and extraction, evidenced by a significant reduction of the PL intensity with the presence Rh on the nanowire surfaces (Fig. 5-7d).

Repeated cycles of water splitting show no degradation of the photocatalytic activity, as shown in Fig. 5-16. Figure 5-17 shows a SEM image of the  $p$ -GaN/ $p$ -In<sub>0.2</sub>Ga<sub>0.8</sub>N nanowire photocatalyst after  $\sim 6$  h of overall water splitting. The  $p$ -GaN/ $p$ -In<sub>0.2</sub>Ga<sub>0.8</sub>N nanowire and the Rh/Cr<sub>2</sub>O<sub>3</sub> co-catalysts are stable over the course of reaction. The high stability of group III-nitride, which has also been confirmed in several other studies [63, 68], is ascribed to the large difference in electronegativity between group III and group V elements [39] that can lead to the absence of surface states within the fundamental energy bandgap [130, 187]. The achievement of efficient and stable water splitting on III-nitride photocatalyst promises viable industrial production of hydrogen by artificial photosynthesis [30].

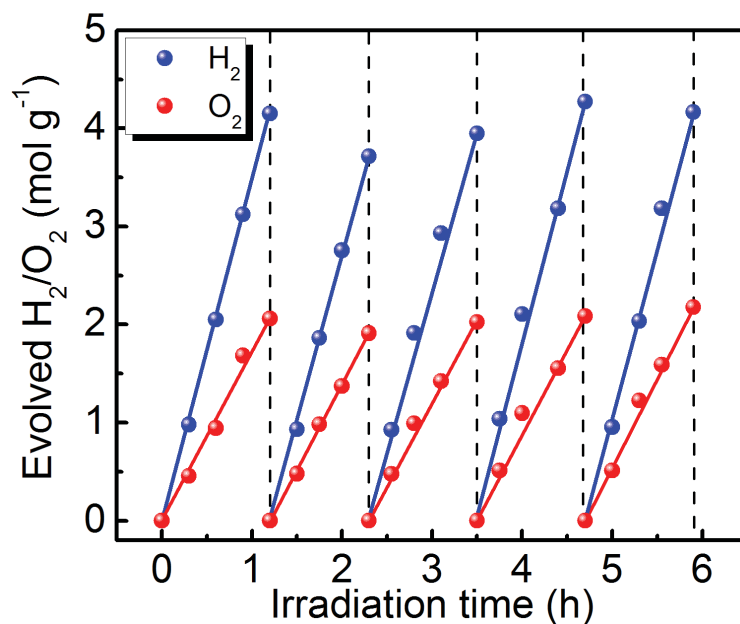


Figure 5-16: Weight normalized evolved H<sub>2</sub> and O<sub>2</sub> from overall neutral (pH~7.0) water splitting on Rh/Cr<sub>2</sub>O<sub>3</sub> core-shell nanoparticle decorated *p*-GaN/*p*-In<sub>0.20</sub>Ga<sub>0.80</sub>N nanowire arrays under full arc 300 W Xenon lamp illumination with AM1.5G filter. The reaction chamber was evacuated after each cycle. No sacrificial reagents were added with water.

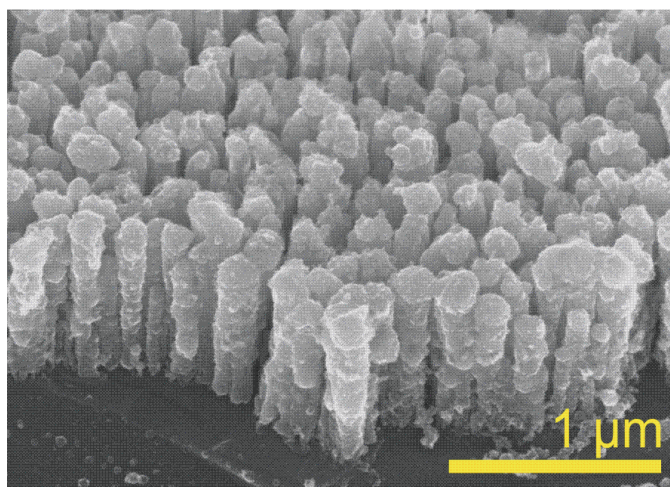


Figure 5-17: SEM image of the *p*-GaN/*p*-In<sub>0.20</sub>Ga<sub>0.8</sub>N nanowire after ~6 h of water splitting, demonstrating the stability of nanowires and Rh/Cr<sub>2</sub>O<sub>3</sub> co-catalyst.

## 5.10 Conclusions

In summary, we have shown that the concept of controlling surface band bending can be extended to InGaN nanowires by overcoming the growth challenges for achieving nearly defect-free Mg doped InGaN nanowires. We have further demonstrated visible light driven efficient and stable overall water splitting on metal-nitride nanowire arrays by minimizing the potential barrier at the nanowire surfaces through precise tuning of the surface Fermi-level. Additionally, the concept of dual-bandgap scheme has been unambiguously demonstrated to enhance the efficiency. Rhodium (Rh)/chromium-oxide ( $\text{Cr}_2\text{O}_3$ ) core-shell nanoparticle decorated *p*-type  $\text{In}_{0.2}\text{Ga}_{0.8}\text{N}$  nanowire arrays show an absorbed photon conversion efficiency of  $\sim 69\%$  for neutral ( $\text{pH}\sim 7.0$ ) water splitting. Moreover, using a double-band *p*-GaN/*p*- $\text{In}_{0.2}\text{Ga}_{0.8}\text{N}$  nanowire heterostructure, we show that the STH conversion efficiency can reach  $\sim 1.8\%$  in the UV and visible spectrum (up to  $\sim 475$  nm). The energy conversion efficiency can further be improved by utilizing multi-band InGaN nanowire photocatalysts with high (up to  $\sim 50\%$ ) indium compositions to enable spontaneous overall water splitting under deep visible and near-infrared light irradiation. However, a number of growth related issues need to be addressed, including indium phase separation, indium surface segregation, and the formation of misfit dislocations due to the large lattice mismatch ( $\sim 11\%$ ) between InN and GaN. The stability and efficiency of this recyclable, wafer-level nanoscale metal-nitride photocatalysts in neutral water promises their potential use for large-scale solar-fuel conversion.

# Chapter-6

## Defect-Engineered GaN:Mg Nanowire Arrays for Overall Water Splitting under Violet Light

### 6.1 Introduction

Metal-oxide based photocatalysts are extensively studied over the last four decades due to their stability, thermodynamic and kinetic potentials for overall water splitting [9]. However, owing to the large band gap of metal-oxides, efficient utilization of solar energy is quite challenging. Therefore, different strategies have been developed to reduce the band-gap of metal-oxides, including the introduction of transition-metal cation with partially filled d orbital (i.e.,  $d^n$ ,  $0 < n < 10$ ) [188] and/or an anion (e.g.,  $C^{4-}$ ,  $N^{3-}$ ,  $S^{2-}$ ) dopants [189, 190], continuous modulation of valence and/or conduction band (oxide, oxysulfide, oxynitride) for efficient harvesting of solar energy [15, 32]. However, most of these strategies are limited to one-half of the redox reaction, i.e., oxidation or reduction. On the other hand, metal-nitrides have a unique combination of thermodynamic and kinetic potential requirements, extreme chemical stability, and band-gap tunability for efficient overall water splitting, utilizing nearly the entire solar spectrum [38, 117].

Here, we have developed fundamentally a different approach for increasing the solar absorption of GaN nanowire arrays by engineering the defects within the fundamental bandgap. We have precisely controlled the Mg dopants in GaN nanowires to introduce donor and acceptor energy states below and above the conduction and valence band, respectively of GaN nanowires. Low-temperature photoluminescence and micro-Raman studies revealed the formation of Mg related acceptor states and nitrogen-vacancy ( $V_N$ ) induced donors states inside the band-gap. Subsequently, photochemical studies with different intra-gap excitation confirm that the bandgap of GaN nanowires can be perturbed for overall neutral water splitting under violet light (upto 450 nm).

## 6.2 Growth, Structural and Optical Characterization

The growth of Mg doped GaN nanowires are discussed in Chapter-3. Prior to growth, a monolayer of Ga seeding layer is used for growth initiation, which results in vertically aligned GaN nanowires along the c-axis with their sidewalls being nonpolar surfaces. These nonpolar surfaces are reported to be energetically stable with unreconstructed and relaxed surface geometries [191]. The Mg effusion cell temperature ( $T_{Mg}$ ) was varied during the growth from 190 to 315 °C, which corresponds to Mg beam-equivalent pressure (BEP) of  $\sim 1 \times 10^{-11}$  to  $\sim 1.5 \times 10^{-9}$  Torr. The growth temperature and duration for GaN nanowire were  $\sim 750$  °C and 4 hrs, respectively. For a particular sample the  $T_{Mg}$  is step-wise increased to avoid nanowire coalescence. The secondary electron mass spectroscopy (SIMS) reveals Mg concentration of  $\sim 1.3 \times 10^{20}$  cm $^{-3}$  from Mg doped ( $T_{Mg}=250$  °C) GaN epilayer.

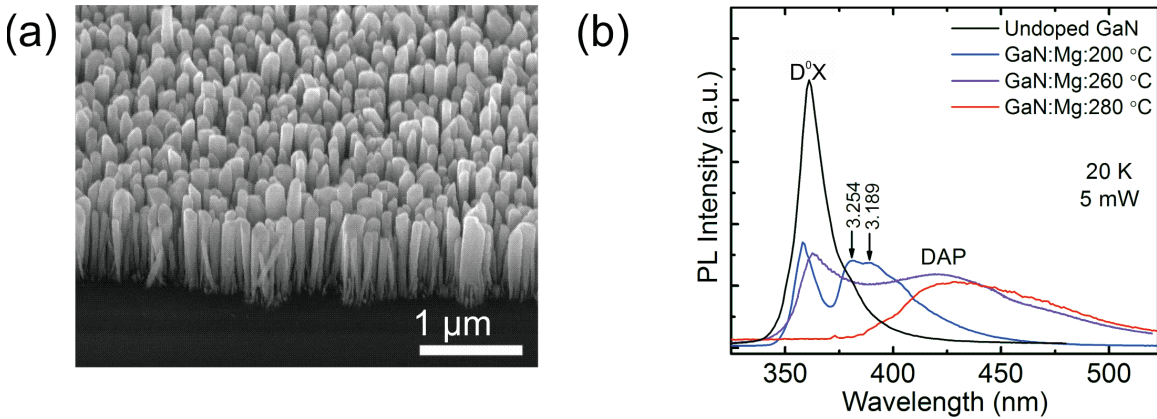


Figure 6-1: (a) A 45° tilted high resolution scanning electron microscopy image of as grown GaN:Mg:260 °C sample. (b) Low temperature (20 K) PL spectrum of GaN:Mg samples in comparison to undoped GaN sample.

Figure 6-1a shows a 45° tilted high resolution SEM image of as-grown Mg doped ( $T_{Mg}=260$  °C) GaN (denoted as GaN:Mg:260 °C hereafter) nanowire arrays. The nanowires are vertically aligned to the substrate, with an average height of  $\sim 600$  nm, and diameter of  $\sim 40$ -100 nm. Mg doping in GaN nanowire promotes lateral growth owing to increased probability of Ga atom incorporation in nonpolar surfaces; therefore the

GaN:Mg nanowire density is higher than the undoped GaN nanowires [96]. To reveal the optical properties of the GaN:Mg nanowires, a 266 nm diode-pumped solid state Q-switched laser is utilized. Figure 6-1b shows the low-temperature (20 K) photoluminescence (PL) spectra of as-grown GaN:Mg nanowires compared to an unintentional doped GaN nanowire sample. The unintentional doped GaN PL is dominated by a single peak at  $\sim 3.435$  eV, corresponding to donor-bound exciton ( $D^0X$ ). For the lightly Mg doped ( $T_{Mg}=200$  °C) sample, in addition to the  $D^0X$ , two additional peaks are clearly resolved at 3.254 eV and 3.189 eV. The energy difference between these peaks is  $\sim 65$  meV, inconsistent with longitudinal-optical (LO) phonon energy of GaN ( $\sim 92$  meV); ruling out the possibility of the 3.189 eV line being the first phonon replica of the 3.254 eV line [192]. The 3.254 eV emission is attributed to the conduction band to Mg-related acceptor level (e-A) transition.

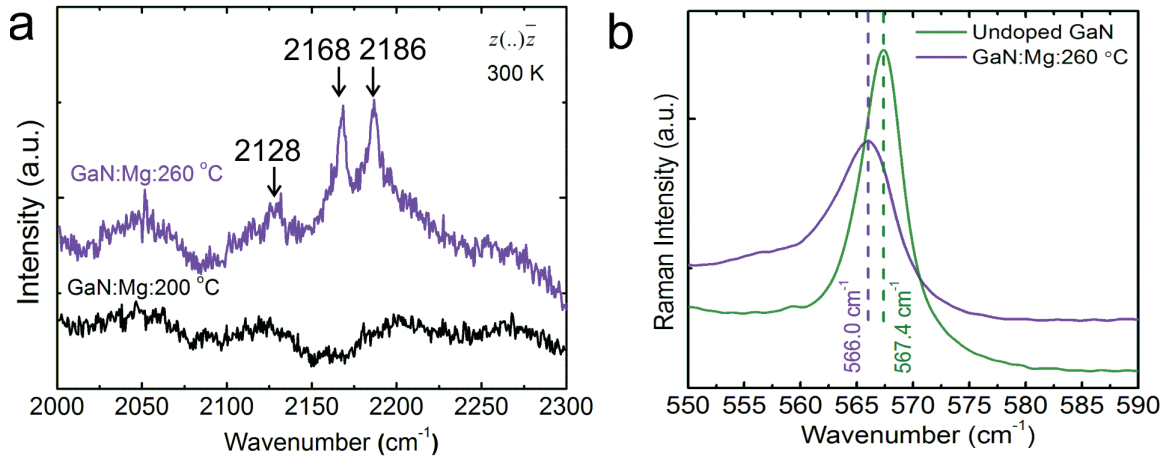


Figure 6-2: (a) Micro-Raman spectra of GaN:Mg:260 °C and GaN:Mg:200 °C nanowires. The curves are vertically shifted for clarity. (b)  $E_2$  Raman line from GaN:Mg:260 °C and undoped GaN nanowires.

Assuming a bandgap of GaN at low temperature of 3.478 eV, a Mg-related acceptor level of  $\sim 220$  meV is deduced, which is very close to the reported values [192]. The 3.167 eV line is most likely due to the Mg related defects in GaN, which make complexes with Mg acceptor levels [192, 193].

With further increase in Mg flux ( $T_{Mg}=260\text{ }^{\circ}\text{C}$ ), a new broad emission peak centered at  $\sim 2.95\text{ eV}$  is clearly revealed. This peak is attributed to the donor-acceptor-pair (DAP) transition [194] between the  $V_N$  related deep donor states and shallow Mg acceptor states. The Mg-related acceptor level is located at  $\sim 220\text{ meV}$  above the valence band. On the other hand, the formation energy of  $V_N$  is reported to be in the range of  $160\text{ meV}$  to  $250\text{ meV}$  [195]. With increase in  $T_{Mg}$ , Mg incorporation in GaN nanowire can be increased as confirmed from SIMS analysis[196]. Our recent angle resolved X-ray photoelectron spectroscopy analysis suggests that the  $E_F-E_V$  decreases with increase in  $T_{Mg}$ . As predicted by Van de Walle [197], the formation energy of 3+ charge state of  $V_N$  decreases with  $E_F-E_V$ . This suggests that  $V_N$  related donor type native defect is most likely present in GaN at high Mg doping level, and acts as compensating centers in  $p$ -type GaN [151]. Despite the N-rich (III/V < 1) growth condition, the  $V_N$  related defects can be formed along the growth direction due to higher diffusion lengths of Ga compared to N adatoms on the nonpolar surfaces which forms the nanowire sidewall [102]. Additionally, the presence of Mg may limit the availability of active nitrogen on the nanowire sidewalls. The presence of  $V_N$  in heavily Mg doped GaN nanowire is indeed revealed from micro-Raman analysis. As shown in Fig. 6-2a, micro-Raman measurement clearly shows three distinct modes in the high energy region at  $2139\text{ cm}^{-1}$ ,  $2166\text{ cm}^{-1}$  and  $2186\text{ cm}^{-1}$  from GaN nanowire sample with  $T_{Mg}=260\text{ }^{\circ}\text{C}$  [198, 199]. These spectroscopic features can be attributed to the Mg-induced local vibrational modes (LVM) associated with  $V_N$  [199]. For comparison, no Raman modes are observed from the low Mg doped ( $T_{Mg}=200\text{ }^{\circ}\text{C}$ ) GaN nanowires. Furthermore, as shown in Fig. 6-2b the  $E_2$  Raman line at  $576.4\text{ cm}^{-1}$  for GaN:Mg:200  $^{\circ}\text{C}$  sample is very close to that of undoped GaN nanowires as reported by Furtmayr *et al* [97]. The decrease in  $E_2$  peak to  $566\text{ cm}^{-1}$  for GaN:Mg:260  $^{\circ}\text{C}$  reveals the increased tensile strain in GaN nanowires at higher Mg doping levels. This increased tensile strain further identified as a fingerprint of the formation of  $V_N$  in

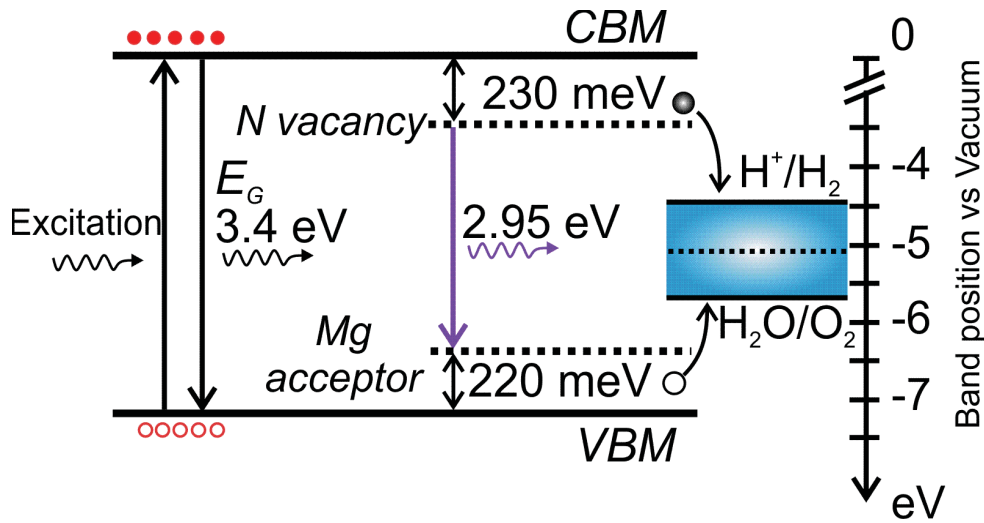


Figure 6-3: Schematic energy band diagram of GaN:Mg:260 °C nanowires illustrating the formation of  $V_N$  and Mg related intra-gap states along with the redox potential of water (vs vacuum level).

GaN:Mg nanowires [151]. The degradation in the crystal quality of the GaN:Mg nanowires is further confirmed from the increment of full-width-at-half-maximum (FWHM) of the  $E_2$  Raman line [196]. At very high Mg flux ( $T_{Mg}=280$  °C), the DAP emission red-shifts with progressive disappearance of the band-edge emission. This is attributed to the emergence of high density of deep energy states and deterioration of crystalline quality caused by the incorporation of high density of Mg, consistent with the luminescence of MBE and MOCVD grown GaN films [194, 200]. Based on the above analysis, a schematic energy level diagram is shown in Fig. 6-3, along with the redox potential of water (vs vacuum level). The Mg-related acceptor level is located at  $\sim 220$  meV above the valence band. The  $V_N$  level is located at  $\sim 230$  meV below the conduction band. Therefore, the intra-gap defect related energy states straddle the redox potential of water with  $\sim 0.7$  eV and  $\sim 1.00$  eV overpotentials for water oxidation and reduction, respectively.

In order to test the photocatalytic activity of the GaN:Mg nanowire photocatalyst through intra-gap photon absorption,  $H_2$  and  $O_2$  half-reactions were individually

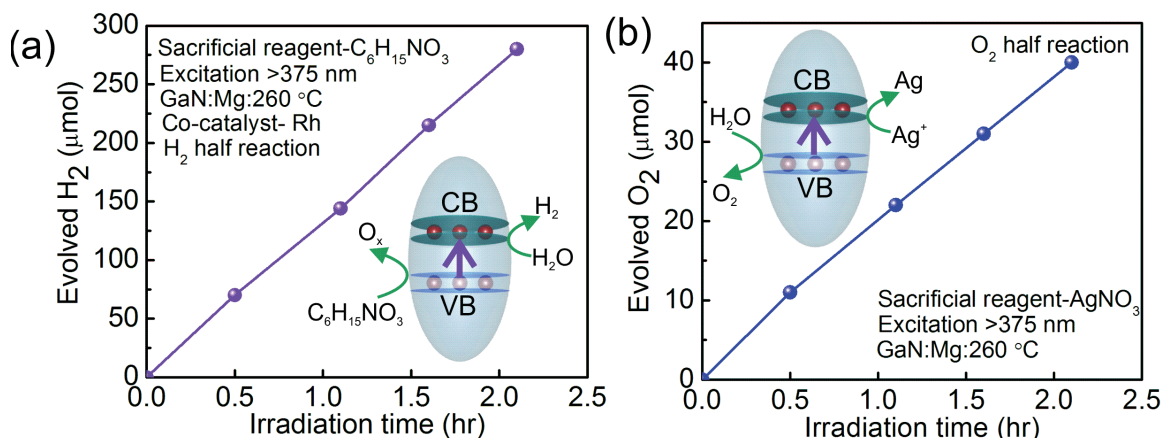


Figure 6-4: (a) Evolution of H<sub>2</sub> from GaN:Mg:260 °C nanowire in presence of C<sub>6</sub>H<sub>15</sub>NO<sub>3</sub> hole scavenger and Rh co-catalyst. (b) Evolution of O<sub>2</sub> from GaN:Mg:260 °C nanowire in presence of AgNO<sub>3</sub> as electron acceptor.

performed in presence of respective sacrificial reagents using different long-pass filters under a 300 W Xenon lamp. A ~3 cm<sup>2</sup> wafer sample is used which corresponds to ~0.42 mg GaN material, considering the fill factor of the nanowires on the silicon substrate. Triethanolamine (C<sub>6</sub>H<sub>15</sub>NO<sub>3</sub>) hole scavenger and Rh co-catalyst is used to conduct H<sub>2</sub> half-reaction. In case of O<sub>2</sub> half-reaction, AgNO<sub>3</sub> is used as electron acceptor. Fig. 6-4a and 6-4b show the evolution of H<sub>2</sub> and O<sub>2</sub> from respective half-reactions with intra-gap excitation >375 nm of the GaN:Mg ( $T_{Mg}=260$  °C) sample. The evolution of H<sub>2</sub> and O<sub>2</sub> reveals that the intra-gap states satisfy the thermodynamic and kinetic potentials for water photolysis. The reduced activity of water oxidation can be directly correlated to the presence of potential barrier caused by the downward band-bending at this doping level [201]. In a nanoscale photocatalyst wherein the carrier extraction efficiency is no longer diffusion limited, the charge carrier transport toward the semiconductor-water interface is mostly determined by the near-surface band structure. As discussed in Chapter-3, the near-surface band structure of GaN nanowires can be precisely tuned with optimum Mg dopant incorporation to achieve a flat-band condition of the GaN:Mg nanowires at equilibrium with water. This allows efficient carrier extraction from the nanowire photocatalyst for efficient and stable overall water splitting. The photocatalytic activity of

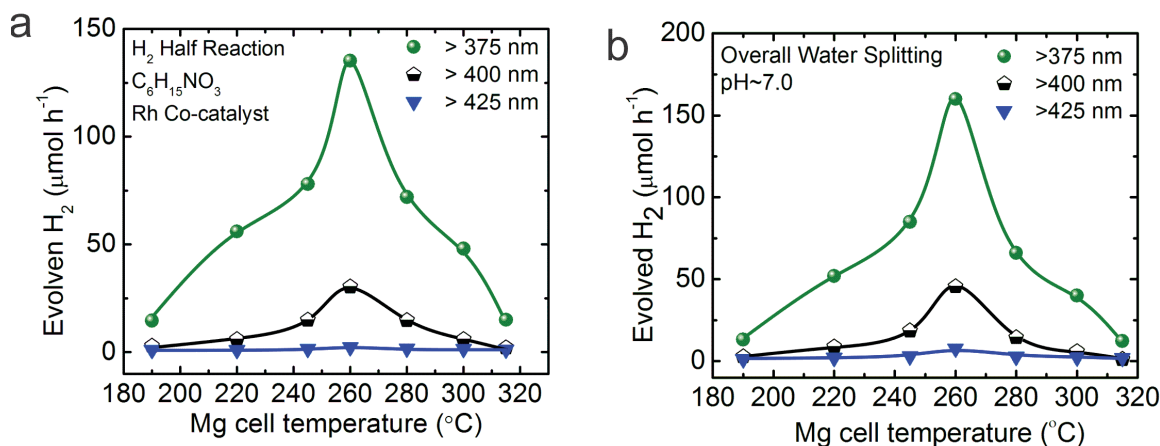


Figure 6-5: (a) Evolution of H<sub>2</sub> from GaN:Mg nanowire samples in presence of C<sub>6</sub>H<sub>15</sub>NO<sub>3</sub> hole scavenger and Rh co-catalyst with different intra-gap excitation using 300 W Xenon lamp. (b) Evolution of H<sub>2</sub> from overall neutral water splitting from the GaN:Mg samples with different intra-gap excitation using 300 W Xenon lamp.

all the GaN:Mg samples were further tested in presence of C<sub>6</sub>H<sub>15</sub>NO<sub>3</sub> hole scavenger and Rh co-catalyst, as shown in Fig. 6-5a. The photocatalytic activity increased with  $T_{\text{Mg}}$  upto  $T_{\text{Mg}}=260$   $^{\circ}\text{C}$ , after that the activity decreased. The H<sub>2</sub> evolution rates are  $\sim 135$ ,  $\sim 30$  and  $\sim 2$   $\mu\text{mol/hr}$  with excitation  $>375$ ,  $>400$  and  $>425$  nm, respectively, for the GaN:Mg:260  $^{\circ}\text{C}$  sample. No activity is observed with excitation  $>450$  nm for all the samples. This further confirms that the Si substrate does not take part in the photocatalytic reaction.

### 6.3 Overall Water Splitting under Violet Light

The GaN:Mg nanowire samples were subsequently used for overall neutral water splitting. For efficient separation and extraction of the photogenerated carriers, Rh/Cr<sub>2</sub>O<sub>3</sub> core/shell co-catalyst nanoparticles were photodeposited on the GaN:Mg nanowires from liquid precursor as discussed in previous chapters. Fig. 6-5b shows the H<sub>2</sub> evolution rate in overall neutral water splitting for GaN:Mg samples with different intra-gap excitation. No sacrificial reagent is added with water. The rate of H<sub>2</sub> evolution is estimated from 4 hrs of overall water splitting under 300 W Xenon lamp irradiation.

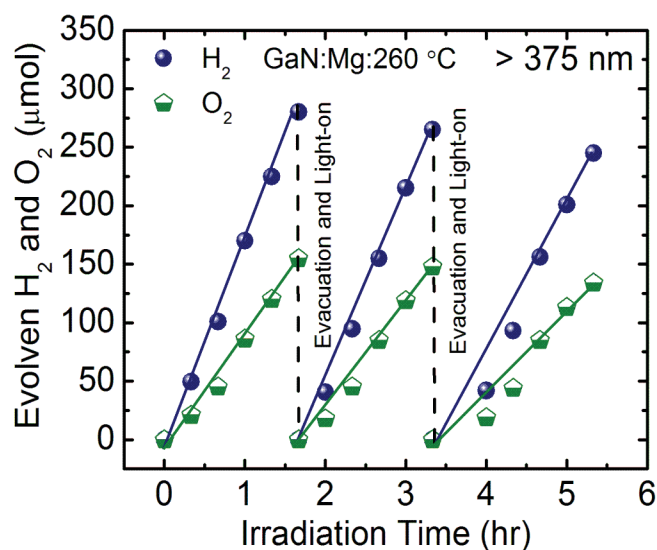


Figure 6-6: Repeated cycles of overall neutral water splitting for GaN:Mg: 260 °C sample showing the stability of the intra-gap states.

The undoped GaN nanowire did not show any activity with intra-gap excitation. On the other hand the activity of GaN:Mg samples increased with  $T_{Mg}$  upto 260 °C, after that the activity decreased, following the same trend as the H<sub>2</sub> half reaction (Fig. 6-5a). The H<sub>2</sub> evolution rates are ~160, ~45 and ~5 μmol/hr with excitation >375, >400 and >425 nm, respectively, for the  $T_{Mg}$ =260 °C sample. The photocatalytic activity decreased with increase in wavelength, limited by the intra-gap optical absorption of the nanowire catalyst. Significant activity was observed for excitation up to 450 nm, which is consistent with the intra-gap broad emission spectrum of GaN:Mg nanowires.

Figure 6-6 shows repeated cycles of overall neutral water splitting for GaN:Mg:260 °C sample without the presence of any sacrificial reagents. The H<sub>2</sub> and O<sub>2</sub> evolution in nearly 2:1 ratio confirms stoichiometric evolution of H<sub>2</sub> and O<sub>2</sub> for overall water splitting. The repeated cycles further confirm the stability of the intra-gap states of GaN:Mg nanowire photocatalyst. Upon intra-gap excitation, electron and hole can generate in the intra-gap states. In a semiconductor with high concentration of defect states, carrier hopping conduction via the defect band/states becomes an important process for electrons and holes to transport towards the semiconductor-liquid interface. This can occur either

via the formation of extended states by the overlapping of defect states or by hopping between localized defect states. Such hopping conduction or impurity band conduction has been observed previously for Mg doped GaN, AlGaN and other materials. As the lateral dimension (40-100 nm) of the GaN:Mg nanowires is much smaller than the diffusion lengths (200-300 nm) of the photoexcited charge carriers, carrier transport through the impurity band, formed by either Mg dopant or nitrogen vacancies, can lead to efficient charge carrier transfer towards the nanowire/water reaction interface. This can occur either via the formation of extended states by the overlapping of defect states or by hopping between localized defect states [202]. The electron and hole can therefore transport through the defect band toward the nanowire-water interface. The enhanced activity of the GaN:Mg:260 °C sample is attributed to enhanced intra-gap absorption as well as significantly reduced downward band bending [201]. The decreasing trend of the photocatalytic activity at very high Mg-flux ( $T_{\text{Mg}} = 280$  °C and above) is attributed to the degradation of crystalline quality of the GaN nanowires; resulting in non-radiative recombination of the photogenerated carriers. Additionally, the reduced activity at very high Mg-flux ( $T_{\text{Mg}} = 280$  °C and above) may be partly related to self-compensation effect by the nitrogen vacancies, as observed in previous studies.

The absorbed photon conversion efficiency (APCE) of GaN:Mg:260 °C is estimated to be ~43%, ~44% and ~35% for excitation >375 nm, >400 nm and >425 nm, respectively, considering the absorption coefficient of GaN:Mg and the nanowire fill factor on Si substrate (Appendix II). The respective energy conversion efficiency is estimated to be ~1.34%, ~0.56% and ~0.12%, considering the energy of all the incident photons with wavelengths between 375-450 nm, 400-450 nm, and 425-450 nm, respectively (Appendix II). The turnover number in terms of the amount of gas ( $\text{H}_2$  and  $\text{O}_2$ ) evolved per hour to the amount of photocatalyst exceed ~570  $\text{mmol h}^{-1}\text{g}^{-1}$ , ~160  $\text{mmol h}^{-1}\text{g}^{-1}$ , and ~17  $\text{mmol h}^{-1}\text{g}^{-1}$  for excitation >375 nm, >400 nm and >425 nm, respectively. As demonstrated in Chapter-3, the GaN:Mg nanowire showed excellent stability in neutral pH water, which is attributed to the formation of *p*-type GaN with significantly reduced surface band bending. This suppresses carrier recombination and hence accelerates the extraction of the photogenerated e-h pairs for efficient and stable

overall water splitting. The stability may further be attributed to the charge balance between the donor and acceptor states formed due to Mg doping [19]. The stable and overall splitting of pH neutral water may function as an ideal material platform to study the fundamentals of redox reaction kinetics.

## **6.4 Conclusions**

In summary, we show that by engineering the intra-gap defect related energy states in GaN nanowire arrays, efficient and stable overall neutral water splitting can be achieved under violet light. With controlled p-type Mg dopant incorporation in GaN nanowire arrays, the fundamental bandgap of GaN nanowires can be perturbed to absorb violet light (upto 450 nm), while straddling the redox potential for overall water splitting. Thermodynamic and kinetic potentials of the intra-gap states are revealed via independently performing the oxidation and reduction reaction of water. Stable and efficient overall water splitting is further demonstrated with intra-gap excitation upto 450 nm. This defect-band engineering can further be used to enhance solar absorption of Mg doped InGaN towards red or near-infrared photons while maintaining the excellent stability, thermodynamic and kinetic potentials of III-nitride for efficient solar water splitting.

# Chapter-7

## Strategies for Achieving Photochemical Overall Water Splitting under Red Light Irradiation

### 7.1 Introduction

Recent theoretical studies have shown that the conduction and valence band edge of InGaN can straddle the water oxidation and hydrogen reduction potentials for In compositions up to  $\sim 50\%$ , which suggests that photochemical overall water splitting can be possibly realized under red and near-infrared light irradiation [41]. We have also shown in Chapter-4 that overall pure water splitting can be achieved under UV, blue and green light irradiation (upto 560 nm) using multiband InGaN/GaN nanowire heterostructures. However, the apparent quantum efficiency is significantly low at longer wavelengths (only 0.3% at 550 nm), which is attributed to limited light absorption and carrier recombination in the nanowire arrays. Therefore, the efficiency needs to be improved and the absorption edge needs to be extended towards longer wavelengths for efficient harnessing of the solar spectrum. In order to extend the light absorption of InGaN nanowires, the band gap needs to be reduced with further increment of In incorporation. However, the growth of high crystalline quality InGaN with high In content has been extremely challenging for a number of reasons [40, 203-208]. For instance, the large lattice mismatch (11%) between InN and GaN results in solid phase miscibility gap, and the high vapor pressure of In over Ga leads to low In incorporation in InGaN. Additionally, the difference in formation enthalpies for InN and GaN causes strong In surface segregation, which creates In rich clusters with high density of defects [58]. Therefore, non-radiative recombination of the photogenerated carriers significantly limits the device performance [209]. Furthermore, TEM study on InGaN/GaN quantum wells reveals the presence of misfit dislocations in InGaN, when InGaN is grown beyond a critical thickness [177, 210]. This critical thickness exponentially drops with increase in

In content. Therefore, high quality and high In content InGaN with sufficient thickness for efficient solar absorption is quite challenging [211]. Significant research efforts have been made to enhance the In incorporation in InGaN which can function as an ideal material system to achieve high efficiency water splitting by utilizing the entire solar spectrum. In this context we have proposed and developed different strategies to address the above mentioned challenges, as discussed in the following sections.

## 7.2 Development of InGaN Disk-on-wire Nanowire Heterostructures

We have developed hexagonal shaped InGaN nanodisks on GaN nanowire to capture red photons from solar spectrum. We begin the growth of such nanowires by depositing a few monolayers of Ga on the Si (111) substrate to function as the nucleation site for the nanowire growth. The foreign catalyst-free nanowire growth was initiated with the GaN nanowire which is grown for 90 mins under nitrogen rich condition at 770 °C. Our previous studies show that such GaN nanowire template allows the controlled formation of InGaN with excellent electrical and optical properties [156]. The substrate temperature is then reduced to 605 °C to prepare for the growth of InGaN nanowire. Subsequently 10 InGaN/GaN multiple-quantum wells (MQW) each grown for 6 mins (3 mins for InGaN, 3 mins for GaN) were incorporated along the axial dimension, as schematically illustrated in Fig. 7-1a. Such MQW is chosen over the continuous growth of InGaN in order to avoid the formation of misfit dislocations caused by the accumulation of strain along the growth axis [212]. The InGaN MQW is doped with Mg at optimized Mg cell temperature of 200 °C as discussed in Chapter-5, and the GaN barrier layer was left undoped. Figure 7-1b shows a SEM image of the as-grown InGaN/GaN nanowires on Si substrate. This SEM image clearly demonstrates the formation a hexagonal shaped nanodisks on vertically aligned nanowire arrays. Room temperature photoluminescence (PL) further reveals two emission peaks at 590 nm and 640 nm as shown in Fig. 7-1c, which corresponds to an average In composition of 36-41%. The broad emission peak further indicates inter- and intra-nanowire In fluctuations. Figure 7-1d shows a low magnification TEM image of a single disk-on-wire nanowire. The nanowire is nearly 600 nm long with ~100 nm diameter. The nanodisk is about 20-25 nm thick. Figure 7-1e

shows a HRTEM image of the hexagonal shaped nanodisk. The six facets corresponds to the nonpolar m-plane of wurtzite crystal. Detailed energy dispersive X-ray analysis reveals that the nanodisk consists of In rich InGaN, and the vertically aligned nanowire consists of only GaN. Additionally, the In composition in the nanodisk increases from the circumference towards the center. This indicates that an In rich nanowire top may have formed during the growth, which facilitated the formation of such unique hexagonal shaped InGaN nanodisk. The absence of In in the vertically aligned nanowire is attributed to enhanced In adatom migration along the nanowire sidewalls toward the nanowire top. The presence of metal rich nanowire top at low growth temperature leads to two dimensional (2D) growth due to higher cohesive bond between the metal adatoms [213].

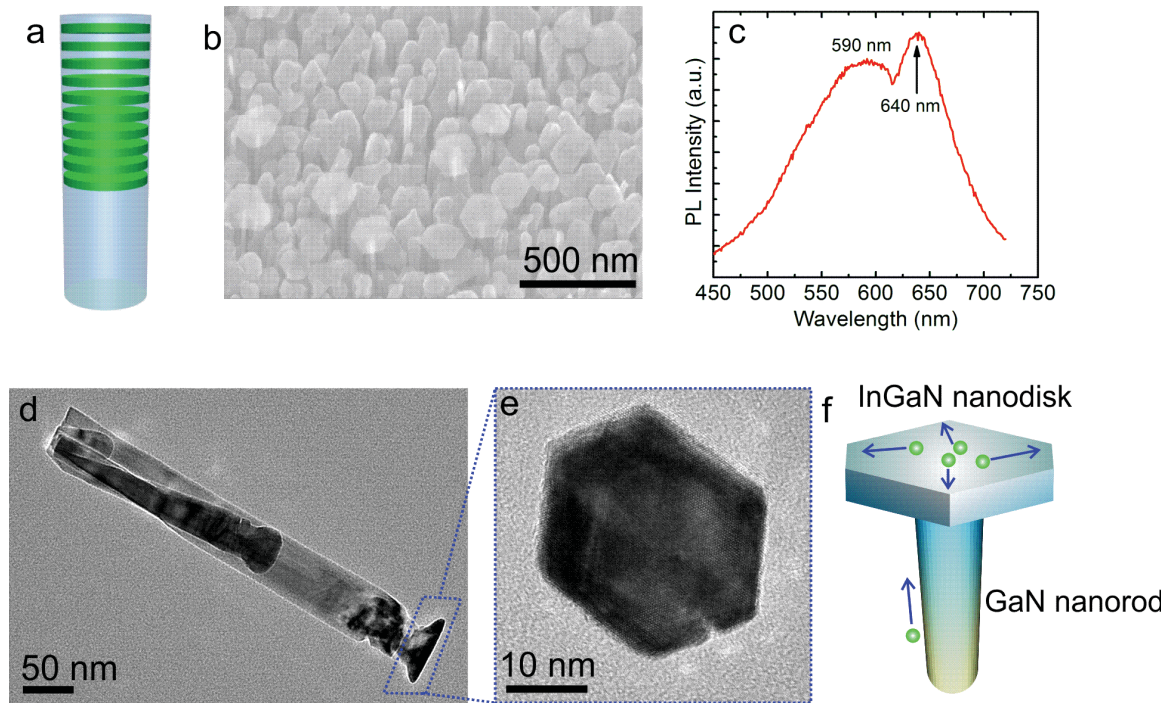


Figure 7-1: (a) Schematic of the InGaN/GaN nanowire heterostructure, (b) SEM image of the as-grown InGaN/GaN disk-on-wire nanostructure, (c) room temperature PL from the as-grown InGaN/GaN disk-on-wire nanostructure, (d) TEM image of a single nanowire showing the formation of InGaN nanodisk on GaN nanowire, (e) HRTEM image of hexagonal shaped InGaN nanodisk, and (f) formation mechanism of InGaN nanodisk on a GaN nanowire.

The formation of hexagonal nanodisk indicates preferential nucleation at the m-plane rather than the nucleation at the c-plane. This can further be attributed to the strain relaxation by lateral crystal expansion. This enhanced lateral growth is due to the low substrate temperature, which suppresses the adatom diffusion along the c-axis. Therefore, a metal-rich layer is formed at the nanowire top, which subsequently grows along the lateral direction to form hexagonal shaped InGaN nanodisks. Figure 7-1f schematically illustrates the formation mechanism of InGaN hexagonal nanodisks on vertically aligned GaN nanowires. This In rich (~40%) hexagonal InGaN nanodisks can be a potential material platform to study the thermodynamic and kinetic potentials of III-nitrides for water splitting under red light. Since the carrier diffusion length is much higher than the dimension of the InGaN nanodisks, the photogenerated carriers can easily diffuse toward the semiconductor-water interface for the redox reaction of water.

In this context, we have done preliminary studies on such unique InGaN nanostructures for water splitting under red light. In order to test the photocatalytic activity for overall water splitting, Rh/Cr<sub>2</sub>O<sub>3</sub> core/shell nanoparticles were photodeposited onto the disk-on-wire nanostructure following the procedure as discussed in Chapter-2. Subsequently, the overall water splitting was performed using a 300 W Xenon lamp under full arc and with different long pass filters to reveal the activity at different wavelengths. While the samples showed high photoactivity (~400 μmol/hr H<sub>2</sub>) under UV light, the visible light (>425 nm) activity was below the detection limit. Despite the fact that the PL results show red light emission due to high In incorporation, the absence of photocatalytic activity under visible light may indicate the following facts. First, light absorption may be significantly limited by the thin (~20-25 nm) InGaN nanodisks and low absorption co-efficient of InGaN at longer wavelengths. Therefore, a small fraction of the low-energy incident photons can be absorbed by the InGaN nanodisks to generate electron-hole pairs. Secondly, the diffusion of the photogenerated carriers toward the nanodisk-water interface may be limited by the local In rich region at the center of the nanodisk. Because of the low In incorporation at the circumference of the nanodisks, a GaN barrier layer may have formed, which may suppress carrier extraction from the nanodisks. To confirm this hypothesis, the InGaN nanodisks-on-GaN

nanowire sample was wet etched by AZ400K (potassium borate) developer solution. The AZ400K developer is commonly used for removing photoresist. The AZ400K is a buffered developer that hydrolyzes in water and forms a mild alkaline solution. The etching recipe used here is AZ400K: DI water at 1:50 ratio at 60° C. The etching time is optimized by analyzing core-level *In 3d* peak from X-ray photoelectron spectroscopy (XPS) before and after etching for different duration. The optimized etched time is found to be 40 mins, wherein the highest intensity *In 3d* peak is observed from XPS analysis. Subsequently, Rh/Cr<sub>2</sub>O<sub>3</sub> core/shell nanoparticles were photodeposited onto the just etched InGaN disk-on-GaN nanowire samples. Finally, Overall water splitting on this sample under visible light (>425 nm) reveals very low (~2 μmol/hr H<sub>2</sub>) photocatalytic activity. This slightly improved activity of etched samples compared to un-etched samples confirm our hypothesis that a GaN barrier layer is formed along the circumference of the hexagonal InGaN nanodisks which suppresses the carrier extraction efficiency. Therefore, optimization of nanowire heterostructure design and growth recipe i.e., growth temperature, doping concentration, growth duration is required to further improve the photocatalytic activity under red light.

### **7.3 InGaN Nanostructures on SiO<sub>x</sub>/Si Nanowires**

In this approach we have developed unique InGaN nanostructures on SiO<sub>x</sub>/Si nanowires in order to increase the effective surface area for efficient water splitting, while avoiding the inherent growth issues to form high quality and sufficiently long InGaN nanowire with high In content. Since the growth of sufficiently long InGaN nanowire is quite challenging, we have limited the growth duration to 30 mins for InGaN. Simultaneously, to enhance the effective surface area, we have fabricated Si nanowire template to grow the InGaN nanostructure. Such small InGaN structures will have extremely high surface to volume ratio as compared to InGaN nanowire. The carrier extraction efficiency will therefore be significantly improved for efficient water splitting. The formation of Si nanowire involves multistep processing of the Si substrate and optimization of the recipe. Optimization of the recipe i.e., Ni thickness, rapid thermal

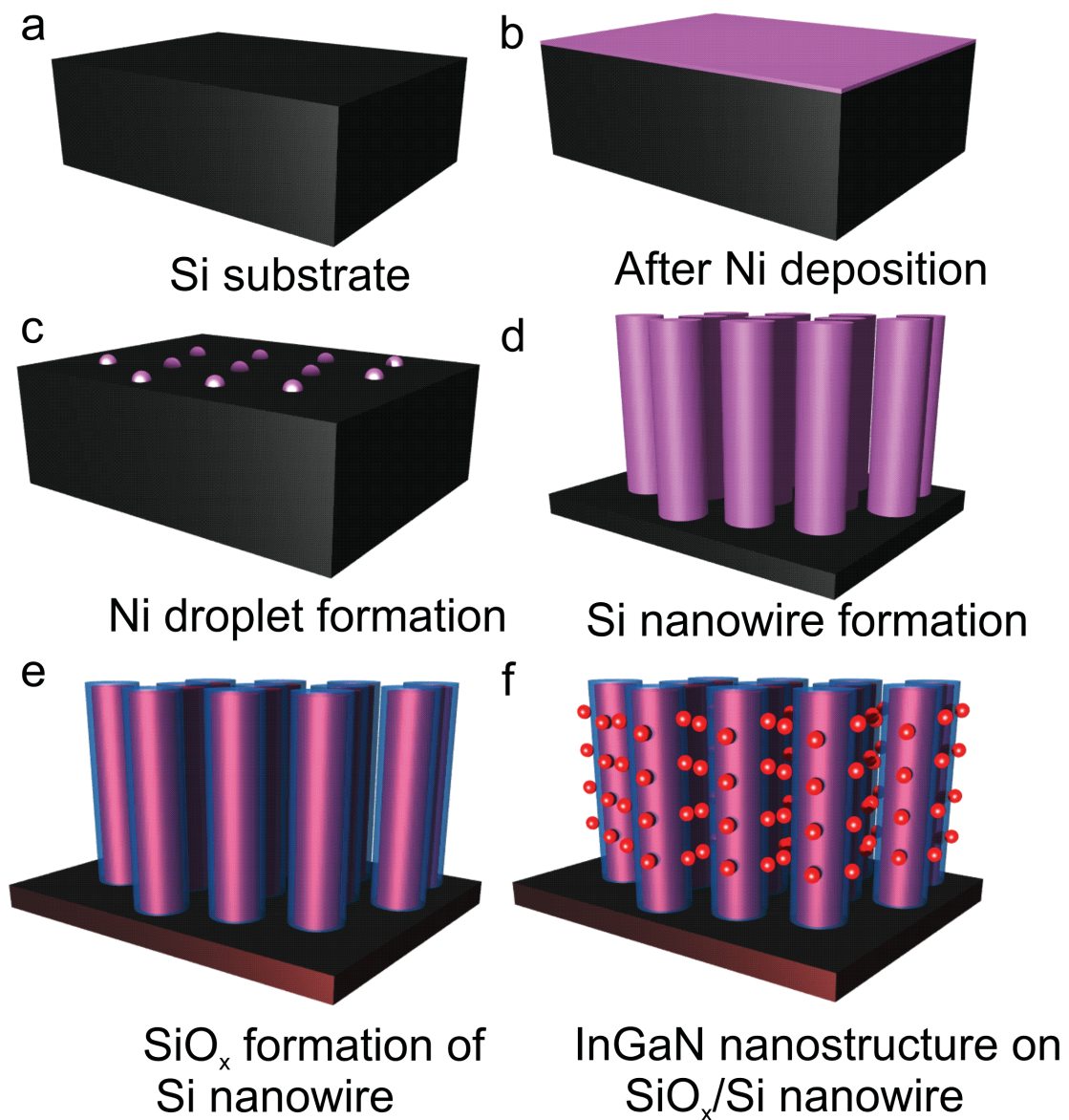


Figure 7-2: Schematic illustration of InGaN nanostructure growth on SiO<sub>x</sub>/Si nanowires. (a) Si substrate, (b) Ni thin film deposition, (c) Ni droplet formation after RTA, (d) Si nanowire formation after RIE, (e) SiO<sub>x</sub> formation after thermal oxidation, (f) MBE growth of InGaN nanostructure on SiO<sub>x</sub>/Si nanowires.

annealing (RTA) temperature, RTA ramping rate, reactive ion etching (RIE) duration, RIE power, N<sub>2</sub> flow rate, thermal oxidation duration and temperature etc. was performed to achieve well dispersed and sufficiently long Si nanowire that is suitable for the growth of InGaN. Figure 7-2 schematically illustrates the multistep process involved in the

formation of InGaN nanostructure on SiO<sub>x</sub>/Si nanowires. The optimized recipe is as follows. A thin (~10 nm) Ni layer is deposited onto Si (100) substrate using e-beam evaporation. The substrate is subsequently annealed using RTA at 900-1000 °C for 30 sec to form Ni droplet on Si substrate. The Si substrate is then etched with RIE for 700 s to form Si nanowire using Ni droplets as etching mask. Figure 7-3a, b show SEM images of the nanostructure formed after RIE etching. Depending on the etching recipe it may form Si nanotube (Fig. 7-3a) or Si nanowire (Fig. 7-3b). The nanowires are nearly 300 nm long with an average diameter of 40 nm. The substrate is then thermally oxidized at 1000 °C for 4 hrs to form a SiO<sub>x</sub> onto the Si nanowires.

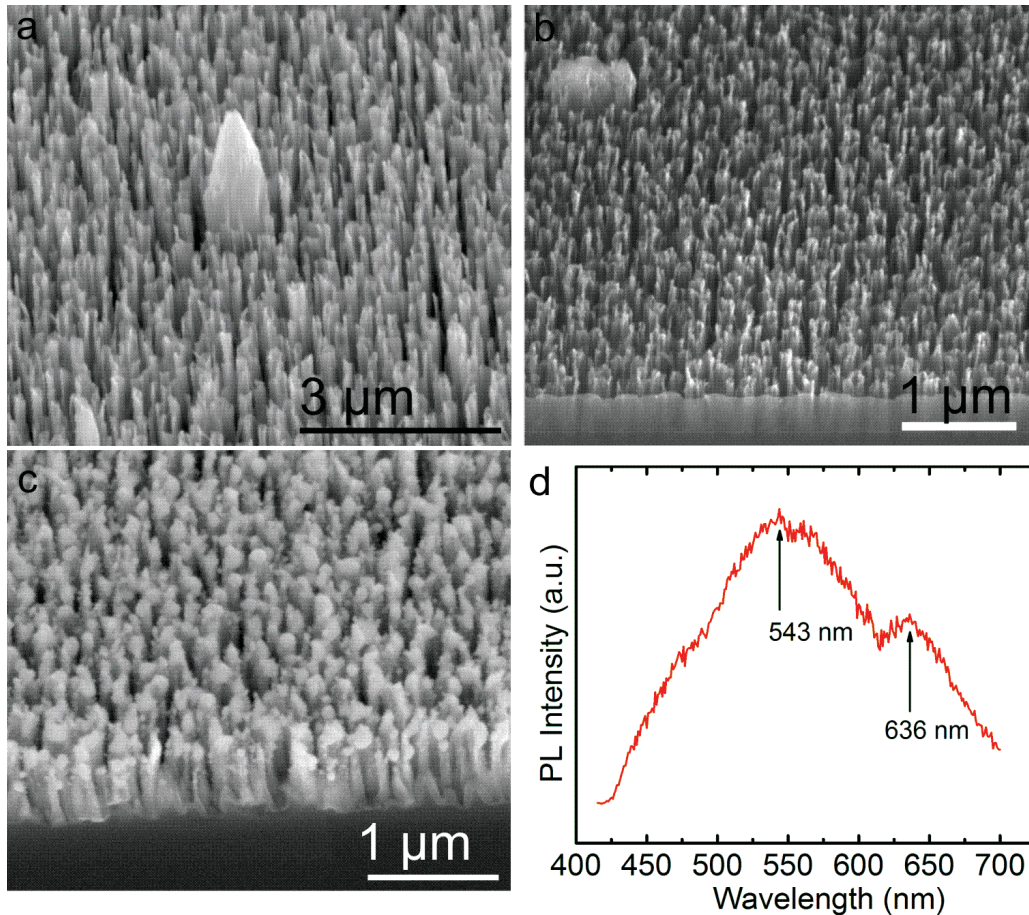


Figure 7-3: SEM image of (a) Si nanotubes, (b) Si nanowires, (c) InGaN nanostructure grown on Si nanowire, (d) Room temperature PL spectrum from InGaN nanostructure grown on SiO<sub>x</sub>/Si substrate.

The purpose of forming  $\text{SiO}_x$  is to suppress carrier leakage from the InGaN to Si nanowires owing to the lower band gap of Si than InGaN, which may reduce carrier extraction for efficient water splitting. The thermally oxidized Si nanowire substrate is then used to grow InGaN nanostructures using MBE. The growth of such nanostructure begins with the deposition of a few monolayer of Ga seeding layer for the nucleation of the nanostructure. The InGaN nanostructure growth proceeds for 30 mins and doped with a Mg cell temperature of 200 °C. Figure 7-3c shows the SEM image of the as-grown InGaN nanostructures on  $\text{SiO}_x/\text{Si}$  nanowires. The InGaN forms nanodots or nanoclusters mostly on the top half of Si nanowires. Because of the shadowing effect by the Si nanowires, In and Ga adatoms did not nucleate at the bottom of the Si nanowires. The high density of the Si nanowires was probably responsible for the formation of nanoclusters at the nanowire top. Figure 7-3d shows room temperature PL spectrum from the as-grown InGaN nanostructures. The PL emission peaks are at 543 nm and 636 nm, indicating high In incorporation in the InGaN nanostructures.

The as-grown InGaN nanostructure on  $\text{SiO}_x/\text{Si}$  nanowire substrate is subsequently used for overall water splitting after photodeposition of Rh/ $\text{Cr}_2\text{O}_3$  core/shell nanoparticles. The photocatalytic activity under visible light ( $>425$  nm) is found to be very low ( $\sim 1\text{-}2$   $\mu\text{mol/hr H}_2$ ). This low activity under visible light could be attributed to a number of reasons, including inefficient visible light absorption by the InGaN nanostructure, carrier localization, low crystalline quality of InGaN, and low carrier extraction efficiency etc. Therefore, further optimization of InGaN growth is required to achieve efficient and stable water splitting under visible light. Moreover, the recipe for the Si nanowire formation needs to be optimized to achieve well dispersed and sufficiently long nanowires that can provide extremely high surface area for the growth of high quality and high In indium content InGaN for overall water splitting under red light. Research along these lines is currently in progress.

## **7.4 Conclusions**

In this chapter we have discussed two different strategies to achieve high quality and high In content InGaN that can function as a viable material platform for water splitting under long wavelength (red) light. Several technical challenges have been discussed which involves engineering the nanowire design, optimization of the growth recipe and growth technique, and well controlled substrate preparation. These challenges need to be addressed for efficient and stable water splitting under red light. Success in addressing these challenges will facilitate capturing the whole solar spectrum more efficiently and hence efficient water splitting can be achieved under sunlight.

# Chapter-8

## Dye-Sensitized Nanowire Photocatalyst for Water Splitting under Visible Light

### 8.1 Introduction

Dye-sensitization is one of the strategies to achieve water splitting under visible light using a wide band gap semiconductor. The general concept of spectral photosensitization was first introduced by Gerischer in 1972 [214]. O'Regan and Grätzel first applied this concept in 1991 to develop dye-sensitized solar cell [215], which has attracted tremendous attention owing to the stability, low cost and device efficiency. The operating principle of dye-sensitized solar cell involves the excitation of a dye and subsequent electron transfer from the dye to the semiconductor. Since the electron transfer step resembles that in dye-sensitized solar cell, dye-sensitized semiconductors can be used as a photocatalyst for solar water splitting [216].

### 8.2 Basic Principle of Dye-Sensitized Photocatalysts

The sensitizer can be an organic dye or inorganic narrow band-gap semiconductor to efficiently harvest visible photons. When visible light excites the adsorbed sensitizer molecules, they inject electrons to the conduction band of the host semiconductor. These electrons can be subsequently used to reduce water to generate  $H_2$  at a catalytic particle such as Pt. For efficient charge injection, the excited energy state of the sensitizer has to be at more negative potential than the conduction band minimum of the host semiconductor [25]. The semiconductor can therefore function as an electron mediator to transfer the electrons from the sensitizer to the co-catalyst for water reduction. On the co-catalyst particle, water reduction kinetically competes with the recombination process with the oxidized sensitizer. An electron donor is needed to reduce the oxidized dye molecules and regenerate subsequent photon absorption. In the absence of any electron

donor, water will function as electron donor. However, in practice a sacrificial reagent such as ethylenediaminetetraacetic acid (EDTA) is commonly used to study the material without the complications caused by the  $\text{H}_2\text{-O}_2$  recombination and the catalysis for oxygen evolving reaction [216]. Therefore, the efficiency of water splitting strongly depends on the carrier generation and injection efficiency of the sensitizer, electron transfer process of the semiconductor and the water reduction efficiency on the co-catalyst surface. A thin (1-2 nm) interfacial blocking layer is sometimes used to suppress the back electron transfer from the semiconductor to the oxidized sensitizer.

The primary concern in dye-sensitized photocatalyst is the strong adsorption of the dye molecule onto the semiconductor surface [216]. Therefore a number of molecules have been developed to create a chemical linkage between the dye and the semiconductor. Ruthenium (II) complex dyes such as  $\text{Ru}(\text{bpy})_3^{2+}$  has been widely used to sensitize  $\text{TiO}_2$  and other wide-gap semiconductors [217-220]. Although dye-sensitization has been applied to a number of materials to enhance the light absorption towards visible wavelengths [218-223], it has yet to be demonstrated on metal-nitride photocatalyst for solar water splitting.

### **8.3 Development of Dye-sensitized InGaN Nanowire Photocatalyst**

Although a number of dye and semiconductor combinations have been developed for water splitting under visible light, *none* of them have reported  $\text{H}_2$  generation using green to orange solar photons. In this study, we have incorporated visible light sensitive dyes on InGaN nanowires for efficient and stable production of  $\text{H}_2$  under 500 nm and beyond solar photons. To our knowledge this is the first attempt to study the photocatalytic activity of dye-sensitized III-nitride nanowires for water splitting under green, yellow and orange solar spectrum (up to 610 nm).

The InGaN nanowires are grown in Si (111) substrate using plasma assisted MBE under nitrogen rich condition. A GaN nanowire template is used for the growth of InGaN nanowires, as schematically illustrated in Fig. 8-1a. The nanowires are *p*-type doped with Mg dopants. Figure 8-1b shows a 45° tilted SEM image of as-grown InGaN nanowires on Si (111) substrate. Scanning transmission electron microscopy-high angle annular dark

field (STEM-HAADF) imaging of a single nanowire, as shown in Fig. 8-1c, shows that the nanowires are nearly 400 nm long and 40-100 nm in diameter. Fig. 8-1c inset shows a HRTEM lattice image, illustrating single crystalline structure of the InGa<sub>0.75</sub>N nanowire. The bandgap and therefore the In content in the nanowire is determined from room temperature PL spectrum from as-grown nanowire ensemble, as shown in Fig. 8-1d. A single and broad PL emission centered at ~507 nm is revealed, which indicates a bandgap of ~2.44 eV, corresponding to an In content of 25% in InGa<sub>0.75</sub>N. In order to enhance the carrier extraction efficiency from the In<sub>0.25</sub>Ga<sub>0.75</sub>N nanowires and to enhance the hydrogen evolution reaction, Rh nanoparticles were photodeposited onto the nanowire surface from liquid precursors. A high resolution STEM-HAADF image as shown in Fig. 8-1e demonstrates successful deposition of Rh nanoparticle onto the In<sub>0.25</sub>Ga<sub>0.75</sub>N nanowires. The nanoparticles are ~3-5 nm in diameter and uniformly distributed on the nonpolar lateral surface of the nanowire. For subsequent experiments ~3 cm<sup>2</sup> wafer sample is used, which corresponds to 0.4 mg of nanowire catalyst.

In this work, we have adopted Merocyanine-540 (MC-540) dye to extend the visible light absorption edge of the nanowires. The MC-540 is a water-soluble anionic cyanine dye (Fig. 8-2a inset shows the molecular structure of MC-540) and is of particular interest owing to their enhanced photostability and spectral properties [224]. For dye adsorption, the Rh nanoparticle deposited In<sub>0.25</sub>Ga<sub>0.75</sub>N nanowires were immersed in 100 mM acetonitrile (AN) and 1 mM MC-540 solution for 12 hrs in dark at room temperature under continuous stirring condition [225]. The pH of the solution was adjusted by adding an appropriate amount of HCl or NaOH. The adsorption of MC-540 dye onto the nanowire surface is confirmed by measuring the absorption spectrum of the MC-540 dye containing AN solution before and after 12 hrs of adsorption. Fig. 8-2a shows the UV-Vis absorption spectrum of 1mM MC-540 (Sigma-Aldrich) before and after dye adsorption at different pH. Before adsorption, a broad absorption spectrum expanding from 450-600 nm is revealed. As can be seen, the dye molecules were almost completely adsorbed onto the nanowire surface at pH~10.0. At near neutral (pH~6.0) and acidic (pH~3.0) solution, the dye adsorption was inefficient. To understand the dye adsorption mechanism, Zeta-

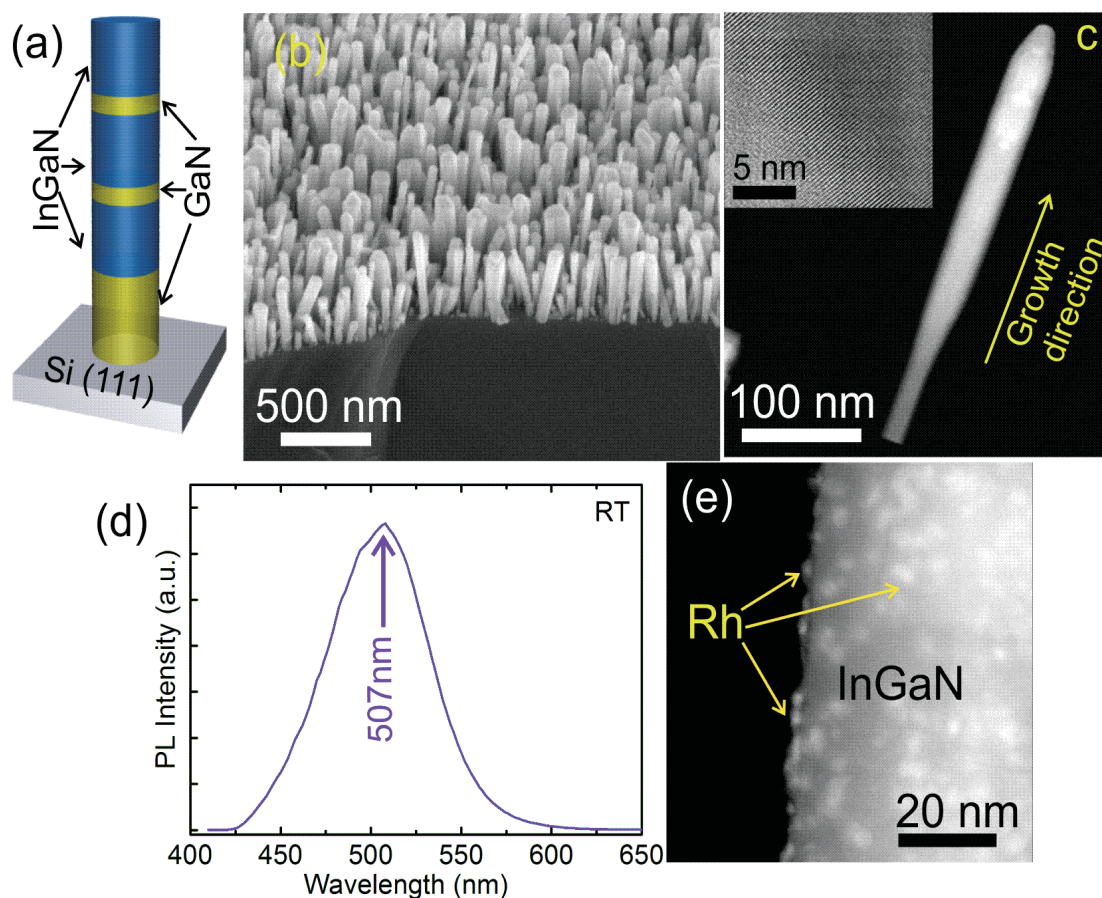


Figure 8-1: (a) Schematic of the nanowire heterostructure. (b) SEM and (c) STEM-HAADF images of as-grown  $\text{In}_{0.25}\text{Ga}_{0.75}\text{N}$  nanowires. The inset shows a HRTEM lattice image of  $\text{In}_{0.25}\text{Ga}_{0.75}\text{N}$  nanowire. (d) Room temperature photoluminescence from  $\text{In}_{0.25}\text{Ga}_{0.75}\text{N}$  nanowire. (e) Rh nanoparticle decorated  $\text{In}_{0.25}\text{Ga}_{0.75}\text{N}$  nanowire.

potential measurement [226] of nanowire-dispersed solution was performed using a NanoBrook ZetaPALS analyser. The charge state of the nanowire surface was found to be positive (+11.3 mV), indicating the fact that the negatively charged dye molecules can be electrostatically adsorbed onto the nanowire surface at basic condition.

The photocatalytic experiments were performed by immersing the dye adsorbed (at pH~10.0) and Rh nanoparticle deposited nanowire samples in 10 mM ethylenediaminetetraacetic acid (EDTA) and 100 mM AN mixture (2:1 ratio) solution and irradiating with 300 W Xenon lamp with different long-pass filters. The EDTA is

used as sacrificial electron donor to reduce the oxidized dye molecules and regenerate for subsequent photon absorption. The AN is used as an organic solvent. Fig. 8-2b illustrates the rate of H<sub>2</sub> evolution from MC-540 dye adsorbed In<sub>0.25</sub>Ga<sub>0.75</sub>N/Rh nanowire samples with different photoexcitation condition. In order to avoid exciting the In<sub>0.25</sub>Ga<sub>0.75</sub>N nanowire, long-pass filters with cut-off wavelengths between 500-610 nm were adopted.

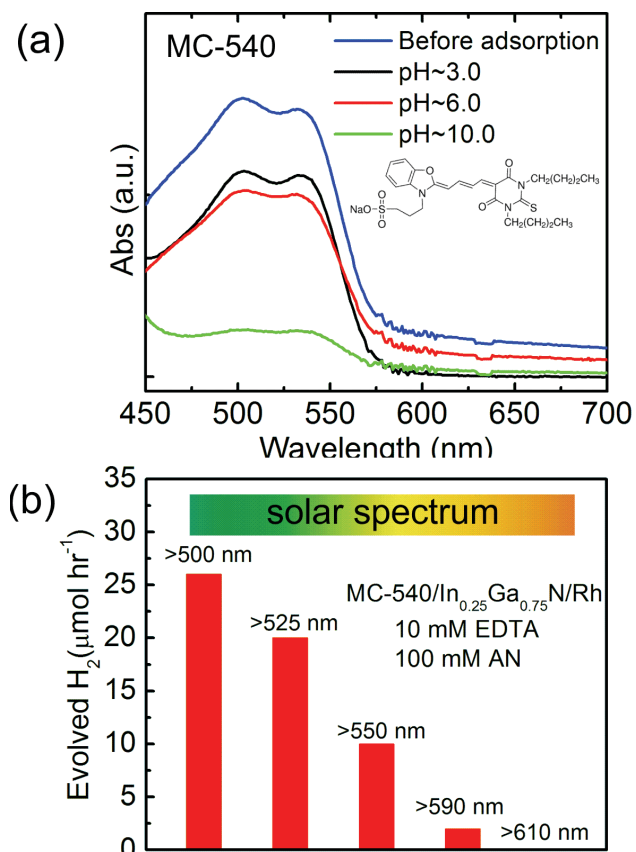


Figure 8-2: (a) UV-Vis absorption spectrum of 100 mM AN and 1 mM MC-540 dye before and after 12 hrs of adsorption. (b) H<sub>2</sub> evolution from 10 mM EDTA and 100 mM AN mixture under 300 W Xenon lamp with different long-pass filter.

The H<sub>2</sub> evolution rate was estimated from 2 hrs of reaction. The photocatalytic activity decreased with increasing wavelength because of a decrease in the number of absorbed photons. This can be well correlated with the absorption spectrum of the dye as shown in Fig. 8-2a. The photocatalytic activity at longer wavelength (>610 nm) is limited by the photoabsorption of the dye. Our control experiment shows that

in the absence of either dye molecules or sacrificial electron donor, no photocatalytic activity is observed for sub-bandgap excitation ( $>500$  nm). This confirms that the observed photocatalytic activity is initiated via photon absorption by the adsorbed dye molecules, and proceeds by subsequent electron injection events followed by the oxidation of the dyes by the sacrificial reagent. The photocatalytic activity observed here is nearly 15 times higher than recently reported dye-sensitized Potassium hexaniobate nanoscrolls (NS- $K_4Nb_6O_{17}$ ) with sub-bandgap excitation [216]. The apparent quantum efficiency is further estimated to be 0.3% for wavelengths between 525-600 nm. Figure 8-3 shows a plot of  $H_2$  evolution with irradiation time from the mixture of EDTA and AN with 525 nm long-pass filter. Steady evolution of  $H_2$  is observed for over 2 hrs. The saturation of  $H_2$  evolution after 2 hrs of photocatalytic reaction can be attributed to the leaching of the MC-540 dye under photoexcitation and photochemical reaction condition [216]. The photocatalytic activity can be recovered when the reaction is repeated after adding more MC-540 dye in the reaction solution.

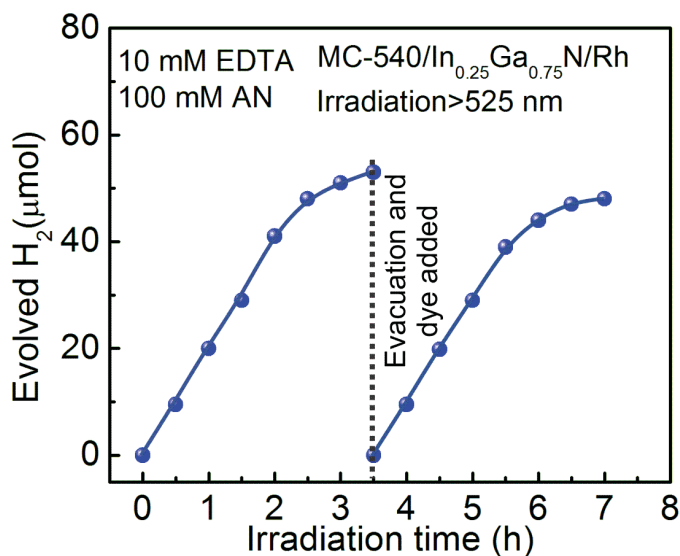
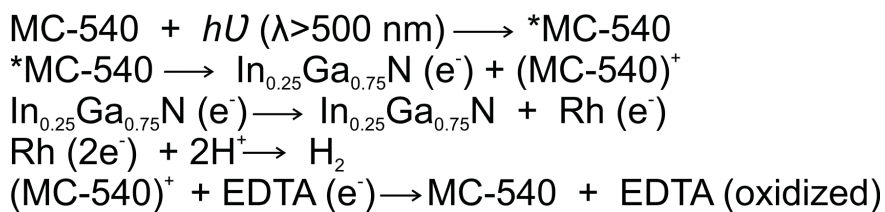


Figure 8-3: Repeated cycles of  $H_2$  evolution from EDTA and AN mixture under 300 W Xenon lamp with 525 nm long-pass filter.

Figure 8-4 illustrates the photocatalytic reaction mechanism of dye-sensitized  $\text{In}_{0.25}\text{Ga}_{0.75}\text{N}$  nanowires under visible light irradiation ( $>500$  nm). The lowest occupied molecular orbital (LUMO) of MC-540 is reported to be located at  $-1.2$  V vs NHE at  $\text{pH}\sim 7.0$  and the conduction band minimum (CBM) of  $\text{In}_{0.25}\text{Ga}_{0.75}\text{N}$  is located at  $-1.0$  V vs NHE at  $\text{pH}\sim 7.0$  [158, 227]. Therefore efficient electron injection is possible from the LUMO of MC-540 to CBM of  $\text{In}_{0.25}\text{Ga}_{0.75}\text{N}$ . When GaN is used as the host semiconductor for the dyes, no photocatalytic activity is observed, indicating the fact that the CBM of GaN is positioned at more negative potential than the LUMO level of the dye. Therefore, electron injection from the dye to the semiconductor is suppressed for GaN. The injected electrons in the CBM of  $\text{In}_{0.25}\text{Ga}_{0.75}\text{N}$  are subsequently transferred to the Rh nanoparticles deposited on the nanowire surface, as illustrated in Figure 8-4. Note that, in the case of *p*-doped nitrides, a downward band bending at the nanowire surface is commonly reported [201]. Therefore, efficient electron extraction from the nanowire to Rh nanoparticle is observed. In contrast, when *n*-type or intrinsic  $\text{In}_{0.25}\text{Ga}_{0.75}\text{N}$  nanowire photocatalyst is used, the photocatalytic activity was substantially reduced. This can be caused by the potential barrier resulting from the presence of an upward band bending of the conduction band on *n*-type and intrinsic nanowire surface [117, 129]. Since the work function of Rh ( $4.9$  eV) is larger than the electron affinity of  $\text{In}_{0.25}\text{Ga}_{0.75}\text{N}:\text{Mg}$  ( $3.95$  eV), the photogenerated electrons in the conduction band can easily migrate from nanowire to Rh nanoparticles. Furthermore, our control experiment reveals that in the absence of Rh nanoparticle, negligible photocatalytic activity is observed, indicating the significant influence of a suitable catalyst site for proton reduction. The EDTA finally reduces the oxidized dye molecules and regenerate for subsequent photon absorption. The reaction mechanism discussed above can be summarized according to the following steps [216, 228]:



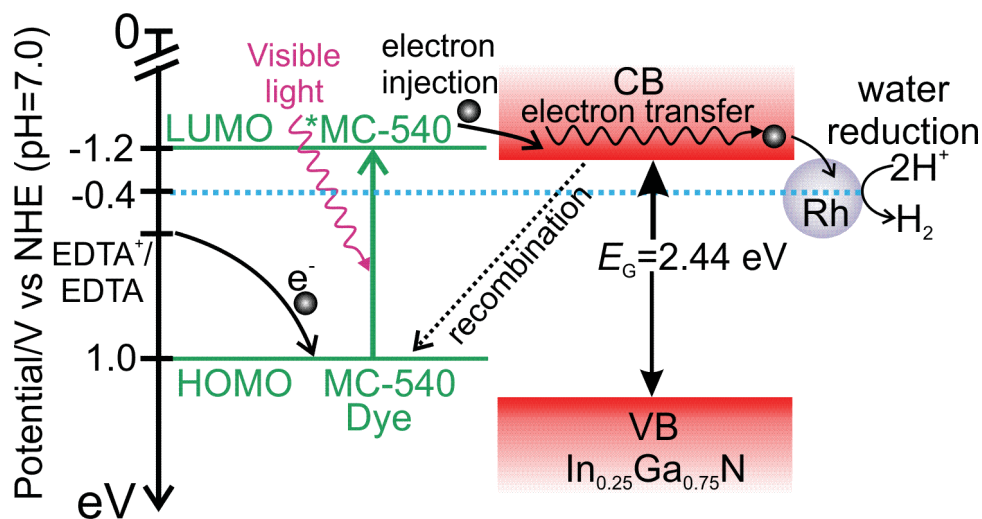


Figure 8-4: Reaction mechanism of MC-540 dye-sensitized  $\text{In}_{0.25}\text{Ga}_{0.75}\text{N}/\text{Rh}$  nanowires.

## 8.4 Conclusion

In summary, we have demonstrated that dye-sensitization of molecular beam epitaxial grown  $\text{In}_{0.25}\text{Ga}_{0.75}\text{N}$  nanowires can be a viable approach for efficient  $\text{H}_2$  production in the presence of sacrificial reagent under green, yellow and orange solar spectrum (up to 610 nm). Although, at present, the quantum efficiency is still low, enhancement of efficiency is in progress by optimizing the nanowire structure, dye-adsorption, and co-catalyst deposition. This work will pave the way to harness deep-visible and near-infrared solar photons using suitable and stable dye molecules and nanowires for efficient and stable water splitting.

# Chapter-9

## Conclusion and Future Directions

### 9.1 Summary of the Thesis Work

Solar water splitting is one of the key steps in artificial photosynthesis for future carbon-neutral, storable, and sustainable source of energy. While a number of metal-oxide based photocatalysts have been developed over the last four decades, success in finding efficient and stable photocatalyst materials responsive to UV and visible light has been very limited. In this thesis work, we have established that III-nitride nanowires can effectively function as a viable photocatalyst for efficient and stable water splitting under both UV and visible light.

In this work, we have performed the design, growth, fabrication, characterization, and performance evolution of novel III-nitride based photocatalyst for photochemical water splitting. We have achieved for the first time, wafer-level photocatalytic overall water splitting on GaN nanowires arrays with the incorporation of rhodium (Rh)/chromium-oxide  $\text{Cr}_2\text{O}_3$  core-shell co-catalysts. The decomposition of neutral water into  $\text{H}_2$  and  $\text{O}_2$  by GaN nanowires was confirmed to be a highly stable photocatalytic process. Additionally, our detailed analysis revealed that one of the major obstacles for achieving efficient and stable overall water splitting over the nanowire photocatalyst is directly related to the uncontrolled surface charge properties. By tuning the Fermi level on the nonpolar surfaces of GaN nanowire arrays through controlled *p*-type Mg dopant incorporation, we have demonstrated that the quantum efficiency can be enhanced by nearly two orders of magnitude. The internal quantum efficiency (IQE) and activity on *p*-type GaN nanowires can reach  $\sim 51\%$  and  $\sim 4.0 \text{ mol H}_2 \text{ h}^{-1} \text{ g}^{-1}$ , respectively under UV light irradiation. The nanowires remain virtually unchanged after over 50,000  $\mu\text{mol}$  gas ( $\text{H}_2$  and  $\text{O}_2$ ) is produced; which is more than 10,000 times the amount of photocatalyst itself ( $\sim 4.6 \mu\text{mol}$ ). Furthermore, in order to utilize abundant visible ( $\sim 43\%$ ) solar spectrum, a

multi-band InGaN/GaN nanowire heterostructure has been developed. The thermodynamic and kinetic potentials of the incorporated InGaN in the InGaN/GaN nanowire heterostructure was tested and found to be suitable for water redox reaction. Subsequently, Rh/Cr<sub>2</sub>O<sub>3</sub> core-shell nanoparticle decorated triple-band InGaN/GaN nanowire led to stable hydrogen production from neutral (pH~7.0) water splitting under UV, blue and green-light irradiation (up to ~ 560 nm), the longest wavelength ever reported. At ~440-450 nm wavelengths, the IQE is estimated to be ~ 13%. Detailed analysis further confirms stable photocatalytic activity of the nanowire heterostructure. In the subsequent work, we have shown that the IQE under visible light can be significantly improved by eradicating the potential barrier on nonpolar surfaces of InGaN nanowires through controlled *p*-type Mg dopant incorporation. By tuning the near surface band bending of both GaN and InGaN nanowires in a double-band heterostructure, an IQE of ~69% has been achieved for neutral (pH~7.0) water splitting, the highest value ever reported under visible light illumination. The dominant effect of near-surface band structure in transforming the photocatalytic performance is elucidated. In the subsequent part of this thesis work, we showed that by engineering the intra-gap defect related energy states in GaN nanowire arrays using high Mg doping, efficient and stable overall neutral water splitting can be achieved under violet light. Overall neutral water splitting on Rh/Cr<sub>2</sub>O<sub>3</sub> co-catalyst decorated Mg doped GaN nanowire is successfully demonstrated with intra-gap excitation upto 450 nm. This defect-band engineering can be a viable approach to extend the solar absorption of oxide and non-oxide photocatalysts. In Chapter-7, we have presented two different strategies, namely, InGaN disk-on-wire nanowire heterostructure and InGaN nanostructure on SiO<sub>x</sub>/Si nanowires to extend the absorption edge of III-nitride nanowire photocatalyst. In the last part of this work, we have presented the first example of dye-sensitized InGaN nanowires for H<sub>2</sub> generation in the presence of sacrificial reagent under green, yellow and orange solar spectrum (up to 610 nm). The stability and efficiency of this recyclable, wafer-level nanoscale III-nitride photocatalysts in neutral water promises their potential use for large-scale solar-fuel conversion.

## 9.2 Future Directions

Solar water splitting is one of the viable approaches to produce storable fuels just from sunlight and water. However, in order for this technology to penetrate into the global energy market, a number of challenges need to be addressed. The first and foremost is the development of an efficient and stable photocatalyst that can perform water splitting by utilizing nearly the entire solar spectrum. III-nitride is the only material system whose band gap can be tuned to encompass nearly the entire solar spectrum. However, some critical challenges are yet to be addressed to utilize the full potential of III-nitride family for solar-fuel conversion. For instance, the growth of high In content (40-50%) and high quality InGaN nanowire is required to achieve efficient and stable overall water splitting beyond blue solar spectrum, which is one of the Holy Grails of solar-fuel community for decades. However, this has been extremely challenging to date, as discussed in Chapter-7. Furthermore, interfacial properties of the III-nitride nanowire photocatalyst and different earth abundant co-catalyst nanoparticles are need to be explored to develop high performance water oxidation and reduction co-catalysts for efficient and stable neutral water splitting under full arc solar spectrum. The developed photocatalyst can further be utilized for photochemical and photoelectrochemical reduction of carbon dioxide into useable liquid fuels (i.e., methanol), which is the second and final step of artificial photosynthesis [7]. We therefore propose the following future works to enable III-nitride nanowire based photocatalyst for solar powered artificial photosynthesis.

### 9.2.1 Plasmon Enhanced Solar-to-Hydrogen Conversion on Metal Nitride Nanowire Arrays

We have demonstrated in previous chapters that co-catalyst decorated GaN and InGaN nanowires exhibit improved performance for photocatalytic water splitting. However, this approach does not address some of the inherent problems of semiconductor photocatalysts [85, 229-231]; namely, (i) very diffuse solar flux, (ii) discrepancy between large photon absorption depth (up to micrometers) and short

diffusion length of minority charge-carriers (few tens on nanometers), (iii) absorption limited to only high-energy photons. The consequence of these problems is that many charge carriers generate in the bulk of semiconductor (far from the active reaction sites on the surface) and recombine instead of participating in photocatalytic reactions. It has been demonstrated recently that plasmonic-metal/semiconductor photocatalyst can alleviate these issues, and therefore enhance the photocatalytic activity [85, 230]. In this scheme, dispersal of noble metal nanoparticles (such as Au, Ag with sizes from tens to hundreds of nanometers) onto the semiconductor photocatalyst remarkably improves the activity under UV and visible light.

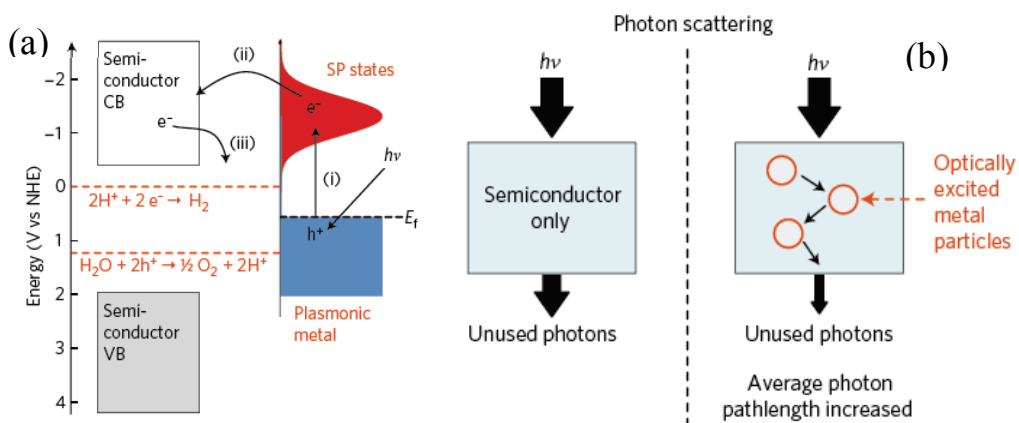


Figure 9-1: (a) Schematic of surface plasmon induced charge transfer mechanism, (b) Schematic illustration of the scattering mechanism [229].

To explain this plasmonic enhancement, it has been hypothesized that the photo-excited metallic surface plasmon resonance (SPR) transfers energy to the nearby semiconductor and increases the concentration of energetic charge carriers in the near surface region of the semiconductor, which can subsequently take part in photocatalytic reactions. If the plasmonic metal nanostructures are in direct contact with the semiconductor (similar to co-catalyst/semiconductor photocatalyst), the photo-excited energetic charge carriers in the plasmonic metal can directly inject into the semiconductor surface, as shown in Fig. 9-1a. On the other hand, if the plasmonic metal and semiconductor are separated by a thin non-conductive layer, the energy transfer can take

place through near-field electromagnetic and resonant photon-scattering mechanism [229]. In case of near-field electromagnetic mechanism, the plasmonic metal nanostructures acts as nanosized concentrators that can amplify the electric fields of incident photons a few orders of magnitude [229]. Because of this intense field, the rate of electron-hole formation increases significantly at the near surface region (top ~10 nm) of the semiconductor, from where they can easily migrate toward the surface. Therefore enhanced photocatalytic activity is expected. Additionally, the plasmonic nanostructures can enhance the rate of electron-hole formation by increasing the average path length of incident photons by scattering mechanism, as depicted in Fig. 9-1b.

A major advantage of using plasmonic nanostructures is to extend the absorption edge of large bandgap photocatalysts to visible wavelengths [85, 232]. The resonance wavelengths of the noble metal nanoparticles can be tuned to fall in the visible wavelengths by changing their size, shape and surrounding environment [85, 233]. By dispersing those visible light responsive nanoparticles onto the large bandgap photocatalyst, visible light activity can be achieved.

Although a number of plasmonic nanostructures have been developed and successfully applied to enhance the photocatalytic activity of UV and visible light responsive metal-oxide photocatalysts [231], plasmonic enhancement has yet to be reported for metal-nitrides [15]. Therefore, we propose to explore controlled deposition of well-dispersed noble metal (such as Ag, Au) nanostructures (nanoparticles, nanorods, nanostars) onto III-nitride nanowire arrays to enhance and extend the absorption spectrum for efficient and stable overall water splitting. For example, because of the large lattice mismatch and In phase-separation, it is quite challenging to develop high In content InGaN that can split water under red light. Hence, noble metals with resonance wavelength in red wavelengths can be incorporated onto moderate In content InGaN to operate under red light.

### **9.2.2 Development of Earth Abundant Co-catalyst for Efficient Water Splitting**

Most of the commonly used co-catalysts used for solar-fuel generation are made of expensive noble metals (such as platinum, gold, rhodium, and ruthenium). However, for

wide-spread penetration to the global energy market, earth abundant, efficient and less expensive co-catalyst materials are urgently required for solar-fuel generation. Therefore, the next step of this project would be to explore earth abundant, robust and efficient co-catalysts for photochemical and photoelectrochemical water splitting.

Graphene, a 2D network of  $sp^2$ -hybridized carbon atoms of hexagonal structure can be a potential earth-abundant material as co-catalyst. Graphene possesses excellent properties, such as exceptionally high conductivity ( $10^6 \text{ Scm}^{-1}$ ), high mobility ( $200000 \text{ cm}^2 \text{ V}^{-1} \text{ s}^{-1}$ ), large theoretical specific surface area ( $2630 \text{ m}^2 \text{ g}^{-1}$ ), and excellent optical transmittance ( $\sim 97.7\%$ ) [234]. Therefore, the photoexcited carriers can easily migrate to graphene, where they can take part in water reduction reaction to generate  $\text{H}_2$ . Because of the high work function (4.42 eV), graphene can accept electron from most of the semiconductor photocatalyst [235]. Therefore, the recombination of the carriers can be greatly suppressed with simultaneous enhancement in photocatalytic activity. Hence, graphene can be used as an electron acceptor and transporter. Additionally, graphene/graphene<sup>-</sup> has a reduction potential of -0.08 more negative than that of  $\text{H}^+/\text{H}_2$  [236]. Therefore, reduced graphene oxide (RGO) can be an attractive cost-effective co-catalyst to replace precious noble metals. In addition to serve as a co-catalyst, functionalized graphene (RGO) with suitable oxidation level can work as a host photocatalyst, where photoexcited carriers can be generated [237]. Furthermore, with band-gap tuning by controlling the reduction degree, RGO can work as a photosensitizer to extend the absorption edge of the host photocatalyst [238]. Therefore, we propose to explore different techniques to incorporate graphene (RGO) onto the GaN and InGaN nanowires arrays, such as photoreduction, hydrothermal, and spin-coating.

In addition to graphene, other earth abundant and less expensive co-catalysts need to be explored as well. Primary focus should be on transition metals such as Fe, Co, Cu and Ni [239]. Although these materials are not very efficient as hydrogen reduction catalysts (HER) in their metallic state, different complexes of Co(I/II) and Ni(0/II) have shown great interest in recent years. Because of the presence of a variety of oxidation states, these transition metal complexes can easily participate in electron transfer from the semiconductor and mechanistically in the catalytic cycle of water reduction. Therefore,

different techniques (such as photoreduction etc.) need to be investigated to anchor transition metal complexes onto the metal nitrides nanowires. Additionally, recent studies have shown that two-dimensional molybdenum disulfide (MoS<sub>2</sub>) can efficiently catalyze water reduction reaction because of their substantial amount of catalytic edge sites with high surface energy [240]. Therefore, MoS<sub>2</sub> nanocrystalline layers can be an attractive cost-effective co-catalyst for the metal-nitride nanowires. Solvothermal technique can be used to synthesis MoS<sub>2</sub> nanocrystalline layers.

In addition to water reduction co-catalyst, we propose to explore earth abundant water oxidation co-catalyst to extend the efficiency of water oxidation for O<sub>2</sub> evolution. Since four-electron water oxidation is a multi-step process and also the rate determining step in overall water splitting, the development of earth-abundant water oxidation co-catalyst is highly important. Cobalt-Phosphate (Co-Pi) has drawn great deal of attention recently as cost-effective oxygen evolving complex [33, 241]. The feasibility of incorporating Co-Pi on the metal-nitride nanowires needs to be explored.

Furthermore, with controlled dopant incorporation in metal-nitride nanowires, and with optimized optical excitation conditions, we propose to explore high efficiency overall water splitting without any co-catalyst incorporation under visible light irradiation.

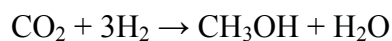
### 9.2.3 III-Nitride Nanowires for CO<sub>2</sub> Reduction

Solar water splitting not only has the potential to mitigate the energy crisis but also has the capability to reduce CO<sub>2</sub> from the environment. The electrons and protons released from water oxidation reaction can be combined with CO<sub>2</sub> to produce liquid alcohol or hydrocarbon fuel (CO, CH<sub>4</sub> or CH<sub>3</sub>OH), as follows [12, 242]:





Liquid fuel (i.e., CH<sub>3</sub>OH) can also be produced by catalytic hydrogenation of CO<sub>2</sub> and H<sub>2</sub>, wherein H<sub>2</sub> has been obtained from solar water splitting, as follows [243]:



The produced methanol can be used directly in a “Direct Methanol Fuel Cell” [244]. The required CO<sub>2</sub> for the above reactions can be captured from fossil fuel burning power plants or other industries. Considering the diminishing fossil fuel resources, the CO<sub>2</sub> in air can also be used for the above reactions. Since the concentration of CO<sub>2</sub> in air is very low (0.037%), new technologies need to be developed to efficiently and economically capture CO<sub>2</sub> from air. Therefore, environment purification (i.e., CO<sub>2</sub> reduction) and energy production (i.e., liquid fuel) can be achieved simultaneously. Although H<sub>2</sub> has the highest energy density by mass (143 MJ Kg), it suffers from low volumetric energy densities. On the other hand, hydrocarbon fuels offer the optimum volumetric energy density, and therefore can alleviate hydrogen storage issues [245]. Further, hydrocarbon fuels can be used in existing gasoline infrastructure with limited modifications. Hence, building expensive liquid H<sub>2</sub> infrastructure can be avoided. Therefore, there is an immense potential in solar water splitting both for carbon-free energy and environment. Research and development in this area is under advancement.

### 9.3 Conclusions

Solar energy is the ultimate solution to mitigate the current and future energy crisis. However, for widespread market penetration, solar energy has to be harnessed more efficiently and stored for large scale long-term applications. Solar water splitting allows producing H<sub>2</sub> gas, a clean, renewable and carbon-free energy carrier. Solar water splitting can also be used for CO<sub>2</sub> reduction from environment with simultaneous production of hydrocarbon fuel. However, many significant challenges need to be addressed for translating this technology from R&D laboratory to the commercial world. How soon this technology will reach marketplace depends on breakthroughs in discovery research.

# List of Publications

## Patents

---

1. Zetian Mi, **M. G. Kibria**, “High Efficiency Broadband Semiconductor Nanowire Devices”, United States Patent App. No. 13/866,155. Filed Apr.19, 2013.
2. Zetian Mi, **M. G. Kibria**, “Methods and Systems Relating to Photochemical Water Splitting”. Provisional Patent Application Submitted (June 2014).

## Peer Reviewed Journal Articles

---

1. **M. G. Kibria**, F.A. Chowdhury, M.L. Trudeau, H. Guo, Z. Mi, “Dye-sensitized InGaN Nanowire Arrays for Efficient Hydrogen Production under Visible Light Irradiation”, *Submitted to Nanotechnology*.
2. **M. G. Kibria**, F.A. Chowdhury, S. Zhao, M.L. Trudeau, H. Guo, and Z. Mi, “Defect-Engineered GaN:Mg Nanowire Arrays for Overall Water Splitting under Violet Light”. *Applied Physics Letter*, 106, 113105 (2015).
3. **M. G. Kibria**, F.A. Chowdhury, S. Zhao, B. AlOtaibi, M.L. Trudeau, H. Guo, and Z. Mi, “Visible Light Driven Efficient Overall Water Splitting Using *p*-type Group III-Nitride Nanowire Arrays”. *Nature Communications*, 6, 6797 (2015).
4. **M. G. Kibria**, S. Zhao, F. A. Chowdhury, Q. Wang, H. P. T. Nguyen, M. L. Trudeau, H. Guo, and Z. Mi, “Tuning the Surface Fermi Level on *p*-type GaN Nanowires for Efficient Overall Water Splitting”, *Nature Communications*, 5, 3825 (2014).
5. **Md G. Kibria**, Hieu P. T. Nguyen, Kai Cui, Songrui Zhao, Dongping Liu, Hong Guo, Michel L. Trudeau, Suzanne Paradis, Abou-Rachid Hakima, and Zetian Mi, “One-Step Overall Water Splitting under Visible Light Using Multiband InGaN/GaN Nanowire Heterostructures”, *ACS Nano*, 7, 7886 (2013).

6. S. Zhao, **M. G. Kibria**, Q. Wang, H. P. T. Nguyen and Z. Mi, “Growth of Large-Scale Vertically Aligned GaN Nanowires and Their Heterostructures with High Uniformity on SiO<sub>x</sub> by Catalyst-Free Molecular Beam Epitaxy”, *Nanoscale*, 5, 5283 (2013).
7. Q. Wang, X. Liu, **M. G. Kibria**, S. Zhao, H. P. T. Nguyen, K. H. Li, Z. Mi, “*p*-Type Dopant Incorporation and Surface Charge Properties of Catalyst-free GaN Nanowires Revealed by Micro-Raman Scattering and X-ray Photoelectron Spectroscopy”, *Nanoscale*, 6, 9970 (2014).
8. Shun Li, Jianming Zhang, **Md Golam Kibria**, Zetian Mi, Mohamed Chaker, Dongling Ma, Riad Nechache and Federico Rosei, “Remarkably Enhanced Photocatalytic Activity of Laser Ablated Au Nanoparticle Decorated BiFeO<sub>3</sub> Nanowires under Visible-Light”, *Chemical Communication*, 49, 5856 (2013).
9. D. Wang, A. Pierre, **Md. G. Kibria**, K. Cui, X. Han, K. Beavan, H. Guo, S. Paradis, H. Abou-Rachid, and Z. Mi “Wafer-level Photocatalytic Water Splitting on GaN Nanowire Arrays Grown by Molecular Beam Epitaxy,” *Nano Letter*, 11, 2353 (2011).
10. S. Zhao, Z. Mi, **M. G. Kibria**, Q. Li and G. T. Wang, “Understanding the Role of Si Doping on Surface Charge and Optical Properties: Photoluminescence Study of Intrinsic and Si-doped InN Nanowires”, *Physical Review B*, 85, 245313 (2012).
11. Kai Cui, Saeed Fatholouloumi, **Md. Golam Kibria** and Zetian Mi, “Molecular Beam Epitaxial Growth and Characterization of Catalyst-Free InN/In<sub>x</sub>Ga<sub>1-x</sub>N Core/Shell Nanowire Heterostructures on Si(111) Substrates”, *Nanotechnology*, 23, 085205 (2012).
12. B. AlOtaibi, H. P. T. Nguyen, S. Zhao, **M. G. Kibria**, S. Fan, and Z. Mi, “Highly Stable Photoelectrochemical Water Splitting and Hydrogen Generation Using a

Double-Band InGaN/GaN Core/Shell Nanowire Photoanode”, *Nano Letter*, 13, 4356 (2013).

13. H. P. T. Nguyen, S. Zhang, A. T. Connie, **M. G. Kibria**, Q. Wang, I. Shih, and Z. Mi, “Breaking the Carrier Injection Bottleneck of Phosphor-Free Nanowire White Light-Emitting Diodes”, *Nano Letter*, 13, 5437 (2013).
14. Q. Wang, A. T. Connie, H. P. T. Nguyen, **M. G. Kibria**, S. Zhao, S. Sharif, I. Shih and Z. Mi, “Highly Efficient, Spectrally Pure 340 nm Ultraviolet Emission from  $\text{Al}_x\text{Ga}_{1-x}\text{N}$  Nanowire Based Light Emitting Diodes”, *Nanotechnology*, 24, 345201 (2013).
15. B AlOtaibi, M Harati, S Fan, S Zhao, H P T Nguyen, **M G Kibria** and Z Mi, “High efficiency Photoelectrochemical Water Splitting and Hydrogen Generation Using GaN Nanowire Photoelectrode”, *Nanotechnology*, 24, 175401 (2013).
16. S. Zhao, B. H. Le, D. P. Liu, X. D. Liu, **M. G. Kibria**, T. Szkopek, H. Guo, and Z. Mi, “*p*-Type InN Nanowires”, *Nano Letter*, 13, 5509 (2013).
17. S. Zhao, S. Fatholouloumi, K. H. Bevan, D. P. Liu, **M. G. Kibria**, Q. Li, G. T. Wang, Hong Guo, and Z. Mi, “Tuning the Surface Charge Properties of Epitaxial InN Nanowires”, *Nano Letter*, 12, 2877 (2012).

## Conference/Meeting Presentations/Proceedings

---

1. Zetian Mi, **M. G. Kibria**, and F. A. Chowdhury, “Efficient and Stable Overall Water Splitting Using *p*-type III-Nitride Nanowires under Visible Light Irradiation”, MRS Spring Meeting, San Francisco, April 6-10, 2015.
2. **Md Golam Kibria**, Faqrul Alam Chowdhury and Zetian Mi, “Achieving artificial photosynthesis with nanowires”, SPIE Newsroom, 9 February 2015, DOI: 10.1117/2.1201501.005751

3. (Invited) Z. Mi, **M. G. Kibria**, “High Efficiency One-Step Solar-to-Hydrogen Conversion on Metal-Nitride Nanowires”. International Conference on Electronic Materials and Nanotechnology for Green Environment (ENGE-2014), Jeju Island, South Korea, Nov 16-19, 2014.
4. Zetian Mi, **Md Kibria**, Bandar AlOtaibi, Faqrul Chowdhury, Shizhao Fan, “High Efficiency Water Splitting on InGaN Nanowire Arrays under Ultraviolet and Visible Light Irradiation” *International Conference on New Advances in Materials Research for Solar Fuels Production*, Montréal, Canada, 24-26 June 2014.
5. **M. G. Kibria**, F. A. Chowdhury, H. P. T. Nguyen, S. Zhao, and Z. Mi, “Overall Water Splitting under Broadband Light Using InGaN/GaN Nanowire Heterostructures”. *IEEE Summer Topical Meeting Series*, Montreal, Quebec, Canada, July 14-16, 2014. (*Nominated for Best Student Poster Award*)
6. **M. G. Kibria**, F. A. Chowdhury, H. P. T. Nguyen, S. Zhao, and Z. Mi, “Overall Water Splitting under Broadband Light Using InGaN/GaN Nanowire Heterostructures”. *Proceedings of IEEE Summer Topical Meeting Series*, Pages 19-20, July 14, 2014.
7. B. AlOtaibi, S. Fan, H. P. T. Nguyen, S. Zhao, **M. G. Kibria**, and Z. Mi, “Photoelectrochemical Water Splitting and Hydrogen Generation Using InGaN/GaN Nanowire Arrays”. *IEEE Summer Topical Meeting Series*, Montreal, Quebec, Canada, July 14-16, 2014.
8. B. AlOtaibi, S. Fan, H. P. T. Nguyen, S. Zhao, **M. G. Kibria**, and Z. Mi, “Photoelectrochemical Water Splitting and Hydrogen Generation Using InGaN/GaN Nanowire Arrays”. *Proceedings of IEEE Summer Topical Meeting Series*, Pages 206-207, July 14, 2014.
9. Zetian Mi, Hieu P. T. Nguyen, Shaofei Zhang, Ashfiqua T. Connie, **Md G. Kibria**, Qi Wang, Ishiang Shih “Phosphor-free InGaN/GaN/AlGaN core-shell dot-in-a-wire white light-emitting diodes” *Proc. SPIE 9003, Light-Emitting Diodes:*

*Materials, Devices, and Applications for Solid State Lighting XVIII*, 900306, February 27, 2014.

10. Zetian Mi, **Md G. Kibria**, “High Efficiency and Highly Stable Water Splitting on InGaN Nanowire Arrays under Visible Light Irradiation”, *SPIE Solar Hydrogen and Nanotechnology IX*, San Diego, California, United States, August 17 – 21, 2014.
11. Zetian Mi, **Md G. Kibria**, Bandar AlOtaibi, Faqrul A. Chowdhury, Shizhao Fan, Songrui Zhao, and Hieu P. T. Nguyen, “High Efficiency Water Splitting Using InGaN Nanowire Photocatalysts and Photoelectrodes” *The 15th IUMRS-International Conference in Asia (IUMRS-ICA 2014)*, Fukuoka, Japan, August 24-30, 2014.
12. Zetian Mi, **M. G. Kibria**, F. A. Chowdhury, and S. Zhao, “High Efficiency Overall Water Splitting Using III-Nitride Nanowire Arrays: A Step Closer to Artificial Photosynthesis”, *Molecules and Materials for Artificial Photosynthesis*, Cancun, Maxico, February 06-09, 2014.
13. **M. G. Kibria**, F. A. Chowdhury, Z. Mi, “Tuning the Surface Charge Properties of p-GaN Nanowire Arrays for High Efficiency Water Splitting”, *MRS Spring Meeting*, San Francisco, April 21-25, 2014.
14. **M. G. Kibria**, F. A. Chowdhury, S. Zhao, Z. Mi, “Band-Engineered InGaN Nanowires Arrays for High Efficiency Water Splitting Under Visible Light Irradiation”, *North American Molecular Beam Epitaxy (NAMBE)*, Banff, Alberta, Oct 5-11, 2013. (**Best Student Oral Presentation**)
15. **M. G. Kibria**, F. A. Chowdhury, S. Zhao, Q. Wang, Z. Mi, “Doping Effect on Photocatalytic Activity of GaN Nanowires Arrays for Overall Water Splitting”, *McGill Engineering Research Showcase (MERS)*, Oct 18, 2013.
16. H.P.T. Nguyen, **M.G. Kibria**, A. Connie, Q. Wang, I. Shih, Z. Mi, “High-power Phosphor-free InGaN/GaN/AlGaIn Dot-in-a-wire Core-shell White Light Emitting Diodes”, *North American Molecular Beam Epitaxy (NAMBE)*, Banff, Alberta, Oct 5-11, 2013.

17. **M. G. Kibria**, F. A. Chowdhury, S. Zhao, Z. Mi, "Doping Effect on Photocatalytic Activity of GaN Nanowires Arrays for Pure Water Splitting", *MRS Fall Meeting*, Boston, USA, Nov 25-30, 2012.
18. **M. G. Kibria**, H. P. T. Nguyen, K. Cui, S. Zhao, D. Liu, H. Guo, S. Paradis, A.-R. Hakima, Z. Mi, "Photocatalytic Pure Water Splitting Under Visible Light Using Multi-band InGaN/GaN Nanowire Heterostructures Grown By Molecular Beam Epitaxy", *North American Molecular Beam Epitaxy (NAMBE)*, Georgia, October 14-17, 2012.
19. B. Alotaibi, M. Harati, **M. G. Kibria**, S. Fan, Songrui Zhao, Hieu P. T. Nguyen, and Zetian Mi, "Photoelectrochemical Hydrogen Generation on InGaN Nanowire Arrays", *MRS Fall Meeting*, Boston, USA, Nov 25-30, 2012.
20. **M. G. Kibria**, Z. Mi, H. P. T. Nguyen, S. Zhao, D. Liu, K. H. Bevan, H. Guo, S. Paradis, A.-R. Hakima, and M. Trudeau, "Harnessing Energy from Sunlight and Water Using III-Nitride Nanowire Arrays", *Next Generation Solar*, Montreal, Quebec, Canada, May 14-15, 2012.
21. B. AlOtaibi, M. Harati, **Md. G. Kibria**, S. Fan, H. P. T. Nguyen, S. Zhao, and Z. Mi, "Photoelectrochemical Hydrogen Production Using GaN Nanowire Arrays", *Photonics North*, Montreal, Quebec, Canada, June 6-8, 2012.
22. Yoshihiko Nagai, **Md Golam Kibria**, Zetian Mi and Robert Sladek, "Oligonucleotide Functionalization of Indium Nitride Nanowires for Biosensor Application". *Photonics North*, Montreal, Quebec, Canada, June 6-8, 2012.
23. **M. G. Kibria**, K. Cui, A. Shih, M. Harati, D. Wang, Z. Mi, "Photocatalytic Water Splitting on III-Nitride Nanowires", *MRS Fall Conference*, Boston, USA, Nov. 28-Dec.02, 2011.
24. Z. Mi, H. P. T. Nguyen, K. Cui, **Md. G. Kibria**, D. Wang and I. Shih, "Harvesting Solar Energy Using Group-III Nitride Nanowires", *Photovoltaics Canada*, 2nd National Scientific Conference, Ottawa, Canada, May 16-16, 2011.

25. Z. Mi, P. Bianucci, K. Cui, **Md G. Kibria**, Y. Nagai, and R. Sladek, “Self-organized III-V semiconductor microtube and nanowire lasers and integrated DNA sensors on a silicon platform”, Nano-DDS, *Polytechnic Institute of New York University*, Brooklyn, USA, Aug. 29-Sep.01, 2011.

# APPENDIX-1

## Internal quantum efficiency (IQE) and apparent quantum efficiency (AQE) calculation

In order to derive the internal quantum efficiency (IQE) for the photocatalytic overall water splitting, the number of incident photons in the wavelength range of 200-365 nm were estimated from the lamp spectrum, which represents the overlapped wavelength between the absorption spectrum of GaN nanowires and the power spectrum of the lamp. The absorbed photons were estimated based on the GaN nanowire height of 600 nm, the absorption coefficient of GaN in the wavelength of 200-365 nm, and nanowire fill factor (on the silicon substrate). The fill factor was estimated from the top view SEM image of the GaN nanowire arrays for all the samples. The estimated fill factors for samples A, B, C, D, E and F are 27%, 30%, 35%, 39%, 40% and 41%, respectively. The light reflection from the water-GaN interface was estimated using the refractive indices of water and GaN. The IQE was derived from the following process:

First, the reflection co-efficient of GaN,  $r_{GaN}(\lambda)$ , is derived from the reflectance of GaN,  $R_{GaN}(\lambda)$ .

$$r_{GaN}(\lambda) = \left( \frac{1 + \sqrt{R_{GaN}(\lambda)}}{1 - \sqrt{R_{GaN}(\lambda)}} \right) \quad (1)$$

The reflectance at water-GaN interface is then derived as follows:

$$R_{W/G}(\lambda) = \left( \frac{r_{GaN}(\lambda) - r_W}{r_{GaN}(\lambda) + r_W} \right)^2 \quad (2)$$

where  $r_W$  is the reflection co-efficient of water (1.33). The transmittance at water-GaN interface can then be calculated as follows:

$$T_{W/G}(\lambda) = 1 - R_{W/G}(\lambda) \quad (3)$$

The wavelength dependent absorption (%) by GaN nanowire can be written as:

$$\gamma_{abs}(\lambda) = 1 - e^{-\alpha(\lambda)z} \quad (4)$$

where  $z$  is the length of the nanowire and  $\alpha(\lambda)$  is the absorption co-efficient of GaN. The absorbed power (mW) by the GaN nanowires,

$$P_{abs}(\lambda) = P_{incident}(\lambda) \times T_{W/G}(\lambda) \times \gamma_{abs}(\lambda) \times A_{sample} \times \beta_{ff} \quad (5)$$

where  $A_{sample}$  is the sample area (2.8 cm<sup>2</sup>) and  $\beta_{ff}$  is the nanowire fill factor calculated from the top view SEM images of all the samples.  $P_{incident}(\lambda)$  was derived from the lamp spectrum taking into account the light reflection at the air-water interface. The incident power density was estimated to be 677 mW/cm<sup>2</sup> in the wavelength range 200-365 nm. The total absorbed power by the GaN nanowire was estimated to be 652.7 mW.

The number of absorbed photons per second is calculated from,

$$N_{ph}(\lambda) = \frac{P_{abs}(\lambda)}{E_{ph}(\lambda)} \quad (6)$$

where  $E_{ph}(\lambda) = \frac{hc}{\lambda}$ . The total number of absorbed photons per second in 200-365 nm wavelengths can then be calculated as follows:

$$N_{ph}(200 - 365) = \int_{200}^{365} \frac{P_{abs}(\lambda) \times \lambda}{hc} d\lambda \quad (7)$$

The estimated  $N_{ph}(200 - 365) = 1 \times 10^{18}$  per second. The IQE is then derived from the following equation:

$$IQE = 2 \times \frac{\text{Number of evolved } H_2 \text{ molecules per hour}}{\text{Number of absorbed photons per hour}} \times 100 \% \quad (8)$$

$$IQE = 2 \times \frac{I_{H_2} \times 10^{-6} \times N_a}{N_{ph}(200-365) \times 3600} \times 100 \% \quad (9)$$

where  $N_a$  is the Avogadro's number, and  $I_{H_2}$  is the evolved H<sub>2</sub> ( $\mu mol$  per hour) from overall water splitting reaction.

For the estimation of apparent quantum efficiency (AQE), we considered all the incident photons in the wavelength range 200-365 nm that can be absorbed by the GaN nanowire photocatalyst (i.e., no reflection at the water-GaN interface, absorption coefficient  $\alpha(\lambda) = 1$  and nanowire fill factor  $\beta_{ff} = 100\%$ ). The estimated  $N_{ph}(200 - 365) = 2.91 \times 10^{18}$  per second.

## APPENDIX-2

### **Estimation of apparent quantum efficiency (AQE), absorbed photon conversion efficiency (APCE) and energy conversion efficiency (ECE) of the double-band GaN/InGaN nanowire photocatalyst.**

#### **2.1 The simplified nanowire model for the efficiency calculation**

Light propagation and absorption inside a layered structure (Fig. 5-4a) can generally be calculated by using a multi-layer reflectivity model. However, because of the negligible mismatch in refractive index between GaN and InGaN for the Indium composition (~20-30%) used in our structure, reflection from GaN/InGaN interfaces can be ignored for both UV (average reflection~0.05%) and visible light (average reflection~0.005%). Moreover, GaN absorption spectrum excludes visible light whereas InGaN can absorb both UV and visible spectrum. Furthermore, a stepwise calculation for the five-layered GaN/InGaN heterostructures (Fig. 5-4a) shows that the GaN cap-layers (~6 nm) in between the InGaN layers absorb very small fraction of UV (<1% of total light transmitted through the nanowires). Considering all these factors, the multilayered structure (Fig. 5-4a) can be simplified as a two-layered structure, having a ~130 nm thick *p*-GaN layer (optimally doped at  $T_{Mg}=270$  °C) on top, followed by a lumped ~185 nm thick InGaN layer (optimally doped at  $T_{Mg}=200$  °C).

In order to derive the AQE for the photocatalytic overall water splitting, the number of incident photons in the wavelength range of 200-475 nm (PL peak ~475 as shown in Fig. 5-4b) was estimated from the lamp spectrum (and corresponding filter transmission spectrum), which represents the overlapped wavelength between the absorption spectrum of InGaN/GaN nanowires and the power spectrum of the lamp. The AQE and APCE were derived using the following process. The incident power on the sample can be expressed as:

$$P_{incident}(\lambda) = \rho_{incident}(\lambda) \times A_{sample} \times \beta_{ff} \quad (1)$$

where  $A_{sample}$  is the sample area ( $\sim 3.0 \text{ cm}^2$ ) and  $\beta_{ff}$  is the nanowire fill factor. The  $\beta_{ff}$  is assumed to be unity (assuming all the incident photons are absorbed) for the calculation of AQE, and 42.3% for the estimation of APCE.  $\rho_{incident}(\lambda)$  is the incident power intensity on the sample, which was derived by measurements using a broadband detector (Thermopile Sensor, Newport-818P-100-55) and taking into account the power spectrum of the lamp (as shown below) and optical filter, while mimicking the experimental configuration.

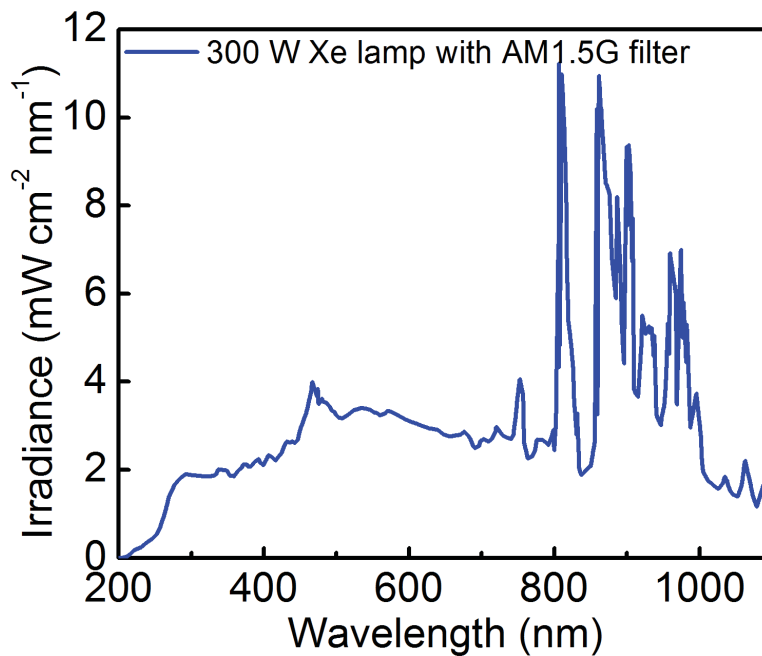


Figure A1: Typical output spectral distribution of 300 W Xenon lamp with AM1.5 G filter onto the sample surface.

## 2.2 Calculation of the AQE and APCE using AM1.5G optical filter in the UV and visible wavelength range (200-475 nm)

In what follows, we first describe the calculation of the AQE and APCE with the use of AM1.5G optical filter. The total incident power on the sample is estimated to be 1464

mW in the wavelength range of 200-475 nm with AM1.5G filter. The number of incident photons per second, as a function of wavelength is calculated from,

$$N_{ph}(\lambda) = \frac{P_{incident}(\lambda)}{E_{ph}(\lambda)} \quad (2)$$

where  $E_{ph}(\lambda) = \frac{hc}{\lambda}$  is the photon energy for the corresponding wavelength. The total number of incident photons per second within 200-475 nm wavelength range can be calculated as follows:

$$N_{ph,inc}(200 - 475) = \int_{200}^{475} \frac{P_{incident}(\lambda) \times \lambda}{hc} d\lambda \quad (3)$$

The AQE is then derived from the following equation:

$$AQE = 2 \times \frac{\text{Number of evolved H}_2 \text{ molecules per hour}}{\text{Number of incident photons per hour}} \times 100 \% \quad (4)$$

The amount of absorbed power depends on the optical properties of the different layers involved, namely, water, GaN and InGaN. For the simplified model of our structure, there are only three layers and hence two corresponding interfaces, which are water/GaN and GaN/InGaN interface. Considering the large refractive index mismatch between GaN and water, on average ~10% of the incident power (both UV and visible) is reflected back from the nanowires-top surface. The absorbed power can be calculated using the refractive indices and absorption coefficients of the materials, which is estimated to be ~ 230.9 mW in the wavelength range 200-475 nm with the use of an AM1.5G optical filter. The APCE of the structure is then estimated from equation (4) by replacing the number of incident photons with that of the absorbed photons, derived as:

$$N_{ph,abs}(200 - 475) = \int_{200}^{475} \frac{P_{absorbed,GaN+InGaN}(\lambda) \times \lambda}{hc} d\lambda \quad (5)$$

The AQE and APCE, corresponding to the entire absorption spectrum (200-475 nm) for the double-band structure, which includes both UV and visible photons, were derived to be ~20% and ~74.5%, respectively. The light trapping and scattering effect have not been taken into account for the estimation of APCE. Clearly, this APCE of the nanowire

structure is only limited by the charge transport efficiency to the solid-liquid interface ( $\eta_{transport}$ ) and the efficiency of interfacial charge transfer ( $\eta_{interface}$ ).

### 2.3 Calculation of the AQE and APCE in the visible wavelength range (400-475 nm)

From equations (3)-(5), the total incident (on the  $\sim 3 \text{ cm}^2$  sample) and absorbed (by the nanowires) power in the visible wavelength range (400-475 nm) were calculated to be 843 mW and 152 mW, which corresponds to  $\sim 12.3\%$  and  $\sim 68.5\%$  AQE and APCE, respectively.

### 2.4 Calculation of the ECE using AM1.5G filter in the UV and visible wavelength range (200-475 nm)

The ECE was calculated to be  $\sim 7.5\%$  from the following equation, considering the total incident power intensity in the wavelength range 200-475 nm ( $488 \text{ mW/cm}^2$ ), and  $\text{H}_2$  evolution rate of  $\sim 1660 \text{ } \mu\text{mol/hr}$  (generated under full arc illumination with AM1.5G filter).

$$ECE = \frac{H_2 \left( \frac{\text{mmol}}{\text{s}} \right) \times 237 \text{ kJ} \times 1000}{\rho_{incident\_total} \left( \frac{\text{mW}}{\text{sq.cm}} \right) \times A_{sample}(\text{sq.cm})} \times 100 \% \quad (6)$$

## References

- [1] T. R. Cook, D. K. Dogutan, S. Y. Reece, Y. Surendranath, T. S. Teets, and D. G. Nocera, "Solar Energy Supply and Storage for the Legacy and Nonlegacy Worlds," *Chemical Reviews*, vol. 110, pp. 6474-6502, 2010.
- [2] N. S. Lewis and D. G. Nocera, "Powering the planet: Chemical challenges in solar energy utilization," *Proceedings of the National Academy of Sciences*, vol. 103, pp. 15729-15735, 2006.
- [3] J. A. Turner, "A Realizable Renewable Energy Future," *Science*, vol. 285, pp. 687-689, 1999.
- [4] R. E. Blankenship, D. M. Tiede, J. Barber, G. W. Brudvig, G. Fleming, M. Ghirardi, *et al.*, "Comparing Photosynthetic and Photovoltaic Efficiencies and Recognizing the Potential for Improvement," *Science*, vol. 332, pp. 805-809, 2011.
- [5] S. C. Whitfield, E. A. Rosa, A. Dan, and T. Dietz, "The future of nuclear power: Value orientations and risk perception," *Risk Analysis*, vol. 29, pp. 425-437, 2009.
- [6] D. Abbott, "Keeping the energy debate clean: How do we supply the world's energy needs?," *Proceedings of the IEEE*, vol. 98, pp. 42-66, 2010.
- [7] K. Rajeshwar, R. D. McConnell, and S. Licht, *Solar hydrogen generation*. New York, Springer, 2008.
- [8] L. Vayssieres, *On solar hydrogen and nanotechnology*. John Wiley & Sons, 2010.
- [9] A. Kudo and Y. Miseki, "Heterogeneous photocatalyst materials for water splitting," *Chemical Society Reviews*, vol. 38, pp. 253-278, 2009.
- [10] M. G. Walter, E. L. Warren, J. R. McKone, S. W. Boettcher, Q. Mi, E. A. Santori, *et al.*, "Solar Water Splitting Cells," *Chemical Reviews*, vol. 110, pp. 6446-6473, 2010.
- [11] A. Fujishima and K. Honda, "Electrochemical Photolysis of Water at a Semiconductor Electrode," *Nature*, vol. 238, pp. 37-38, 1972.
- [12] A. Kubacka, M. Fernandez-Garcia, and G. Colon, "Advanced nanoarchitectures for solar photocatalytic applications," *Chemical Reviews*, vol. 112, pp. 1555-1614, 2011.
- [13] X. Chen, C. Li, M. Graetzel, R. Kostecki, and S. S. Mao, "Nanomaterials for renewable energy production and storage," *Chemical Society Reviews*, vol. 41, pp. 7909-7937, 2012.
- [14] F. E. Osterloh, "Inorganic nanostructures for photoelectrochemical and photocatalytic water splitting," *Chemical Society Reviews*, vol. 42, pp. 2294-2320, 2013.
- [15] H. Tong, S. Ouyang, Y. Bi, N. Umezawa, M. Oshikiri, and J. Ye, "Nano-photocatalytic Materials: Possibilities and Challenges," *Advanced Materials*, vol. 24, pp. 229-251, 2012.
- [16] S. S. Mao and S. Shen, "Hydrogen production: Catalysing artificial photosynthesis," *Nat Photon*, vol. 7, pp. 944-946, 2013.

- [17] L. Yang, H. Zhou, T. Fan, and D. Zhang, "Semiconductor photocatalysts for water oxidation: current status and challenges," *Physical Chemistry Chemical Physics*, vol. 16, pp. 6810-6826, 2014.
- [18] J. Li and N. Wu, "Semiconductor-Based Photocatalysts and Photoelectrochemical Cells for Solar Fuel Generation: A Review," *Catalysis Science & Technology*, 2014.
- [19] X. Chen, S. Shen, L. Guo, and S. S. Mao, "Semiconductor-based photocatalytic hydrogen generation," *Chemical Reviews*, vol. 110, pp. 6503-6570, 2010.
- [20] R. Navarro, F. Del Valle, J. Villoria de la Mano, M. Álvarez-Galván, and J. Fierro, "Photocatalytic water splitting under visible light: concept and catalysts development," *Advances in Chemical Engineering*, vol. 36, pp. 111-143, 2009.
- [21] R. Abe, "Recent progress on photocatalytic and photoelectrochemical water splitting under visible light irradiation," *Journal of Photochemistry and Photobiology C: Photochemistry Reviews*, vol. 11, pp. 179-209, 2010.
- [22] K. Maeda and K. Domen, "New Non-Oxide Photocatalysts Designed for Overall Water Splitting under Visible Light," *The Journal of Physical Chemistry C*, vol. 111, pp. 7851-7861, 2007.
- [23] R. Abe, "Development of a new system for photocatalytic water splitting into H<sub>2</sub> and O<sub>2</sub> under visible light irradiation," *Bulletin of the Chemical Society of Japan*, vol. 84, pp. 1000-1030, 2011.
- [24] A. Kudo, "Recent progress in the development of visible light-driven powdered photocatalysts for water splitting," *International journal of hydrogen energy*, vol. 32, pp. 2673-2678, 2007.
- [25] K. Maeda, "Photocatalytic water splitting using semiconductor particles: History and recent developments," *Journal of Photochemistry and Photobiology C: Photochemistry Reviews*, vol. 12, pp. 237-268, 2011.
- [26] K. Maeda and K. Domen, "Photocatalytic Water Splitting: Recent Progress and Future Challenges," *The Journal of Physical Chemistry Letters*, vol. 1, pp. 2655-2661, 2010.
- [27] L. M. Peter and K. Upul Wijayantha, "Photoelectrochemical Water Splitting at Semiconductor Electrodes: Fundamental Problems and New Perspectives," *Chem. Phys. Chem*, 2014.
- [28] M. Grätzel, "Photoelectrochemical cells," *Nature*, vol. 414, pp. 338-344, 2001.
- [29] C. Liu, N. P. Dasgupta, and P. Yang, "Semiconductor Nanowires for Artificial Photosynthesis," *Chemistry of Materials*, vol. 26, pp. 415-422, 2013.
- [30] Y. Tachibana, L. Vayssieres, and J. R. Durrant, "Artificial photosynthesis for solar water-splitting," *Nat Photon*, vol. 6, pp. 511-518, 2012.
- [31] O. Khaselev and J. A. Turner, "A Monolithic Photovoltaic-Photoelectrochemical Device for Hydrogen Production via Water Splitting," *Science*, vol. 280, pp. 425-427, 1998.
- [32] K. Maeda, K. Teramura, D. Lu, T. Takata, N. Saito, Y. Inoue, *et al.*, "Photocatalyst releasing hydrogen from water," *Nature*, vol. 440, pp. 295-295, 2006.

- [33] S. Y. Reece, J. A. Hamel, K. Sung, T. D. Jarvi, A. J. Esswein, J. J. H. Pijpers, *et al.*, "Wireless Solar Water Splitting Using Silicon-Based Semiconductors and Earth-Abundant Catalysts," *Science*, vol. 334, pp. 645-648, 2011.
- [34] D. G. Nocera, "The Artificial Leaf," *Accounts of Chemical Research*, vol. 45, pp. 767-776, 2012.
- [35] A. J. Bard and M. A. Fox, "Artificial photosynthesis: solar splitting of water to hydrogen and oxygen," *Accounts of Chemical Research*, vol. 28, pp. 141-145, 1995.
- [36] M. Graetzel, "Artificial photosynthesis: water cleavage into hydrogen and oxygen by visible light," *Accounts of Chemical Research*, vol. 14, pp. 376-384, 1981.
- [37] A. J. Bard, "Photoelectrochemistry," *Science*, vol. 207, pp. 139-144, 1980.
- [38] J. Wu, "When group-III nitrides go infrared: New properties and perspectives," *Journal of Applied Physics*, vol. 106, p. 011101, 2009.
- [39] D. Zhuang and J. H. Edgar, "Wet etching of GaN, AlN, and SiC: a review," *Materials Science and Engineering: R: Reports*, vol. 48, pp. 1-46, 2005.
- [40] A. G. Bhuiyan, A. Hashimoto, and A. Yamamoto, "Indium nitride (InN): A review on growth, characterization, and properties," *Journal of Applied Physics*, vol. 94, pp. 2779-2808, 2003.
- [41] P. G. Moses and C. G. V. d. Walle, "Band bowing and band alignment in InGaN alloys," *Applied Physics Letters*, vol. 96, p. 021908, 2010.
- [42] J. Beach, R. Collins, and J. Turner, "Band-edge Potentials of n-type and p-type GaN," *Journal of The Electrochemical Society*, vol. 150, pp. A899-A904, 2003.
- [43] S. S. Kocha, M. W. Peterson, D. J. Arent, J. M. Redwing, M. A. Tischler, and J. A. Turner, "Electrochemical Investigation of the Gallium Nitride-Aqueous Electrolyte Interface," *Journal of the Electrochemical Society*, vol. 142, pp. L238-L240, 1995.
- [44] I. Waki, D. Cohen, R. Lal, U. Mishra, S. P. DenBaars, and S. Nakamura, "Direct water photoelectrolysis with patterned n-GaN," *Applied Physics Letters*, vol. 91, p. 093519, 2007.
- [45] S.-Y. Liu, Y.-C. Lin, J.-C. Ye, S. Tu, F. Huang, M. Lee, *et al.*, "Hydrogen gas generation using n-GaN photoelectrodes with immersed Indium Tin Oxide ohmic contacts," *Optics express*, vol. 19, pp. A1196-A1201, 2011.
- [46] S.-Y. Liu, J. Sheu, M. Lee, Y.-C. Lin, S. Tu, F. Huang, *et al.*, "Immersed finger-type indium tin oxide ohmic contacts on p-GaN photoelectrodes for photoelectrochemical hydrogen generation," *Optics express*, vol. 20, pp. A190-A196, 2012.
- [47] S. Kikawa, N. Kobayashi, J. Yamamoto, Y. Ban, and K. Matsumoto, "Flat-Band Potentials of Ga-face and N-face in Free-Standing n-GaN Electrode and Their Effects on Water Electrolysis," *e-Journal of Surface Science and Nanotechnology*, vol. 7, pp. 847-850, 2009.
- [48] Y.-G. Lin, Y.-K. Hsu, A. M. Basilio, Y.-T. Chen, K.-H. Chen, and L.-C. Chen, "Photoelectrochemical activity on Ga-polar and N-polar GaN surfaces for energy conversion," *Optics Express*, vol. 22, pp. A21-A27, 2014.

- [49] J. Benton, J. Bai, and T. Wang, "Enhancement in solar hydrogen generation efficiency using a GaN-based nanorod structure," *Applied Physics Letters*, vol. 102, pp. 173907, 2013.
- [50] M. Ono, K. Fujii, T. Ito, Y. Iwaki, A. Hirako, T. Yao, *et al.*, "Photoelectrochemical reaction and H<sub>2</sub> generation at zero bias optimized by carrier concentration of n-type GaN," *The Journal of Chemical Physics*, vol. 126, pp. 054708-054708, 2007.
- [51] K. Fujii, H. Nakayama, K. Sato, T. Kato, M.-W. Cho, and T. Yao, "Improvement of hydrogen generation efficiency using GaN photoelectrochemical reaction in electrolytes with alcohol," *physica status solidi (c)*, vol. 5, pp. 2333-2335, 2008.
- [52] B. AlOtaibi, M. Harati, S. Fan, S. Zhao, H. Nguyen, M. Kibria, *et al.*, "High efficiency photoelectrochemical water splitting and hydrogen generation using GaN nanowire photoelectrode," *Nanotechnology*, vol. 24, p. 175401, 2013.
- [53] J. Wallys, S. Hoffmann, F. Furtmayr, J. Teubert, and M. Eickhoff, "Electrochemical properties of GaN nanowire electrodes—influence of doping and control by external bias," *Nanotechnology*, vol. 23, p. 165701, 2012.
- [54] A. Nakamura, K. Fujii, M. Sugiyama, and Y. Nakano, "A nitride based polarization-engineered photocathode for water splitting without a p-type semiconductor," *Physical Chemistry Chemical Physics*, vol. 16, pp. 15326-15330, 2014.
- [55] S.-Y. Liu, J. Sheu, Y.-C. Lin, S. Tu, F. Huang, M. Lee, *et al.*, "Mn-doped GaN as photoelectrodes for the photoelectrolysis of water under visible light," *Optics express*, vol. 20, pp. A678-A683, 2012.
- [56] J. Li, J. Y. Lin, and H. X. Jiang, "Direct hydrogen gas generation by using InGaN epilayers as working electrodes," *Applied Physics Letters*, vol. 93, pp. 162107-162107-3, 2008.
- [57] W. Luo, B. Liu, Z. Li, Z. Xie, D. Chen, Z. Zou, *et al.*, "Stable response to visible light of InGaN photoelectrodes," *Applied Physics Letters*, vol. 92, p. 262110, 2008.
- [58] M. Li, W. Luo, B. Liu, X. Zhao, Z. Li, D. Chen, *et al.*, "Remarkable enhancement in photocurrent of In<sub>0.20</sub>Ga<sub>0.80</sub>N photoanode by using an electrochemical surface treatment," *Applied Physics Letters*, vol. 99, pp. 112108, 2011.
- [59] M. Li, W. Luo, Q. Liu, Z. Zhuang, Z. Li, B. Liu, *et al.*, "An efficient In<sub>0.30</sub>Ga<sub>0.70</sub>N photoelectrode by decreasing the surface recombination centres in a H<sub>2</sub>SO<sub>4</sub> aqueous solution," *Journal of Physics D: Applied Physics*, vol. 46, p. 345103, 2013.
- [60] K. Aryal, B. N. Pantha, J. Li, J. Y. Lin, and H. X. Jiang, "Hydrogen generation by solar water splitting using p-InGaN photoelectrochemical cells," *Applied Physics Letters*, vol. 96, p. 052110, 2010.
- [61] N. H. Alvi, P. E. D. Soto Rodriguez, P. Kumar, V. J. Gómez, P. Aseev, A. H. Alvi, *et al.*, "Photoelectrochemical water splitting and hydrogen generation by a spontaneously formed InGaN nanowall network," *Applied Physics Letters*, vol. 104, pp. 223104, 2014.

- [62] Y. J. Hwang, C. H. Wu, C. Hahn, H. E. Jeong, and P. Yang, "Si/InGaN Core/Shell Hierarchical Nanowire Arrays and their Photoelectrochemical Properties," *Nano Letters*, vol. 12, pp. 1678-1682, 2012.
- [63] B. AlOtaibi, H. P. T. Nguyen, S. Zhao, M. G. Kibria, S. Fan, and Z. Mi, "Highly Stable Photoelectrochemical Water Splitting and Hydrogen Generation Using a Double-Band InGaN/GaN Core/Shell Nanowire Photoanode," *Nano Letters*, vol. 13, pp. 4356-4361, 2013.
- [64] L. Caccamo, J. Hartmann, C. Fàbrega, S. Estradé, G. Lilienkamp, J. D. Prades, *et al.*, "Band Engineered Epitaxial 3D GaN-InGaN Core-Shell Rod Arrays as an Advanced Photoanode for Visible-Light-Driven Water Splitting," *ACS applied materials & interfaces*, vol. 6, pp. 2235-2240, 2014.
- [65] J. Kamimura, P. Bogdanoff, J. Lähnemann, C. Hauswald, L. Geelhaar, S. Fiechter, *et al.*, "Photoelectrochemical Properties of (In, Ga) N Nanowires for Water Splitting Investigated by in Situ Electrochemical Mass Spectroscopy," *Journal of the American Chemical Society*, vol. 135, pp. 10242-10245, 2013.
- [66] J. Benton, J. Bai, and T. Wang, "Significantly enhanced performance of an InGaN/GaN nanostructure based photo-electrode for solar power hydrogen generation," *Applied Physics Letters*, vol. 103, pp. 133904, 2013.
- [67] S.-Y. Liu, J. Sheu, Y.-C. Lin, Y.-T. Chen, S. Tu, M. Lee, *et al.*, "InGaN working electrodes with assisted bias generated from GaAs solar cells for efficient water splitting," *Optics express*, vol. 21, pp. A991-A996, 2013.
- [68] R. Dahal, B. N. Pantha, J. Li, J. Y. Lin, and H. X. Jiang, "Realizing InGaN monolithic solar-photoelectrochemical cells for artificial photosynthesis," *Applied Physics Letters*, vol. 104, p. 143901, 2014.
- [69] V. Chakrapani, J. Thangala, and M. K. Sunkara, "WO<sub>3</sub> and W<sub>2</sub>N nanowire arrays for photoelectrochemical hydrogen production," *International Journal of Hydrogen Energy*, vol. 34, pp. 9050-9059, 2009.
- [70] X. Feng, T. J. LaTempa, J. I. Basham, G. K. Mor, O. K. Varghese, and C. A. Grimes, "Ta<sub>3</sub>N<sub>5</sub> nanotube arrays for visible light water photoelectrolysis," *Nano letters*, vol. 10, pp. 948-952, 2010.
- [71] Y. Cong, H. S. Park, S. Wang, H. X. Dang, F.-R. F. Fan, C. B. Mullins, *et al.*, "Synthesis of Ta<sub>3</sub>N<sub>5</sub> Nanotube Arrays Modified with Electrocatalysts for Photoelectrochemical Water Oxidation," *The Journal of Physical Chemistry C*, vol. 116, pp. 14541-14550, 2012.
- [72] J. Sato, N. Saito, Y. Yamada, K. Maeda, T. Takata, J. N. Kondo, *et al.*, "RuO<sub>2</sub>-Loaded β-Ge<sub>3</sub>N<sub>4</sub> as a Non-Oxide Photocatalyst for Overall Water Splitting," *Journal of the American Chemical Society*, vol. 127, pp. 4150-4151, 2005.
- [73] K. Maeda, K. Teramura, N. Saito, Y. Inoue, and K. Domen, "Photocatalytic Overall Water Splitting on Gallium Nitride Powder," *Bulletin of the Chemical Society of Japan*, vol. 80, pp. 1004-1010, 2007.
- [74] T. Kida, Y. Minami, G. Guan, M. Nagano, M. Akiyama, and A. Yoshida, "Photocatalytic activity of gallium nitride for producing hydrogen from water under light irradiation," *Journal of Materials Science*, vol. 41, pp. 3527-3534, 2006.

- [75] N. Arai, N. Saito, H. Nishiyama, K. Domen, H. Kobayashi, K. Sato, *et al.*, "Effects of divalent metal ion ( $Mg^{2+}$ ,  $Zn^{2+}$  and  $Be^{2+}$ ) doping on photocatalytic activity of ruthenium oxide-loaded gallium nitride for water splitting," *Catalysis Today*, vol. 129, pp. 407-413, 2007.
- [76] H. S. Jung, Y. J. Hong, Y. Li, J. Cho, Y.-J. Kim, and G.-C. Yi, "Photocatalysis Using GaN Nanowires," *ACS Nano*, vol. 2, pp. 637-642, 2008.
- [77] J. B. Park, N.-J. Kim, Y.-J. Kim, S.-H. Lee, and G.-C. Yi, "Metal catalyst-assisted growth of GaN nanowires on graphene films for flexible photocatalyst applications," *Current Applied Physics*, 2014.
- [78] W. Lai, Z. Wei, H. Zhi-Biao, and L. Yi, "Photocatalysis of InGaN Nanodots Responsive to Visible Light," *Chinese Physics Letters*, vol. 28, pp. 57301-57304, 2011.
- [79] L. Yuliati, J.-H. Yang, X. Wang, K. Maeda, T. Takata, M. Antonietti, *et al.*, "Highly active tantalum (v) nitride nanoparticles prepared from a mesoporous carbon nitride template for photocatalytic hydrogen evolution under visible light irradiation," *Journal of Materials Chemistry*, vol. 20, pp. 4295-4298, 2010.
- [80] X. Wang, K. Maeda, A. Thomas, K. Takanabe, G. Xin, J. M. Carlsson, *et al.*, "A metal-free polymeric photocatalyst for hydrogen production from water under visible light," *Nat Mater*, vol. 8, pp. 76-80, 2009.
- [81] N. P. Dasgupta, J. Sun, C. Liu, S. Brittman, S. C. Andrews, J. Lim, *et al.*, "25th Anniversary article: semiconductor nanowires—synthesis, characterization, and applications," *Advanced Materials*, vol. 26, pp. 2137-2184, 2014.
- [82] C. Burda, X. Chen, R. Narayanan, and M. A. El-Sayed, "Chemistry and Properties of Nanocrystals of Different Shapes," *Chemical Reviews*, vol. 105, pp. 1025-1102, 2005.
- [83] A. P. Alivisatos, "Perspectives on the physical chemistry of semiconductor nanocrystals," *The Journal of Physical Chemistry*, vol. 100, pp. 13226-13239, 1996.
- [84] J. Jasieniak, M. Califano, and S. E. Watkins, "Size-Dependent Valence and Conduction Band-Edge Energies of Semiconductor Nanocrystals," *ACS Nano*, vol. 5, pp. 5888-5902, 2011.
- [85] X. Zhang, Y. L. Chen, R.-S. Liu, and D. P. Tsai, "Plasmonic photocatalysis," *Reports on Progress in Physics*, vol. 76, pp. 046401, 2013.
- [86] S. Zhao, M. Kibria, Q. Wang, H. Nguyen, and Z. Mi, "Growth of large-scale vertically aligned GaN nanowires and their heterostructures with high uniformity on  $SiO_x$  by catalyst-free molecular beam epitaxy," *Nanoscale*, vol. 5, pp. 5283-5287, 2013.
- [87] N. Wu, J. Wang, D. N. Tafen, H. Wang, J.-G. Zheng, J. P. Lewis, *et al.*, "Shape-Enhanced Photocatalytic Activity of Single-Crystalline Anatase  $TiO_2$  (101) Nanobelts," *Journal of the American Chemical Society*, vol. 132, pp. 6679-6685, 2010.
- [88] R. Wagner and W. Ellis, "Vapor-liquid-solid mechanism of single crystal growth," *Applied Physics Letters*, vol. 4, pp. 89-90, 1964.
- [89] M. Sanchez-Garcia, E. Calleja, E. Monroy, F. Sanchez, F. Calle, E. Munoz, *et al.*, "The effect of the III/V ratio and substrate temperature on the morphology and

- properties of GaN-and AlN-layers grown by molecular beam epitaxy on Si (111)," *Journal of crystal growth*, vol. 183, pp. 23-30, 1998.
- [90] E. Calleja, M. Sánchez-García, F. Sanchez, F. Calle, F. Naranjo, E. Munoz, *et al.*, "Growth of III-nitrides on Si (111) by molecular beam epitaxy doping, optical, and electrical properties," *Journal of crystal growth*, vol. 201, pp. 296-317, 1999.
- [91] M. Yoshizawa, A. Kikuchi, M. Mori, N. Fujita, and K. Kishino, "Growth of self-organized GaN nanostructures on Al<sub>2</sub>O<sub>3</sub> (0001) by RF-radical source molecular beam epitaxy," *Japanese journal of applied physics*, vol. 36, p. L459, 1997.
- [92] D. Tsivion, M. Schwartzman, R. Popovitz-Biro, P. von Huth, and E. Joselevich, "Guided growth of millimeter-long horizontal nanowires with controlled orientations," *Science*, vol. 333, pp. 1003-1007, 2011.
- [93] J. Ristić, M. Sánchez-García, J. Ulloa, E. Calleja, J. Sanchez-Páramo, J. Calleja, *et al.*, "AlGaIn nanocolumns and AlGaIn/GaN/AlGaIn nanostructures grown by molecular beam epitaxy," *physica status solidi (b)*, vol. 234, pp. 717-721, 2002.
- [94] R. Meijers, T. Richter, R. Calarco, T. Stoica, H.-P. Boehm, M. Marso, *et al.*, "GaN-nanowhiskers: MBE-growth conditions and optical properties," *Journal of crystal growth*, vol. 289, pp. 381-386, 2006.
- [95] E. Calleja, M. Sanchez-Garcia, F. Sánchez, F. Calle, F. Naranjo, E. Munoz, *et al.*, "Luminescence properties and defects in GaN nanocolumns grown by molecular beam epitaxy," *Physical Review B*, vol. 62, p. 16826, 2000.
- [96] F. Furtmayr, M. Vielemeyer, M. Stutzmann, J. Arbiol, S. Estrade, F. Peiro, *et al.*, "Nucleation and growth of GaN nanorods on Si (111) surfaces by plasma-assisted molecular beam epitaxy - The influence of Si- and Mg-doping," *Journal of Applied Physics*, vol. 104, p. 034309, 2008.
- [97] F. Furtmayr, M. Vielemeyer, M. Stutzmann, A. Laufer, B. K. Meyer, and M. Eickhoff, "Optical properties of Si- and Mg-doped gallium nitride nanowires grown by plasma-assisted molecular beam epitaxy," *Journal of Applied Physics*, vol. 104, pp. 074309, 2008.
- [98] R. Debnath, R. Meijers, T. Richter, T. Stoica, R. Calarco, and H. Lüth, "Mechanism of molecular beam epitaxy growth of GaN nanowires on Si (111)," *Applied physics letters*, vol. 90, p. 123117, 2007.
- [99] J. Ristić, E. Calleja, S. Fernández-Garrido, L. Cerutti, A. Trampert, U. Jahn, *et al.*, "On the mechanisms of spontaneous growth of III-nitride nanocolumns by plasma-assisted molecular beam epitaxy," *Journal of crystal growth*, vol. 310, pp. 4035-4045, 2008.
- [100] T. Stoica and R. Calarco, "Doping of III-Nitride Nanowires Grown by Molecular Beam Epitaxy," *IEEE Journal of Selected Topics in Quantum Electronics*, vol. 17, pp. 859-868, 2011.
- [101] K. A. Bertness, N. A. Sanford, and A. V. Davydov, "GaN nanowires grown by molecular beam epitaxy," *Selected Topics in Quantum Electronics, IEEE Journal of*, vol. 17, pp. 847-858, 2011.
- [102] S. Fernández-Garrido, V. M. Kaganer, K. K. Sabelfeld, T. Gotschke, J. Grandal, E. Calleja, *et al.*, "Self-Regulated Radius of Spontaneously Formed GaN Nanowires in Molecular Beam Epitaxy," *Nano Letters*, vol. 13, pp. 3274-3280, 2013.

- [103] S. Fernández-Garrido, X. Kong, T. Gotschke, R. Calarco, L. Geelhaar, A. Trampert, *et al.*, "Spontaneous Nucleation and Growth of GaN Nanowires: The Fundamental Role of Crystal Polarity," *Nano Letters*, vol. 12, pp. 6119-6125, 2012.
- [104] D. B. Williams and C. B. Carter, *The Transmission Electron Microscope*. Springer US, 1996.
- [105] R. F. Egerton, *Electron energy-loss spectroscopy in the electron microscope*. Vol. 233. New York: Plenum Press, 1996.
- [106] T. Schmidt, K. Lischka, and W. Zulehner, "Excitation-power dependence of the near-band-edge photoluminescence of semiconductors," *Physical Review B*, vol. 45, p. 8989, 1992.
- [107] A. Smekal, "Zur quantentheorie der dispersion," *Naturwissenschaften*, vol. 11, pp. 873-875, 1923.
- [108] C. V. Raman and K. S. Krishnan, "A new type of secondary radiation," *Nature*, vol. 121, pp. 501-502, 1928.
- [109] E. Smith and G. Dent, *Modern Raman spectroscopy: a practical approach*. John Wiley & Sons, 2005.
- [110] J. F. Moulder, W. F. Stickle, P. E. Sobol, and K. D. Bomben, *Handbook of X-ray photoelectron spectroscopy* vol. 40, Perkin Elmer Eden Prairie, MN, 1992.
- [111] K. Siegbahn and K. Edvarson, " $\beta$ -ray spectroscopy in the precision range of  $1: 10^5$ ," *Nuclear Physics*, vol. 1, pp. 137-159, 1956.
- [112] H. Hu, J. Ding, S. Zhang, Y. Li, L. Bai, and N. Yuan, "Photodeposition of Ag<sub>2</sub>S on TiO<sub>2</sub> nanorod arrays for quantum dot-sensitized solar cells," *Nanoscale research letters*, vol. 8, pp. 1-7, 2013.
- [113] F. E. Osterloh, "Inorganic Materials as Catalysts for Photochemical Splitting of Water," *Chemistry of Materials*, vol. 20, pp. 35-54, 2007.
- [114] K. Domen, "Photocatalytic Water Splitting Using Oxynitride and Nitride Semiconductor Powders for Production of Solar Hydrogen," *The Electrochemical Society*, 57, 2013.
- [115] X. Shen, Y. A. Small, J. Wang, P. B. Allen, M. V. Fernandez-Serra, M. S. Hybertsen, *et al.*, "Photocatalytic Water Oxidation at the GaN (10 $\bar{1}$ 0)-Water Interface," *The Journal of Physical Chemistry C*, vol. 114, pp. 13695-13704, 2010.
- [116] J. Wang, L. S. Pedroza, A. Poissier, and M. V. Fernández-Serra, "Water Dissociation at the GaN(10 $\bar{1}$ 0) Surface: Structure, Dynamics and Surface Acidity," *The Journal of Physical Chemistry C*, vol. 116, pp. 14382-14389, 2012.
- [117] M. G. Kibria, H. P. T. Nguyen, K. Cui, S. Zhao, D. Liu, H. Guo, *et al.*, "One-Step Overall Water Splitting under Visible Light Using Multiband InGaN/GaN Nanowire Heterostructures," *ACS Nano*, vol. 7, pp. 7886-7893, 2013.
- [118] P.-T. Chen, C.-L. Sun, and M. Hayashi, "First-Principles Calculations of Hydrogen Generation Due to Water Splitting on Polar GaN Surfaces," *The Journal of Physical Chemistry C*, vol. 114, pp. 18228-18232, 2010.
- [119] A. V. Akimov, J. T. Muckerman, and O. V. Prezhdo, "Nonadiabatic Dynamics of Positive Charge during Photocatalytic Water Splitting on GaN(10-10) Surface:

- Charge Localization Governs Splitting Efficiency," *Journal of the American Chemical Society*, vol. 135, pp. 8682-8691, 2013.
- [120] A. J. Nozik and R. Memming, "Physical Chemistry of Semiconductor–Liquid Interfaces," *The Journal of Physical Chemistry*, vol. 100, pp. 13061-13078, 1996.
- [121] S. Barbet, R. Aubry, M.-A. d. Forte-Poisson, J.-C. Jacquet, D. Deresmes, T. Melin, *et al.*, "Surface potential of n- and p-type GaN measured by Kelvin force microscopy," *Applied Physics Letters*, vol. 93, p. 212107, 2008.
- [122] M. Bertelli, P. Löptien, M. Wenderoth, A. Rizzi, R. G. Ulbrich, M. C. Righi, *et al.*, "Atomic and electronic structure of the nonpolar GaN(11 $\bar{1}$ 0) surface," *Physical Review B*, vol. 80, p. 115324, 2009.
- [123] C. G. V. d. Walle and D. Segev, "Microscopic origins of surface states on nitride surfaces," *Journal of Applied Physics*, vol. 101, p. 081704, 2007.
- [124] P. V. Kamat, "Photophysical, Photochemical and Photocatalytic Aspects of Metal Nanoparticles," *The Journal of Physical Chemistry B*, vol. 106, pp. 7729-7744, 2002.
- [125] M. Yoshida, K. Takane, K. Maeda, A. Ishikawa, J. Kubota, Y. Sakata, *et al.*, "Role and Function of Noble-Metal/Cr-Layer Core/Shell Structure Cocatalysts for Photocatalytic Overall Water Splitting Studied by Model Electrodes," *The Journal of Physical Chemistry C*, vol. 113, pp. 10151-10157, 2009.
- [126] C. Liu, J. Tang, H. M. Chen, B. Liu, and P. Yang, "A Fully Integrated Nanosystem of Semiconductor Nanowires for Direct Solar Water Splitting," *Nano Letters*, vol. 13, pp. 2989-2992, 2013.
- [127] G. Wang, H. Wang, Y. Ling, Y. Tang, X. Yang, R. C. Fitzmorris, *et al.*, "Hydrogen-Treated TiO<sub>2</sub> Nanowire Arrays for Photoelectrochemical Water Splitting," *Nano Letters*, vol. 11, pp. 3026-3033, 2011.
- [128] D. R. Khanal, W. Walukiewicz, J. Grandal, E. Calleja, and J. Wu, "Determining surface Fermi level pinning position of InN nanowires using electrolyte gating," *Applied Physics Letters*, vol. 95, pp. 173114, 2009.
- [129] D. Wang, A. Pierre, M. G. Kibria, K. Cui, X. Han, K. H. Bevan, *et al.*, "Wafer-Level Photocatalytic Water Splitting on GaN Nanowire Arrays Grown by Molecular Beam Epitaxy," *Nano Letters*, vol. 11, pp. 2353-2357, 2011.
- [130] L. Ivanova, S. Borisova, H. Eisele, M. Dahne, A. Laubsch, and P. Ebert, "Surface states and origin of the Fermi level pinning on nonpolar GaN(1 $\bar{1}$ 00) surfaces," *Applied Physics Letters*, vol. 93, p. 192110, 2008.
- [131] H. Sezen, E. Ozbay, O. Aktas, and S. Suzer, "Transient surface photovoltage in n- and p-GaN as probed by x-ray photoelectron spectroscopy," *Applied Physics Letters*, vol. 98, p. 111901, 2011.
- [132] C. Fàbrega, D. Monllor-Satoca, S. Ampudia, A. Parra, T. Andreu, and J. R. Morante, "Tuning the Fermi Level and the Kinetics of Surface States of TiO<sub>2</sub> Nanorods by Means of Ammonia Treatments," *The Journal of Physical Chemistry C*, vol. 117, pp. 20517-20524, 2013.
- [133] T. Stoica and R. Calarco, "Doping of III-Nitride Nanowires Grown by Molecular Beam Epitaxy," *Selected Topics in Quantum Electronics, IEEE Journal of*, vol. 17, pp. 859-868, 2011.

- [134] E. Cimpoiasu, E. Stern, R. Klie, R. A. Munden, G. Cheng, and M. A. Reed, "The effect of Mg doping on GaN nanowires," *Nanotechnology*, vol. 17, p. 5735, 2006.
- [135] A. Bhattacharyya, W. Li, J. Cabalu, T. D. Moustakas, D. J. Smith, and R. L. Hervig, "Efficient p-type doping of GaN films by plasma-assisted molecular beam epitaxy," *Applied Physics Letters*, vol. 85, pp. 4956-4958, 2004.
- [136] T. S. Cheng, S. V. Novikov, C. T. Foxon, and J. W. Orton, "Mechanisms of magnesium incorporation into GaN layers grown by molecular beam epitaxy," *Solid State Communications*, vol. 109, pp. 439-443, 1999.
- [137] S. Zhao, B. H. Le, D. P. Liu, X. D. Liu, M. G. Kibria, T. Szkopek, *et al.*, "p-Type InN Nanowires," *Nano Letters*, vol. 13, pp. 5509-5513, 2013.
- [138] Z. Zhong, F. Qian, D. Wang, and C. M. Lieber, "Synthesis of p-Type Gallium Nitride Nanowires for Electronic and Photonic Nanodevices," *Nano Letters*, vol. 3, pp. 343-346, 2003.
- [139] J. Arbiol, S. Estradé, J. D. Prades, A. Cirera, F. Furtmayr, C. Stark, *et al.*, "Triple-twin domains in Mg doped GaN wurtzite nanowires: structural and electronic properties of this zinc-blende-like stacking," *Nanotechnology*, vol. 20, p. 145704, 2009.
- [140] S. A. Chambers, T. Droubay, T. C. Kaspar, and M. Gutowski, "Experimental determination of valence band maxima for SrTiO<sub>3</sub>, TiO<sub>2</sub>, and SrO and the associated valence band offsets with Si(001)," *Journal of Vacuum Science & Technology B: Microelectronics and Nanometer Structures*, vol. 22, pp. 2205-2215, 2004.
- [141] C. I. Wu, A. Kahn, N. Taskar, D. Dorman, and D. Gallagher, "GaN (0001)-(1 x 1) surfaces: Composition and electronic properties," *Journal of Applied Physics*, vol. 83, pp. 4249-4252, 1998.
- [142] R. Kirste, M. P. Hoffmann, J. Tweedie, Z. Bryan, G. Callsen, T. Kure, *et al.*, "Compensation effects in GaN:Mg probed by Raman spectroscopy and photoluminescence measurements," *Journal of Applied Physics*, vol. 113, p. 103504, 2013.
- [143] T. Hashizume, "Effects of Mg accumulation on chemical and electronic properties of Mg-doped p-type GaN surface," *Journal of Applied Physics*, vol. 94, pp. 431-436, 2003.
- [144] K. Jeganathan, R. K. Debnath, R. Meijers, T. Stoica, R. Calarco, D. Grutzmacher, *et al.*, "Raman scattering of phonon-plasmon coupled modes in self-assembled GaN nanowires," *Journal of Applied Physics*, vol. 105, p. 123707, 2009.
- [145] H. Hiroshi, "Properties of GaN and related compounds studied by means of Raman scattering," *Journal of Physics: Condensed Matter*, vol. 14, p. R967, 2002.
- [146] K. Maeda, K. Teramura, D. Lu, N. Saito, Y. Inoue, and K. Domen, "Roles of Rh/Cr<sub>2</sub>O<sub>3</sub> (Core/Shell) Nanoparticles Photodeposited on Visible-Light-Responsive (Ga<sub>1-x</sub>Zn<sub>x</sub>)(N<sub>1-x</sub>O<sub>x</sub>) Solid Solutions in Photocatalytic Overall Water Splitting," *The Journal of Physical Chemistry C*, vol. 111, pp. 7554-7560, 2007.
- [147] J. F. Moulder, W. F. Stickle, P. E. Sobol & K. D. Bomben, "Handbook of X-ray photoelectron spectroscopy" Vol. 40, Eden Prairie, MN: Perkin Elmer, 1992.

- [148] C. T. Campbell, "Catalyst-support interactions: Electronic perturbations," *Nature chemistry*, vol. 4, pp. 597-598, 2012.
- [149] F. Furtmayr, M. Vilemeyer, M. Stutzmann, A. Laufer, B. K. Meyer, and M. Eickhoff, "Optical properties of Si- and Mg-doped gallium nitride nanowires grown by plasma-assisted molecular beam epitaxy," *Journal of Applied Physics*, vol. 104, p. 074309, 2008.
- [150] L. Romano, M. Kneissl, J. Northrup, C. Van de Walle, and D. Treat, "Influence of microstructure on the carrier concentration of Mg-doped GaN films," *Applied Physics Letters*, vol. 79, pp. 2734-2736, 2001.
- [151] R. Kirste, M. P. Hoffmann, J. Tweedie, Z. Bryan, G. Callsen, T. Kure, *et al.*, "Compensation effects in GaN:Mg probed by Raman spectroscopy and photoluminescence measurements," *Journal of Applied Physics*, vol. 113, pp. 103504, 2013.
- [152] P. Kozodoy, H. Xing, S. P. DenBaars, U. K. Mishra, A. Saxler, R. Perrin, *et al.*, "Heavy doping effects in Mg-doped GaN," *Journal of Applied Physics*, vol. 87, pp. 1832-1835, 2000.
- [153] Z. Zou, J. Ye, K. Sayama, and H. Arakawa, "Direct splitting of water under visible light irradiation with an oxide semiconductor photocatalyst," *Nature*, vol. 414, pp. 625-7, Dec 6 2001.
- [154] S. Licht, "Multiple Band Gap Semiconductor/Electrolyte Solar Energy Conversion," *The Journal of Physical Chemistry B*, vol. 105, pp. 6281-6294, 2001.
- [155] J. R. Bolton, S. J. Strickler, and J. S. Connolly, "Limiting and realizable efficiencies of solar photolysis of water," *Nature*, vol. 316, pp. 495-500, 1985.
- [156] H. P. T. Nguyen, S. Zhang, K. Cui, X. Han, S. Fatholouloumi, M. Couillard, *et al.*, "p-Type Modulation Doped InGaN/GaN Dot-in-a-Wire White-Light-Emitting Diodes Monolithically Grown on Si(111)," *Nano Letters*, vol. 11, pp. 1919-1924, 2011.
- [157] J. Wu, W. Walukiewicz, K. M. Yu, J. W. Ager, E. E. Haller, H. Lu, *et al.*, "Small band gap bowing in  $\text{In}_{1-x}\text{Ga}_x\text{N}$  alloys," *Applied Physics Letters*, vol. 80, pp. 4741-4743, 2002.
- [158] C. G. Van de Walle and J. Neugebauer, "Universal alignment of hydrogen levels in semiconductors, insulators and solutions," *Nature*, vol. 423, pp. 626-628, 2003.
- [159] N. Kharche, M. S. Hybertsen, and J. T. Muckerman, "Computational investigation of structural and electronic properties of aqueous interfaces of GaN, ZnO, and a GaN/ZnO alloy," *Physical Chemistry Chemical Physics*, vol. 16, pp. 12057-12066, 2014.
- [160] M. Bertelli, P. Löptien, M. Wenderoth, A. Rizzi, R. G. Ulbrich, M. C. Righi, *et al.*, "Atomic and electronic structure of the nonpolar GaN (1 $\bar{1}$ 00) surface," *Physical Review B*, vol. 80, p. 115324, 2009.
- [161] K. Maeda, N. Sakamoto, T. Ikeda, H. Ohtsuka, A. Xiong, D. Lu, *et al.*, "Preparation of Core-Shell-Structured Nanoparticles (with a Noble-Metal or Metal Oxide Core and a Chromia Shell) and Their Application in Water Splitting by Means of Visible Light," *Chemistry – A European Journal*, vol. 16, pp. 7750-7759, 2010.

- [162] R. Leapman and C. Swyt, "Separation of overlapping core edges in electron energy loss spectra by multiple-least-squares fitting," *Ultramicroscopy*, vol. 26, pp. 393-403, 1988.
- [163] M. Mason, "Electronic structure of supported small metal clusters," *Physical review B*, vol. 27, p. 748, 1983.
- [164] K. Maeda, K. Teramura, N. Saito, Y. Inoue, and K. Domen, "Improvement of photocatalytic activity of  $(\text{Ga}_{1-x}\text{Zn}_x)(\text{N}_{1-x}\text{O}_x)$  solid solution for overall water splitting by co-loading Cr and another transition metal," *Journal of Catalysis*, vol. 243, pp. 303-308, 2006.
- [165] C. Hahn, Z. Zhang, A. Fu, C. H. Wu, Y. J. Hwang, D. J. Gargas, *et al.*, "Epitaxial Growth of InGaN Nanowire Arrays for Light Emitting Diodes," *ACS Nano*, vol. 5, pp. 3970-3976, 2011.
- [166] S. F. Chichibu, A. C. Abare, M. S. Minsky, S. Keller, S. B. Fleischer, J. E. Bowers, *et al.*, "Effective band gap inhomogeneity and piezoelectric field in InGaN/GaN multiquantum well structures," *Applied Physics Letters*, vol. 73, pp. 2006-2008, 1998.
- [167] J. Lähnemann, O. Brandt, C. Pfüller, T. Flissikowski, U. Jahn, E. Luna, *et al.*, "Coexistence of quantum-confined Stark effect and localized states in an (In,Ga)N/GaN nanowire heterostructure," *Physical Review B*, vol. 84, p. 155303, 2011.
- [168] A. Kubacka, M. Fernández-García, and G. Colón, "Advanced Nanoarchitectures for Solar Photocatalytic Applications," *Chemical Reviews*, vol. 112, pp. 1555-1614, 2011.
- [169] E. L. Warren, H. A. Atwater, and N. S. Lewis, "Silicon Microwire Arrays for Solar Energy-Conversion Applications," *The Journal of Physical Chemistry C*, vol. 118, pp. 747-759, 2013.
- [170] R. Marschall, "Semiconductor Composites: Strategies for Enhancing Charge Carrier Separation to Improve Photocatalytic Activity," *Advanced Functional Materials*, vol. 24, pp. 2421-2440, 2013.
- [171] J. Piprek and S. Li, "Electron leakage effects on GaN-based light-emitting diodes," *Optical and Quantum Electronics*, vol. 42, pp. 89-95, 2011.
- [172] W. Guo, M. Zhang, P. Bhattacharya, and J. Heo, "Auger recombination in III-nitride nanowires and its effect on nanowire light-emitting diode characteristics," *Nano Lett*, vol. 11, pp. 1434-8, 2011.
- [173] C. G. Van de Walle and D. Segev, "Microscopic origins of surface states on nitride surfaces," *Journal of Applied Physics*, vol. 101, p. 081704, 2007.
- [174] R. Calarco, T. Stoica, O. Brandt, and L. Geelhaar, "Surface-induced effects in GaN nanowires," *Journal of Materials Research*, vol. 26, pp. 2157-2168, 2011.
- [175] N. A. Sanford, P. T. Blanchard, K. A. Bertness, L. Mansfield, J. B. Schlager, A. W. Sanders, *et al.*, "Steady-state and transient photoconductivity in c-axis GaN nanowires grown by nitrogen-plasma-assisted molecular beam epitaxy," *Journal of Applied Physics*, vol. 107, p. 034318, 2010.
- [176] S. Zhang, A. T. Connie, D. A. Laleyan, H. Pham Trung Nguyen, Q. Wang, J. Song, *et al.*, "On the Carrier Injection Efficiency and Thermal Property of

- InGaN/GaN Axial Nanowire Light Emitting Diodes," *Quantum Electronics, IEEE Journal of*, vol. 50, pp. 483 - 490, 2014.
- [177] D. Holec, P. M. F. J. Costa, M. J. Kappers, and C. J. Humphreys, "Critical thickness calculations for InGaN/GaN," *Journal of Crystal Growth*, vol. 303, pp. 314-317, 2007.
- [178] K. D. Goodman, V. V. Protasenko, J. Verma, T. H. Kosel, H. G. Xing, and D. Jena, "Green luminescence of InGaN nanowires grown on silicon substrates by molecular beam epitaxy," *Journal of Applied Physics*, vol. 109, pp. 084336, 2011.
- [179] P. D. C. King, T. D. Veal, P. H. Jefferson, C. F. McConville, H. Lu, and W. J. Schaff, "Variation of band bending at the surface of Mg-doped InGaN: Evidence of p-type conductivity across the composition range," *Physical Review B*, vol. 75, p. 115312, 2007.
- [180] S. Zhao, B. H. Le, D. P. Liu, X. D. Liu, M. G. Kibria, T. Szkopek, *et al.*, "p-Type InN nanowires," *Nano Lett*, vol. 13, pp. 5509-13, 2013.
- [181] R. Marschall, "Semiconductor Composites: Strategies for Enhancing Charge Carrier Separation to Improve Photocatalytic Activity," *Advanced Functional Materials*, vol. 24, pp. 2421-2440, 2014.
- [182] A. Bumajdad and M. Madkour, "Understanding the superior photocatalytic activity of noble metals modified titania under UV and visible light irradiation," *Phys Chem Chem Phys*, vol. 16, pp. 7146-58, 2014.
- [183] K. Kumakura, T. Makimoto, and N. Kobayashi, "Mg-acceptor activation mechanism and transport characteristics in p-type InGaN grown by metalorganic vapor phase epitaxy," *Journal of Applied Physics*, vol. 93, pp. 3370-3375, 2003.
- [184] Z. C. a. T. F. Jaramillo, "Accelerating materials development for photoelectrochemical hydrogen production: Standards for methods, definitions, and reporting protocols," *J. Mater. Res.*, vol. 25, pp. 3-16, 2010.
- [185] S. Mubeen, J. Lee, N. Singh, S. Kramer, G. D. Stucky, and M. Moskovits, "An autonomous photosynthetic device in which all charge carriers derive from surface plasmons," *Nat Nano*, vol. 8, pp. 247-251, 2013.
- [186] L. Liao, Q. Zhang, Z. Su, Z. Zhao, Y. Wang, Y. Li, *et al.*, "Efficient solar water-splitting using a nanocrystalline CoO photocatalyst," *Nat Nano*, vol. 9, pp. 69-73, 2014.
- [187] J. S. Foresi and T. D. Moustakas, "Metal contacts to gallium nitride," *Applied Physics Letters*, vol. 62, pp. 2859-2861, 1993.
- [188] Z. Zou, J. Ye, K. Sayama, and H. Arakawa, "Direct splitting of water under visible light irradiation with an oxide semiconductor photocatalyst," *Nature*, vol. 414, pp. 625-627, 2001.
- [189] R. Asahi, T. Morikawa, T. Ohwaki, K. Aoki, and Y. Taga, "Visible-Light Photocatalysis in Nitrogen-Doped Titanium Oxides," *Science*, vol. 293, pp. 269-271, 2001.
- [190] X. Chen, L. Liu, P. Y. Yu, and S. S. Mao, "Increasing Solar Absorption for Photocatalysis with Black Hydrogenated Titanium Dioxide Nanocrystals," *Science*, vol. 331, pp. 746-750, 2011.
- [191] J. E. Northrup and J. Neugebauer, "Theory of GaN (10 $\bar{1}$ 0) and (11 $\bar{2}$ 0) surfaces," *Physical Review B*, vol. 53, pp. R10477-R10480, 1996.

- [192] Y. Park, J. Na, R. Taylor, C. Park, K. Lee, and T. Kang, "The recombination mechanism of Mg-doped GaN nanorods grown by plasma-assisted molecular-beam epitaxy," *Nanotechnology*, vol. 17, p. 913, 2006.
- [193] Y. Koide, D. E. Walker, B. D. White, L. J. Brillson, M. Murakami, S. Kamiyama, *et al.*, "Simultaneous observation of luminescence and dissociation processes of Mg–H complex for Mg-doped GaN," *Journal of Applied Physics*, vol. 92, pp. 3657-3661, 2002.
- [194] D. Dewsnip, J. Orton, D. Lacklison, L. Flannery, A. Andrianov, I. Harrison, *et al.*, "MBE growth and characterization of magnesium-doped gallium nitride," *Semiconductor science and technology*, vol. 13, p. 927, 1998.
- [195] B. Z. Qu, Q. S. Zhu, X. H. Sun, S. K. Wan, Z. G. Wang, H. Nagai, *et al.*, "Photoluminescence of Mg-doped GaN grown by metalorganic chemical vapor deposition," *Journal of Vacuum Science & Technology A*, vol. 21, pp. 838-841, 2003.
- [196] Q. Wang, X. Liu, M. G. Kibria, S. Zhao, H. P. T. Nguyen, K. H. Li, *et al.*, "p-Type dopant incorporation and surface charge properties of catalyst-free GaN nanowires revealed by micro-Raman scattering and X-ray photoelectron spectroscopy," *Nanoscale*, vol. 6, pp. 9970-9976, 2014.
- [197] S. M. Myers, A. F. Wright, M. Sanati, and S. K. Estreicher, "Theoretical properties of the N vacancy in p-type GaN(Mg,H) at elevated temperatures," *Journal of Applied Physics*, vol. 99, pp. 113506, 2006.
- [198] H. Harima, T. Inoue, S. Nakashima, M. Ishida, and M. Taneya, "Local vibrational modes as a probe of activation process in p-type GaN," *Applied Physics Letters*, vol. 75, pp. 1383-1385, 1999.
- [199] A. Kaschner, H. Siegle, G. Kaczmarczyk, M. Strassburg, A. Hoffmann, C. Thomsen, *et al.*, "Local vibrational modes in Mg-doped GaN grown by molecular beam epitaxy," *Applied Physics Letters*, vol. 74, pp. 3281-3283, 1999.
- [200] U. Kaufmann, M. Kunzer, M. Maier, H. Obloh, A. Ramakrishnan, B. Santic, *et al.*, "Nature of the 2.8 eV photoluminescence band in Mg doped GaN," *Applied Physics Letters*, vol. 72, pp. 1326-1328, 1998.
- [201] M. G. Kibria, S. Zhao, F. A. Chowdhury, Q. Wang, H. P. Nguyen, M. L. Trudeau, *et al.*, "Tuning the surface Fermi level on p-type gallium nitride nanowires for efficient overall water splitting," *Nat Commun*, vol. 5, p. 3825, 2014.
- [202] E. Arushanov, S. Siebentritt, T. Schedel-Niedrig, and M. C. Lux-Steiner, "Defect band transport in p-type CuGaSe<sub>2</sub>," *Journal of Physics: Condensed Matter*, vol. 17, p. 2699, 2005.
- [203] S. C. Jain, M. Willander, J. Narayan, and R. V. Overstraeten, "III-nitrides: Growth, characterization, and properties," *Journal of Applied Physics*, vol. 87, pp. 965-1006, 2000.
- [204] M. A. Hoffbauer, T. L. Williamson, J. J. Williams, J. L. Fordham, K. M. Yu, W. Walukiewicz, *et al.*, "In-rich InGaN thin films: Progress on growth, compositional uniformity, and doping for device applications," *Journal of Vacuum Science & Technology B*, vol. 31, pp. 03C114, 2013.

- [205] Ö. Tuna, H. Hahn, H. Kalisch, C. Giesen, A. Vescan, M. V. Rzheutski, *et al.*, "MOVPE growth, optical and electrical characterization of thick Mg-doped InGaN layers," *Journal of Crystal Growth*, vol. 370, pp. 2-6, 2013.
- [206] I. h. Ho and G. B. Stringfellow, "Solid phase immiscibility in GaInN," *Applied Physics Letters*, vol. 69, pp. 2701-2703, 1996.
- [207] O. Ambacher, "Growth and applications of group III-nitrides," *Journal of Physics D: Applied Physics*, vol. 31, p. 2653, 1998.
- [208] F. Yam and Z. Hassan, "InGaN: An overview of the growth kinetics, physical properties and emission mechanisms," *Superlattices and Microstructures*, vol. 43, pp. 1-23, 2008.
- [209] S. Pereira, M. Correia, E. Pereira, C. Trager-Cowan, F. Sweeney, K. O'donnell, *et al.*, "Structural and optical properties of InGaN/GaN layers close to the critical layer thickness," *Applied physics letters*, vol. 81, pp. 1207-1209, 2002.
- [210] C. A. Parker, J. C. Roberts, S. M. Bedair, M. J. Reed, S. X. Liu, and N. A. El-Masry, "Determination of the critical layer thickness in the InGaN/GaN heterostructures," *Applied Physics Letters*, vol. 75, pp. 2776-2778, 1999.
- [211] R. Singh, D. Doppalapudi, T. Moustakas, and L. Romano, "Phase separation in InGaN thick films and formation of InGaN/GaN double heterostructures in the entire alloy composition," *Applied Physics Letters*, vol. 70, pp. 1089-1091, 1997.
- [212] B. Reuters, M. Finken, A. Wille, B. Holländer, M. Heuken, H. Kalisch, *et al.*, "Relaxation and critical strain for maximum In incorporation in AlInGaN on GaN grown by metal organic vapour phase epitaxy," *Journal of Applied Physics*, vol. 112, p. 093524, 2012.
- [213] T. K. Ng, A. Gasim, D. Cha, B. Janjua, Y. Yang, S. Jahangir, *et al.*, "The formation of hexagonal-shaped InGaN-nanodisk on GaN-nanowire observed in plasma source molecular beam epitaxy," in *SPIE OPTO*, pp. 898613-898613-6, 2014.
- [214] H. Gerischer, "Electrochemical Techniques for the study of Photosensitization," *Photochemistry and Photobiology*, vol. 16, pp. 243-260, 1972.
- [215] B. O'Regan and M. Gratzel, "A low-cost, high-efficiency solar cell based on dye-sensitized colloidal TiO<sub>2</sub> films," *Nature*, vol. 353, pp. 737-740, 1991.
- [216] K. Maeda, M. Eguchi, W. J. Youngblood, and T. E. Mallouk, "Niobium oxide nanoscrolls as building blocks for dye-sensitized hydrogen production from water under visible light irradiation," *Chemistry of Materials*, vol. 20, pp. 6770-6778, 2008.
- [217] E. Bae and W. Choi, "Effect of the Anchoring Group (Carboxylate vs Phosphonate) in Ru-Complex-Sensitized TiO<sub>2</sub> on Hydrogen Production under Visible Light," *The Journal of Physical Chemistry B*, vol. 110, pp. 14792-14799, 2006.
- [218] Y. I. Kim, S. Salim, M. J. Huq, and T. E. Mallouk, "Visible-light photolysis of hydrogen iodide using sensitized layered semiconductor particles," *Journal of the American Chemical Society*, vol. 113, pp. 9561-9563, 1991.
- [219] H. Ozawa, M.-a. Haga, and K. Sakai, "A Photo-Hydrogen-Evolving Molecular Device Driving Visible-Light-Induced EDTA-Reduction of Water into Molecular

- Hydrogen," *Journal of the American Chemical Society*, vol. 128, pp. 4926-4927, 2006.
- [220] H. Park and W. Choi, "Visible-Light-Sensitized Production of Hydrogen Using Perfluorosulfonate Polymer-Coated TiO<sub>2</sub> Nanoparticles: An Alternative Approach to Sensitizer Anchoring," *Langmuir*, vol. 22, pp. 2906-2911, 2006.
- [221] W. J. Youngblood, S.-H. A. Lee, Y. Kobayashi, E. A. Hernandez-Pagan, P. G. Hoertz, T. A. Moore, *et al.*, "Photoassisted overall water splitting in a visible light-absorbing dye-sensitized photoelectrochemical cell," *Journal of the American Chemical Society*, vol. 131, pp. 926-927, 2009
- [222] W. J. Youngblood, S.-H. A. Lee, K. Maeda, and T. E. Mallouk, "Visible light water splitting using dye-sensitized oxide semiconductors," *Accounts of chemical research*, vol. 42, pp. 1966-1973, 2009.
- [223] R. Abe, K. Shinmei, K. Hara, and B. Ohtani, "Robust dye-sensitized overall water splitting system with two-step photoexcitation of coumarin dyes and metal oxide semiconductors," *Chem. Commun.*, pp. 3577-3579, 2009.
- [224] A. C. Khazraji, S. Hotchandani, S. Das, and P. V. Kamat, "Controlling dye (Merocyanine-540) aggregation on nanostructured TiO<sub>2</sub> films. An organized assembly approach for enhancing the efficiency of photosensitization," *The Journal of Physical Chemistry B*, vol. 103, pp. 4693-4700, 1999.
- [225] R. Abe, K. Sayama, and H. Arakawa, "Dye-sensitized photocatalysts for efficient hydrogen production from aqueous I<sup>-</sup> solution under visible light irradiation," *Journal of Photochemistry and Photobiology A: Chemistry*, vol. 166, pp. 115-122, 8/12/ 2004.
- [226] S. Li, J. Zhang, M. G. Kibria, Z. Mi, M. Chaker, D. Ma, *et al.*, "Remarkably enhanced photocatalytic activity of laser ablated Au nanoparticle decorated BiFeO<sub>3</sub> nanowires under visible-light," *Chemical Communications*, vol. 49, pp. 5856-5858, 2013.
- [227] R. Abe, K. Sayama, and H. Arakawa, "Efficient hydrogen evolution from aqueous mixture of I<sup>-</sup> and acetonitrile using a merocyanine dye-sensitized Pt/TiO<sub>2</sub> photocatalyst under visible light irradiation," *Chemical Physics Letters*, vol. 362, pp. 441-444, 2002.
- [228] R. Abe, K. Sayama, and H. Sugihara, "Effect of Water/Acetonitrile Ratio on Dye-Sensitized Photocatalytic H<sub>2</sub> Evolution under Visible Light Irradiation," *Journal of Solar Energy Engineering*, vol. 127, pp. 413-416, 2004.
- [229] S. Linic, P. Christopher, and D. B. Ingram, "Plasmonic-metal nanostructures for efficient conversion of solar to chemical energy," *Nature materials*, vol. 10, pp. 911-921, 2011.
- [230] S. C. Warren and E. Thimsen, "Plasmonic solar water splitting," *Energy & Environmental Science*, vol. 5, pp. 5133-5146, 2012.
- [231] W. Hou and S. B. Cronin, "A Review of Surface Plasmon Resonance-Enhanced Photocatalysis," *Advanced Functional Materials*, vol. 23, pp. 1612-1619, 2013.
- [232] Z. Liu, W. Hou, P. Pavaskar, M. Aykol, and S. B. Cronin, "Plasmon resonant enhancement of photocatalytic water splitting under visible illumination," *Nano letters*, vol. 11, pp. 1111-1116, 2011.

- [233] J. Lee, S. Mubeen, X. Ji, G. D. Stucky, and M. Moskovits, "Plasmonic photoanodes for solar water splitting with visible light," *Nano letters*, vol. 12, pp. 5014-5019, 2012.
- [234] A. K. Geim and K. S. Novoselov, "The rise of graphene," *Nat Mater*, vol. 6, pp. 183-191, 2007.
- [235] X. Wang, L. Zhi, and K. Mullen, "Transparent, Conductive Graphene Electrodes for Dye-Sensitized Solar Cells," *Nano Letters*, vol. 8, pp. 323-327, 2007.
- [236] J. Zhang, J. Yu, M. Jaroniec, and J. R. Gong, "Noble Metal-Free Reduced Graphene Oxide-Zn<sub>x</sub>Cd<sub>1-x</sub>S Nanocomposite with Enhanced Solar Photocatalytic H<sub>2</sub>-Production Performance," *Nano Letters*, vol. 12, pp. 4584-4589, 2012.
- [237] G. Xie, K. Zhang, B. Guo, Q. Liu, L. Fang, and J. R. Gong, "Graphene-Based Materials for Hydrogen Generation from Light-Driven Water Splitting," *Advanced Materials*, vol. 25, pp. 3820-3839, 2013.
- [238] Y. Zhang, N. Zhang, Z.-R. Tang, and Y.-J. Xu, "Graphene Transforms Wide Band Gap ZnS to a Visible Light Photocatalyst. The New Role of Graphene as a Macromolecular Photosensitizer," *ACS Nano*, vol. 6, pp. 9777-9789, 2012.
- [239] P. Du and R. Eisenberg, "Catalysts made of earth-abundant elements (Co, Ni, Fe) for water splitting: recent progress and future challenges," *Energy & Environmental Science*, vol. 5, pp. 6012-6021, 2012.
- [240] S. Min and G. Lu, "Sites for High Efficient Photocatalytic Hydrogen Evolution on a Limited-Layered MoS<sub>2</sub> Cocatalyst Confined on Graphene Sheets—The Role of Graphene," *The Journal of Physical Chemistry C*, vol. 116, pp. 25415-25424, 2012.
- [241] Z.-G. Zhao, J. Zhang, Y. Yuan, H. Lv, Y. Tian, D. Wu, *et al.*, "In-Situ Formation of Cobalt-Phosphate Oxygen-Evolving Complex-Anchored Reduced Graphene Oxide Nanosheets for Oxygen Reduction Reaction," *Sci. Rep.*, vol. 3, 2013.
- [242] S. C. Roy, O. K. Varghese, M. Paulose, and C. A. Grimes, "Toward solar fuels: photocatalytic conversion of carbon dioxide to hydrocarbons," *ACS Nano*, vol. 4, pp. 1259-1278, 2010.
- [243] B. Kumar, M. Llorente, J. Froehlich, T. Dang, A. Sathrum, and C. P. Kubiak, "Photochemical and photoelectrochemical reduction of CO<sub>2</sub>," *Annual review of physical chemistry*, vol. 63, pp. 541-569, 2012.
- [244] G. A. Olah, "Beyond oil and gas: the methanol economy," *Angewandte Chemie International Edition*, vol. 44, pp. 2636-2639, 2005.
- [245] S. Bensaid, G. Centi, E. Garrone, S. Perathoner, and G. Saracco, "Towards artificial leaves for solar hydrogen and fuels from carbon dioxide," *ChemSusChem*, vol. 5, pp. 500-521, 2012.